Interactions in colloidal systems

Jardine, Roger

Award date:
2001

Awarding institution:
University of Bath

INTERACTIONS IN COLLOIDAL SYSTEMS

Submitted by Roger S. Jardine

for the degree of

Doctor of Philosophy

of the University of Bath

2001

ProQuest LLC
789 East Eisenhower Parkway
P.O. Box 1346
Ann Arbor, MI 48106-1346

Acknowledgements

This work was supported by the Engineering and Physical Sciences Research Council. I would like to thank Alfons van Blaaderen for his generous assistance with the confocal microscopy experiments. I thank my flatmates, Claire and Phil for their friendship and I also thank those in the lab; Phil, Neil, David, Simon, Simon and Jeremy, for many valuable discussions. I would also like to acknowledge Gareth Price who made his extensive laboratory facilities available to me.

Finally, I would particularly like to thank Paul Bartlett for all the assistance he has given me and the enthusiasm he has shown throughout this work.

To Andrea

Summary

Stable poly(methyl methacrylate) [PMMA] colloids were prepared by dispersion polymerization. Fluorescent dyes were synthesized, and were included in the PMMA colloids to produce fluorescent colloids, suitable for viewing with fluorescent laser scanning confocal microscopy. The possibility of resolving well-separated PMMA colloids using fluorescence laser scanning confocal microscopy is demonstrated.

In suspensions of the PMMA particles with a sufficiently low polydispersity homogenously nucleated crystals are formed and the phase behaviour of these colloids show good agreement with hard-sphere theory.

Mixtures of two colloidal samples of different sizes were also prepared. The phase behaviour and structures shown in the light scattering data of these binary mixtures is compared with theoretical data. The predicted phase diagram is dominated by the existence of superlattices. The use of fluorescence laser scanning confocal microscopy enables the detection of a partial superlattice which would be difficult to detect using light scattering techniques.

A novel binary mixture of colloids and microemulsions with a size ratio of $\sim$0.1 is studied and correlations and ordering of the particles are examined in small-angle neutron scattering experiments. The results show that the addition of even a small quantity of microemulsion has a dramatic effect on the colloidal interactions. The colloid-colloid structure factor has been described by a potential based on the hard-sphere model which is modified to include a depletion attraction and a simple repulsive step.

Contents

Chapter 1

General Introduction

Colloids are found throughout nature and in many modern manufactured materials. A brief history of colloidal science and discovery is given in this chapter, together with some of the important principles that stem from the science behind the behaviour of colloidal systems.

1.1 Introduction

The first evidence of the nature of colloidal systems was recognized as long ago as 1774, when colloidal systems of gold particles were described by Juncher and Macquer as being *"extremely finely divided gold in a fluid"* [1]. The term colloid was first used by Graham in 1861 when he distinguished between those solutions which would pass through a membrane and those solutions which would did pass through, but remained on one side of the membrane. Solutions of the latter type, Graham termed colloids, the word being derived from the Greek word for glue, $\kappa o \lambda \lambda \alpha$.

Before the experiments of Graham, Brown observed the seemingly random motion of suspended pollen grains using a microscope in 1828 [2]. This irregular motion is now referred to as Brownian motion and is the result of random collisions of the solvent molecules with the particles. The molecular motion of the solvent is thus displayed via the random motion of the pollen particles. Brownian motion was explained by Einstein [3, 4] and Langevin [5] at the beginning of the twentieth century. Colloidal particles can be considered as thermodynamically equivalent to atoms, as recognized by Onsager in his pioneering work on the phase behaviour of lyotropic colloids [6], thus paving the way for an area of research using colloids as models for investigating atomic theories. Indeed, the nature of phases shown in colloidal suspensions is analogous to those shown in atomic systems. Crystalline phases of colloidal particles are discussed in this work.

Most consider that the range of sizes that may constitute a colloidal particle is somewhat imprecise and that any limits are a result of two criteria. First, the particle must be large enough to interact with the solvent in an averaged way. Motion is then described by macroscopic properties of the solvent, *e.g.*

temperature. This occurs when the size of the particle is at least ten times the length of a solvent molecule. Secondly, the particles must be small enough that the motion they exhibit is generally due to Brownian motion. In particular, large particles may exhibit motion that is mostly due to the earth's gravitational field, and sedimentation occurs. These criteria set the diameter of a colloidal particle between 1 nm and 1 μm(which is the IUPAC definition [7]).

The size of a typical colloidal particle is some 10^3 times larger than that of an atom, making colloidal systems experimentally more accessible to direct observation than atomic systems.

The size of colloidal particles means the use of visible light is appropriate as an experimental tool for probing colloidal systems, for example light scattering and light microscopy are both methods used in this work to measure properties of colloidal systems.

In addition to being more accessible on a spatial scale, the size of colloidal particles means that observation of events is also more accessible on a temporal scale than it is for atomic systems. Diffusion and relaxation times are substantially longer [8], so phase transitions, for example, may occur on a timescale of the order of seconds or minutes, allowing easier observation. In addition the relatively slow speed of these transitions allows metastable phases such as glasses and gels to be studied.

As well as being experimentally more accessible than atomic systems, colloidal systems have the useful property that the interaction between the particles can be altered, as the interaction depends upon many factors including, the nature of the dispersant, colloidal particle and particle surface. A wide range of colloidal systems, consisting of many different materials have been investigated, resulting

in the study of numerous interparticle potentials [9, 10]. Particular interest has been shown in colloidal systems displaying behaviour commensurate with a hard-sphere repulsive interaction. This is a very simple interaction and forms a good starting point for developing theories to account for the behaviour of both atomic and colloidal systems.

The study, both experimental and theoretical, of the structures and processes found within colloidal systems is a growing field encompassing many areas of chemistry and physics [11]. In order to study the fundamental principles behind the properties of various colloidal systems, the synthesis of model colloidal dispersions, containing particles with a well defined range of properties such as size, composition and interactions, has been a subject of some interest for many years [12, 13].

Colloidal systems are also an important constituent in many everyday materials. Items as varied as paint [14, 15], ice-cream [16], pesticide [17] and make-up [18, 19] include colloidal particles. The colloidal systems present in these examples and the many other products and processes of commercial importance are generally too complex to facilitate any general insights into colloidal science as they contain a complex collection of materials with a large range of particle sizes, shapes and interactions.

The remainder of this introductory chapter will expand on the concept of particle interaction and present a few of the model colloidal systems most commonly used for experiment today. In this work monodisperse poly(methyl methacrylate) spheres have been used as model particles and the particle interactions and behaviour of this system are also presented in this chapter.

1.2 Colloidal Interaction and Stability

A fundamental aspect in much of the science used in the preparation of materials containing colloids is the control of the stability of colloidal suspensions to prevent flocculation and aggregation. Understanding the reasons for the stability of colloidal dispersions has been a major theme in the development of colloidal science for over one hundred years. The early experiments by Hardy [20], which showed that the additions of electrolytes in certain concentrations to stable dispersions had a catastrophic effect and led to immediate instability, have been widely studied. However it was not until the 1940s that a clear theoretical insight was given to enable a physical picture of colloidal stability to be formed. To understand the reasons for colloidal stability and the rich variety of phases formed we consider briefly the form of interactions between colloidal particles. (For a detailed overview see references [21] and [22].)

Since colloids can be considered as thermodynamically equivalent to atoms, a useful starting point in describing colloidal interactions is the theory of simple molecular liquids [23]. For molecular systems where intermolecular interactions are negligible, only the kinetic energy associated with the motion of the centre of mass of each molecule contributes to the intermolecular mode of motion. Such kinetic energy will give rise to equilibrium bulk behaviour of an ideal gas system. The fundamental property that determines the existence of various states of matter is the intermolecular interaction. The total potential energy for of a system of N particles can be written as;

$$U(N) = U(\mathbf{r}_1, \mathbf{r}_2 ... \mathbf{r}_N) \tag{1.1}$$

where $r_i (i = 1, 2...N)$ denotes the position of the ith particle. For a colloidal system this describes the free energy of a system configuration. It is then often assumed that the total energy can be written as the sum of the interactions between all pairs of molecules in the system, *i.e.*

$$U(\mathbf{r}_1, \mathbf{r}_2 ... \mathbf{r}_N) = \sum_{pairs} u(\mathbf{r}_i, \mathbf{r}_j) \tag{1.2}$$

It is important to acknowledge that three-,four- and higher-body interactions exist. Even in simple atomic systems three body interactions are required to explain some properties. Unfortunately for complex molecules little is known about the nature of these many-body interactions. Choosing an effective pair potential between particles often compensates for these effects by including some effects of the many-body interactions within the pair-potential model.

The pairwise interaction potential of a simple monatomic liquid has the general form shown in Figure 1.1. The interaction depends only on the centre-to-centre separation of the molecules. At large separations, $r > \sigma$, the interaction is attractive due to the van der Waals attraction. At small separations, overlap of the electron orbitals of the two molecules gives rise to a repulsion which rises steeply as the centre-to-centre separation decreases. These effects are commonly modelled via a Lennard-Jones potential U_{LJ} as a function of the centre to centre separation between atoms, r.

$$U_{LJ}(r) = 4\varepsilon \left[\left(\frac{d}{r} \right)^{12} - \left(\frac{d}{r} \right)^{6} \right] \tag{1.3}$$

where d can be considered as the diameter of the atom, and ε gives the depth of

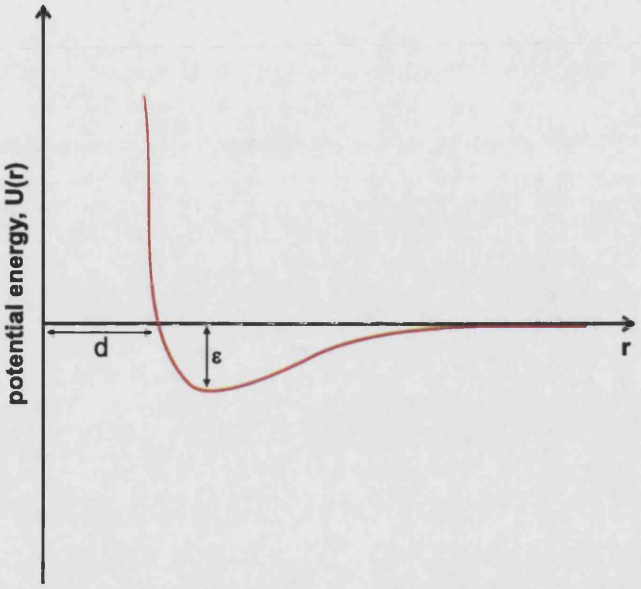

Figure 1.1: The potential energy of interaction betweens two atoms, such as argon, separated by a distance r, where d is the collision diameter, and ε gives the depth of the potential well

the potential well.

The Lennard-Jones pair potential illustrated in Figure 1.1 shares certain features with the potential derived for two spherical, charged colloidal particles. To successfully model colloidal pair-potentials it is necessary to account for factors particular to the colloidal system under consideration. In common with the Lennard-Jones theory, many of the potentials used to model colloidal systems are derived by a separate consideration of repulsive and attractive forces which are added together.

It has been well known that an attractive force exists between atoms since the work of van der Waals in 1873. The nature of this attraction was more fully understood in 1930 when London explained how fluctuations in the charge den-

sity within the electron clouds of atoms and molecules can give rise to an oscillating dipole moment. By integrating this attractive force over all the atoms in a colloidal particle an attractive van der Waals potential is formed. This van der Waals attraction is a function of the contrast between the frequency-dependent dielectric-constant of the particle and the dispersion medium [24]. This attractive force is always present between two bodies of matter, and between a collection of atoms such as a colloidal particle leads to a relatively long range interaction which acts over 10-100 nm. This attraction leads to the aggregation of colloidal particles unless a repulsive force can be introduced to prevent it. Two common methods for introducing a repulsive element to the colloidal interaction are *charge stabilization* and *static stabilization.*

1.2.1 Charge Stabilization

Charge stabilization is usually found in colloidal systems with polar dispersant media, most commonly aqueous systems. A surface charge forms on the colloid, generated via ionization of surface groups, ion adsorption, etc. This surface charge generates an increased concentration of counter-ions close to the particle surface and a diffuse layer of co-ions in the surrounding solution. Overlap of this electrical double layer gives rise to a repulsive force resulting in a repulsive part to the interaction of the colloidal particles [22]. The rate of decrease of the repulsion, as the centre-to-centre separation increases, is strongly dependant on the electrical double layer thickness, which is related to the concentration of electrolytes. At low electrolyte concentrations electrostatic repulsion provides a long range force, whereas at high electrolyte concentrations the repulsive energy term falls rapidly.

Derjaguin and Landau [20] and Verwey and Overbeek [22] introduced the idea

that the sum of the electric double layer repulsion and the van der Waals attraction could be used to construct a pair potential function for the interaction between two colloidal particles, often referred to as the DLVO potential [25]. The form of the DLVO potential is shown in Figure 1.1. Detailed analyses were proposed for interaction between flat plates and between spheres. These analyses were verified experimentally by the use of soap films [26] and molecularly smooth mica plates [27], which allowed the van der Waals attraction between smooth surfaces to be measured down to distances of the order of a few nanometres. This technique was extended and developed [28] and many measurements have been made between mica surfaces in liquids. These measurements obtained a direct measurement of the net force of interaction between macroscopic surfaces and have provided much valuable information [21]. However, the time scale of these measurements is relatively long [29], and generally, to measure colloidal interactions we need to take into account Brownian motion within the dispersion, which means that any direct measurement of the nature of colloidal interaction can be difficult. Recently a technique to enable the direct measurement of colloidal forces in charged systems has been developed using atomic force microscopy [30, 31, 32]. With this technique the colloid is attached to the end of an atomic force microscope [AFM] cantilever. A flat surface of interest is then cycled toward the colloid and the cantilever deflection is measured. These measurements show good agreement with DLVO theory [30]. However, as yet the technique is not well suited to particles with diameters smaller than a few micrometres, due to restrictions in attaching the colloid to the cantilever tip.

Another common method for introducing a repulsive element to the interaction between colloidal particles is steric stabilization.

1.2.2 Steric Stabilization

Steric stabilization involves attaching polymers to the colloidal surface, which prevent the colloidal particles from getting within close range of each other, thereby diminishing any effect of van der Waals attractive forces.

Many types of polymers are used to provide stabilization and different methods for attaching polymers to the particle surface are available [33]. Steric stabilization is equally effective in both aqueous and non-aqueous systems, however for non-aqueous systems charge stabilization is not generally practical, and so steric stabilization is particularly important for the many industrial processes involving non-aqueous colloidal systems. In order to prevent coagulation, the polymeric layer must ensure the particles are separated by a distance where van der Waals attractive forces are insignificant. This can be achieved by having a sufficiently thick layer of polymer, by using, for example, a polymer of a suitable molecular weight extended in a good solvent.

It has been shown that the most effective steric stabilizers are amphipathic block or graft copolymers [33]. These consist of two chemically bound homopolymer components, a lyophobic anchor polymer and a lyophilic stabilizing chain. The anchor units are ideally insoluble in the dispersion medium, encouraging the anchor polymer to attach to the colloidal particle surface, limiting desorption of the stabilizer during movement and collisions. The stabilizing polymer chains must be soluble in the dispersion medium, extending out into the medium, away from the particle surface.

Quantitative theories of steric stabilization are complex [34, 35]. A large number of phenomena give rise to the interaction forces between two stabilizing layers of polymer [36]. In general the interactions depend on the density of polymer cov-

erage at the particle surface, the method and strength of the anchoring between stabilizing polymer and colloid and the solvency of various components in the dispersion media. Prediction of polymer conformations at particle surfaces [37] indicates that the repulsion in stabilized systems stems from the decrease in entropy due to the restriction of available movement for the polymer segments in overlapping stabilizing layers [38].

The possibility of direct measurement of forces between sterically stabilized colloids has recently emerged with the development of a technique known as optical trapping. Optical trapping is achieved using a laser beam, focussed to a diffraction-limited spot, particles in the solvent are attracted and trapped in three dimensions into the region of highest light intensity. The force required to hold the particle can be measured, and therefore can be used to measure the properties of colloidal interactions and colloidal dynamics [39] and to manipulate colloids [40]. This technique is still emerging, but has the potential to provide exciting new insights into fundamental processes in colloidal science.

1.3 Model systems

There are many colloidal model systems consisting of metallic particles, such as gold, silver, mercury and platinum. Non-metallic systems include carbon, sulfur,and selenium. There are also many different methods to prepare these particles, including chemical, electrochemical and mechanical methods. Three of the most commonly used model systems are polystyrene in polar dispersants and nonaqueous suspensions of silica and poly(methyl methacrylate) [PMMA].

1.3.1 Polystyrene

The first model colloidal system consisted of charge stabilized polystyrene spheres [41] and were among the first polymeric latex particles to be made available commercially. The particles consist of many polystyrene molecules, associated so that the ends of the chains containing the hydrophilic groups are generally at the surface of the particle. In a polar suspension medium the surface groups ionize and the particles acquire a charge. These particles therefore interact via a charge-stabilized mechanism, and the strength of the interaction can be modified by adding electrolyte. Polystyrene systems are still popular as models today in experiments where a tunable interaction is required as the synthesis is straightforward and a large body of knowledge exists on the properties of the polystyrene particles. However the van der Waals attractions between the particles are strong, since there is a substantial refractive index mismatch between polystyrene and most polar liquids. Strong electrostatic repulsion is therefore required to stabilize the colloids and the inherent complexity of this attraction/repulsion system led research into sterically stabilized model systems.

1.3.2 Silica

Colloidal silica has a wide range of technological applications and is one of the most common model colloidal systems in use today. Silica colloids may be prepared by several methods, Iler [42] has a comprehensive review of the literature. On initial preparation colloidal silica is a charge stabilized colloidal system, however, it is rarely used as a model colloid in this form as it has a complex surface chemistry [10]. Modification of the silica particle is generally undertaken to add steric stabilization to the particle [43]. The most commonly used steric stabilizer

is comprised of stearyl chains approximately 2 nm in length, with one end chemically attached to the surface of the particles. These particles can be synthesized with diameter ranging from 20 nm to 1 μm with a small average spread of sizes. The distribution of particle size is usually expressed in terms of the polydispersity, σ, where $\sigma = \sqrt{< r^2 >}/ < r >$ and r is the particle radius and the brackets indicate an ensemble average. Typical polydispersities for colloidal silica range from ~0.2 at 20 nm to ~0.02 at 1 μm . The refractive index, $n_D \sim 1.45$ allows the particles to be dispersed in a variety of liquids whose refractive indices are similar to those of the particles. The resulting index-matched suspensions remain nearly transparent, even at high volume fractions of colloid and are suitable for light scattering studies.

Although the repulsive interaction from the steric stabilizer is very strong over the short distance of the stearyl chain, these particles can still carry a residual charge making the particle interaction more complex. Another drawback with silica based colloidal systems is the considerable density mismatch between the particles and solvents, meaning colloids of over 500 nm may suffer from non-negligible sedimentation [44].

1.3.3 Poly(methyl methacrylate) [PMMA]

The system used throughout this work is a system which has been used increasingly over recent years cite310,23,116,granular and consists of spherical particles of poly(methyl methacrylate) created by dispersion polymerization techniques [45, 46]. These particles are prevented from flocculating by coating them with a layer of a *comb* polymer, consisting of a PMMA backbone with poly(12-hydroxystearic acid) [PHSA] *teeth*. The length of the densely-packed PHSA stabilizer molecules is about 10 nm.

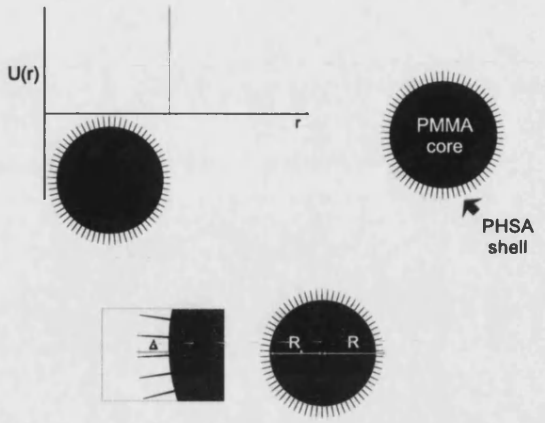

Figure 1.2: The colloids used in this work are sterically stabilized polymer colloids consisting of a polymer core of poly(methyl methacrylate) [PMMA] (with a radius defined as R_c), stabilized by a thin shell of poly(12-hydroxystearic acid [PHSA] (Δ defines thickness of shell

PMMA in colloidal particles has a refractive index of $n_D \sim 1.49$. A one-component, non-polar dispersant with a refractive index identical to that of the PMMA particle has so far proved elusive, and a combination of two liquids has generally been used to provide an index match. Most studies, including this one, have used a mixture of cis/trans decahydronapthalene [Decalin] $n_D = 1.47$ and a small amount of carbon disulfide [CS_2] $n_D = 1.63$. Carbon disulfide is known to penetrate the PMMA cores of the particle slightly, resulting in an increase in radius of approximately 3%, however this penetration is complete within hours, after which the particle properties remain constant over many months [47].

Although the particles and dispersion medium have a very close density match, it is inevitable that the earth's gravitational pull will result in sedimentation over time. With colloids subjected to time-averaged zero gravity by slowly rotating the samples at one revolution per day the sedimentation is negligible over many months [48]. To completely eliminate gravitational effects, some experiments have been carried out in the microgravity environment provided by the NASA Space

Shuttle [49, 50].

Since there is almost no electrostatic charge present in the PMMA colloidal system, it is suggested that any interaction between particles would be dominated by the steric repulsion. Indeed, it has been shown that the interactions between the particles in the system described above, increases from near zero when the polymer layer first overlap, to many kT over distances of a few nanometres. The scale over which there is interaction is therefore small compared to typical particle radii of a few hundred nanometres, and the interaction can be described as essentially hard-sphere [51, 52, 53]. The hard-sphere interaction is one of the simplest imaginable, the form of the interaction is illustrated in Figure 1.2. The PMMA colloidal system, described briefly above and in more detail in Chapters 3 and 4, thus provides a good basis for experiments which may provide insight into the processes occurring in atomic systems as well as aiding understanding of more complex colloidal systems.

1.4 Colloidal Phase Behaviour

The thermodynamic properties (phase behaviour, structure etc.) of a suspension of colloidal particles, are determined by the form of the interparticle potential. The nature of this potential can vary greatly, according to the properties of the particle and suspension medium. Typically in the case of a stable suspension, a repulsion is followed by an attraction, the form of the interparticle potential thereby usually qualitatively resembles that of the Lennard-Jones potential of atoms [10]. Hence, colloidal suspensions can demonstrate a range of equilibrium phase behaviour, similar to that of a one component atomic system. If the interparticle potential is carefully controlled, colloidal systems can for example, exhibit tran-

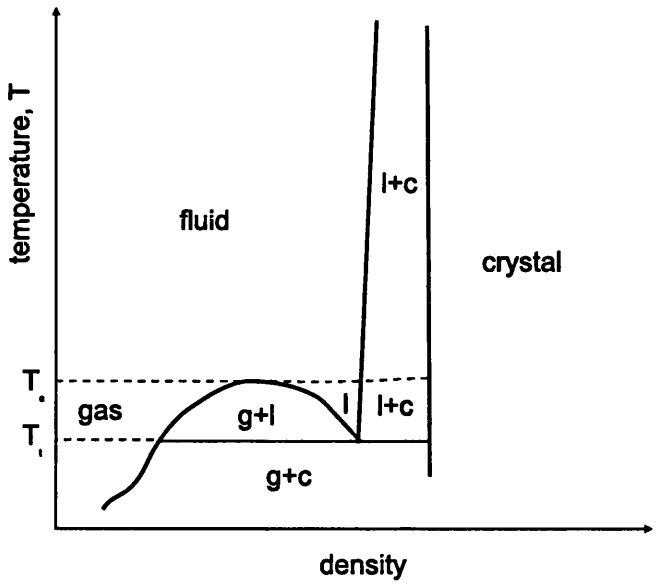

Figure 1.3: Temperature-density projection of a "generic" phase diagram of spherical colloids, containing phases equivalent to gas(g), liquid(l) and crystalline(c) atomic phases.

sitions analogous to gas-liquid and liquid-solid phase transitions [54]. However, although the interaction potential of non-metallic atoms is assumed to be temperature and density independent, the interaction potential of colloidal particles in a dispersion is often affected by temperature, concentration and other suspension conditions. For example the van der Waals interactions of sterically stabilized colloids are usually temperature dependent. Assuming a colloidal pair-potential which is temperature-independent, Figure 1.3 represents the phase diagram of "generic" colloids, interacting with a typical colloidal potential containing both attractive and repulsive contributions.

Where the attractive part of the pair-potential is weak, the temperature (room temperature) will be much larger than the critical temperature, T_C, corresponding to a supercritical isotherm, $T > T_C$. In this region the phase diagram is

split into three distinct sections. At low ϕ the state is fluid, and as the volume fraction is increased, so the osmotic pressure increases until the freezing concentration is reached, at which point crystallization occurs. Between the freezing and melting concentrations, the increasing osmotic pressure results in an increase in the amount of the crystalline phase. At the melting concentration, the osmotic pressure again increases with increasing volume fraction, and the crystal is compressed. A great many experimental studies of colloidal phase behaviour have concentrated around the supercritical region between melting and freezing volume fractions.

In this work we consider the phase behaviour of hard-sphere systems since an assembly of hard sphere colloids constitutes one of the simplest, yet most important models of condensed-matter physics [55, 56]. Hard-spheres have no critical point so that all observed behaviour is supercritical. There was initially much controversy [159] over whether such a system with no attractive part to the interaction potential could crystallize. The debate began when the possibility of a freezing transition was first observed in a computer simulation by Alder and Wainwright in 1957 [58]. These findings were then quantitatively confirmed by Hoover and Ree in 1968 [59]. They found that as the concentration is increased, an assembly of hard spheres undergoes a first-order freezing transition at a volume fraction, $\phi_f = 0.494$ and a melting transition of $\phi_m = 0.545$, with the hard-spheres forming a close-packed crystalline structure. An attractive part to the pair potential is therefore not required to organize particles into crystals. One of the first experimental studies into the freezing of hard-sphere colloids was carried out by Kose and Hachisu [60]. Suspensions with an approximately hard-sphere interaction were prepared using PMMA colloids dispersed in benzene. Crystallization was observed to occur in several samples. In a number of subsequent experimental studies the phase behaviour of hard-sphere colloids was investigated in more

comprehensive detail, using the same PMMA-PHSA system of colloidal spheres as used in this study [61, 62, 53]. Samples were prepared spanning the range between freezing and melting transitions. Crystalline phases were observed, with samples containing coexisting colloidal fluid and polycrystalline phases. The fractions of the samples occupied by the polycrystalline phase were measured and scaled, the results showing close comparison with the transitions predicted by the Monte-Carlo hard-sphere simulation by Hoover and Ree [59]

These many results give a strong indication that the phase behaviour shown by this PMMA-PHSA system is very similar to the phase-behaviour expected for hard-spheres and gives further indication that the hard-sphere interaction is a good approximation for the interactions in these model colloidal suspensions.

1.5 Crystal Structure

Ordered arrays of colloids have captured the attention of physicists for at least fifty years. For example the unusual mechanical properties of bentonite sols or the fascinating optical properties of Schiller layers in iron oxide sols are thought to stem from the ordering of monodisperse inorganic particles [62]. It was clear that long-range ordered crystals of monodisperse colloidal particles existed within nature. For example, investigation into the bushy stunt virus revealed highly-ordered close-packed arrays of the almost spherically shaped particles [63]. The ordered structures of these and other virus particles can be complex, and have yet to be replicated using model particles. Other natural examples have stimulated research in synthetic colloidal crystals however, in particular the investigation of crystalline structure of opal gems by Sanders. Trying to answer the question of whether opal contained voids capable of holding water, Sanders discovered in

1964, using electron microscopy, that the opal gems consist of uniform spheres of amorphous silica regularly arranged over large areas [64]. Because of the difference between the refractive index of the silica particles and the voids, the Bragg refraction of light gives the opals their sparkling or opalescent quality. Iler was able to reproduce the natural processes of opal formation to recreate the structures within the laboratory [42] by the slow formation and sedimentation of silica spheres over periods of years. The lack of control over natural specimens and the slow processes involved in synthetic opal formation meant neither became popular as tools for scientific research. All of the recent research into colloidal crystals has been brought about by the development of simple methods for preparing monodisperse synthetic colloids.

In hard-sphere PMMA suspensions, homogeneously nucleated crystals form at volume fractions about the melting point transition. The structure of these crystals has been determined by static light scattering [SLS] (see Section 2.3) and transmission electron microscopy [TEM]. The results show that the crystals comprise of close-packed structures of hexagonally packed layers (see Figure 1.4).

Starting with a single hexagonal close packed plane, labelled position A, there are two possibilities for the position of the next layer; Position B can be obtained by a displacement relative to A of $^1/_3\mathbf{a}+{}^2/_3\mathbf{b}$, and position C is obtained by a displacement relative to A of $^2/_3\mathbf{a}+{}^1/_3\mathbf{b}$, where $\mathbf{a}$ and $\mathbf{b}$ are hexagonal lattice vectors in the plane. So, for example, a *face-centred cubic* [fcc] close-packed structure can be generated by the sequence $ACBACB...$ or its symmetric twin $ABCABC...$ whilst a *hexagonal close-packed* [hcp] structure can be generated by the stacking sequence generated by the representation $ABABAB$. However, close packing can be equally well achieved by randomly stacked layers, to enable the labelling of such stacking, the probability that the relative positions of the reference layer and a layer two layers away from the reference layer are equal is labelled ξ , thus

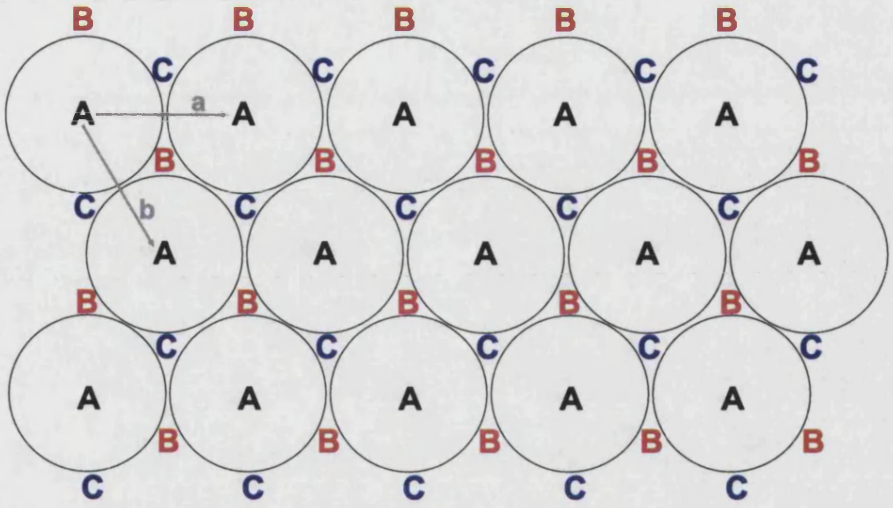

Figure 1.4: Schematic view of a hexagonally close-packed layer with the two possibilities, where B and C show the positions of the sphere centres for alternate layer positions

ξ=0 gives hcp crystal and ξ=1 gives an fcc crystal. There is little reason to expect there to be a preference for one layer position over another in a system with hard-sphere interactions, and indeed measurements have shown this value to be ξ ~0.5 for crystals formed in hard-sphere PMMA systems indicating a *randomly stacked close-packed* [rscp] crystal structure [65, 66].

1.5.1 Binary Mixtures of Hard-Sphere Colloids

Binary mixtures contain two distinct types of particles, generally both particles are of the same composition, but have different radii. This introduces added complexity compared to a one-component system, and with it the possibility that mixtures may exhibit more complex behaviour, and form a richer range of

phases than a simple one-component system. The first evidence for the formation of complex binary structures came from the observations on opal by Sanders [64]. In addition to the one component crystal structures he found, in a unique sample Sanders discovered opal containing silica spheres of two different sizes, 210 nm and 362 nm (giving a size ratio of α=0.58). Sanders identified two crystalline structures in the opal specimen, with the relative numbers of each sphere denoted as LS_2 and LS_{13}, where L and S are the large and small spheres, respectively. Identical structures exist in atomic systems, the LS_2 structure found in opal is identical to the structure found in the alloy AlB_2 for example.

If the colloidal particles in binary mixtures are identical in every respect except size, we can expect the relative stability of various phases formed to be sensitive to the size ratio $\alpha = \sigma_S/\sigma_L$, where σ_S and σ_L are the diameters of the small and large spheres. Questions regarding the effect of the relative size difference on the behaviour of the mixture, and the stability and structure of phases formed is raised. Computer simulation of hard-spheres [67] shows that as the spheres become more dissimilar in size, so the degree of miscibility of the two hard-sphere components reduces until at $\alpha < 0.875$ the phase diagram contains a eutectic point. Freezing then occurs by a process of size segregation to give two solid phases, one containing mainly small spheres, the other mainly large. For $\alpha \geq 0.85$ the behaviour is well defined, with density functional arguments [68, 69] in good agreement with computer simulation [67]. The understanding of the behaviour of hard sphere mixtures with a smaller size ratio is more limited. In view of the scarcity of results from simulation, experimental measurements of the phase behaviour of hard-sphere colloids have an important role to play.

Bartlett *et al.* studied binary mixtures of PMMA-PHSA colloidal spheres at size ratios of α=0.31 as inspired by the opal structures and α=0.58 [71, 72]. Examples of both LS_2 (see Figures 1.6 and 1.5) and LS_{13} (Figure 1.7) were observed in the

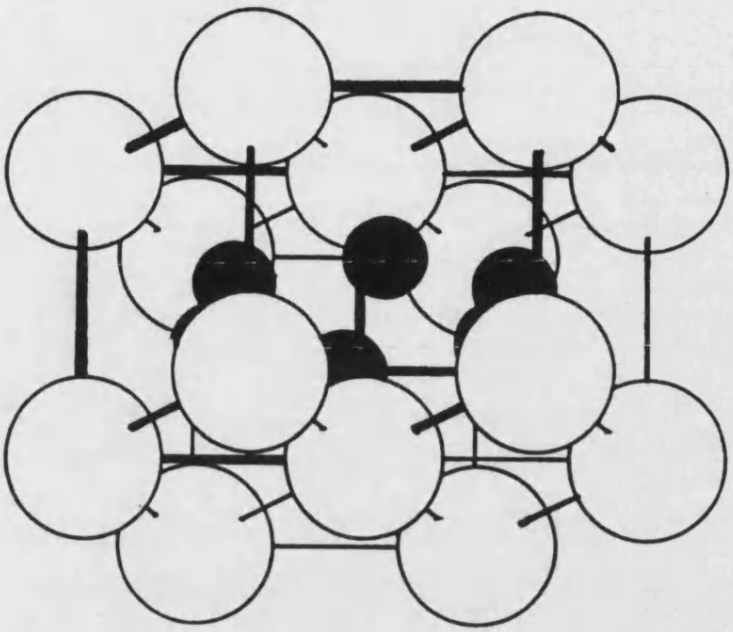

Figure 1.5: Schematic view of a the crystal structure of LS_2. The large spheres (L) are packed in horizontal hexagonal layers with plane layers of the smaller spheres (S) interleaved. The unit cell is outlined in bold. (from Yoshimura and Hachisu, 1983)

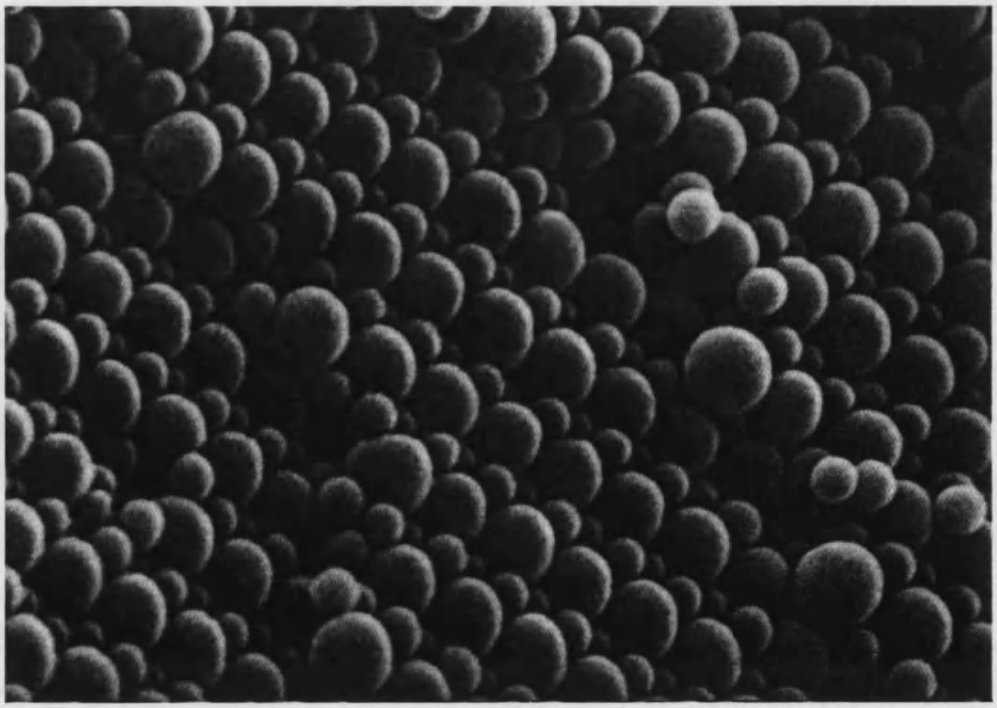

Figure 1.6: An electron micrograph of the LS_2 crystalline phase showing the (011) face (From Bartlett and van Megan [70])

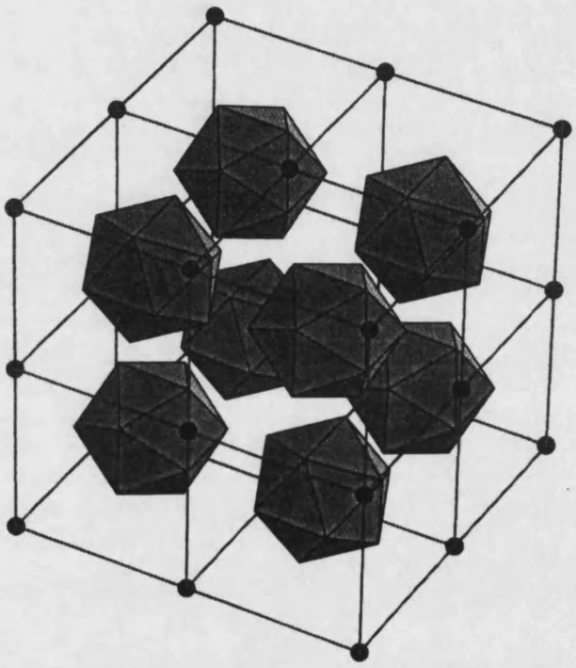

Figure 1.7: Schematic view of a the crystal structure of LS_{13}. The large spheres (L) are located at the corners of the face-centred cubic unit cell with the smaller spheres (S) at the vertices and centres of each of the shaded icosahedra. The full unit contains 112 particles. (From Bartlett and van Megan [70])

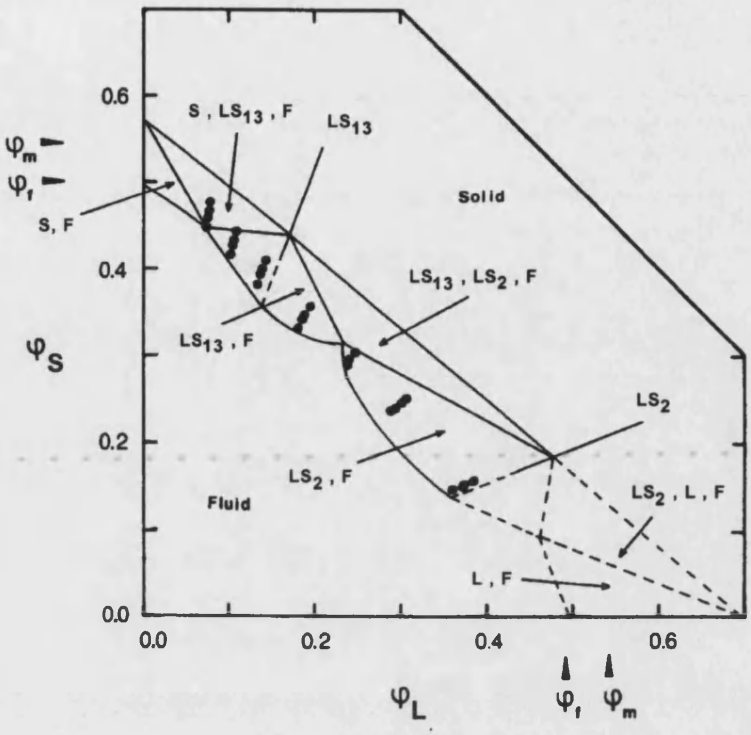

Figure 1.8: The phase diagram for a binary system of hard spheres. The axes are the partial volume fractions φ_L and φ_S and φ_f and φ_m are the freezing and melting fractions for the one-component suspensions. (From Bartlett and van Megan [70])

complex phase diagram illustrated in Figure 1.8. The complexity seen from a system of hard-sphere colloids of two sizes is perhaps the most surprising finding.

Given the complexity of both the phase behaviour and the structures formed in these systems, it would seem interesting to investigate other size ratios by experimental methods. As yet, no theory is able to predict the formation of structures, *a priori*, at any given hard-sphere size ratio.

Chapter 6 presents a detailed experimental study done at a ratio α=0.39 and compares the results with those available from cell-model simulations.

Chapter 2

Scattering Techniques for Probing Colloidal Systems

A range of techniques utilizing the scattering of electromagnetic radiation has been used to examine the behaviour of the colloidal systems studied in this thesis. This chapter aims to summarize the theoretical and practical matters that arise from using scattering techniques to examine these systems and to present the reader with the understanding required to interpret results from scattering experiments which are presented in later chapters.

2.1 Introduction

The most common way of observing an object is to look at it. This is actually a scattering experiment, since light emitted from a source (e.g. a light bulb) is scattered by an object, the scattered light being is detected and analysed by the eye. A feature immediately noticeable by the naked eye in many colloidal systems, is the milk-like opacity. This arises from the discrete variations in the refractive index which cause isotropic scattering of light. These discrete variations are due to the colloidal particles, which are of a size comparable with the wavelengths of visible radiation. The scale of detection is low using the naked eye but by using more specific detection equipment we can measure the scattering more precisely.

The crux of the problem is to relate the scattering of the radiation to the properties of the scatterer. The angular distribution, intensity, and polarization of the scattered radiation can impart information which probes, amongst other data, the size, shape and composition of the scattering particle and information regarding the arrangements of the particles. This has made scattering an indispensable tool for colloid chemists.

A commonly used probe for determining the structure and also the dynamics of colloidal particles is light scattering, since the wavelength of visible light is comparable to the colloidal size and therefore is also of a similar magnitude to the distances that characterize the structure of colloidal materials. Light scattering experiments can essentially be divided into two kinds, those where an average of the intensity of the scattered light is examined, called *static light scattering* [SLS], and those where the interest lies in the temporal fluctuations of the scattered intensity, called *dynamic light scattering* [DLS]. Complementary information is provided by X-ray scattering and neutron scattering, where the

wavelength is much smaller and information regarding composition of the colloid, for example can be retrieved. In neutron scattering experiments the different scattering lengths of hydrogen and deuterium can also be exploited to retrieve additional information, using contrast matching techniques.

There are many ways to interpret the scattering of electromagnetic radiation, from complex and sophisticated quantum mechanical solutions through to a simple classical approach, and there are many examples in the literature [73, 74, 75, 10, 76, 77]. Here a brief review of scattering using a classical approach is presented, with an emphasis on the physical significance of the terms and equations, leading to a practical understanding of the scattering techniques applied here.

2.2 Scattering theory

2.2.1 Rayleigh (point) scattering

For an isolated particle of size much smaller than the wavelength of the incident radiation the instantaneous field which it experiences due to the electromagnetic wave is uniform over its extent. For simplicity, we consider a single atom (see Figure 2.1). If the incident field oscillates harmonically, then the electrons will respond proportionally, inducing a dipole . The atom thus acts as an oscillating dipole, radiating scattered waves in all directions.

The scattered intensity detected at point $\mathbf{r}$, is given by

$$I_{Rayleigh} = \frac{16\pi^4\alpha^2 \sin^2\phi}{\lambda^4 r^2} I_0 \tag{2.1}$$

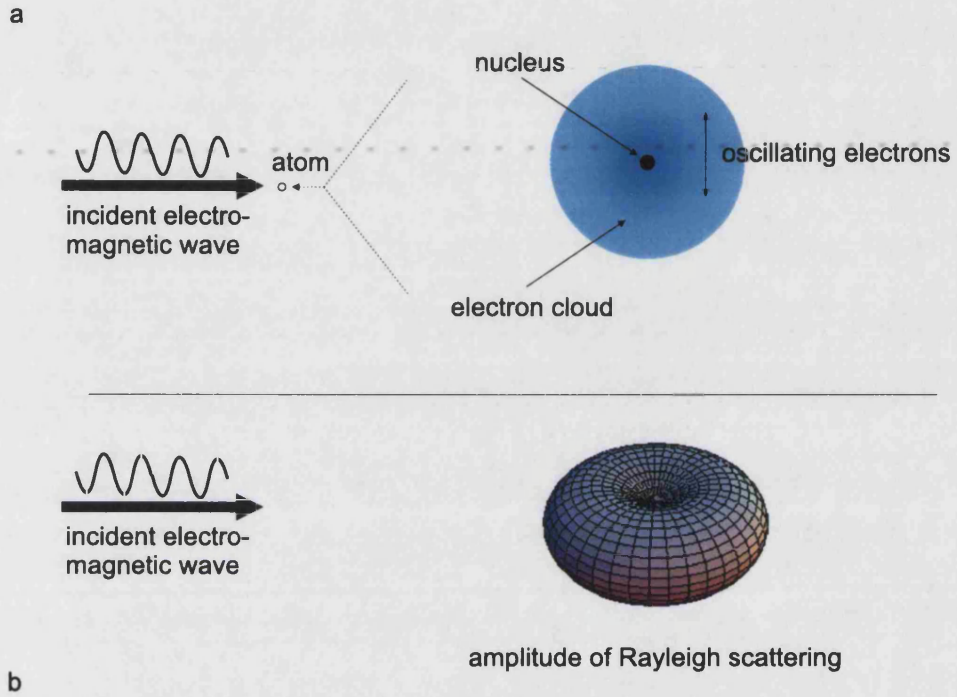

Figure 2.1: a) The oscillating incoming electromagnetic wave interacts with the electrons in the atom, inducing a dipole resulting in radiation of waves from the scattering atom. b) Amplitude of Rayleigh scattering by the atom (at the centre of the "doughnut"). The electromagnetic waves are polarized with the electric fields in the vertical direction. The doughnut shape illustrates the relative intensity of radiation scattered around the atom. There is no scattering into the vertical direction. The intensity is greatest and constant in the plane perpendicular to the plane of polarization.

where I_0 is the intensity of the incident radiation, λ is the wavelength of the radiation in vacuo, α is a measure of the polarizability, and ϕ is the angle between the plane of polarization and the detection vector, $\mathbf{r}$. Of note is the dependance on ϕ, (the intensity is greatest in directions perpendicular to the polarization of the incident field, and zero in directions parallel to it), and the dependance on wavelength which is proportional to λ^{-4}.

2.2.2 Rayleigh-Gans-Debye [RGD] scattering

Whilst the scattering described above pertains to particles much smaller than the wavelength of the incident radiation *e.g.* atoms or molecules, Rayleigh also developed an approximate theory for particles of any shape and size having relatively weak polarizability.

If we consider the depiction in Figure 2.2, each Brownian particle is considered divided into infinitesimally small volume elements, a number of which are shown.

Each volume element is treated as a Rayleigh point scatterer, and the incident radiation is unaffected by the rest of the particle. The phase shift corresponding to any point in the particle should be negligible, and so the phase of each volume elements wavelet is dependent only on its position and not on the properties of the particle. For this approximation to be valid the difference between the refractive index of the particles, n_1 and the refractive index of the dispersion medium, n_2 can not become too large for a given size of particle i.e.

$$|n_1 - n_2| \cdot {}^{R}/_{\lambda} \ll 1 \tag{2.2}$$

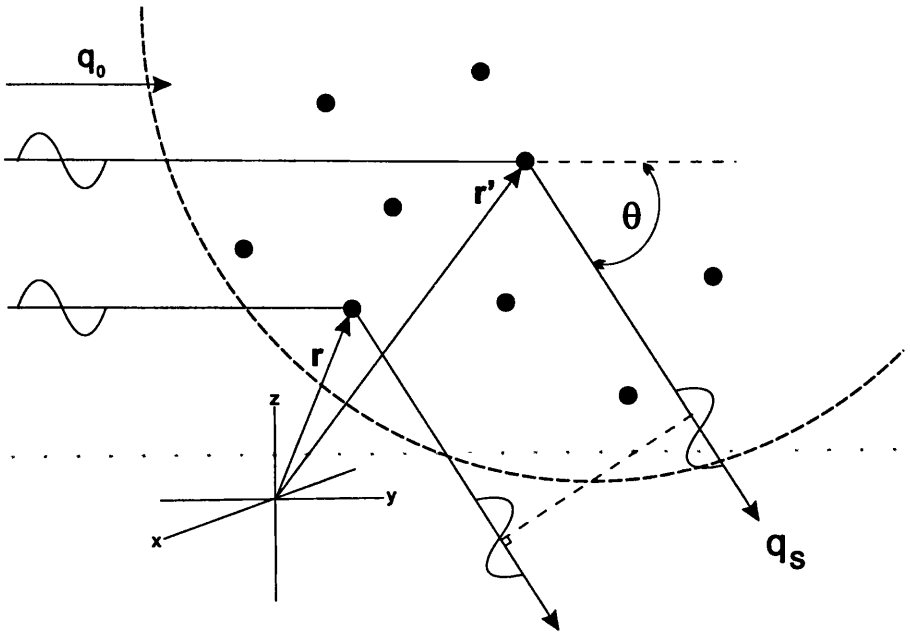

Figure 2.2: Rayleigh-Gans-Debye scattering. Each particle (indicated by the dashed line) can be considered to be composed of many Rayleigh point scatterers (indicated by the solid circles).

We can then examine the phase shift in electric field amplitude scattered by two volume elements shown in Figure 2.2 at positions given by $\mathbf{r}$ and $\mathbf{r}'$, in a direction characterized by θ, the angle between the propagation direction of the incident radiation ($\mathbf{q}_o$), and the direction in which the scattered field is detected ($\mathbf{q}_s$). The phase shift is equal to

$$(\mathbf{r} - \mathbf{r}') \cdot \mathbf{Q}$$

where $\mathbf{Q}$ is the scattering vector,

$$\mathbf{Q} = \mathbf{q}_o - \mathbf{q}_s$$

whose magnitude, Q, is given by

$$Q = |\mathbf{Q}| = \frac{4\pi}{\lambda} \cdot \sin\left(\frac{\theta}{2}\right) \tag{2.3}$$

To every volume element at a position $\mathbf{r}$, we can associate a phase equal to $\mathbf{r} \cdot \mathbf{Q}$. The total scattered electric field strength is equal to the sum of $\exp[i\mathbf{r} \cdot \mathbf{Q}]$ over all the volume elements, weighted by the scattering strength of the volume elements. Let us denote the scattering strength of a volume element at $\mathbf{r}$ as $f(\mathbf{r})$. The scattered field amplitude is then

$$E(\mathbf{Q}) = \int_{V_s} f(\mathbf{r}) \exp[i\mathbf{Q} \cdot \mathbf{r}]\, d\mathbf{r} \tag{2.4}$$

where V_s is the *scattering volume*, the illuminated region of the sample from which scattering is detected. The above equation may be rewritten in order to usefully distinguish between radiation scattered from volume elements within single particles and radiation scattered from different particles. Since the material surrounding the particles is assumed to be non-scattering, Equation 2.4 can be written as the sum of the volumes occupied by the N colloidal particles in the scattering volume, i.e.

$$E(\mathbf{Q}) = \sum_{i=1}^{N} \int_{V_i} f(\mathbf{r}) \exp[i\mathbf{Q} \cdot r] d\mathbf{r} \tag{2.5}$$

This gives an integration range, V_i, which is the volume occupied by particle i, and V_i depends upon the location of particle i. To account for this we introduce a *position coordinate* $\mathbf{r}_i$, which is a fixed point inside particle i relative to the centre of mass of the particle, and we change for each i, the integration variable to $\mathbf{r}'$, where $\mathbf{r}' = \mathbf{r} - \mathbf{r}_i$. The new integration range V_i^0 is the volume occupied by the particle with its position coordinate at the origin. Equation 2.5 can be

rewritten in terms of its new variables as

$$E(\mathbf{Q}) = \sum_{i=1}^{N} \exp[i\mathbf{Q} \cdot \mathbf{r}_i] \int_{V_i^0} f(\mathbf{r}') \exp[i\mathbf{Q} \cdot \mathbf{r}'] \, d\mathbf{r}' \tag{2.6}$$

where the exponential functions containing the position coordinate $\mathbf{r}_i$, describes the interference of radiation scattered from different particles, whilst the integral over V_i^0 is the scattering amplitude of the radiation scattered by particle i, that is, it describes the interference of radiation scattered from different volume elements from within a particle. This term is often referred to as the *particle scattering amplitude.* For clarity we abbreviate it here to $B_i(\mathbf{Q})$

$$B_i(\mathbf{Q}) = \int_{V_i^0} f(\mathbf{r}') \exp[i\mathbf{Q} \cdot \mathbf{r}'] d\mathbf{r}' \tag{2.7}$$

we can simplify Equation 2.6 to read,

$$E(\mathbf{Q}) = \sum_{i=1}^{N} B_i(\mathbf{Q}) \exp[i\mathbf{Q} \cdot \mathbf{r}_i] \tag{2.8}$$

The scattered electric field strength, given in Equation (2.8), is calculated for an instantaneous configuration of particles. Compared to the time scale of photons scattering, Brownian motion of the particles is slow, *i.e.* many photons are scattered in a time interval over which the configuration of the Brownian particles does not significantly change. The measured instantaneous intensity is therefore the intensity averaged over many scattering time intervals and for spherical particles equals

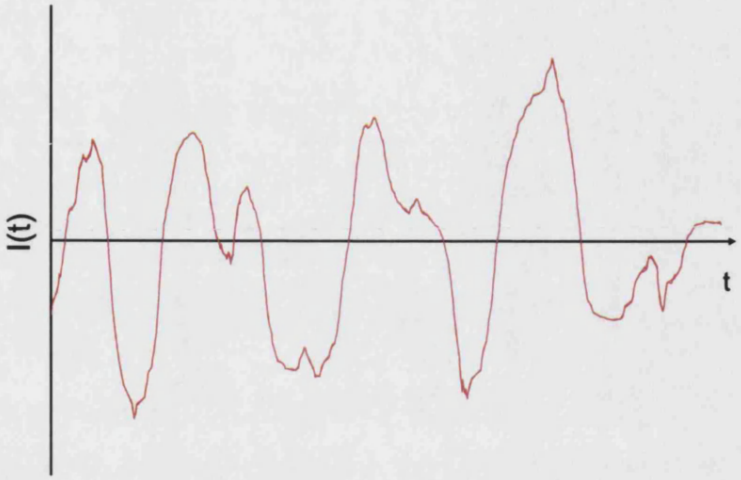

Figure 2.3: The fluctuating intensity of scattered radiation due to Brownian motion of colloidal particles

$$I(Q,t) \equiv |E(\mathbf{Q},t)|^2 \tag{2.9}$$

The time dependence of the scattered electric field strength is now denoted explicitly, and refers to the time dependence of the positions of the particles.

A change in the configuration of the Brownian particles thus changes the instantaneous scattered intensity $I(Q,t)$ and the intensity fluctuates due to Brownian motion around a mean value I, as depicted in Figure 2.3.

We can therefore make two kinds of measurement of the fluctuating intensity. The first is a measure of the ensemble averaged properties of the scattered light

fluctuations and therefore reveals averaged properties of density fluctuations in a sample. Experimentally this kind of measurement is often undertaken with many kinds of electromagnetic radiation, neutrons, X-rays and particularly light, in which case it is referred to as *static light scattering.* The second type of measurement is usually performed with light and is known as *dynamic light scattering* [DLS] (also referred to as *photon correlation spectroscopy* [PCS] [9] or *intensity fluctuation spectroscopy* [75]). In a DLS experiment the dynamics of the fluctuations of the scattered light are measured therefore probing the dynamics of density fluctuations within the sample.

2.3 Static Light Scattering

2.3.1 Theory

In a static scattering experiment, the mean intensity

$$I(\mathbf{Q}) = < I(\mathbf{Q}, t) > \tag{2.10}$$

is measured as a function of angle, which at a given wavelength, sets the magnitude of wavevector $\mathbf{Q}$ as given in Equation (2.3). (The brackets $< .. >$ indicate an ensemble average over all orientations and positions of the Brownian particles. Experimentally, this ensemble average is achieved by averaging over a period of time which is much larger than the time required for the Brownian particles to reach all accessible configurations). For spherical, optically isotropic particles we have that $B_i(\mathbf{Q}) = B_i(Q)$ and $B_i(Q)$ is given by [1];

$$
\begin{aligned}
B_i(Q) &= \int_{V_i^0} \frac{\epsilon(r') - \epsilon_f}{\epsilon_f} \exp[i\mathbf{Q}\cdot\mathbf{r}']d\mathbf{r}' \\
&= 4\pi \int_0^R r'^2 \frac{\epsilon(r') - \epsilon_f}{\epsilon_f} \frac{\sin(Qr')}{Qr'} dr'
\end{aligned} \tag{2.11}
$$

where $\epsilon(r)$ is the isotropic dielectric constant of particle i at radius r within the particle, R is the particle radius and ϵ_f is the dielectric constant of the fluid.

From Equations (2.9 and 2.8), the average scattered intensity is given by

$$
< I(Q) >= \sum_{i=1}^{N}\sum_{j=1}^{N} B_i(Q)B_j(Q) < \exp[i\mathbf{Q}\cdot(\mathbf{r}_i - \mathbf{r}_j)] > \tag{2.12}
$$

If we consider that all the particles are identical, all $B_i(Q)$ are the same, $B(Q)$. Equation (2.12) can then be written

$$
< I(Q) >= N[B(Q[0])]^2 \cdot P(Q) \cdot S(Q) \tag{2.13}
$$

where $P(Q)$ is the squared particle scattering amplitude, normalized to unity at $Q = 0$, and is referred to as the *form factor* i.e.

$$
P(Q) = \left[\frac{B(Q)}{B(Q[0])}\right]^2 \tag{2.14}
$$

and $S(Q)$ is the *static structure factor.*

Form Factor

The form factor accounts for the interference of the scattered electric fields from different volume elements within a particle and the static structure factor describes the interference of fields scattered from different particles.

For optically homogeneous spherical particles, $\epsilon(r)$ is a constant, and the form factor $P(Q)$ is readily calculated from Equations (2.14) and (2.11) to give

$$P(Q) = 9\left[\frac{QR\cos(QR) - \sin(QR)}{(QR)^3}\right]^2 \tag{2.15}$$

The form of $P(Q)$ for optically homogeneous spherical particles is shown in Figure 2.4. The form factor tends to zero at certain scattering angles (the first zero occurs at QR=4.49) where the scattered intensity vanishes due to destructive interference, and hence no information about the structure factor can be obtained experimentally from these angles.

In a dilute solution the interparticle interactions are insignificant and the static structure factor, $S(Q) \rightarrow 1$. In the particular case of monodisperse hard-spheres, it can be seen from Equation 2.13 that scattering measurements on such dilute solutions provide a measure of the particle form factor $P(Q)$. Once the form factor is known, scattering from non-dilute suspensions will yield the static structure factor, $S(Q)$.

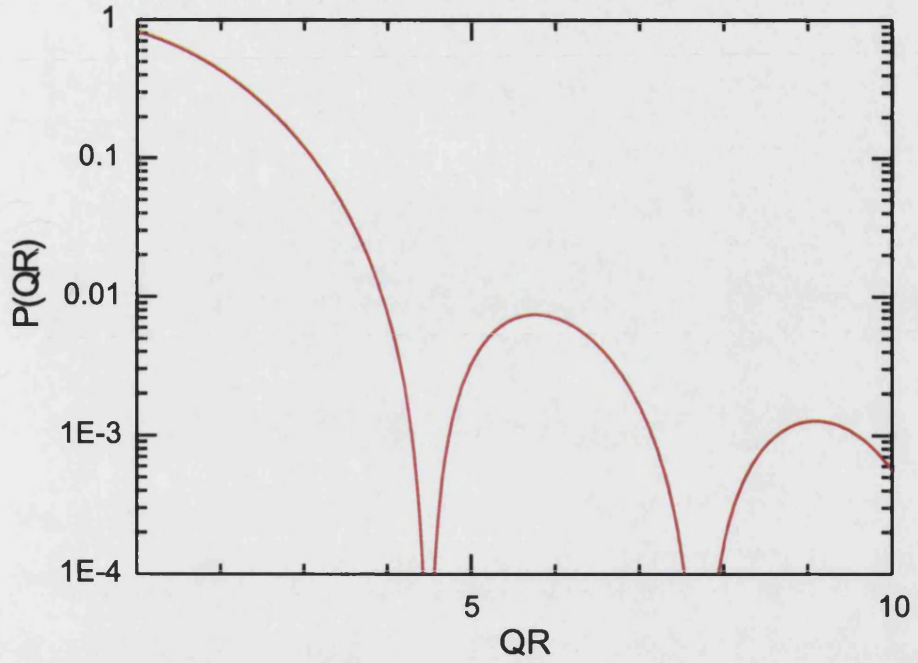

Figure 2.4: Form factor of homogeneous spheres

Static Structure Factor

The static structure factor describes the scattering produced as a consequence of interference of fields scattered from different particles;

$$S(Q) = {}^1\!/_N \sum_{i=1}^{N} \sum_{j=1}^{N} < \exp[i\mathbf{Q} \cdot (\mathbf{r}_i - \mathbf{r}_j)] > \qquad (2.16)$$

It can be shown that the structure factor gives access to the Fourier transform of the *pair correlation function*, $g(r)$, where $r = (r_i - r_j)$. The pair correlation function describes the probability of finding a particle at point r from a given particle. This function is useful in connecting statistical mechanics with thermodynamics, leading to determination of numerous properties *e.g.*, isothermal compressibilities. Unfortunately, the inversion of $S(Q)$ to give $g(r)$, involves serious technical

and numerical difficulties [78].

Static scattering techniques are used in the determination of crystal structure in Chapters 4 and 6 where interpretation of the structure factor is restricted to identifying peaks in the scattering and mapping these peaks to the Bragg reflections of an appropriate crystal structure. In chapter 7 static scattering methods are used with a neutron source to measure scattering from a novel mixture of colloid and microemulsion. The structure factor from these experiments is modelled to give an interpretation of the interparticle potential in this system.

2.4 Dynamic Light Scattering [DLS]

2.4.1 Introduction

Although dynamic light scattering may be said to date from 1914 when Brillouin described the frequency distribution of light scattered by density fluctuations [79], rapid growth and development of the field did not occur until the early 1960s. This was mainly due to the difficulty of obtaining precise, reliable results using the classical optical sources available up to that point. The development of the laser in the early 1960s, along with the adoption of detectors based upon photomultiplier tubes and the use of photon correlation techniques, has seen the use of DLS techniques extend to a wide variety of systems [75], including for example, applications within fluid mechanics and biological systems. One of the first uses of DLS [80], and probably the most common use of dynamic light scattering techniques today, concerns the analysis of mean particle size and size distribution of macromolecular dispersions. The technique of dynamic light scattering is used in this work to provide a measure of mean particle radius and

polydispersity for the colloids and microemulsions used throughout this study.

2.4.2 Theory

In section 2.3 we examined static scattering experiments, where the ensemble averaged intensity I (Equation 2.13) was measured and the results interpreted to give information regarding average ensemble structure. In this section we examine measuring the time dependence of the fluctuating intensity of scattered light, usually referred to as *dynamic light scattering.* The fluctuations in scattered light are due to fluctuations in density caused by the movments of particles by Brownian motion. Analysis of these fluctuations in scattered light therefore reveals information regarding the motion of the particles in the system, which can be used, for example, to estimate particle size.

The simplest function that characterizes these fluctuations of intensity is the *intensity auto-correlation function* [IACF],

$$g_{\text{IACF}}(\mathbf{Q},\tau) =< I(\mathbf{Q},t) \cdot I(\mathbf{Q},t+\tau) > \tag{2.17}$$

For an equilibrium system there is no preferred instance in time, i.e. g_{IACF} is not dependent on t, but on the time lag,τ, alone. In terms of the electric field amplitude, the IACF is a four point average,

$$g_{\text{IACF}}(\mathbf{Q},\tau) =< E(\mathbf{Q},0)E^*(\mathbf{Q},0)E(\mathbf{Q},\tau)E^*(\mathbf{Q},\tau) >$$

Given that the scattering volume contains a large number of particles and that the system is ergodic, it can be shown that the field $E(\mathbf{Q},\tau)$ is a complex Gaussian variable (with a zero average). As first shown by Siegert [81], the intensity auto-correlation function is related to the *electric field auto-correlation function* [EACF] by

$$g_{\text{IACF}}(\mathbf{Q},\tau) \equiv I^2 + |g_{\text{EACF}}(\mathbf{Q},\tau)|^2 \tag{2.18}$$

It is convenient to rewrite this with the auto-correlation functions normalized,

$$g_I(\mathbf{Q},\tau) \equiv \frac{g_{\text{IACF}}(\mathbf{Q},\tau)}{I^2} \tag{2.19}$$

$$g_E(\mathbf{Q},\tau) \equiv \frac{g_{\text{EACF}}(\mathbf{Q},\tau)}{I} \tag{2.20}$$

where by definition, as $\tau \to 0$, $g_E \to 1$ and $g_I \to 2$, and the Siegert relation can now be written as

$$g_I(\mathbf{Q},\tau) = 1 + |g_E(\mathbf{Q},\tau)|^2 \tag{2.21}$$

For identical spherical particles, g_E is obtained by substituting Equation 2.8 into 2.20 and 2.21,

$$g_E(\mathbf{Q},\tau) = \frac{1}{S(Q)}\frac{1}{N}\sum_{i,j=1}^{N} < \exp[i\mathbf{Q}\cdot(r_i(0) - r_j(\tau))] > \tag{2.22}$$

Although dynamic light scattering studies have been undertaken on non-dilute

colloidal systems, rigorous results have been rare [82]. In a dilute suspension, particle interactions may be neglected and their positions are uncorrelated. Thus cross-terms ($i \neq j$) average to zero and only diagonal-terms survive. Furthermore the static structure factor $S(Q)$ is equal to 1 for non-interacting particles and

$$g_E(\mathbf{Q},\tau) = \frac{1}{N}\sum_{i=1}^{N} < \exp[i\mathbf{Q}\cdot(r_i(0) - r_i(\tau))] > \tag{2.23}$$

The displacement of a free Brownian particle is a Gaussian variable with mean square value,

$$< |r_i(0) - r_i(\tau)|^2 >= 6D_o\tau \tag{2.24}$$

where the free particle diffusion coefficient D_o is simply related to the radius of a Brownian particle through the Stokes-Einstein relation [83],

$$D_o = \frac{k_B T}{6\pi\eta R} \tag{2.25}$$

where k_B is Boltzmans constant and η and T are, respectively, the viscosity and temperature of the dispersion medium. Combining equations 2.23,2.24 and 2.25 gives;

$$g_E(\mathbf{Q},\tau) = \exp(-D_o\mathbf{Q}^2\tau) \tag{2.26}$$

and the electric field auto-correlation function for a dilute system of identical

spherical particles is a single exponential.

Hence measuring the fluctuations in the intensity of scattered light via the intensity auto-correlation function available through dynamic light scattering techniques can provide a measure of the free particle size; A radius determined in this way is commonly referred to as the*hydrodynamic radius.*

2.4.3 Polydispersity Effects in Dynamic Light Scattering

In practical situations, even when using model colloids, the particles being measured are never exactly identical, and may vary in size, shape, optical properties etc. The effects of size polydispersity are significant and are discussed in this subsection.

For the case of a dilute dispersion of identical spherical particles the electric field auto-correlation function was given by Equation 2.23;

$$g_E(\mathbf{Q},\tau) = \frac{1}{N}\sum_{i=1}^{N} < \exp[i\mathbf{Q}\cdot(r_i(0) - r_i(\tau))] >$$

The summations over all particles may be replaced by weighted integrals with respect to the radius. To account for the polydispersity of particle sizes the integrals are weighted by a probability density function [pdf] of the distribution of particle radii, denoted $G(r)$. We can rewrite the electric field auto-correlation function as

$$g_E^{poly}(\mathbf{Q},\tau) = \frac{\int_0^\infty G(r)B^2(\mathbf{Q},r)\exp\left[-D_o(r)\mathbf{Q}^2\tau\right]\,dr}{\int_0^\infty G(r)B^2(\mathbf{Q},r)\,dr} \qquad (2.27)$$

The electric field auto-correlation function is related to the distribution of particle sizes, $G(r)$, via a Laplace transform. Solving $G(r)$ from Equation 2.27 is known as Laplace inversion, and recovery of the distribution of particle radii from an imperfect set of results is an ill-posed problem. By its nature any measured form of $g_I(Q,\tau)$ is only an estimate and is inherently noisy and incomplete. Small errors in $g_I(Q,\tau)$ can produce very large errors in $G(r)$ and attempts to recover too much information can result in physically unreasonable solutions, therefore only limited information can be retrieved. A number of data analysis techniques are available to extract information from the measured data [84], including cumulant-expansion, regularized inversion (as used in the widespread CONTIN analysis [85]) and methods of maximum entropy, however here we only consider cumulant expansion. For sufficiently narrow distributions, the cumulant expansion [86] is one of the simplest approaches and requires no knowledge of the form of the pdf of distribution sizes. The cumulant generating function may be defined as;

$$\ln|g_E(\tau)| = -\bar{\Gamma}\tau + \frac{1}{2!}\mu_2\tau^2 - \frac{1}{3!}\mu_3\tau^3 + ... \tag{2.28}$$

where Γ is the decay rate or D_oQ^2 and

$$\bar{\Gamma} = \int_0^\infty \Gamma \cdot G(\Gamma)d\Gamma \tag{2.29}$$

$$\mu_n = \int_0^\infty (\Gamma - \bar{\Gamma})^n G(\Gamma)d\Gamma \tag{2.30}$$

this can be simplified to

$$\ln|g_E(\tau)| = -AQ^2\tau + \frac{B}{2}Q^4\tau^2... \tag{2.31}$$

with $AQ^2 = \kappa_1$, being the first cumulant, $\frac{B}{2}Q^4 = \kappa_2$, the second cumulant etc., where A,B... are related to the moments of the particle size distribution. The first cumulant, κ_1, is directly proportional to the intensity weighted average diffusion coefficient, $D_e(Q)$;

$$D_e(Q) = \frac{\kappa_1}{Q^2} = \frac{kT}{6\pi\eta} \cdot \frac{\bar{r}^5}{\bar{r}^6} \tag{2.32}$$

The second cumulant, κ_2, when suitably normalized by κ_1^2, gives an indication of the departure of the correlation function from a single exponential, and can be used as an unconventional measure of the width of the particle-size distribution function.

$$\frac{\kappa_2}{\kappa_1^2} = \frac{\bar{r^6}\bar{r^4}}{(\bar{r}^5)^2} - 1 \tag{2.33}$$

Cumulants beyond κ_2 are seldom used since over-fitting of the data will only render the other parameters less precise. Hence the cumulant expansion method of analysis gives a reasonable measure of average size, is easily implemented and offers fast results, usually done with appropriate computer software. Other measurements of the particle size distribution, including polydispersity, cannot be measured using cumulant analysis at single values of Q.

Improved measurements can be made by taking measurements at more than one angle [87]. Pusey and van Megan calculated the variation in the effective diffusion coefficient,$D_e(Q)$, with scattering angle [88]. $D_e(Q)$ shows a characteristic variation with scattering angle which is sensitive to polydispersity as shown in Figure 2.5, enabling more accurate measurements of polydispersity (theoretically as low as 0.01). This can be understood intuitively by returning to the form factor of a spherical particle shown in Figure 2.4. As the angle of detection changes, so the intensity of scattered radiation changes also, in particular note the minima at

QR=4.49. As the size of the particle changes, so the angles at which these minima occur will also change, as will the entire intensity function. This results in detection of different sections of the particle size distribution at different angles, and therefore measuring at multiple angles enables more accurate measurements of polydispersity.

Assuming a theoretical form for the distribution of particle radii, allows the angular variation in the effective diffusion coefficient to be calculated [89]. The two parameter Schultz distribution [90, 91, 89] is mathematically simple;

$$G(r) = \frac{r^Z}{Z!}\left(\frac{Z+1}{\bar{r}}\right)^{Z+1} \exp\left[-\frac{r}{\bar{r}}(Z+1)\right] \tag{2.34}$$

where Z is a measure of the width of the distribution. The polydispersity, is related to Z, by

$$\sigma^2\left(\equiv \frac{\bar{r^2}}{\bar{r}^2} - 1\right) = \frac{1}{Z+1} \tag{2.35}$$

The variation in apparent size for Schultz distributions with various polydispersities is shown in Figure 2.5. Thus by making DLS measurements at many values of Q, the variation in apparent size can be fitted to a calculated Schultz distribution, enabling accurate estimation of the polydispersity of a colloidal dispersion.

2.4.4 Apparatus and Experimental Considerations

This section introduces experimental considerations and other practical aspects involved in configuring a dynamic light scattering experiment.

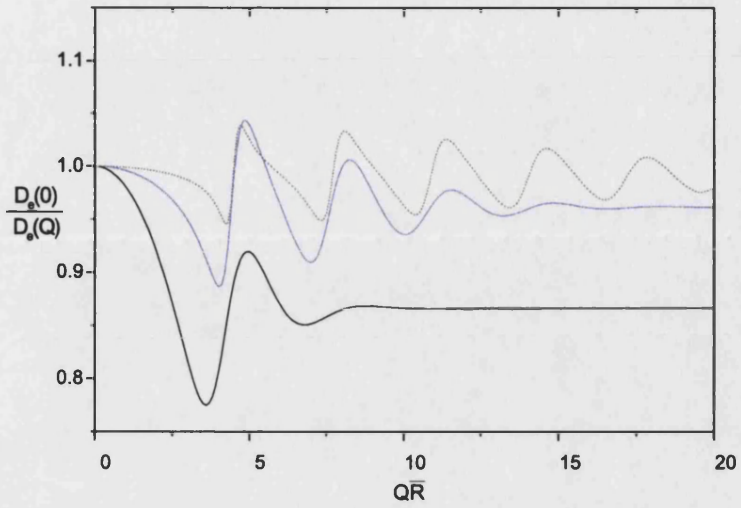

Figure 2.5: Graph showing the variation of apparent size as a function of the reduced scattering vector $Q\bar{R}$. The different curves illustrate the variation in effect at different polydispersities; $\sigma = 0.2$ *solid line*, $\sigma = 0.1$ *dotted line*, $\sigma = 0.05$ *dashed line*

The major components that make up the apparatus required for a typical dynamic light scattering experiment have been discussed in detail in the literature [9]. Details of the particular dynamic light scattering setup used in this study are given briefly, to give specific configuration details and to highlight experimental considerations. Figure 2.6 gives a schematic view of the apparatus used.

Light Source

A Coherent Innova 300 series Krypton/Argon ion laser was used as the light source for the light scattering experiments. Laser light provides a well collimated, stable beam with an intensity which is unavailable from conventional light sources at similar costs. The principle wavelengths used from this source are 488.0 nm, 514.0 nm and 647.1 nm.

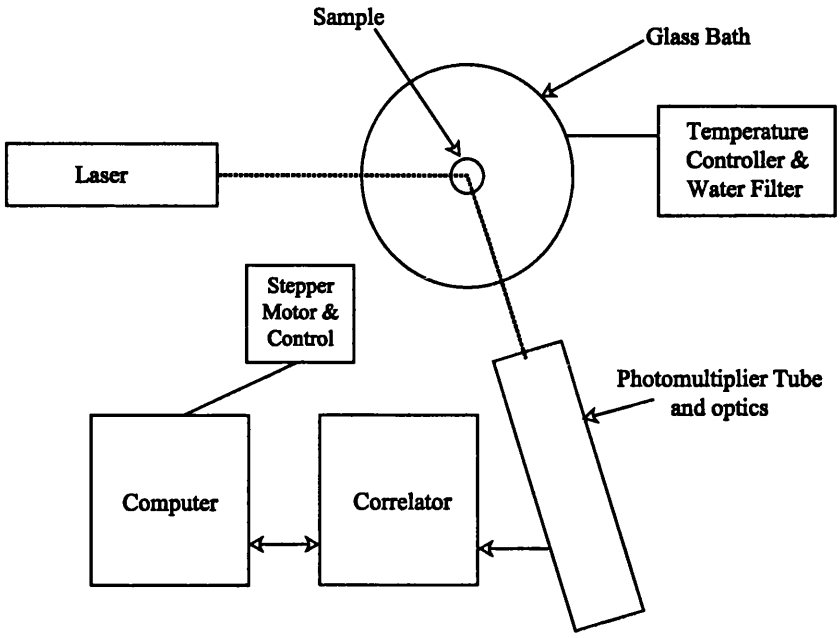

Figure 2.6: Schematic of apparatus used for DLS experiments

Sample Bath

The laser passes through a flat section of the bath wall through the temperature controlled water into the sample cell. Convection currents in a cell can lead to substantial distortion of the results since movement of the scattering particles by forces other than the assumed Brownian forces would lead to inaccurate particle sizing. Precise temperature control can virtually eliminate this problem. To minimize dust or other unwanted particles in the bath the water was regularly pumped through a 0.2 μm filter. The sample cells typically used in obtaining the result were either cylindrical cells 1 cm in diameter or 1 cm path length square cells. Whilst it would seem desirable to use cylindrical cells to make measurements at many different angles the optical quality of drawn cylindrical cells is not as high of that of square cells with ground polished sides and as long as refraction from the cell surface is carefully corrected for, square cells may easily be used.

Photomultiplier Tube [PMT]

The scattered light passes through the bath wall to the photomultiplier optics. The lens and a pair of apertures define an optical axis and careful alignment is required to ensure accurate measurement of the illuminated volume of the sample. A photon scattered from the section of sample in the detection volume travelling at the same angle as the detection angle may then hit the cathode, usually made of one or more alkali metals, which will absorb the photon and immediately emit an electron. The electron is accelerated by an electric field and then collides with a sheet of metal, the dynode, knocking out several electrons. This group of ejected electrons is accelerated again before colliding with a second dynode, each electron in the group knocking out another group of electrons and so on for another 12 or more dynodes until the initial emitted electron has cascaded to yield around 10^6 electrons. These electrons form a detectable pulse. To ensure that the pulse is suitable input for the digital correlator, the pulse is modified by a pulse amplifier-discriminator. The small pulse is amplified and converted into a standard logic pulse, and any small photomultiplier pulses, probably arising from non-photon detection sources, are filtered out. The photomultiplier tube was mounted on a goniometer arm, which allowed the angle between incident radiation and detection to be altered between 10° and 150° $\pm$ 0.1° by a computer-controlled stepper motor.

Correlator

The correlator is a purpose-built digital computer, enabling the adding, counting and correlation of the pulses corresponding to detected photons. This enables the determination of the intensity autocorrelation function, $g_I(\mathbf{Q}, \tau)$. The correlator

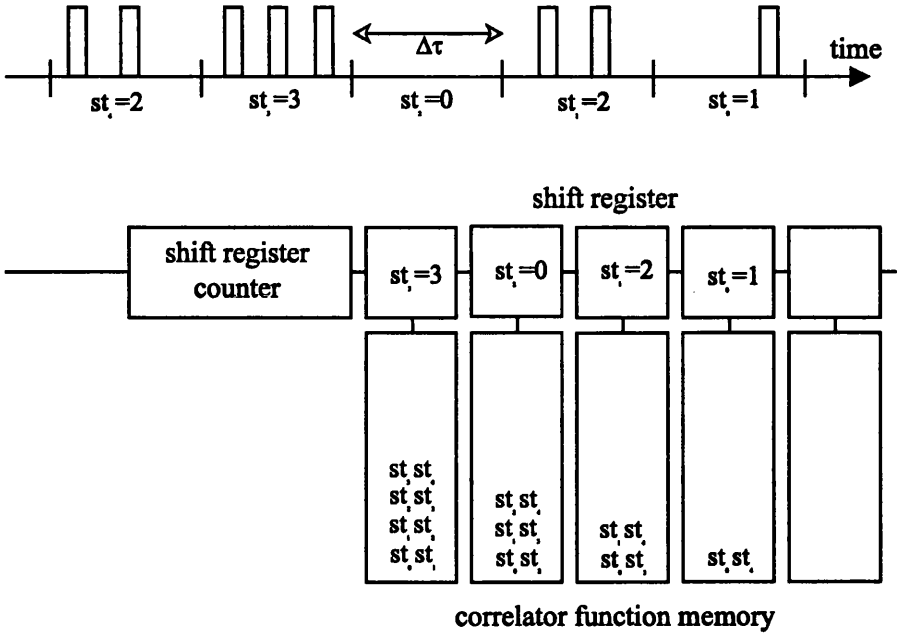

Figure 2.7: Schematic of correlator operation

used was a Malvern correlator, with 128 channels, 4 bit shift register and a minimum sample time of 100ns. A brief description of the operation of a correlator is included below.

Electronic logic pulses arrive at the correlator, each representing a photon detection event. The operation of the correlator is determined by the sample time generator, which divides times into intervals of equal length, $\Delta\tau$, the line at the top of Figure 2.7 illustrates an example sequence of pulses. The number of pulses occurring during each sample time is counted by the shift register counter. At the end of each sample time, the number in the shift register counter is entered into the first channel of the shift register, the number that was in the second channel of the shift register is moved to the third channel, and so on. Also during each sample time, each pulse received by the input triggers the adding of each of the

numbers stored in the shift register to the number stored in the associated channel of the correlation function memory. The lower half of Figure 2.7 illustrates the accumulation of counts in each channel after five sample times. In the first channel, the values can be seen to be

$$G(\Delta\tau) = \sum_{n=0}^{N-1} st_n st_{n+1} \tag{2.36}$$

in the second channel is equal to

$$G(2\Delta\tau) = \sum_{n=0}^{N-1} st_n st_{n+2} \tag{2.37}$$

and in general, the xth channel will contain

$$G(x\Delta\tau) = \sum_{n=0}^{N-1} st_n st_{n+x} \tag{2.38}$$

which is a good approximation to the true correlation function as long as the change in G over the period $\Delta\tau$ is small. A number of special channels are available that may be delayed by a substantial amount, to give a measured baseline.

Chapter 3

Synthesis of Hard-Sphere Polymer Colloids

Monodisperse poly(methyl methacrylate) [PMMA] colloidal spheres have been synthesized by dispersion polymerization. The synthesis of a fluorescent dye suitable for inclusion into the PMMA colloid synthesis is described and fluorescently labelled PMMA colloids have been produced. The synthesis of deuterated PMMA colloids suitable for contrast-matching neutron scattering experiments is also described.

3.1 Introduction

Progress in colloid science has been furthered via a number of important developments in the field of polymer colloids, initiated by the discovery of stable, monodisperse, polymer dispersions in 1947 [92]. Stable dispersions of polymer particles are often referred to as *latices* (by analogy with the natural rubber latex) and may be prepared using various polymerization techniques. Emulsion polymerization has been used to prepare aqueous dispersions of polymer colloids since the late 1920s [93]. Non-aqueous dispersions, which form a significant proportion of modern, industrially important colloidal systems, are prepared by the dispersion polymerization technique [45].The first non-aqueous colloidal dispersions were not synthesized until the early 1960s [12], and as a result the behaviour of these colloidal systems is less well investigated than the behaviour of aqueous polymer colloid dispersions. Despite this, knowledge and understanding of non-aqueous dispersions has increased gradually over recent years and well-characterized dispersions of monodisperse polymer particles in non-aqueous media are readily available as model colloids. These model colloids, which do not exhibit the large variation in properties such as particle size and shape that are commonplace in industrial systems, provide us with the means to control and simplify the behaviour of colloids and are a valuable tool in the study of colloidal systems. The insights gained from the study of model colloids are valuable for developing and understanding more complex industrially-important systems. Research into the detailed behaviour of these model colloids is therefore currently of considerable interest.

The model particle used in this study is one which has been used increasingly in recent years and consists of a poly(methyl methacrylate)[PMMA] spherical particle coated with a thin ($\approx$10 nm) layer of a stabilizing polymer, poly(12-

hydroxystearic acid)[PHSA] [46, 94, 95, 45]. Further detail on the composition and synthesis of the colloid is given in Section 3.2.

Modifications to the standard PMMA model particle have been introduced to increase the number of techniques available to study the particles and structures formed by this colloidal system.

A commonly employed technique for probing on a colloidal scale is small-angle neutron scattering [SANS]. The technique is made more powerful by the ability to vary the relative scattering powers of the components being studied without changing the chemistry of the system by, for example, replacing hydrogen by deuterium. The synthesis of deuterated PMMA colloids (studied using SANS methods in Chapter 7) is described in Section 3.2.

Several experimental techniques available to study the structure and dynamics of colloidal dispersions rely in some way on fluorescence, for example, fluorescence recovery after photobleaching (FRAP, [96]), fluorescence correlation spectroscopy (FCS, [97, 98]) and the technique utilized in this study, fluorescence laser scanning confocal microscopy (LSCM, [99]). Section 3.3 details the synthesis of a fluorescent dye and the inclusion of this dye into the polymer colloid.

3.2 Experimental

3.2.1 The dispersion polymerization reaction

The production of polymer dispersions in organic media was an important development in colloid science; the first patents in this field appeared in the early

1960s [12, 45] and the technique of dispersion polymerization was originally invented to develop paints and films with a non-aqueous medium [45]. Although any type of polymerization mechanism may be employed *e.g.* condensation, ring-opening, free radical addition *etc.*, a vast majority of systems have utilized free radical initiated polymerization using azo or peroxide initiators with vinyl and acrylic monomers such as vinyl acetate, vinyl chloride, acrylonitrile and methyl methacrylate. The essence of dispersion polymerization is that for polymerization to proceed the monomer which is to be polymerized must be soluble in the dispersion medium and the polymer thus produced must be insoluble in the dispersion medium. The insoluble polymer can then be considered to precipitate out of solution but particle flocculation via van-der-Waals forces is prevented by the amphipathic polymeric stabilizer. In the simplest form of dispersion polymerization, the monomer together with a small amount of polymeric dispersant stabilizer and an initiator is dissolved in a non-polar, hydrocarbon medium and heated to reflux. Polymer particles are formed at a very early stage of the reaction, often after only a few seconds and a faint opalescence can be observed in the reaction mixture as insoluble polymer precipitates out from an initially homogeneous reaction mixture to form light-scattering nuclei. The opalescent mixture whitens and turns opaque as polymerization continues. The rate of polymerization can be monitored by measuring total solids, unused monomer *etc.* and is shown to increase steadily to a maximum value, followed by a reduction in rate as the availability of the monomer decreases as it is consumed [45]. A typical dispersion polymerization reaction may achieve conversions of over 95% within an hour [100].

For the synthesis of model particles, control of the particle size and particle size distribution is of the utmost importance and identifying the factors affecting particle formation and growth is therefore of considerable interest. A multi-step

mechanism for particle nucleation has been proposed by Morrison, Gilbert and Napper [101] (reviewed in [100]), and is illustrated in Figure 3.1.

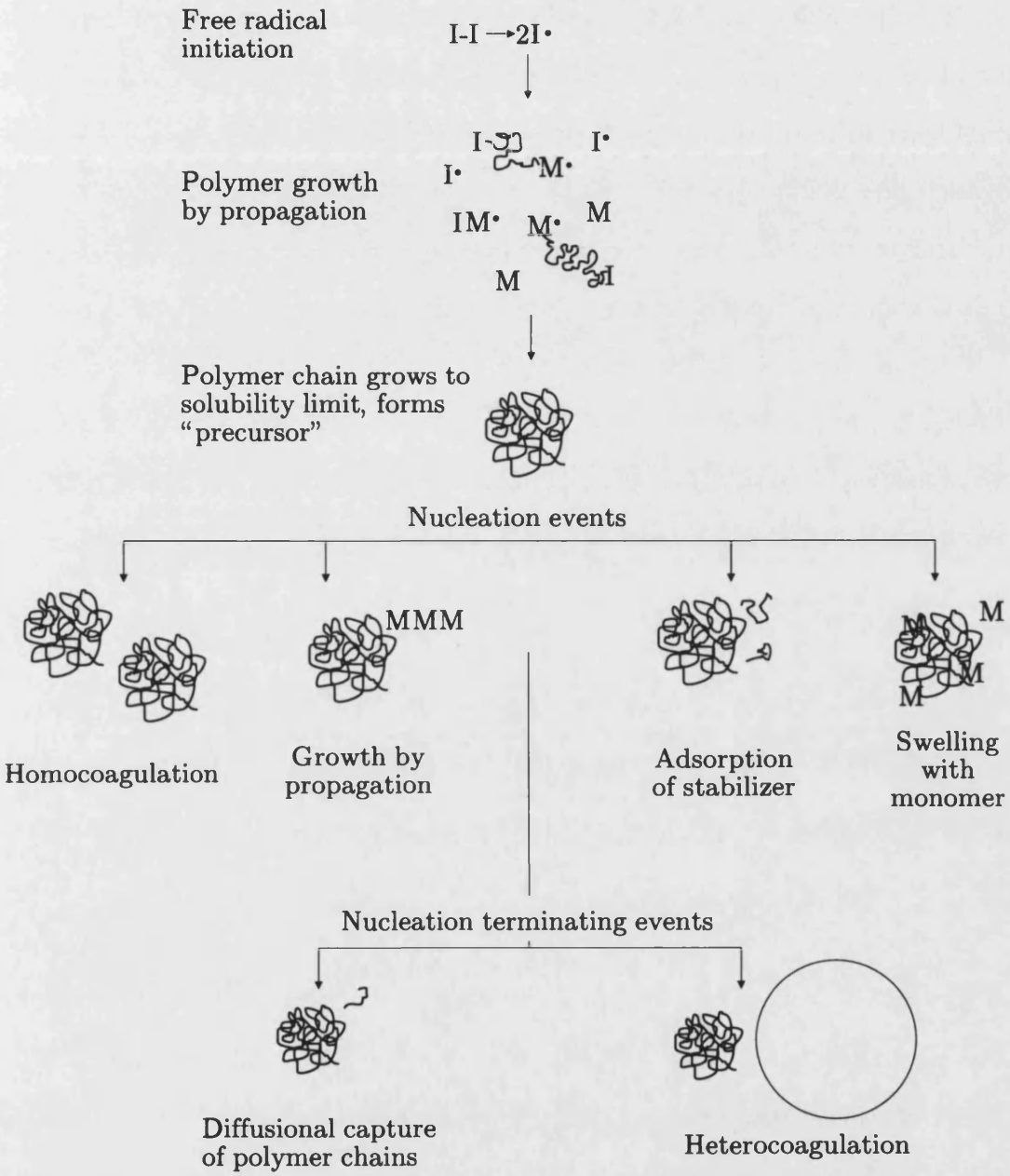

Figure 3.1: Schematic representation of the coagulative nucleation process

It is suggested that the polymerization begins with the growth of polymer chains in the dispersion medium. These chains grow to a point where they reach their solubility limit, the *precursor* stage. There are a number of potential events which may then lead the precursors to the formation of colloidally stable nu-

clei. Collision with another precursor will result in homocoagulation and an increase in particle size. Growth by propagation of the polymer chain or by adsorption of stabilizer may also take place. Finally the precursor may swell with monomer, with polymerization taking place within the particles. Once the nucleation period has been completed, particle growth occurs via a number of possible mechanisms. The nuclei can absorb monomer, collide with a precursor or capture smaller polymer chains. This mechanism is very general in its nature, and although this mechanism and other general theories have been established to explain the facts and trends, as yet no precise quantitative model has been established and more research will need to be performed to fully confirm and expand this mechanism. However, previous experiments have shown that some important factors to consider when trying to control particle properties would include solvency of the dispersion medium, stabilizer concentration and initiator concentration.

3.2.2 Dispersion polymerization of methyl methacrylate

The dispersion polymerization reaction most widely used to create non-polar model colloids is the synthesis of poly(methyl methacrylate) spheres, stabilized with poly-12-hydroxystearic acid (*e.g.* [45, 46, 100, 94, 102, 103]). For the PMMA system used in this study the components used are shown in Figure 3.1.

All the reaction components are soluble in the dispersion medium and a clear solution results before the reaction is initiated. The reaction is initiated using a free-radical initiator, α,α'azo-bis-isobutyronitrile [ADIB]. The high initial concentration of the polar monomer, MMA, provides good solvency for any PMMA polymer formed. As the monomer is consumed the solvency of the polymer in the dispersion medium decreases and a point is reached where the PMMA

Monomer	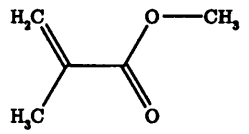 methyl methacrylate [MMA]
Initiator	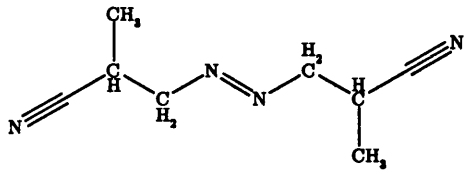 α,α'azo–bis–isobutyonitrile [ADIB]
Stabilizer	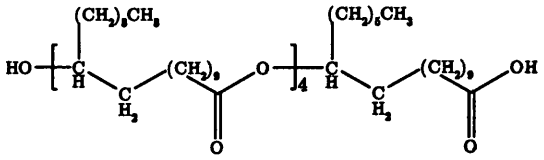 poly(12–hydroxystearic acid) [PHSA] based
Dispersion medium	2/3 hexane, 1/3 dodecane by volume

Table 3.1: PMMA dispersion polymerization reaction components

becomes insoluble. Approximately 8 minutes after the reaction is started, the transparent mixture turns slightly opaque as the nuclei of insoluble polymer form. The stabilizer contains a PMMA backbone which is therefore also under conditions of decreasing solvency and adsorbs onto the surface of the particles formed, thereby providing steric stabilization. This period of nucleation and stabilization is thought to be relatively short, leading to a constant number of particles which can then adsorb monomer and grow over a longer period of time leading to a monodisperse system [46, 104]. The higher the initial concentration of monomer the longer the polymer chains are allowed to grow in solution before becoming insoluble and separating. By varying the solvency and stabilizer conditions it is possible to achieve a range of particle sizes. The synthesis of PMMA/PHSA colloids has been investigated in a number of studies, with the studies by Pathmamaon-

haran *et al.* [102] and Antl *et al.* [46] being of particular importance. Antl *et al.* studied the effects of varying the initial concentration of the methyl methacrylate monomer between 5% and 50%. The results are illustrated in Figure 3.2

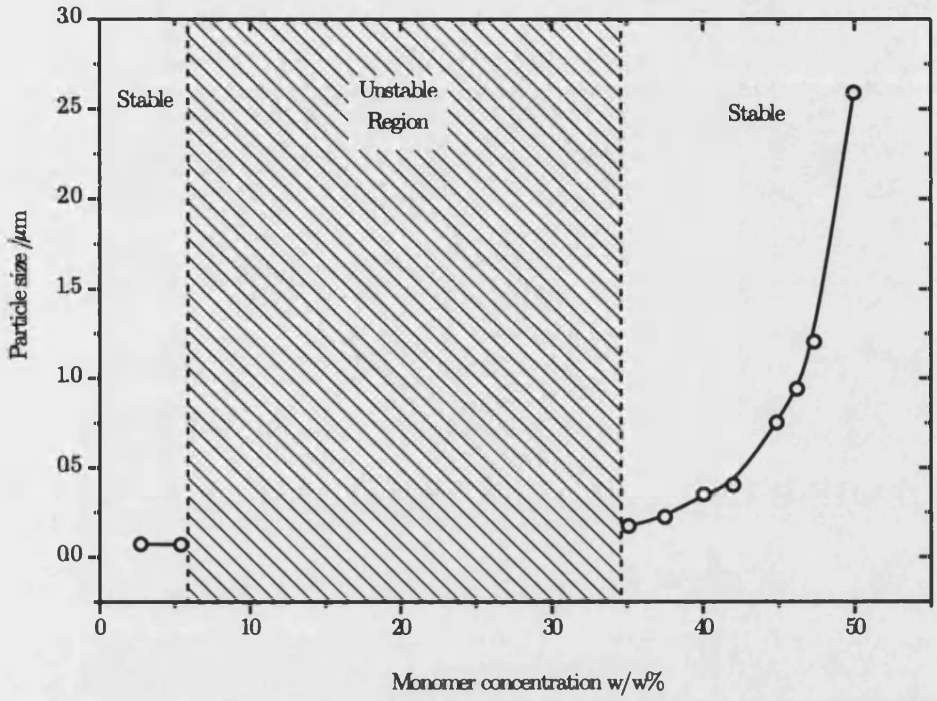

Figure 3.2: Particle size vs monomer concentration, from Antl *et al* [46]

Three distinct regions can be observed in the results. For monomer concentrations below 8.5%, small stable particles are formed with a diameter of approximately 80nm. For reactions with a monomer concentration between 8.5% and 34%, Antl *et al.* experienced coagulation or flocculation before completion of the reaction and no stable colloidal dispersions were formed. In the monomer concentration range between 35% and 50% stable dispersions were formed with the resulting particle size increasing with initial monomer concentration. The significant increase in particle size with the increase in monomer concentration can be explained in terms of the nucleation theory outlined in Section 3.2.1. In a later study by Pathmamanoharan *et al.* [102] it was shown that stable particles could be prepared in a monomer concentration range 8.5% to 34% by varying the amount of stabilizer used. Using data collated from these two studies enabled a

range of stable particles to be synthesized.

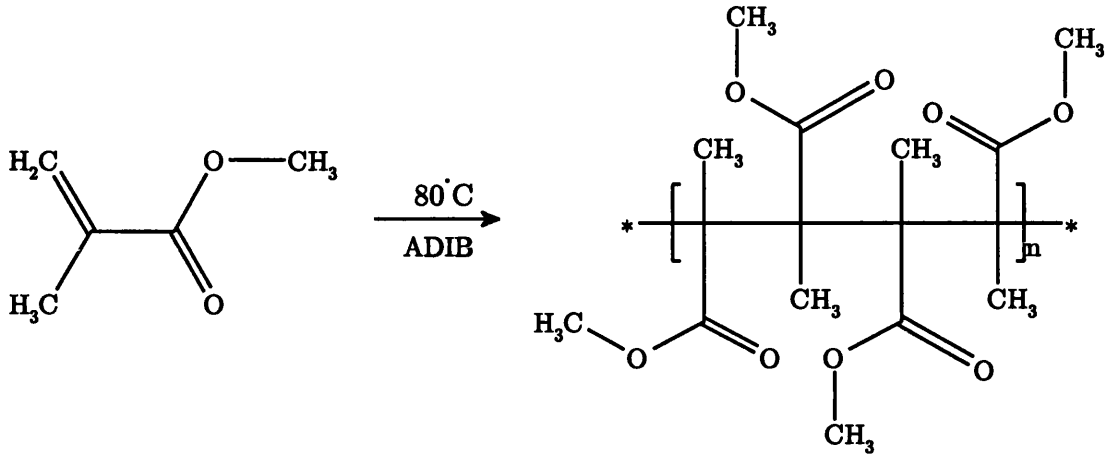

methyl methacrylate poly(methyl methacrylate)

Figure 3.3: Polymerization of methyl methacrylate

3.2.3 Materials

The materials hexane (95+%, Aldrich Chemical Co.), n-dodecane (99+%, Avocado), decahydronapthalene [Decalin] (98%,cis/trans mix, Acros), octyl mercaptan [1-octanethiol] (97+%, Aldrich), diethanolamine (99%, Aldrich), methyl-d_3 methacrylate-d_5 [*d*-MMA] (99 atom% D, stabilized by up to 0.5% hydroquinone-d_6, Polymer Laboratories) and methacrylic acid [MAA] (99%, inhibited by 250ppm hydroquinone, Aldrich), were all used as supplied. The methyl methacrylate [MMA] (99%, inhibited by 10–100ppm hydroquinone monomethyl ether, Aldrich) was distilled under vacuum to remove the inhibitor. The initiator, α,α'azo-bis-isobutyronitrile [ADIB] (97%, BDH) was recrystallized from acetone. The MAA, MMA and *d*-MMA, were kept refrigerated.

3.2.4 Purification of the stabilizer

The stabilizer used was formed by reaction of poly(12-hydroxy-stearic-acid) [PHSA], with glycidyl methacrylate to give a macromonomer, and then copolymerizing this macromonomer with methyl methacrylate and glycidyl methacrylate, see Figure 3.5 [105].

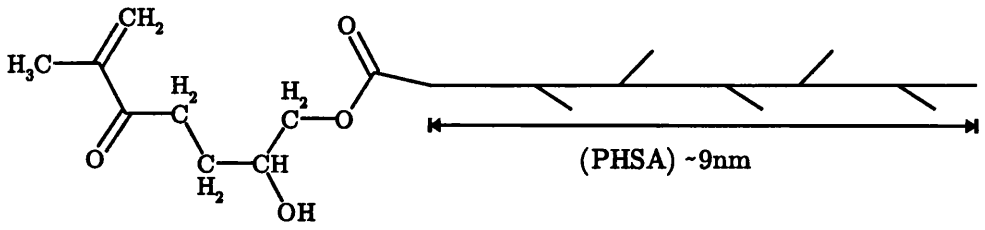

Figure 3.4: Schematic representation of the PHSA-GMA component of the stabilizing macromonomer

The stabilizer used was kindly supplied by Neil Hunt [106]. The stabilizer was prepared in acetate solvents which are known to dissolve PMMA, so the stabilizer was separated from the acetate solvents before further use. This was done by adding the stabilizer drop wise to an excess of methanol at 0 °C. The resulting precipitate was then filtered from the methanol and dried in-vacuo at 45 °C. The precipitated stabilizer was then added to dodecane at 120 °C and stirred. A 30% (by weight) solution of stabilizer in dodecane was produced.

3.2.5 Preparation of the latices

PMMA colloidal dispersions were prepared by a single-stage dispersion polymerization process following the methods described by Antl *et al.* [46]. The initiator [ADIB], monomer [MMA], and stabilizer [MMA-PHSA-GMA] were weighed into a 250ml round bottom flask. The organic dispersion medium, a 2:1 ratio of hex-

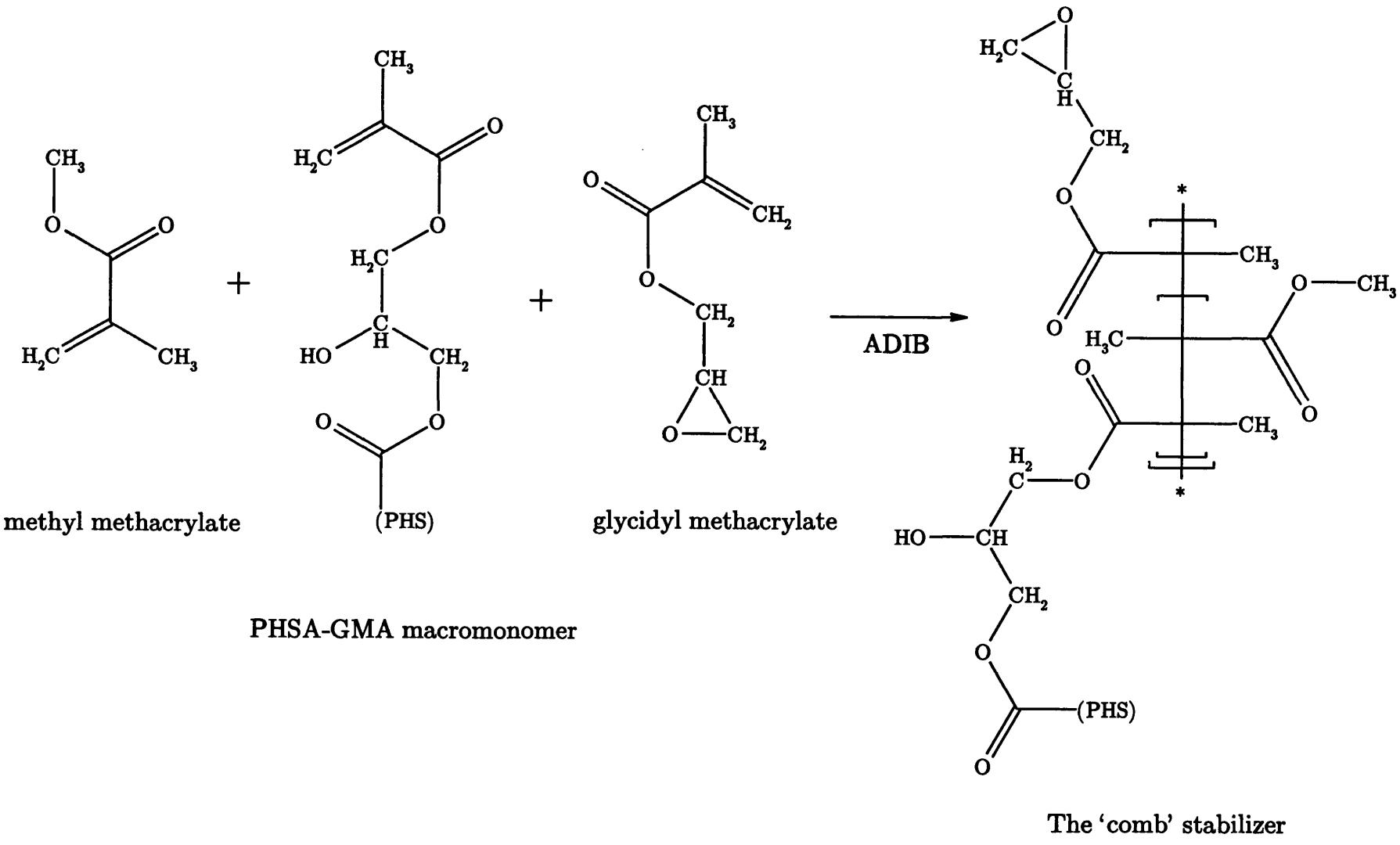

Figure 3.5: Scheme of synthesis of the comb-stabilizer

ane and dodecane was then added, followed by the methacrylic acid. A chain transfer agent, octyl mercaptan, was added to restrict the molecular weight of the polymer and thus give particles with a smooth surface. The mixture was stirred briefly to achieve homogeneity. A water condenser was fitted to the flask in a vertical position and the flask was then submerged in an oil bath at 80 °C. The contents of the flask were not stirred during the reaction as it has been shown that stirring has no effect at the volumes being considered here [46]. After approximately 8 to 10 minutes the mixture turned from transparent to opaque as the light scattering nuclei formed. The growth of the nuclei continues as the reaction proceeds for a total reaction time of 2 hours.

3.2.6 Locking stage

Initially the stabilizer is attracted to the surface of the colloid by the solvency conditions of the polymerization reaction. To create a stronger bond between the stabilizer and the PMMA, the stabilizer was covalently linked to the particle surface by a further reaction.

Complementary reactive groups are included in the stabilizer and dispersed polymer. During the locking stage at the higher reaction temperature of 120 °C, the acid groups, resulting from the inclusion of methacrylic acid in the monomer mixture in the previous stage, react with the epoxide group on the stabilizer backbone, covalently linking the two. The amount of glycidyl methacrylate added to the comb stabilizer affects the strength of surface-anchoring of the stabilizer. If the number of reactive groups on the stabilizer is too small, inadequate resistance to solvents is obtained. If there are too many reactive groups on the macromonomer the stabilization will not extend a great enough distance to prevent attraction of the particles via van der Waals forces and flocculation would

occur. An appropriate balance was determined to be approximately 3% glycidyl methacrylate by weight on the total stabilizer weight [105].

To covalently link the reactive groups a locking reaction was carried out as follows; The condenser was switched to a horizontal position and the hexane removed by distillation at 80 °C. A volume of dodecane equal to the initial volume of hexane was then added, and a base catalyst, diethanolamine was added in the proportion of 0.2% by weight on the total weight of the preparation. The water condenser was then returned to the vertical reflux position. The temperature of the oil bath was increased to 120°C and the contents of the flask were allowed to reflux overnight.

3.2.7 Cleaning the colloidal dispersion

After being allowed to reflux overnight the resulting dispersion was filtered through glass wool to remove any aggregates formed. This dispersion was then further cleaned by centrifugation. This was necessary to remove excess stabilizer and unreacted monomer and to create a homogeneous dispersion medium suitable for creating samples to determine phase behaviour as described in Section 4.2.1. The dispersion was centrifuged in a Beckman high-speed centrifuge using an SS34 rotor at up to 10,000rpm for two hours. The supernatant was replaced with decalin by carefully decanting the supernatant from the centrifuge tube and pipetting into the tube an amount of decalin, equal in volume to the supernatant removed. The colloids were then redispersed by shaking the dispersion for up to 24 hours. The presence of stabilizer in the supernatant was monitored by IR-spectroscopy using the carbonyl stretching frequency at 1720cm^{-1}. Experience showed that to satisfactorily remove the stabilizer the process of centrifuging the latex and replacing the supernatant should be carried out a further three times.

3.2.8 Details of latices prepared

All colloidal dispersion were prepared by a single-stage dispersion polymerization process as described on page 60. Experiments to synthesize stable monodisperse colloids are grouped here into two sections;

Preparations with monomer weight concentration between 40–55%

Those reactions with a monomer weight concentration range between 40–55% are prepared under similar conditions to those prepared by Antl *et al.* [46], i.e. with a stabilizer concentration kept at a constant rate of 5% by weight of the monomer used. A number of preparations were carried out and are summarized in Table 3.2

Preparations with monomer weight concentration less than 40%

Those reactions with a monomer weight concentration below 40% are prepared using a smaller weight fraction of monomer, combined with an increased fraction of stabilizer to attempt to produce smaller colloids as produced by the methods used by Pathmamanoharan *et al.* [102] (See section 3.2.2) A number of preparations were carried out accordingly, the details are summarized in Table 3.3. These colloids were prepared for the small angle neutron scattering experiments described in Chapter 7. Deuterated methyl methacrylate was used in place of methyl methacrylate in preparations RSJC8(d) and RSJC9(d) to synthesize colloids suitable for contrast matching scattering techniques.

All colloidal dispersions formed were stable and did not coagulate. Particle and

dispersion characterization is given in Chapter 4.

Sample Code	RSJC1	RSJC2	RSJC3	RSJC4	RSJC5
MMA (%TPW)	47.54	46.68	47.04	46.00	55.00
Initiator (%TPW)	0.40	0.44	0.40	0.42	0.39
Stabilizer (as % of monomer)	5.00	4.94	5.00	5.00	5.00
Octyl Mercaptan (as % of monomer)	0.51	0.35	0.51	0.48	0.51
Hexane: Dodecane	2.00	2.09	2.00	2.00	2.00
Total Preparation Weight [TPW] (/g)	65.04	66.76	65.04	65.00	64.96

Table 3.2: Details of unmodified PMMA Preparations

Sample Code	RSJC6	RSJC7	RSJC8(d)	RSJC9(d)
Monomer (%TPW)	33.00	34.01	34.96	34.94
Initiator (%TPW)	0.38	0.41	0.40	0.40
Stabilizer (as % of monomer)	20.00	20.06	20.01	19.56
Octyl Mercaptan (as % of monomer)	0.50	0.59	0.55	0.52
Hexane: Dodecane	2.21	2.00	2.01	2.00
Total Preparation Weight [TPW] (/g)	67.00	15.03	15.12	15.56

Table 3.3: Details of Smaller PMMA and d-PMMA Preparations

3.3 Synthesis of Fluorescent Polymer Colloids

Introduction

Fluorescence is a form of luminescence which occurs after photons of light are absorbed by a molecule known as a fluorophore in the ground electronic state. The molecule is raised to an excited state as a result of electron transfer to a higher energy orbit. This excess energy is dissipated when the electron returns to the original ground state, releasing a quantum of light. The time required for absorption is immediate, approximately 10^{-15} s, whereas the fluorescence lifetime is approximately 10^{-8} s. An important characteristic of a fluorescent probe is the wavelength of maximum absorption or excitation. The photobleaching of probes is also a problem, especially in microscopic techniques where small areas may be scanned many times. The technique of fluorescent staining is used extensively in cell biology, as is the technique of fluorescent laser scanning confocal microscopy, leading to many of the commercially available dyes being developed specifically for this area [107]. The majority of biological systems are polar in their nature and this means a large number of the more commonly used dyes are unsuitable for inclusion into the PMMA dispersion polymerization. The dye chosen in this study is a derivative of the 4-chloro-7-nitrobenzo-2-oxa-1,3-diazole [NBD-Cl] precursor, derivatives of which are commonly used as fluorescent tags for lipids, fatty acids, and other less-polar biological features [108]. The NBD-Cl was coupled with a secondary amine, following a modified procedure similar to that described by Monti *et al.* [109], to activate the fluorescent properties of the molecule. This was then further reacted with methacrylic acid to attach a methyl methacrylate monomer unit to the dye to facilitate inclusion of the dye into the PMMA colloid.

3.3.1 Synthesis of a suitable fluorescent dye

Materials

The materials sodium hydrogencarbonate (95+%, Aldrich), 2-(methylamino)ethanol [MEA] (99%,Aldrich), 4-chloro-7-nitrobenzo-2-oxa-1,3-diazole [NBD-Cl] (98% Aldrich) methacryoyl chloride [MACl] (90%, Aldrich), triethylamine [TEA] (99%, Aldrich) and HCl(1.0*M* solution, Aldrich) were all used as supplied. The tetrahydrofuran [THF] (99.5+%, Alrdich), was dried with 5Å molecular sieve. The methanol (99.5+%, BDH) and ethanol were distilled before use.

Stage 1

2.52 g (30 mmol) of sodium hydrogencarbonate and 0.74 g (9.9 mmol) of MEA were dissolved in 20 cm^3 of H_2O in a round bottomed flask. 1.99 g (10 mmol) of NBD-Cl was dissolved in 80 g of methanol which was added to the flask. The reagents were warmed for 3 hours at 55 °C whilst being stirred continuously. After 3 hours the methanol was removed by rotary evaporation and the remainder was left to cool to room temperature. The mixture was acidified to pH[1.5] with 28 cm^3 of 1M HCl. The solution was cooled in ice and the orange solid was filtered and washed with distilled water. The resulting bright orange powder was dried in-vacuo at 40–45 °C.

Stage 2

0.450 g (1.8 mmol) of the stage 1 product (NBD–$N(CH_3)C_2H_4OH$) was added to 10 cm^3 of THF, then 0.6 cm^3 (4.3 mmol) of TEA was added. The mixture was

stirred at 0 °C and 0.5 cm^3 (5.1 mmol) of MACl was added dropwise. The mixture was stirred continuously at 0 °C for two hours and then left overnight. The THF was removed by vacuum distillation, and the remaining solid was dried under vacuum at <40 °C. The solid was recrystallized from a THF/ethanol mixture and washed with ether. See reaction scheme, Figure 3.6.

Results

Stage 1 Product

A bright orange solid was synthesized with a yield of approximately 70% and a melting point of 164–166° C.

The results from elemental analysis of the stage 1 product give good agreement with the calculated elemental fractions for the assumed product NBD-MAE, as shown in Table 3.4.

	N	C	H
Expected%	23.52	45.38	4.23
Found%	23.7	45.3	4.26

Table 3.4: Stage 1 product elemental analysis

Mass Spectrometry The mass of NBD-MAE is 238.2 g/mol. This is in good agreement with the results from mass spectrometry as seen in Figure 3.7. The main peak at 238 m/z corresponds to the unfragmented NBD-MAE. The peak at 222 m/z corresponds to a fracture of the N-O bond in the nitro group, and the peak at 193 m/z corresponds to cleavage at HO–CH_2···CH_2–N–. The peak at 476 m/z indicates some dimerization of the unfragmented NBD–MAE molecule.

Step 1

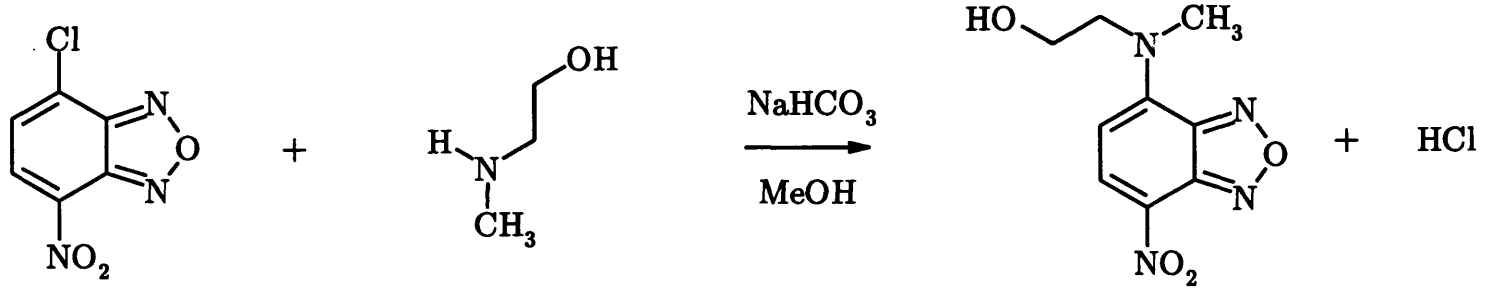

NBD-Chloride 2-(methylamino)ethanol NBD-MAE

Step 2

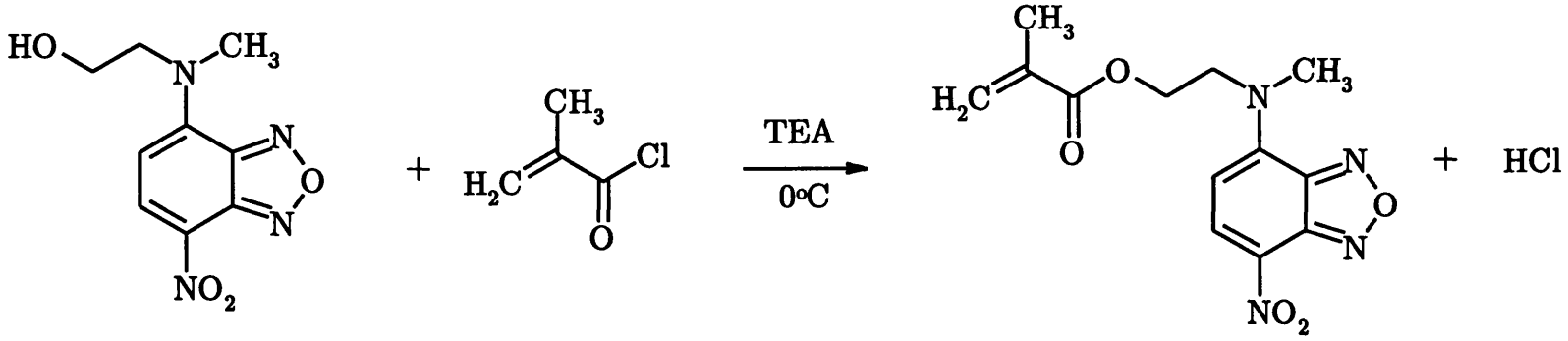

NBD-MAE methacyryoyl chloride NBD-MMA

Figure 3.6: Scheme of synthesis for the NBD–MMA fluorescent tag

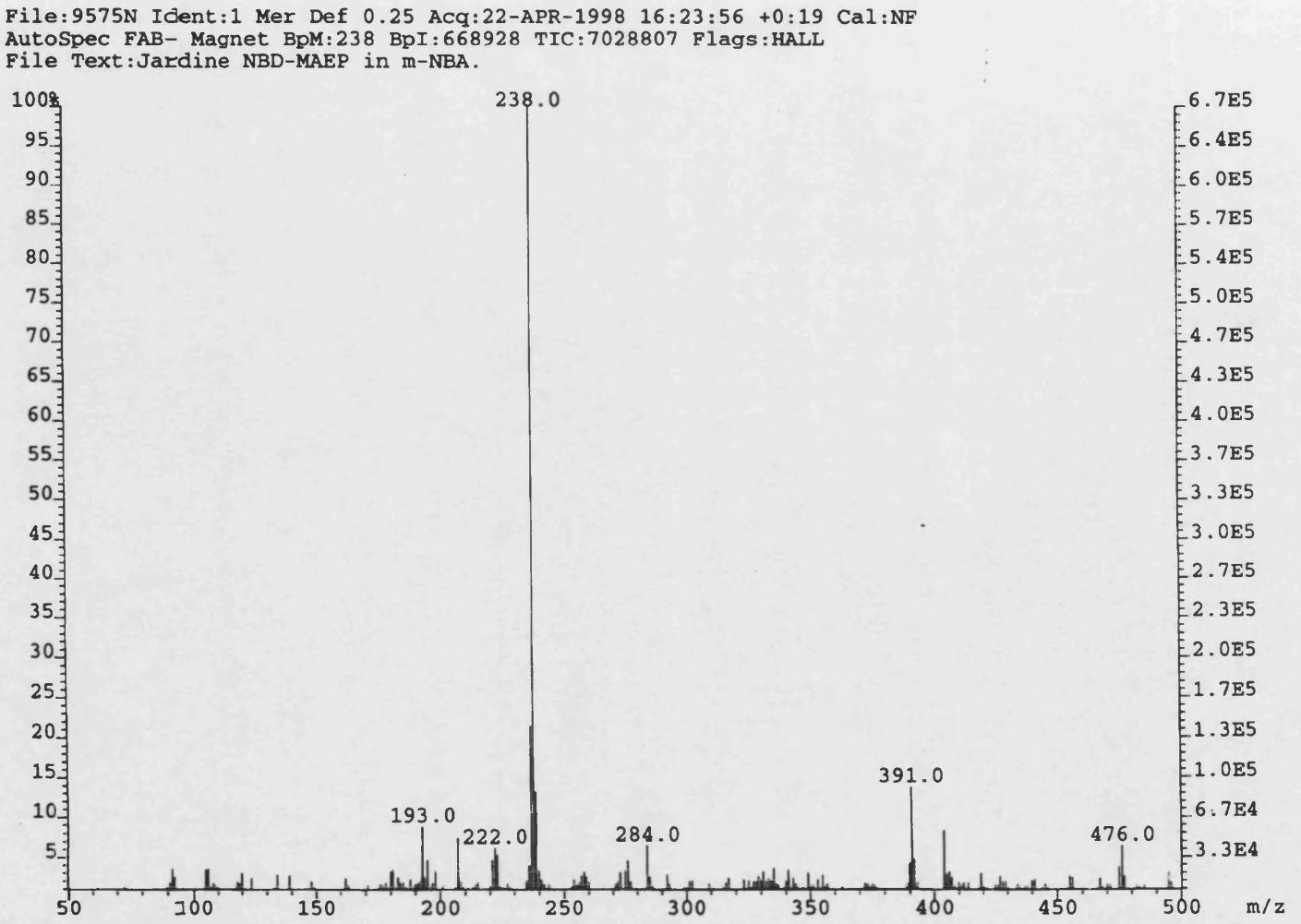

Figure 3.7: Mass Spectrum of Stage 1 product

Position	Multiplicity	Splitting	Assigned Molecule
8.45 ppm	d	J=9 Hz	-N-CCHCC$\underline{H}$C-NO_2
6.44 ppm	d	J=9 Hz	-N-CC$\underline{H}$CHC-NO_2
3.78 ppm	t	J=5.5 Hz	-N-$CH_2C\underline{H}_2OH$
3.74 ppm	t	J=5.5 Hz	-N-$C\underline{H}_2CH_2OH$
2.51 ppm	s		$C\underline{H}_3$-N-

Table 3.5: ^{1}H-NMR of stage 1 product in DMSO-d_6

^{13}C-NMR in DMSO-d_6: 146–102 ppm, (6 aromatic ring carbons); 58.47 ppm (-N-$\underline{C}H_2CH_2OH$); 57.34 ppm (-N-$CH_2\underline{C}H_2OH$); 30.67 ppm ($\underline{C}H_3$-N-)

Fluorescence Data

Excitation and emission spectra were determined with a Perkin-Elmer fluorimeter, see Figure 3.8. The reaction produced a highly fluorescent product which was excitable at a wavelength of 488nm, with an emission maxima at a wavelength of 519nm and is therefore highly suitable for excitation and detection by laser scanning confocal microscopy.

Conclusions of Stage 1 Synthesis

It can be concluded from the data that stage 1 of the reaction proceeds as shown in Figure 3.6 and that the reaction product is indeed 2-(Methyl-(8-nitrobenzo[1,2,5]oxadiazol-4-yl)-amino)-ethanol [NBD-MAE]. The reaction produced a highly fluorescent product from non-fluorescent precursors.

Stage 2 Product

An orange solid was synthesized with a yield of approximately 36%.

The results from elemental analysis of the stage 2 product do not give good

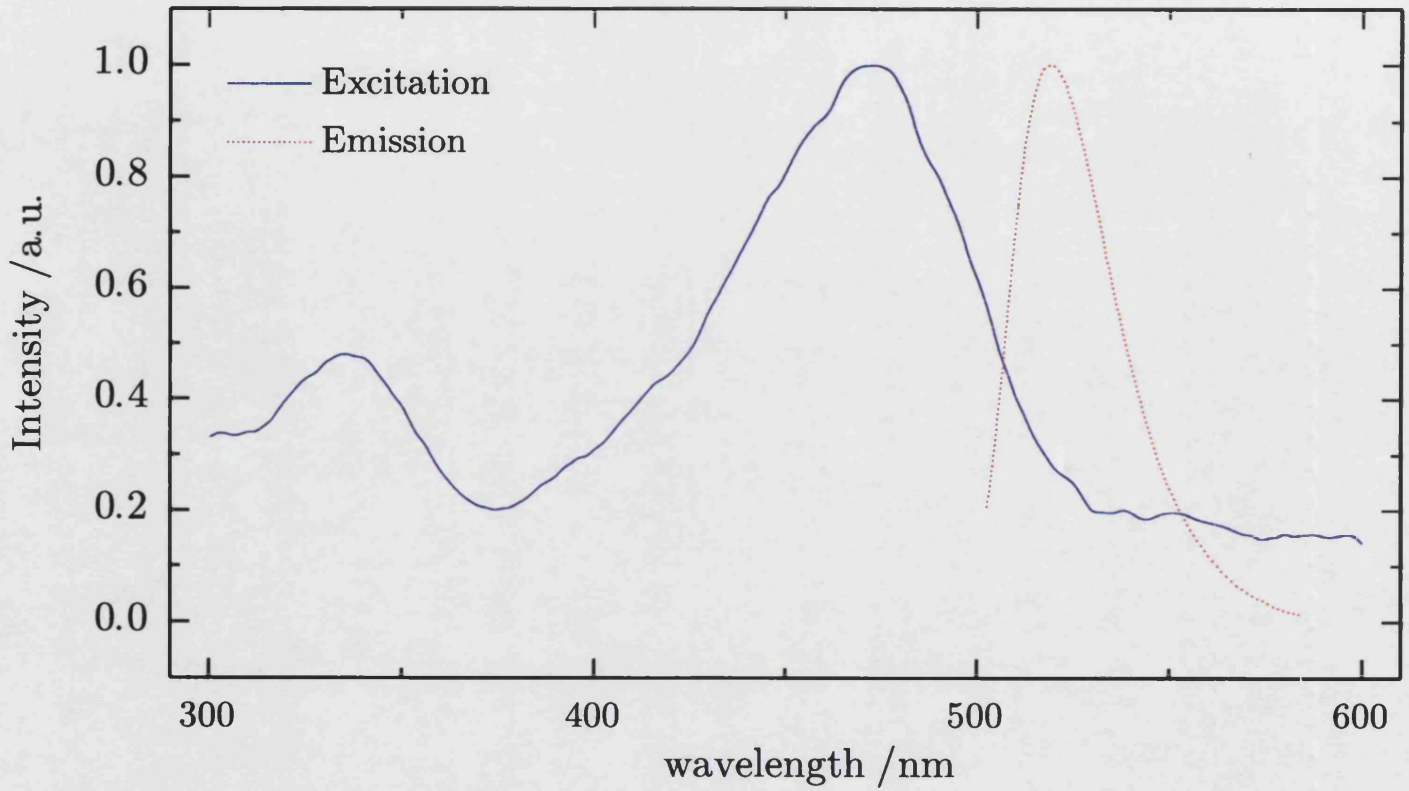

Figure 3.8: The fluorescence excitation (–) and emission (···)spectra of NBD–MAE in decalin. Measurements were made at an excitation wavelength of 488nm and emission wavelength of 525nm.

agreement with the calculated elemental fractions, as shown in Table 3.6.

	N	C	H
Expected%	18.29	50.98	4.61
Found%	10.9	48.6	9.90

Table 3.6: Stage 2 product elemental analysis

Mass Spectrometry The mass of NBD-MMA is 306.28 g/mol.The results from mass spectrometry as seen in Figure 3.9 indicate the presence of triethylamine and other large molecules.

Conclusions of Stage 2 Synthesis

Despite repeated attempts to produce more conclusive data from stage 2 of the NBD-MMA synthesis, the reaction was never clean enough to prove that the reaction proceeds as detailed in Figure 3.6. However, the reaction produced a highly fluorescent product with excitation and emission spectra that were shifted slightly from the NBD-MAE spectra.

3.3.2 Incorporating the fluorescent dye into the polymerization reaction

The latices were prepared by a single-stage dispersion polymerization process as described on page 60, with the exception of the addition of the fluorescent tag, which was briefly dispersed in the methacrylic acid component before being added.

A number of preparations were carried out with varying fluorophore concentrations as shown in table 3.7. Each experiment was made to a total preparation

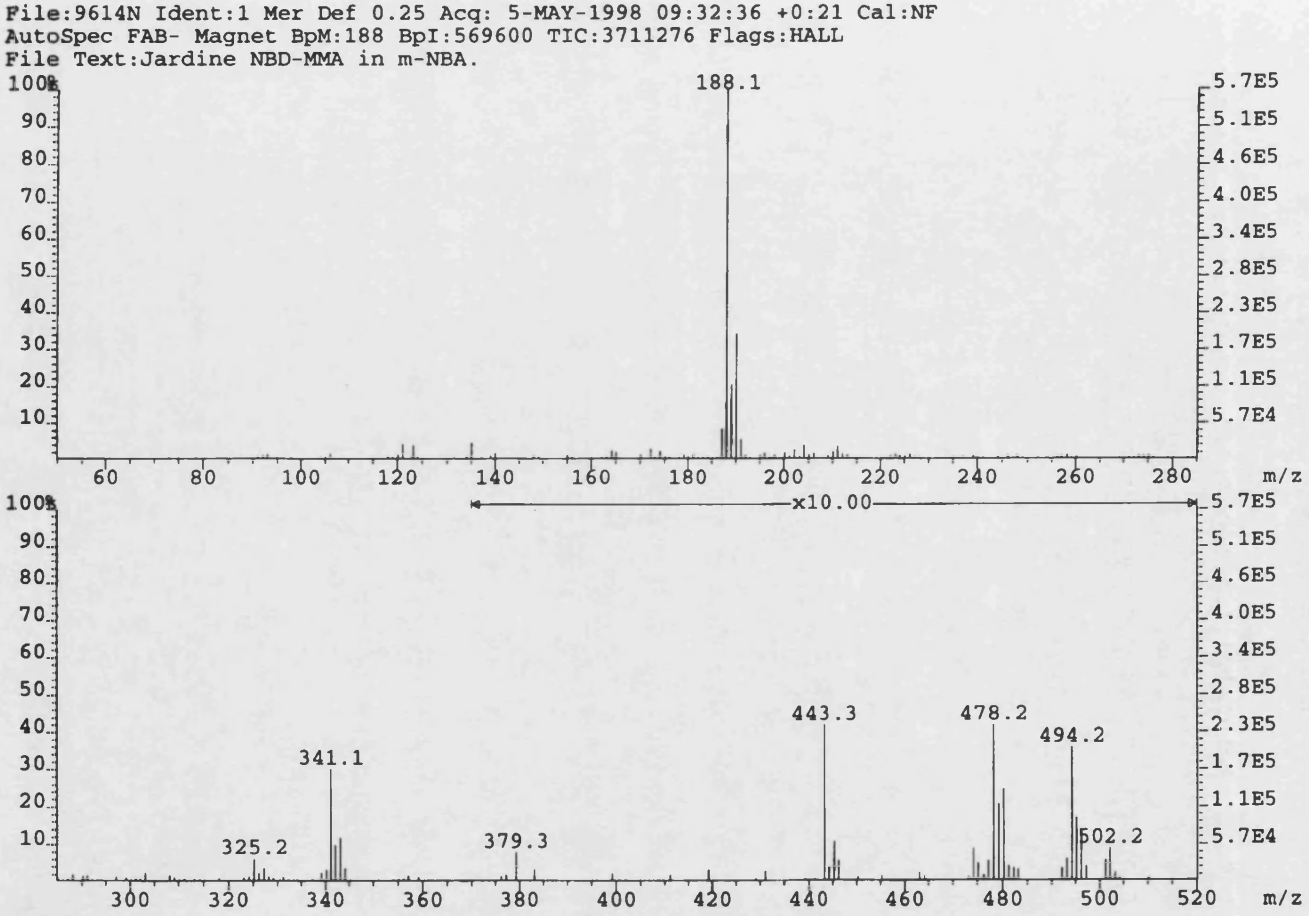

Figure 3.9: Mass Spectrum of Stage 2 product

weight of approximately 65g.

	RSJF1	RSJF2	RSJF3	RSJF4	RSJF5
MMA (%TPW)	47.47	47.38	46.42	46.90	49.50
Initiator (%TPW)	0.40	0.41	0.39	0.40	0.39
Stabilizer (as % of monomer)	5.15	5.01	5.29	5.08	5.04
Octyl Mercaptan (as % of monomer)	0.50	0.52	0.51	0.50	0.54
Hexane: Dodecane	2.00	2.01	2.00	2.00	2.00
Fluorescent Tag (as % of monomer)	0.22	0.23	2.02	0.91	1.01
Total Preparation Weight [TPW] (/g)	65.08	65.17	65.21	64.81	65.02

Table 3.7: Preparation details of fluorescent latices

The fluorescent tag used in each preparation was the product of the reaction shown in figure 3.6, except for the dispersion named RSJF5. The fluorescent tag used in the RSJF5 polymerization was the product of the first stage of the reaction shown in figure 3.6, the NBD–MAE. This substitution of fluorescent tag was used to verify whether the MMA adduct was necessary for the dye to become fixed within the colloidal particle.

3.4 Conclusions

A range of different PMMA colloids have been synthesized in this study. Stable PMMA colloids within the size range 250 to 1100 nm have been prepared using a monomer weight concentration range between 45–50% under similar conditions to those prepared by Antl *et al.* [46]. Smaller colloids, in the range 95 to 115 nm have been prepared using a monomer weight concentration range between 30–

35% under similar conditions to those prepared by Pathmamanoharan *et al.* [102]. Colloids suitable for use in neutron scattering experiments were prepared, using deuterated methyl methacrylate was used in place of methyl methacrylate resulting in stable, PMMA colloids suitable for use with contrast matching techniques.

Fluorescent dyes, NBD-MMA and NBD-MAE have been synthesized, intended for inclusion into PMMA colloids for detection by fluorescent laser scanning confocal microscopy. The fluorophores were fixed within the particles and did not cause coagulation of the fluorescent colloidal dispersions produced, which were stable.

All colloidal dispersions synthesized were stable and did not coagulate. Particle sizes, interactions and other particle characterization is presented in Chapter 4.

Chapter 4

Characterization of PMMA colloids

The polymer colloids as synthesized in Chapter 3 are characterized here. The particle radius and polydispersity are obtained and the phase behaviour of the colloidal dispersions is determined.

4.1 Particle properties: Size and polydispersity

Transition electron microscopy [TEM] and light scattering methods are used to measure the radius and polydispersity of the colloidal dispersions synthesized and thus determine whether the particles are suitable for use as model particles.

As discussed in Chapter 2, the Brownian motion of colloidal particles causes light scattered from a colloidal dispersion to fluctuate with time. Detection and autocorrelation of these fluctuating intensities is an accurate method for measuring diffusion coefficients from which a mean particle radius and particle polydispersity can be reliably interpreted. TEM measurements are used to confirm the validity of the DLS results.

4.1.1 Dynamic Light Scattering

The multi-angle DLS approach of Pusey and van Megan [88] (described in section 2.4.3) is used here to obtain measurements of size and polydispersity of colloidal particles. The study of sample RSJF1 is used to establish the methodology, and results for all colloids are presented in Table 4.1.

For scattering measurements glass cuvettes were used, rinsed with distilled acetone. Trans-decalin filtered through $2\,\mu$m Millipore filters was added to a small amount of colloid to give dilute dispersions with a colloid volume fraction of the order of 1×10^{-3}.

Dynamic light scattering measurements were performed with a Coherent Innova 300 series Argon/Krypton laser operating at 488 nm or 647.1 nm. The lower wavelength was used due to the greater power available at that wavelength, the higher

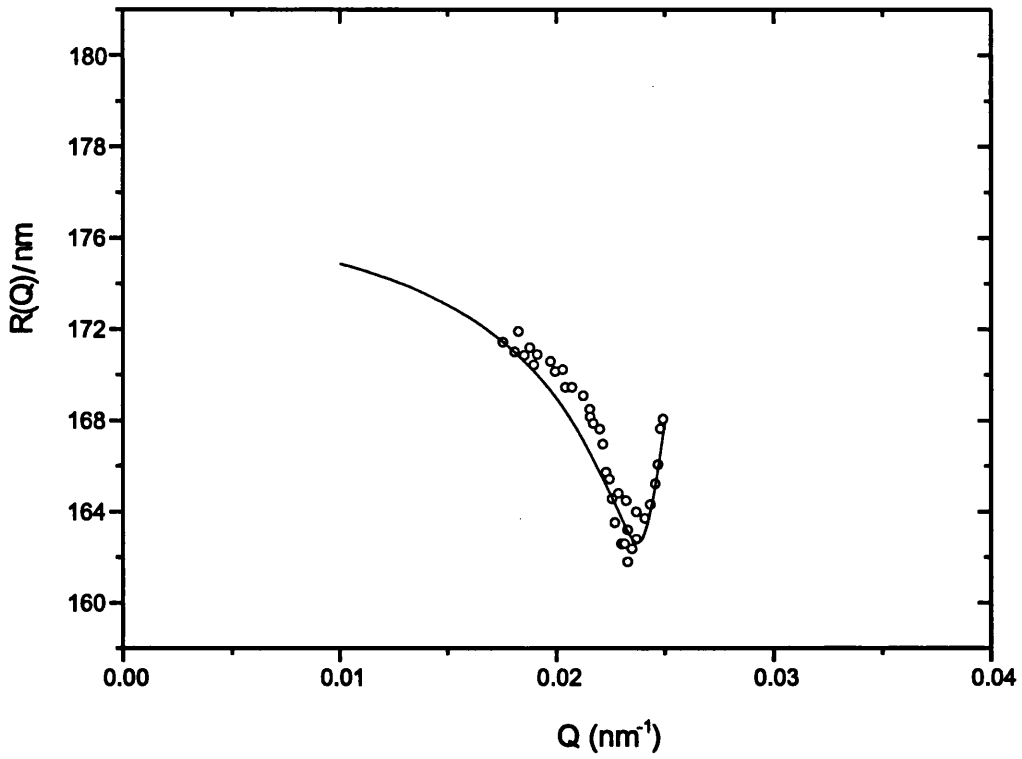

Figure 4.1: The effect of polydispersity on detected size at varying angles. The circles show the apparent size, as measured by DLS, from sample RSJF1. The line shows the calculated variation in detected size,$R(Q)$, for a Schultz distribution of spheres sizes with a mean radius of 175 nm and a polydispersity, σ=0.07

wavelength was used for scattering experiments involving fluorescent particles, as it is not absorbed by the fluorescent dye thereby avoiding fluorescence which may distort measurements. Intensity autocorrelation functions as described in Chapter 2 were measured using a Malvern 128 point correlator (described in detail in Section 2.4.4). Effective diffusion coefficients, $D_e(Q)$, were obtained from cumulant fits of the autocorrelation functions measured over a range of scattering angles between 40° and 120°. From these diffusion coefficients the hydrodynamic radius was calculated using the Stokes-Einstein relations. Figure 4.1 shows the results of multi-angle DLS measurements, from a dilute suspension of the colloid denoted RSJF1, together with a fit, calculated for a Schultz distribution of hard-spheres.

Results

Particle codes with the prefix RSJ were synthesized as part of this work and the synthesis is described in Chapter 3. Other particles were synthesized prior to this work [106].

Latex	Monomer (%TPW)	Stabilizer (%MW)	Diameter (R_{DLS}/nm)	Polydispersity (σ_{DLS})
RSJC1	47.54	5.00	850	0.08
RSJC2	46.68	4.94	320	0.08
RSJC3	46.54	5.00	320	0.10
RSJC4	46.00	5.00	360	0.11
RSJC5	55.00	5.00	1090	0.07
RSJC6	33.00	20.00	101	-
RSJC7	34.01	20.06	111	-
RSJC8(*d*)	34.96	20.01	98	-
RSJC9(*d*)	34.94	19.56	101	0.11
RSJF1	47.47	5.15	350	0.07
RSJF2	47.38	5.01	405	0.10
RSJF3	46.42	5.29	326	0.09
RSJF4	46.90	5.08	237	0.13
RSJF5	49.50	5.04	612	0.07
NH10	47.00	5.00	575	-
NH25	53.00	5.00	1042	0.08
NH31	53.00	5.00	916	0.07

Table 4.1: Particle diameters and polydispersities as determined by dynamic light scattering. ([TPW]=Total Preparation weight, [MW]=monomer weight (d)=deuterated colloid)

4.1.2 Transmission Electron Microscopy

Although previous work has demonstrated the reliability of results from the dynamic light scattering set-up used in this work, by a thorough comparison of DLS and TEM results [106], TEM measurements were carried out on one sample for further validation.

For TEM measurements a dilute solution of colloid in hexane was prepared with

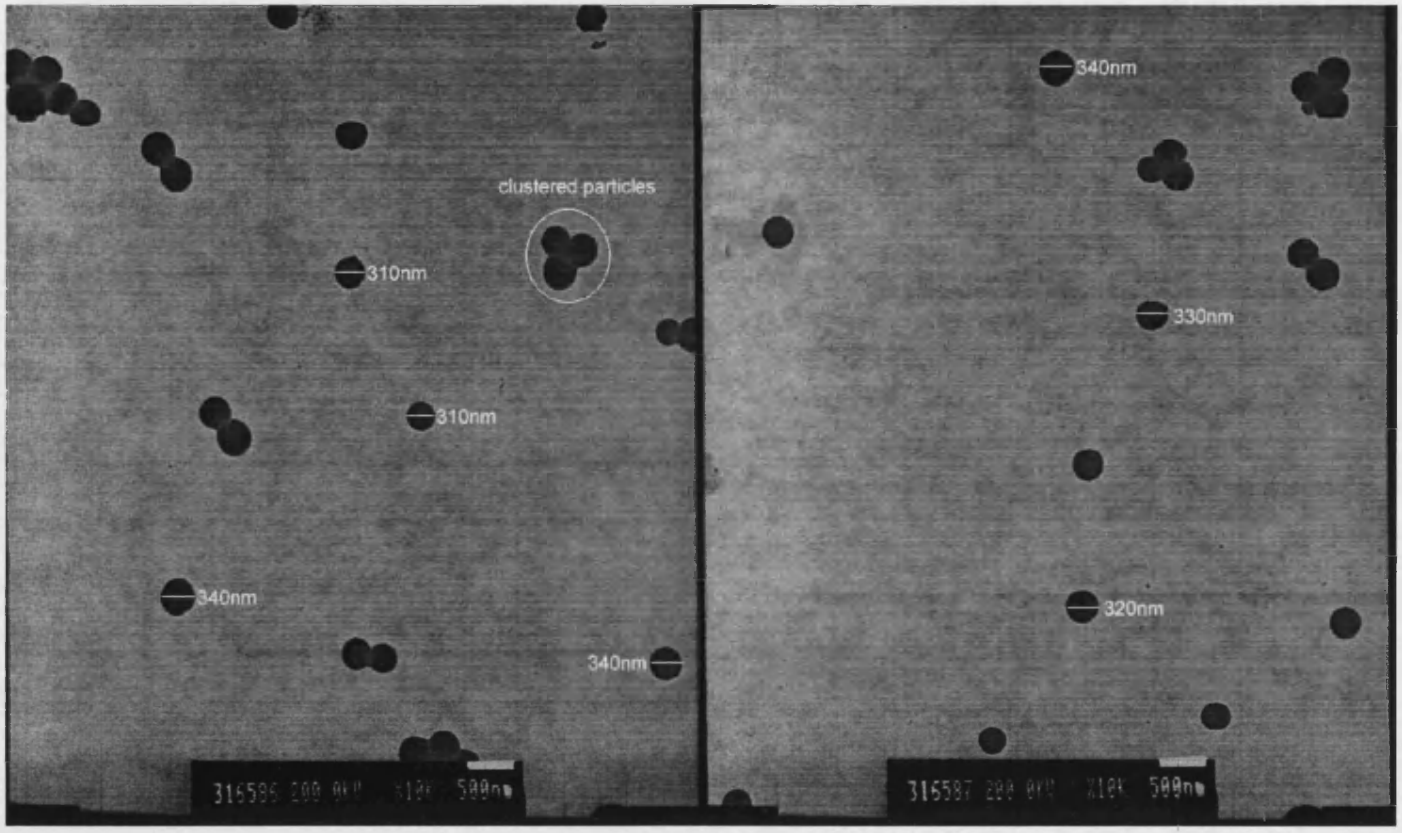

Figure 4.2: Transmission electron micrographs of colloid RSJF1. Clusters, distorted particles and artefacts were not analysed.

a volume fraction of $\sim$ 0.015. A single drop of the solution was applied to a microscope slide and the hexane was left to evaporate. The slide was then placed in a vacuum evaporator, and coated with a thin layer of carbon. This sample would deform under the focussed electron beam of TEM due to the PMMA particles, so the film and particles were carefully removed from the slide into a water bath, where the PMMA particles were dissolved using 1,4-dioxane. Pieces of the carbon shell were then mounted onto TEM grids and allowed to dry. Electron micrographs were taken of the areas of interest. Two examples are shown in Figure 4.2. Computer analysis of the micrographs enabled measurement of the mean particle radius, as given in Table 4.2.

Latex	Diameter (R_{TEM}/nm)	Diameter (R_{DLS}/nm)
RSJF1	330	350
NH31	897	916

Table 4.2: Particle sizes as determined by transmission electron microscopy [TEM] compared with sizes determined by dynamic light scattering

The results for TEM show slightly smaller sizes than for DLS. This is typical [53, 106, 110], and most likely reflects the fact that DLS measures the hydrodynamic size, which will take into account the PHSA stabilizing layer of the PMMA particles.

4.2 Interparticle properties: Phase behaviour

The interaction potential of suspended colloidal spheres can assume a varied range of forms. These are qualitatively comparable to the pair potential of atoms and colloidal suspensions can display a similar range of phase behaviour to simple atomic systems including fluid to crystal and crystal to glass transitions. The sim-

plicity of the hard-sphere potential makes it a suitable starting point for investigation of phases and phase transitions . An understanding of the phase behaviour of a system of equally sized hard-spheres was first developed by Alder and Wainwright in the 1950s who discovered a phase transition in a molecular dynamics simulation of up to 500 hard-sphere particles [58, 111]. These findings were established quantitatively by Hoover and Ree in 1968 [59]. For hard sphere systems with a low sphere volume fraction the stable phase is a disordered fluid. Above the melting volume fraction, $\phi_m = 0.545$, the equilibrium phase is crystalline although in systems prepared at high enough volume fractions, $\phi > 0.57$, homogeneous crystallization is suppressed by the formation of long-lived metastable glassy states [112]. For systems with a particle volume fraction between the freezing, $\phi_f = 0.494$, and melting volume fractions, a crystalline phase is formed with a volume proportional to the particle volume fraction (see Figures 4.3 and 4.4). Complementing these computational studies there have been many detailed studies on the phase behaviour of model colloidal systems [53]. Pusey and van Megan found a variety of phase behaviour in PMMA colloidal systems which fitted well with hard-sphere theory [61, 113]. By measuring the volume of the crystalline phase in a range of samples covering the melting and freezing points, a phase diagram can be constructed and compared with the phase behaviour obtained from computational studies.

4.2.1 Experimental and Results

The colloidal particles as synthesized in Section 3.2 are suspended in decalin. The mass fraction of polymer in a dispersion was determined by drying samples of the dispersion in pre-heated glass ampules. The solvent was evaporated in-vacuo at <60 °C over a period of days until a constant mass was achieved. Samples

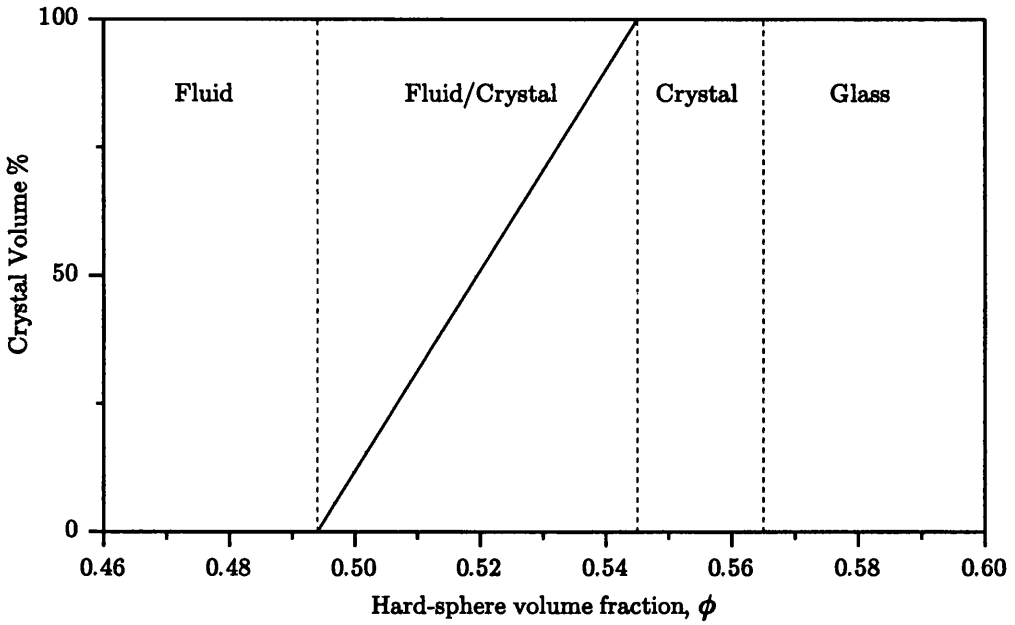

Figure 4.3: Phase diagram of hard-sphere suspensions.

of the dispersion are then prepared in 1 cm path-length cuvettes with a range of estimated final volume fractions covering the range of volume fractions between freezing and melting densities. To minimize the van der Waals attractions and to reduce multiple scattering so as to aid examination by eye and by light scattering, the refractive index of the dispersion media is increased by the addition of carbon disulfide to be closer to the refractive index of the colloid. Carbon disulfide is added by eye to the dispersion medium so that at visible wavelengths the refractive index of the dispersion medium closely matches the refractive index of the colloid. Carbon disulfide is known to penetrate the PMMA core of the colloids slightly, resulting in an increase in the diameter of the colloid of approximately 3%. This issue has been studied in detail by Ottewill and Livsey [47]. After adding CS_2 the particles were left for 24 hours. The swelling of the particles due to penetration of CS_2 is complete after a few hours and the particle characteristics are then constant for many months [47]. After 24 hours additional CS_2 was added as necessary to complete the index match of the solvent to the swollen colloids. The amount of CS_2 required for a close refractive index match was found on

average to be a mass fraction of approximately 0.32, in reasonable agreement with van Megen *et al.* [53]. The density of the colloidal particle is uncertain as it is affected by the swelling due to CS_2 and in addition, the density of the solvated stabilizing layer is, at present, uncertain.

The index-matched samples were then separated by centrifugation and a weighed amount of the supernatant was removed to create samples with varying core volume fractions, spanning the expected freezing and melting concentrations. The samples were sealed to minimize solvent evaporation using silicon grease and parafilm around the cuvette stoppers. The samples were then tumbled to redisperse the compressed colloid. After redispersion, samples with particle diameters of less than $\approx$600 nm were left undisturbed at room temperature, samples containing larger colloids were subjected to time-averaged zero gravity by slowly rotating the samples at one revolution per day in the vertical plane, following the methods described by Bartlett *et al.* [48].

Between the melting and freezing transitions where colloidal crystal and fluid coexist, Bragg reflecting crystallites form due to homogeneous crystallization occurring throughout the bulk of the sample. These macroscopic crystallites ($\approx$50 μm) then settle due to gravity and a fluid-crystal boundary can be observed, see Figure 4.4.

This boundary was carefully measured using a cathetometer or video techniques. Periodically monitoring the interface position at varying intervals of time provides a measure of the extent of compression of the crystal arising from gravitational forces [52, 68]. Extrapolating the fluid-crystal interface position to zero time gives the equilibrium volume fraction of the crystalline phase (See Figure 4.5). Estimates of crystalline volume fraction taken within 2 days of initial crystallization are within experimental error of the zero time estimate and these values have

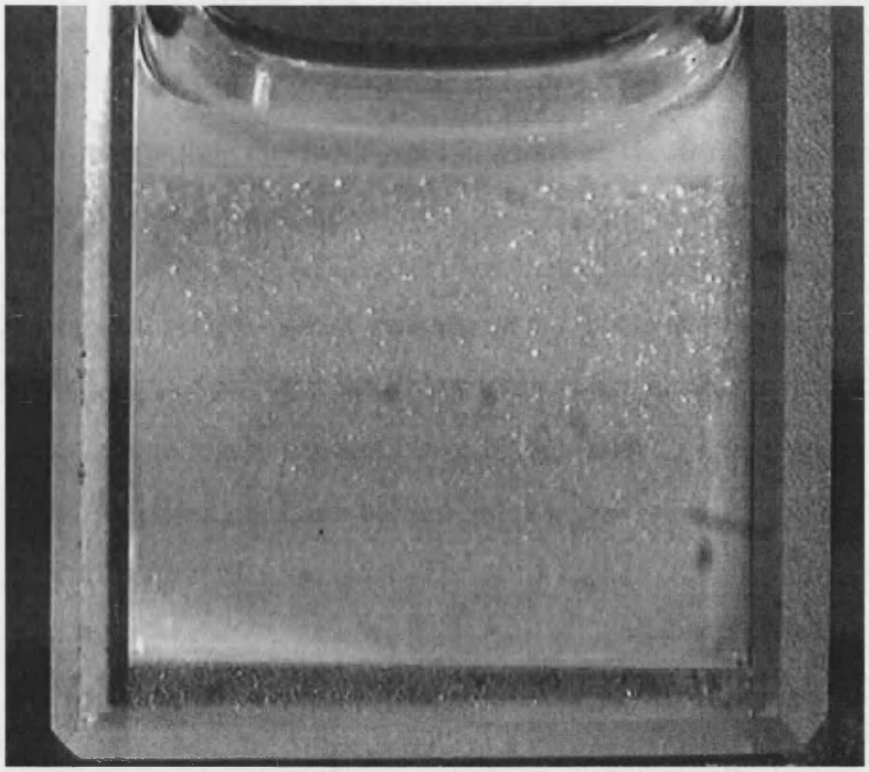

Figure 4.4: Fluid-Crystal boundary in colloid PBM10 (sample 3B)

been used interchangeably throughout.

The crystal fractions of various crystallizing samples are shown for sample PBM10 in Figure 4.6. The extrapolation to 0 and 100% crystal volume provides, respectively, the freezing and melting core volume fractions, χ_f and χ_m.

The samples are prepared precisely by weight fraction but due to the uncertainty in the density of the PMMA colloids it is difficult to accurately determine the hard-sphere volume fractions. It is therefore assumed that the core volume fraction corresponding to the freezing transition, χ_f, is equal to the effective hard-sphere volume fraction, $\phi_f = 0.494$. The hard-sphere volume fractions of the samples, ϕ, were then obtained by the appropriate scaling of the core volume fraction, χ

$$\phi = \phi_f \cdot \frac{\chi}{\chi_f} \tag{4.1}$$

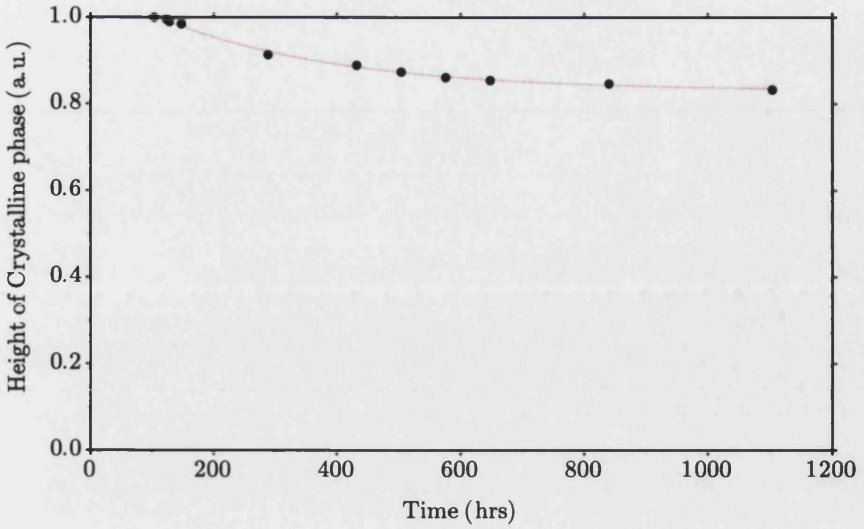

Figure 4.5: Gravitational compression of crystals of PBM10 as a function of time.

The experimental values for the scaling factor, ϕ_f/χ_f, the resulting hard-sphere melting volume fraction, ϕ_m, and quality of fit of the data points to the scaled phase, R^2, are presented in Table 4.3.

Latex	ϕ_f/χ_f	ϕ_m	R^2
RSJF1	1.19 ± 0.01	0.548 ± 0.007	0.9811
RSJF5	1.28 ± 0.02	0.549 ± 0.007	0.8636
PBM10	1.21 ± 0.01	0.548 ± 0.007	0.9922
NH31	1.25 ± 0.02	0.548 ± 0.007	0.8664

Table 4.3: Phase behaviour of PMMA colloids

The experimental values show consistency, and the scaling factors are in good agreement with those from similar experiments by van Megen *et al.* [53]. The values for the hard-sphere melting fraction are in good agreement with the theoretical value of 0.545 ± 0.002 predicted using computer simulation by Hoover and Ree [59]. This experimental result is a strong indication that the interaction of these PMMA/PHSA colloidal particles closely approximates a hard-sphere interaction. It also indicates that the tagging of particles using the NBD-MMA and NBD-MAE fluorescent dyes, present in samples RSJF1 and RSJF5 respectively, has no significant effect on the phase behaviour of the colloid.

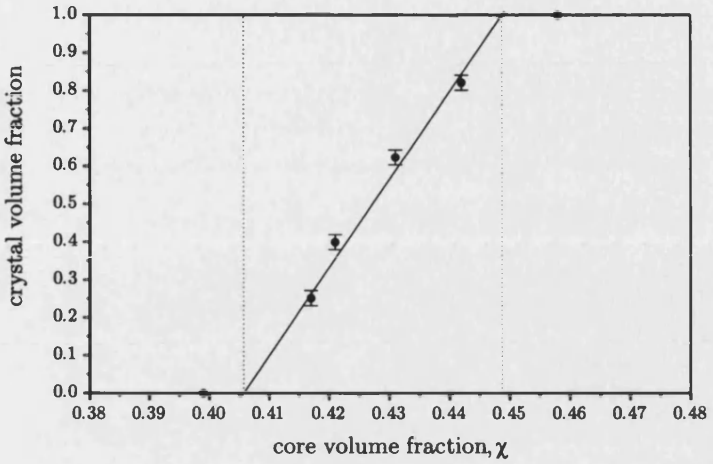

Figure 4.6: Volume fraction of crystal formed in sample PBM10, depicted as a function of core volume fraction, χ

Samples of index-matched dispersions with volume fractions outside the freezing to melting range were also monitored. Samples at volume fractions $\phi < \phi_f$ which were not subjected to time-averaged zero gravity showed no sign of crystallization initially, but after a period of many days sedimentary crystals are formed at the bottom of the cuvette by the gradual settling of the particles. These sedimentary crystals eventually form into pillars of sedimentary crystals. For samples with volume fractions $\phi > \phi_m$ the samples are fully crystalline, as the volume fraction increases so the number of crystallites formed increases and the average size of crystallite decreases. At $\phi \approx 0.565$ homogeneous crystallization is suppressed as larger heterogeneously nucleated crystals form slowly at cell walls and other discontinuities. For volume fractions $\phi > 0.575$ the majority of the sample volume remains in an amorphous state, with a phase separation near the meniscus, above which large heterogeneous crystals form.

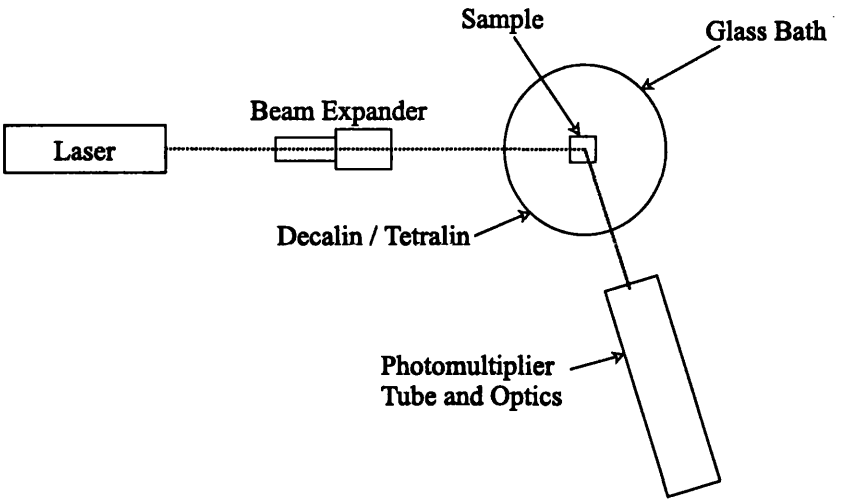

Figure 4.7: Schematic illustration of the static light scattering setup

4.3 Static Light Scattering of Colloidal Crystals

In the present work, the average structure of colloidal systems was probed using static light scattering, with the intention of discovering and identifying colloidal crystal structures within the system. The equipment used is shown in Figure 4.7.

Suspensions were sealed within optical quality 1 cm^2 rectangular glass cuvettes from Hellma. The cuvette was places at the centre of a 15 cm diameter cylindrical bath filled with a mixture of tetralin (1,2,3,4-tetrahydronapthalene) and decalin (decahyrdronapthalene) to give a close index match to the suspension. The sample was illuminated by a parallel expanded beam from the krypton-argon laser described on page 46, which then passed through a rectangular aperture with an area of approximately 1 cm^2. This expanded beam illuminated the sample through an optically flat window in the wall of the cylindrical bath. The large scattering volume ($\sim$1 cm^3) allowed for scattering from many ($>10^6$) randomly

oriented crystallites, giving a proper orientational average of the scattering from a suspension of crystallites [113]. This scattered light was focused by the cylindrical bath, which acts as a cylindrical lens, onto a vertical slit, before passing through onto a photomultiplier tube [PMT]. This photomultiplier tube was mounted onto a computer controlled turntable, which rotated about the bath axis. This allowed for scattered intensities to be measured over a range of angles from $\theta = 20°$ to $140°$ with a resolution of approximately $0.05°$.

In PMMA suspensions the homogeneously nucleated crystallization process provides samples composed of many small ($\leq 50\,\mu$m) randomly oriented crystallites which enable the use of the visible analogue of X-ray powder crystallography to study these crystallites. The angular dependence of the scattered light was measured. Figures 4.9 and 4.10 show typical structure factors for a polycrystalline sample. The pattern for a polycrystalline sample of hard-spheres can be identified by the presence of one or more sharp, Bragg reflections on top of a diffuse background. This distinctive pattern can be understood in terms of a random stacking of hexagonal close-packed planes of particles [113]. These measured powder pattern profiles were compared with those calculated for a variety of close-packed crystals.

4.3.1 Calculation of crystal scattering patterns

Starting with one layer of hexagonally close-packed particles, with the position of those particles labelled A, there are two possibilities for the position of the particles in the next layer, B and C (see Figure 1.4). Either of these choices lead to a close packed structure, for example a face-centred cubic [fcc] crystal is built up by stacking layers with positions corresponding to the sequence $ABCABC...$ or the symmetric twinned structure $ACBACB...$, and an hexagonal close-packed [hcp]

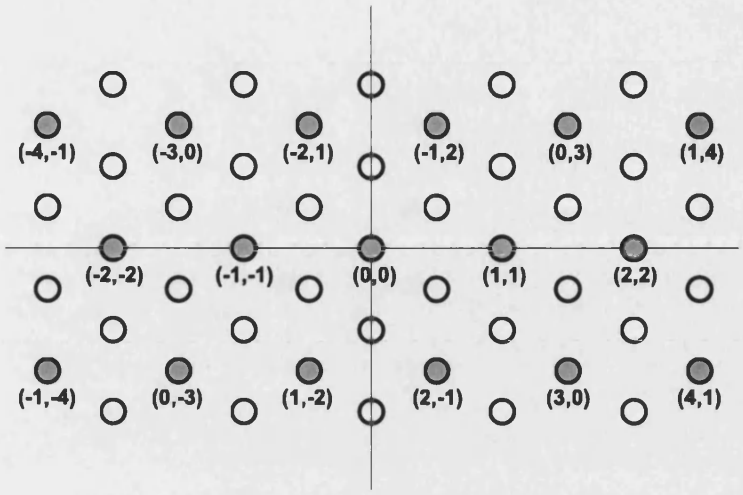

Figure 4.8: Schematic illustration of Bragg rods. The shaded circles correspond to Bragg rods with crystallographic indices $(h-k)=3n$

structure is formed by stacking hexagonal layers in the sequence $ABABAB....$

Calculation of the powder pattern for a given crystal consists of determining the crystal reciprocal-space structure and then averaging over all orientations [114]. The reciprocal-space structure for crystals with close-packed structure was independently calculated by Wilson [115] and Hendricks [116] in 1942. Close packed structures can be visualized in terms of stacked slices of hexagonally arranged close packed particles. The scattering from a single layer of hexagonally arranged particles consists of Bragg rods in reciprocal space, normal to the plane of the layer.

The positions of the rods in the plane of the layer is hexagonal, with a rod spacing in reciprocal space of $a^* = \frac{4\pi}{a\sqrt{3}}$, where a is the lattice constant of the original lattice. A system of Bragg rods (h,k) can be indexed as shown in Figure 4.8. The stacking of layers of hexagonally arranged colloidal hard spheres is expected to adopt a degree of randomness [113]. The probability that layers n and $n+2$ have different positions can be defined as α, where an α value of 0 would correspond

to a hcp structure, an α value of 1 would correspond to a fcc structure, and a randomly stacked close-packed [rscp] structure would have an α value of 0.5. The actual position of the Bragg rods is determined only by the interparticle spacing in the layer, and the stacking of the layers produces modulations of intensity along the Bragg rods. When the layers are close-packed the Bragg rods can be separated into two distinct types, which are affected differently by randomness in the stacking sequence.

For the rods with indices $(h-k) = 3n$, where n is an integer, the intensity variations are independent of the stacking sequence, and the scattering intensity appears at the points (h,k,l), at integral values of l, which correspond to those Bragg reflections common to both fcc and hcp structures [117]. For Bragg rods with indices $(h-k) \neq 3n$, the intensity distribution varies with index l along lines (h,k), in a manner determined by the stacking probability α. For the fcc structures reciprocal-lattice points occur at $l = m \pm \frac{1}{3}$ with m as an integral. For the hcp structures reciprocal-lattice points occur at $l = m \pm \frac{1}{2}$. If stacking faults occur, the intensity maximum is broadened and spread along the rods. For randomly stacked layers ($\alpha = 0.5$), the intensity is continuously distributed along these rods with a maximum at $l = m \pm \frac{1}{2}$ and a minimum at $l = m$ with an intensity ratio of 9:1. The two sets of rods contribute in a qualitatively different way to the observed powder diffraction pattern. The high intensity along the $(h-k) = 3n$ rods, when orientationally averaged, generate sharp peaks in the diffraction pattern. The $(h-k) \neq 3n$ rods, with the intensity continuously distributed along the rods, contribute a broad scattering curve, with relatively few features to distinguish. The random-stacked close-packed powder pattern of colloidal hard-spheres thus shows a combination of sharp Bragg peaks, and the broad diffuse regions of scattering, and these features can be seen in the powder scattering profiles shown in Figures 4.9 and 4.10.

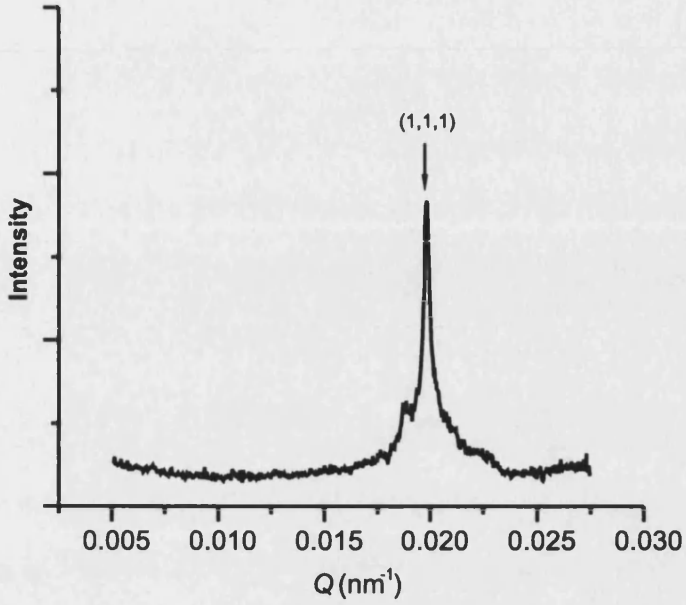

Figure 4.9: Light scattering from a suspension of the PMMA colloid RSJF1. The arrow indicates the position of the dominant reflection from a close-packed crystal with a lattice parameter of 385 nm

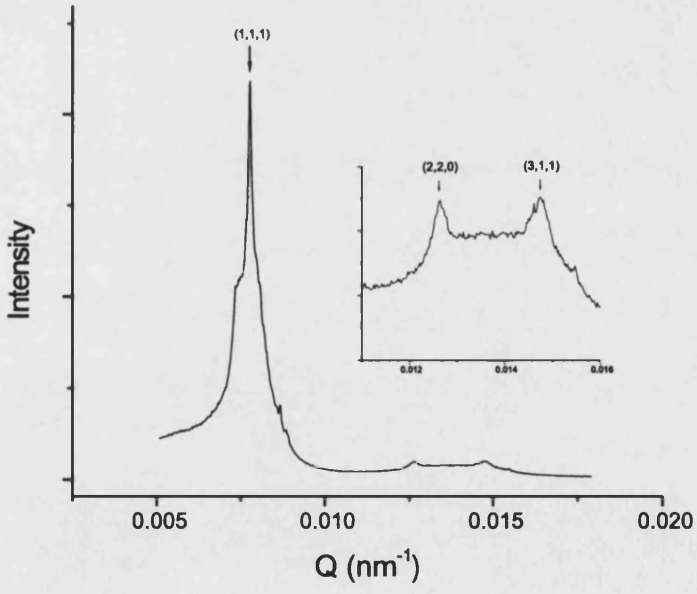

Figure 4.10: Light scattering from a suspension of the PMMA colloid NH31. The arrows indicate the expected Bragg reflections from a close packed crystal with a lattice parameter of 985 nm. The inset shows part of the scattering profile, enlarged for clarity.

The position of these sharp peaks reveals information about the crystal lattice. There is a straightforward relationship between the Q values of peaks and the Miller indices (h,k,l). For a fcc lattice, scattering occurs when h, k, l are all odd or all even, and the following condition is satisfied;

$$\left(\frac{Q(a)}{2\pi}\right)^2 = h^2 + k^2 + l^2$$

where a is the length of an equivalent fcc cell. For a hcp lattice the following conditions must be met for scattering to occur; firstly $1/3(2h + k) = n$,(where n is an integer), l must be odd and

$$\left(\frac{Q(a)}{2\pi}\right)^2 = \frac{8}{3}(h^2 + k^2 + hk) + \frac{3}{4}l^2$$

For a randomly stacked close packed structure only those peaks present in both hcp and fcc scattering patterns appear. Table 4.4 lists some scattering indices for hcp, fcc and rscp structures.

By matching the peaks in the static light scattering pattern from the colloidal crystal with those calculated for an rscp structure, measures of the lattice parameter and particle diameter are obtained as illustrated in Figures 4.9 and 4.10. The crystal lattice length of the crystallizing PMMA colloids used in this work are presented in Table 4.5. The corresponding particle diameters are shown in Table 4.5, calculated from the crystal lattice parameter by assuming that the crystal has a volume fraction of 0.545.

It can be seen from Table 4.5 that both sets of measurements show similar results.

$\left(\frac{Q(a)}{2\pi}\right)^2$	fcc (h,k,l)	hcp (h,k,l)	rscp
2.67	-	100	-
3.00	111	002	present
3.42	-	101	-
4.00	200	-	-
5.67	-	102	-
8.00	220	110	present
9.42	-	103	-
10.67	-	200	-
11.00	311	112	present

Table 4.4: Initial reciprocal space reflection points for hcp, fcc and rscp crystal structures

Sample	ϕ	$a \pm 6$ nm	$D_{SLS} \pm 6$ nm	$D_{DLS} \pm 10$ nm
RSJF1	0.42	385	338	350
NH31	0.55	985	897	916

Table 4.5: Light crystallography measurements of the lattice parameter, a, and particle diameters of PMMA colloids

4.4 Conclusions

It can be concluded from the data presented in Chapter 4 that the methods of colloid synthesis described in chapter 3 can be used as a means of preparing PMMA colloids with a range of sizes between 100 nm and 1000 nm. The polydispersity of colloids prepared in such a way can be as low as 0.07, although the precise control of the polydispersity has not been fully established. In suspensions of PMMA particles with a sufficiently low polydispersity homogenously nucleated crystals are formed. In samples with a colloid volume fraction between a melting and freezing volume fraction, the volume of these crystallites is proportional to the volume fraction of colloid in the dispersion. The phase behaviour of these samples show good agreement with hard-sphere theory. Light scattering studies of the crystalline samples indicates that crystals formed have a randomly-stacked close-packed structure.

Chapter 5

Fluorescent Laser Scanning Confocal Microscopy of PMMA colloids

In this chapter the technique of fluorescence laser scanning microscopy is reviewed. Fluorescence and bleaching characteristics of fluorescently labelled PMMA particles are given and confocal micrographs are presented which show local structure within colloidal dispersions.

5.1 Introduction

The most commonly used methods for studying the structure of colloidal dispersions have been light and neutron scattering techniques. A limitation of diffraction techniques, which provide the average structure factor in reciprocal space, is that it is hard to obtain information about local structures such as vacancies, defects and coexistence of multiple phases. In addition to this the structure of certain binary crystal structures are almost indistinguishable by scattering techniques unless time-consuming contrast labelling techniques are used (See Chapter 6). Direct observation with a microscope however, yields real-space information on the particle positions. Scanning electron microscopy [SEM] can yield real-space information on crystalline samples with a resolution on the nanometre scale, however colloidal samples cannot be viewed within a dispersion, but instead must be dried down and coated with gold or carbon in a vacuum. Although SEM is often used to give precise measurements of colloidal size, and also to confirm the structure of colloidal crystallites the possibilities of further investigation are severely restricted by the harsh environment required for SEM. Conventional light microscopy can be used to study colloidal dispersions, but the resolving power of the conventional light microscope is much worse than that of the SEM, and because of the opacity of concentrated colloidal dispersions, it is almost impossible to study structures within the bulk of the sample. Conventional light microscopy has been used to study two-dimensional colloidal crystals, for example between two glass plates [118] or to study the growth and development of crystal shape [119]. Kose *et al.* among others observed an ordered structure using an inverse conventional light microscope [120]. For very dilute suspensions of latex particles in water (<0.1 % vol), they were able to visualize 30 crystal layers starting from the glass wall. However in more concentrated systems, the range was much more limited (3 layers at 8% vol). Ise *et al.* studied the dependance

of interparticle distances on particle concentration and other factors, by using video-enhanced light microscopy and computerized image processing [121, 122]. Dynamic motions were also studied and local ordering was observed, which could not have been gathered using scattering techniques [123]. Poon *et al.* measured the stacking disorder in crystalline colloids using microscopy techniques using an ingenious method of measuring the kinks in the pattern of lines visible on the crystal surfaces [65].

More recently the laser scanning confocal microscope [LSCM] [99] has been used in colloid science to study concentrated colloidal systems. Yoshida *et al.* used LSCM to examine the local structure in dispersions of polystyrene spheres. Due to the improved depth resolution offered by LSCM they were able to probe deep into the bulk of the sample, and reported on the existence of large-scale voids within the dispersion [124].

The combination of laser scanning confocal microscopy with fluorescence techniques results in a system which offers increased resolution and contrast. Colloidal systems of sterically stabilized fluorescent silica spheres have been synthesized by van Blaaderen and Verhaegh [125], and fluorescent laser-scanning confocal microscopy [FLSCM] studies using these fluorescent silica spheres have investigated crystalline stacking disorder [66], and the real-space structure of hard-sphere glasses [126]. Recently van Blaaderen *et al.* imaged sections of template-directed colloidal crystals using FLSCM, where the structure of the colloidal crystal lattice is tailored by the use of a patterned template [127, 128].

An aim of this work was to create novel systems of fluorescent, sterically stabilized PMMA colloids, the local structure of which could then be examined using FLSCM. The fluorescent properties of PMMA colloids synthesized (see Chapter 3) are detailed and FLSCM micrographs illustrating the resolution of

individual fluorescent particles, and the local structure are presented.

5.1.1 Concepts in Laser Scanning Confocal Microscopy

In this section some basic principles pertaining to lateral and axial resolution and to depth of field are discussed, and a simple outline of some of the concepts involved in confocal microscopy.

Lateral Resolution

The foundation of light microscopy was established over a century ago by Abbe [129]. He showed how the diffraction of light by the specimen, and by the objective lens determined the resolution of the image. The role of the numerical apertures [NA] of the lenses was also established;

$$d_{min} = \frac{\lambda_o}{NA_{obj} + NA_{cond}} \tag{5.1}$$

where d_{min} is the minimum spacing in a periodically spaced grating that can just be resolved, λ_o is the wavelength of the incident light *in vacuo* and NA_{obj} and NA_{cond} are the numerical apertures of the objective and condenser lenses respectively. The NA is the product of the sine of the half angle (v) of the cone of light and the index of refraction of the medium (n) (see Figure 5.1).

Equation 5.1 demonstrates that the NA of the objective and condenser lens affects the image resolution for line grating objects. A complementary method of defining the limit of resolution exists for point objects. The image formed of an infinitely

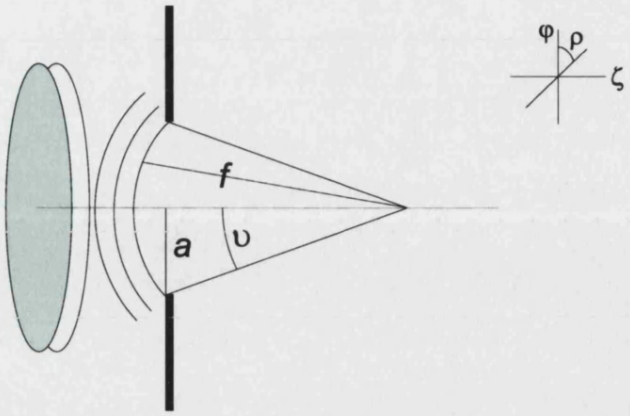

Figure 5.1: Illustration describing some microscopic terms including numerical aperture [NA] and f-number [f/#] for a converging spherical wavefront. NA= $\eta \cdot \sin \upsilon, f/\# = f/2a$, where η is the index of refraction of the medium and υ is the half angle of the cone of light diverging to an illuminated spot. The optical axis is along ζ and φ is the azimuth and ρ a radial variable.

small luminous point consists of a circular diffraction image, with a bright disk surrounded by concentric rings of light, each ring becoming progressively weaker further from the disk. The radius r_{Airy} of the first ring depends on λ and the NA of the objective and is defined as

$$R_{Airy} = 0.61 \cdot \frac{\lambda_o}{NA_{obj}} \tag{5.2}$$

Two equally bright spots in the sample plane, separated by distance d, are said to be resolved if d is larger or equal to the radius of the Airy disk [99].

Axial Resolution

The definition for axial resolution is approached in a similar way. If two points are separated by a small distance along the axis of the microscope, then the points are resolved if the diffraction images can be seen as two. The distribution of energy formed above and below focus must be derived from wave optics. The intensity distribution was been calculated by Linfoot and Wolf [130] and is reproduced in Born and Wolf[131]. The distance from the centre of the 3D point spread function to the first axial minimum is given as

$$z_{min} = \frac{2\lambda_o \eta}{(NA_{obj})^2} \tag{5.3}$$

where η is the refractive index of the object medium. z_{min} can therefore be used as a measure of the limit of axial resolution of the microscope optics.

Depth of Field

The depth of field in a microscope is the depth of the microscope image that appears to be sharply in focus. This depth has been determined experimentally, and the contribution of various factors has been explored by Berek [132]. The major factor to consider in conventional bright-field microscope, is the geometric and diffraction-limited spreading of the light beam arising from a single point in the sample in planes above and below the plane of focus. Considering only the diffraction-limited spreading, the apparent depth of field can be shown to be

$$\delta = \frac{1}{4}(z_{min-} - z_{min+}) \tag{5.4}$$

i.e. one quarter of the distance between the first axial maximum above (z_{min+}) and below (Z_{min-}) the central maximum in the 3D point spread function [133]. However in conventional fluorescence and dark-field imaging, the exciting light that contributes to each point of the final image produces significant intensity above and below focus, and thus fluorescent objects that are out of focus produce unwanted light that is collected by the objective and thereby reduces the contrast of the in-focus image. It is for these reasons that the depth of field is difficult to define when using fluorescent microscopy but it is considered that the apparent depth of field is very much greater than the axial resolution. By using confocal techniques the depth of field can be restricted to the axial resolution of the microscope.

Confocal Imaging

A simple picture of the confocal process is illustrated in Figure 5.2.

In conventional light microscopy, the lens forms an image of all points in a sample, both from those points in focus, and those not in focus. By modifying this setup by including a pinhole at the focal point, we image all light from this point, and very little light from those points out of focus. With a light source which is also confocal to the existing focus, most light shines on the point in focus and very little light reaches those out-of-focus points. There are several advantages gained from this optical system:

- Reduced blurring of the image from light scattering
- Greatly increased effective axial resolution
- Improved image contrast

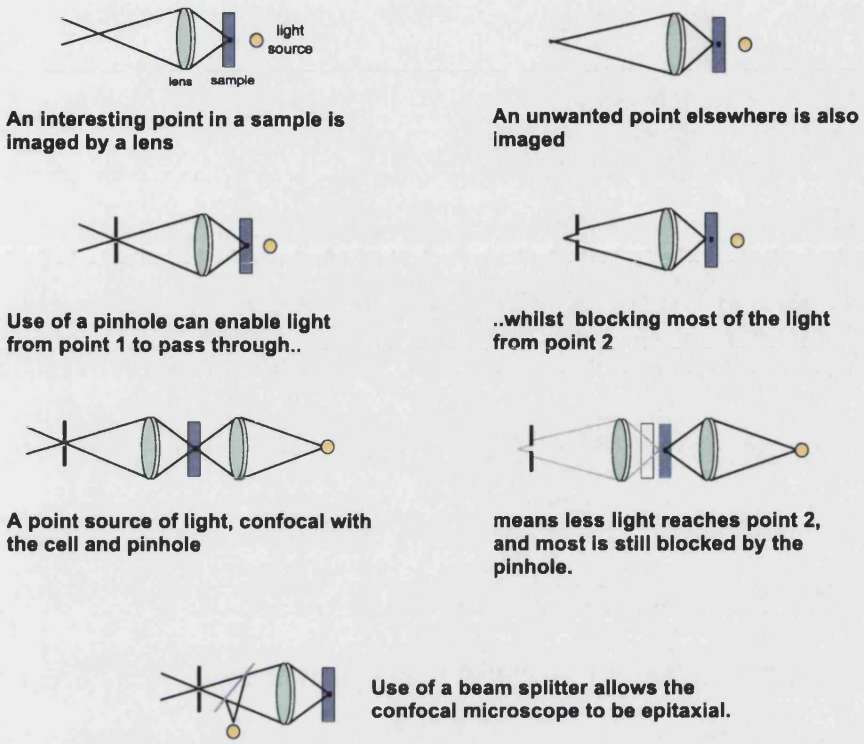

Figure 5.2: Schematic diagram illustrating discrimination of Confocal Microscopy

This illumination and detection of light from one point, and rejection of light from other points leads to the high contrast and depth discrimination properties of the confocal microscope that have found many applications, particularly in the biological sciences [134].

Many comprehensive accounts of the applications of confocal microscopy are available [134, 99, 135, 136], whilst detailed reports on the optics [137, 138, 139, 140] and history [141] are also reported elsewhere. Here I will detail the setup of a typical laser-scanning confocal microscope arrangement and describe the specific configuration of the two confocal microscopes used in this study.

A typical arrangement of a laser scanning confocal microscope is illustrated in Figure 5.3.

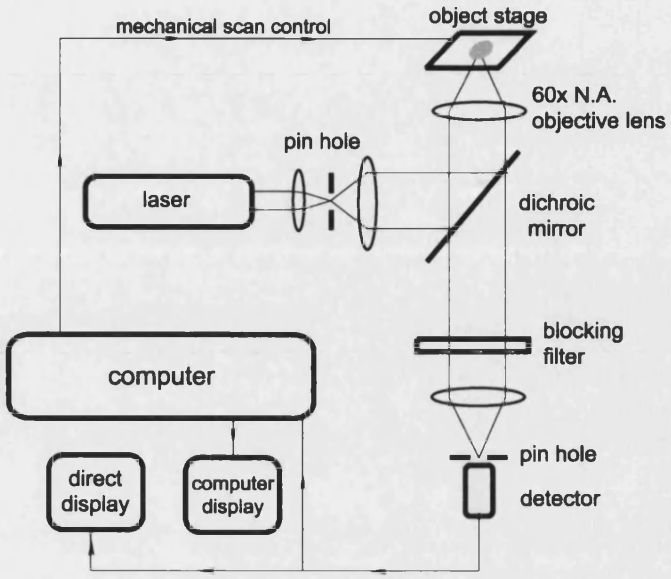

Figure 5.3: Schematic diagram illustrating a typical microscope setup

Illumination

The most common source of illumination for confocal scanning microscopes is the laser. The laser offers a number of properties which make it an ideal light source for confocal microscopy [142].

- High degree of monochromaticity
- Small divergence
- High brightness
- High degree of spatial and temporal coherence
- Plane polarized emission

Many lasers may be used, but argon ion lasers are popular since the lines available (488 nm and 514 nm) are useful for exciting many chromophores and fluorophores.

The noise on a typical argon ion laser is around 1% RMS [143], The laser light may be directed at the sample from the side opposite the observer, or, more commonly for fluorescence microscopy, may come from the same side as the observation, when it is known as *epitaxial.* Epitaxial microscopy also has the advantage that only one objective lens is then required (see Figure 5.2).

Scanning

Since in a confocal microscope only one 'spot' is imaged, a method of imaging over a more useful area is required, this is achieved by scanning the spot over an area of the sample. For reasons of speed it makes sense to move the laser beams rather than the object, and most commercial confocal microscopes take this laser-scanning approach. Typically two small mirrors mounted on galvanometers enable the angle of the beam to be changed, resulting in the ability to scan the laser beam in a raster pattern, similar to that in a television screen. Stage scanners are often also used to simplify the movement of the imaged area around the sample.

Detection

Detectors for confocal microscopy are mostly based on photomultiplier tubes [PMT] [144]. The PMT has good sensitivity, particularly in the visible region, and insignificant noise. For epitaxial microscopes some method of beamsplitting is required to separate the illumination and observation beams. Fluorescent imaging has the advantage of being able to separate out any incident light by the use of a dichroic mirror, thereby detecting only the emitted fluorescence. In practical use however the incident and emission radiation are at similar wavelengths so ideal

separation is not usually possible, but fluorescent scanning confocal microscopy still provides the potential for high contrast imaging.

Instrument Resolution

The preferred method for measuring the axial resolution of a confocal microscope is to move a surface through the focal plane and plot the measured intensity of the detected signal against the optical axis. The width of the curve at half the maximum intensity (*full-width half-maximum*[FWHM]) is then usually taken as a practical measure of the axial resolution.

5.2 Experimental and Results

5.2.1 Characterization of Fluorescent PMMA colloids

In this section we describe the characterization of the PMMA colloids synthesized in Chapter 3. The amounts of dye incorporated, fluorescence excitation and emission were measured and the bleachability of the PMMA spheres was measured using a laser scanning confocal microscope [LSCM] [99].

The excitation and emission spectra for the PMMA particles labelled RSJF1 is shown in Figure 5.4. From the figure it follows that the wavelength used for excitation in LSCM (488 nm) is close to the excitation maximum and that emission is taking place within the range detectable by the confocal microscopes used in this study.

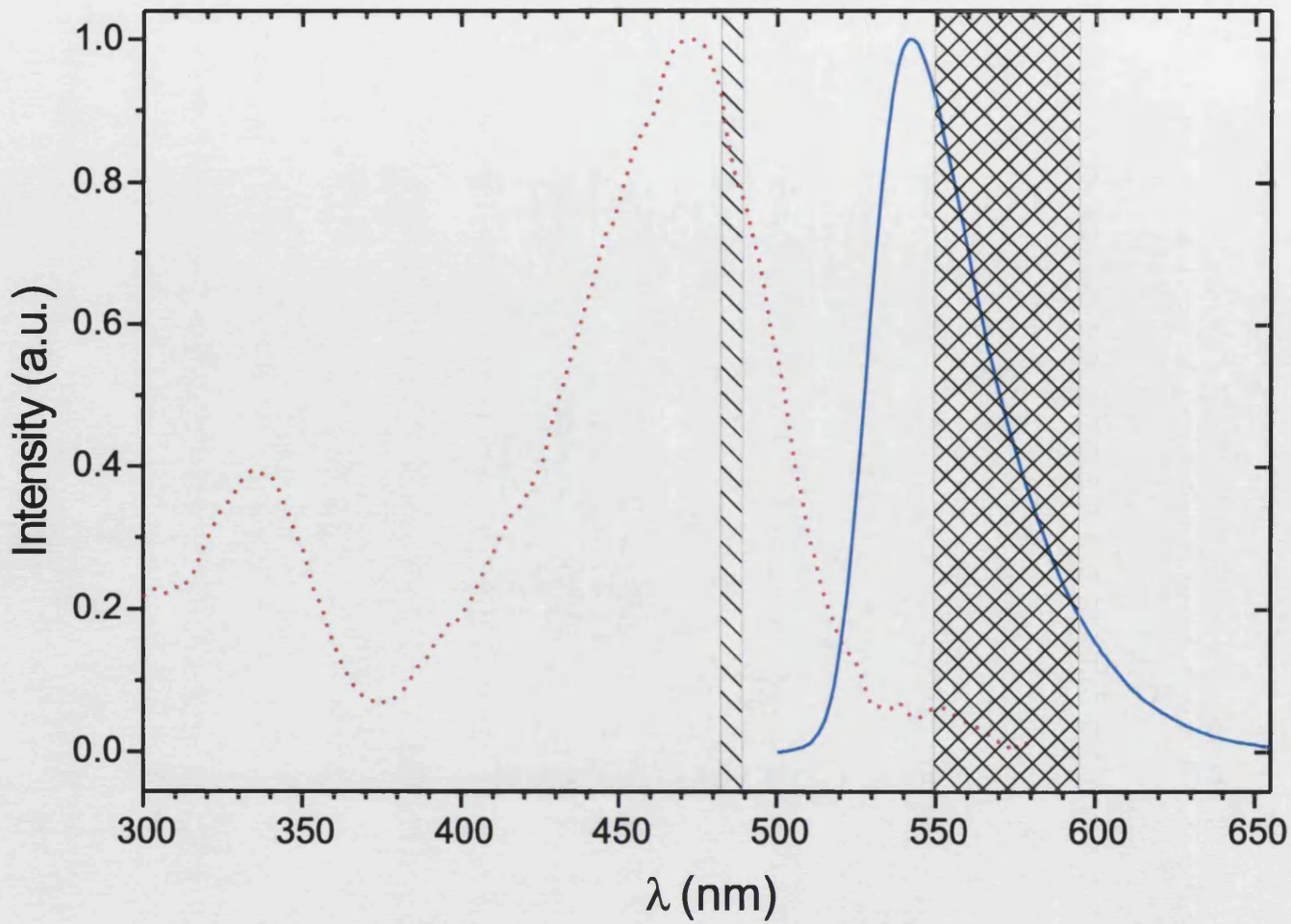

Figure 5.4: Fluorescence excitation and emission spectra of RSJF1. The lines are denoted as follows;*dotted line*, excitation;*solid line*, emission. The hatched area show the area of excitation by the laser scanning confocal microscopes and the crossed area denotes the detection range of the LSCM.

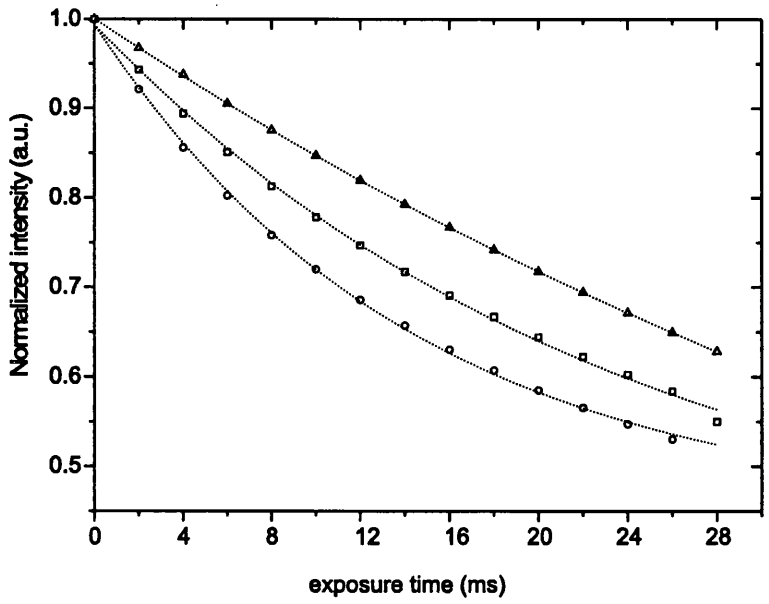

Figure 5.5: Fluorescence intensity versus exposure time for the NBD-MMA and NBD-MAE labelled PMMA colloidal spheres, and are labelled as follows; *triangle*-RSJF5, *square*-RSJF1, *circle*-RSJF3. The dashed lines are provided as guides to the eye.

5.2.2 Bleaching

Samples of each fluorescent colloid were studied to measure the sensitivity to bleaching of the colloids. To make sure that the colloidal particles were immobile for these tests a glassy sediment was made by centrifuging the samples at 1500rpm. A scan of the sediment close to the glass wall was made parallel to the capillary tube approximately once every 2 milliseconds. Each scan consisted of an area varying in brightness with the presence and absence of colloid. Each area was averaged and the average intensity of the first and subsequent scans is plotted against time in Figure 5.5. The data is shown in Table 5.1

The extent of bleaching is different for all the particles although the forms of the bleaching curves are similar. Even after many scans the intensities still decrease, suggesting that the intensity of fluorescence will eventually decrease to zero. The

Sample Code	Fluorescent monomer %
RSJF1	0.2
RSJF3	2.0
RSJF5	1.0

Table 5.1: Composition of fluorescent PMMA colloids in laser-scanning confocal microscopy.

mechanism for the bleaching of fluorescent dyes inside polymer particles is complex and is not well understood.

5.2.3 Composition

The composition of samples studied by confocal microscopy is shown in Table 5.2

Figure	Colloid S	Colloid L	$fracN_S N_L$	Totalϕ
5.6	RSJF1	NH31	0.1	0.53
5.7	RSJF1	NH31	0.1	0.53
5.8	RSJF1	NH31	0.1	0.53
5.10	RSJF1	NH31	1.0	0.53
5.11	RSJF1	NH31	1.0	0.53
5.12	RSJF1	NH31	1.0	0.53
5.14	RSJF1	NH31	1.0	0.53
5.13	RSJF1	NH31	1.0	0.53
5.15	NH25	RSJF5	0.07	0.49
5.16	NH25	RSJF5	0.07	0.49
5.17	RSJF5	-	-	0.42

Table 5.2: Composition of samples shown in micrographs (Figures 5.6 to 5.15)

The colloidal dispersions were drawn into flat capillary tubes (Vitro Dynamics),

200 μm thick and 2mm wide, sealed off with epoxy resin (Araldite).

Crystals grew more quickly in the flat capillaries than in square cells with a path length of 1 cm. Although exact quantitative measurements were not carried out, crystallization occurred within days for dispersions in the capillary cells, whereas crystallization of the same dispersion in the square cells took of the order of weeks or months. This may suggest that wall effects were more influential in the capillary cells, although there was no indication that the crystallization within these cells was not homogeneous. The sectioning ability of the confocal microscope confirmed that the crystals formed in these cells were not to be found at or near the cell walls, but were in the bulk of the sample.

5.2.4 Micrographs

Confocal micrographs of colloidal dispersions have been obtained using one of two microscopes used in this study.

Those micrographs labelled BR were obtained using a Biorad MRC 500 mounted on a Nikon Optiphot-2 equipped with an Argon ion laser. The laser line used had a wavelength of 488 nm. A BHS (Biorad) filter was used which allowed detection of fluorescence above 515nm. Unless otherwise stated the objective used was 60x magnification, 1.4N.A. oil immersion lens. Images in the x-y plane were achieved by optical scanning, and movement in the z-axis was achieved by computer controlled focus of the stage.

Although the resolution of the BioRad MRC500 was poor, it was possible to distinguish individual colloids. Micrographs in Figure 5.8 show the ability to image larger non-fluorescent colloids among a 'sea' of smaller fluorescent ones.

Figure 5.8 shows an images from a glassy sample of a mixture of non-fluorescent colloid NH31 and fluorescent colloid RSJF1, in which the well-separated fluorescent colloids can be resolved. In addition Figure 5.6 shows the presence of non-homogeneous crystalline growth in one sample, illustrating the experimental possibilities even at low resolution.

Those micrographs labelled LE were obtained using a Leica TCS 4D confocal microscope. The main features of the Leica TCS 4D confocal microscope are illustrated in Figure 5.9.

The laser line used with the Leica TCS had a wavelength of 488 nm and the appropriate filter was chosen to allow detection of fluorescence above 515nm. Images in the x-y plane were achieved by laser scanning, scanning of one section of 512x512 took $\frac{1}{3}$ of a second. The Leica TCS has a theoretical x/y resolution of 0.2 μm [FWHM] and a corresponding z-resolution of better than 0.4 μm [FWHM] using the N.A. 1.32 lens with a glass-oil interface.

5.3 Summary and Conclusions

Several techniques rely on fluorescence, e.g. fluorescence recovery after photobleaching, [FRAP] [96], fluorescence correlation spectroscopy [97], and the synthesis of fluorescent model particles is of interest to those wishing to use these techniques. The primary reason for synthesizing fluorescent colloids in this work was to investigate the possibility of probing fluorescent colloidal systems using fluorescent laser scanning confocal microscopy. It is clear that the most useful feature of the confocal microscope setup is the increased effective axial resolution, which allows sections within the volume of a sample to be imaged. Combined

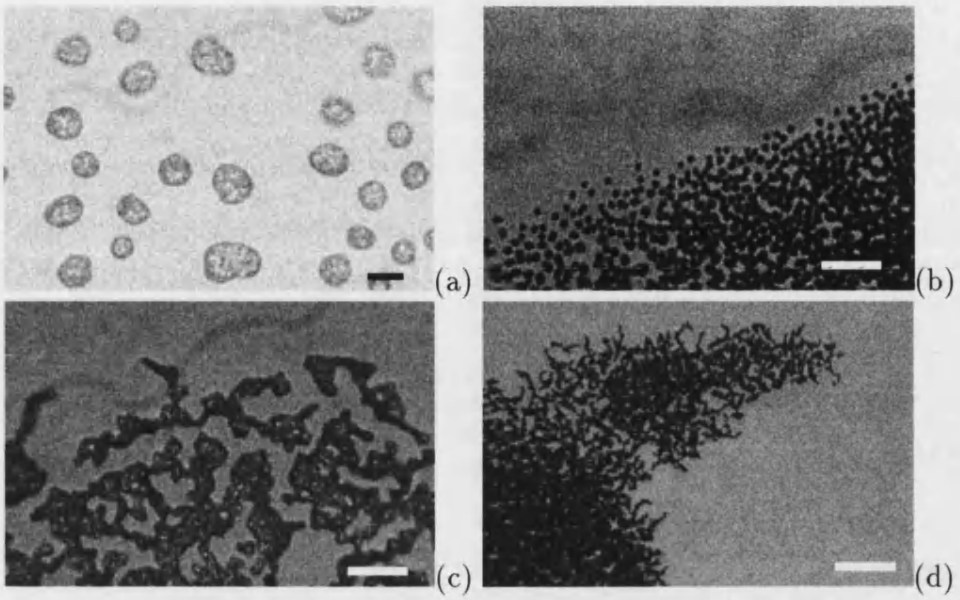

Figure 5.6: Micrographs BR-F1-A10B(A)(a)-(d) show views of sedimentary crystallites in this mixture of NH31 and RSJF1 colloids. The bar sizes are (a) 10 μm, (c) 25 μm, (b) and (d) 100 μm

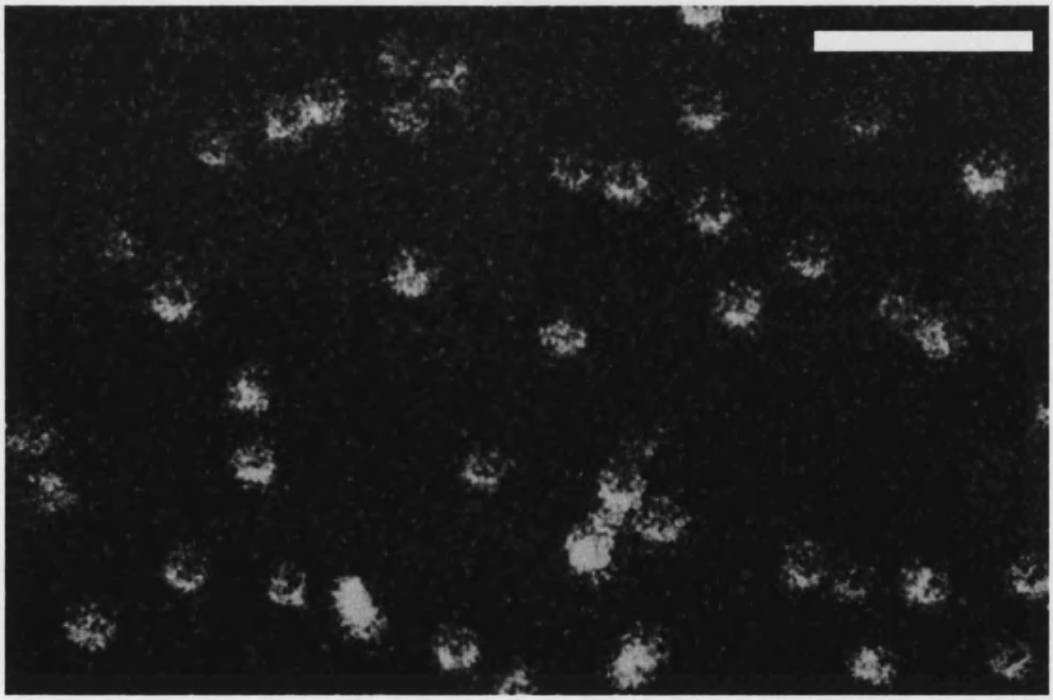

Figure 5.7: . Micrograph BR-F1-A10B(A)1 shows the resolution of individual fluorescent colloids (RSJF1) in a glassy mixture of NH31 and RSJF1 with a number ratio of 10:1. The bar size is 5 μm

with the spectral filtering of fluorescent microscopy, this allows the resolution of individual fluorescent colloids within the bulk of the sample and provides a direct means of monitoring the positions of particles and determining the local structures of colloidal fluids, whether ordered or disordered.

This initial work provides a basis for further experiments using fluorescent hard-sphere PMMA spheres, and the results presented here clearly indicate the possibility of resolving individual well-separated PMMA colloids using fluorescence laser scanning confocal microscopy in concentrated and crystallizing dispersions of PMMA spheres labelled with fluorescent dyes based on NBD-derivatives. The micrographs presented also illustrate the future potential of using such techniques to study the local structure of dispersions of fluorescent PMMA colloids within the bulk of a sample. A more detailed analysis of one of the micrographs (Figure 5.14) is undertaken in the following chapter, revealing ordered structure within the crystallite which could not have been detected using scattering techniques.

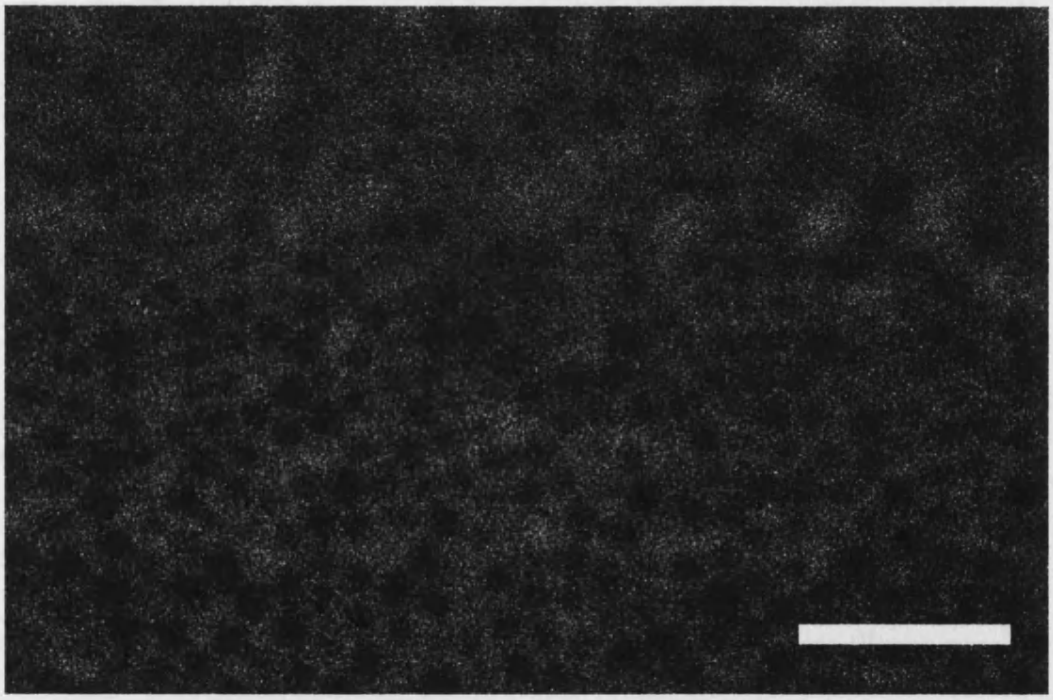

Figure 5.8: Micrograph BR-F1-A10B(A)3 shows the possibility to view non-fluorescent colloids in this mixture of NH31 and RSJF1 colloids. The bar size is $5\,\mu$m

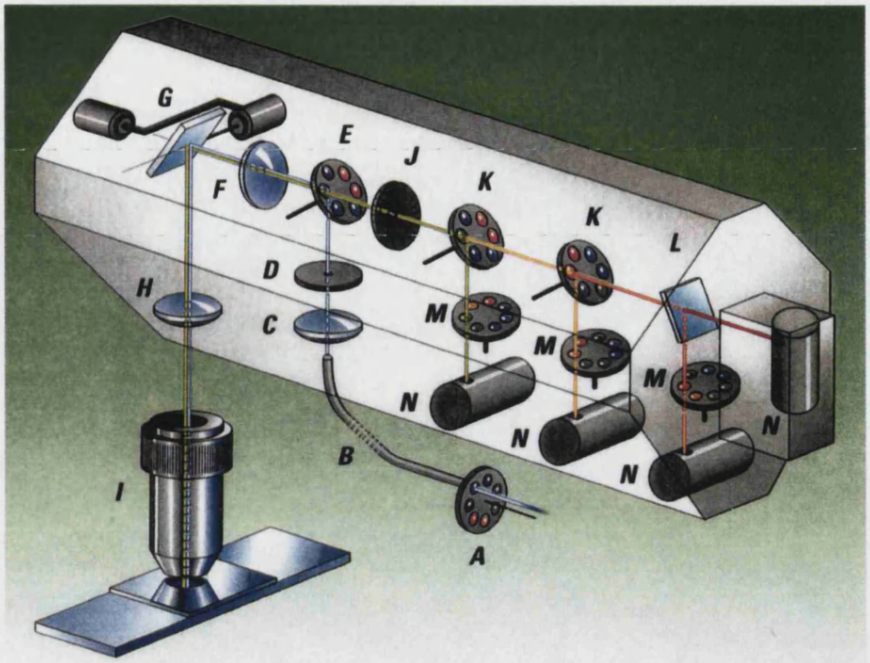

A Excitation Filter Wheel
B Fibre Optical Laser Coupling
C Lens
D Source Pinhole
E Excitation Beam Splitter Wheel
F Pinhole Lens
G Scan Mirror
H Scan Lens
I Microscope Objective
J Variable Detector Pinhole
K Detector Beam Splitter Wheels
L Detector Beam Splitter
M Barrier Filter Wheels
N Photomultipliers 1 – 4

Figure 5.9: Illustration of the Leica TCS 4D Confocal Microscope. The unit is centred around a dual-galvanometer, single mirror scanning unit (G) with on-line position-feedback and linearization. The scanner features a maximum x-scanning frequency of 1000 Hz and bidirectional scanning with phase shift compensation and a high duty cycle for maximum efficiency of light collection. After selection by a laser line filter mounted near the laser (A), laser light is delivered to the scanning unit through optical fibres (B) to ensure mechanical isolation from vibration. The dichroic beamsplitters mounted in the motor-driven filter wheel (E) are carefully adjusted to maintain axial alignment. Additional beamsplitters after the pinhole (K,L) in combination with barrier filters mounted in wheels (M) are all motor-driven and provide a wide range of spectral adjustment to the signals that strike the four photomultiplier tubes (N). The size of the confocal detection pinhole and the selection of all filters are entirely computer controlled. The system uses the Leica infinity-corrected, Delta objective (I), which is fully corrected for chromatic aberration. Fine focussing is provided by a galvanometer driven z-stage with fast and reproducible z-positioning. For further details see [145]

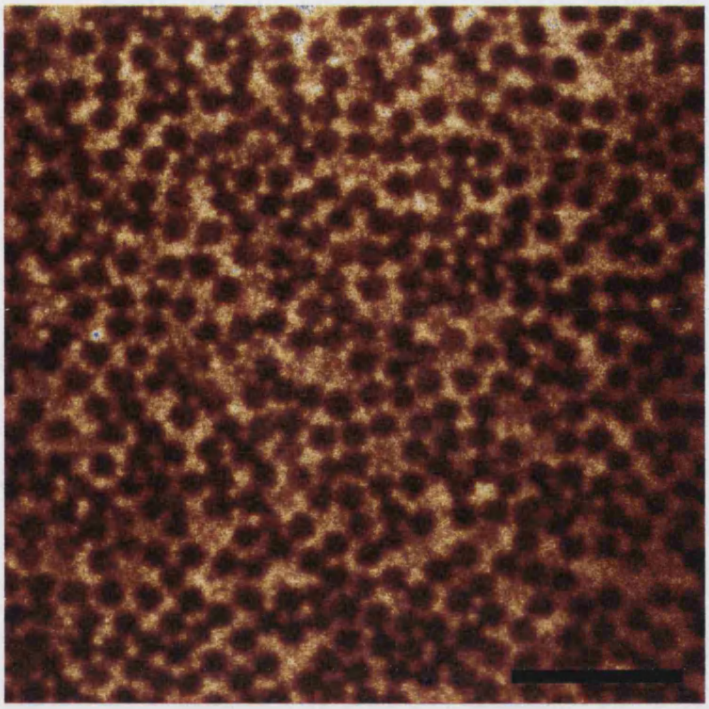

Figure 5.10: Micrograph LE-F1-AB(A)7 demonstrates the possibility of viewing large non-fluorescent spheres among a sea of smaller fluorescent spheres.(Bar length=6μm)

Figure 5.11: Micrograph LE-AB(A)-14 demonstrates the ability to image a large area of a colloidal dispersion, and the resolution of the confocal microscope allows the resolution of individual colloids. Instant visual assessment of the structure of different areas of the dispersion is possible.(Bar length=25μm)

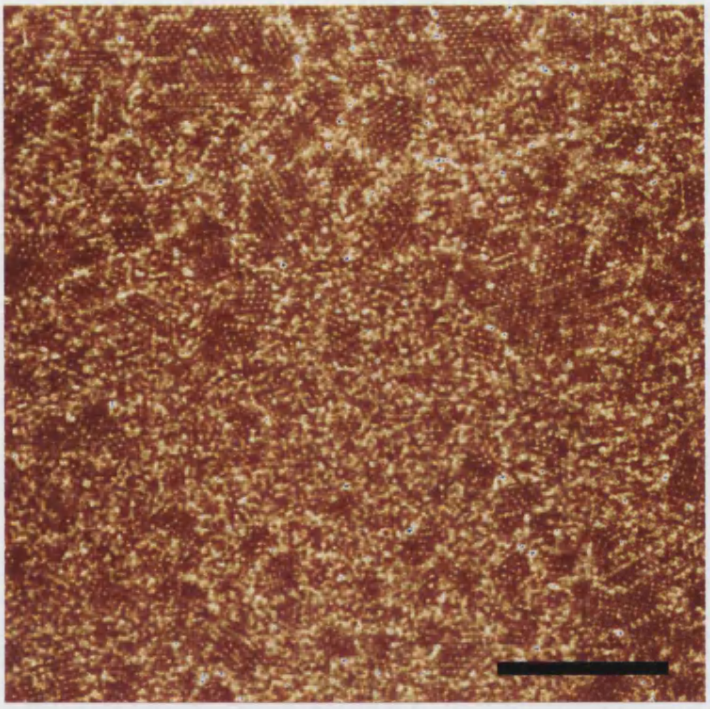

Figure 5.12: Using the resolution of the confocal microscope to image large areas, it can be seen in this micrograph (LE-F1-AB(A)-3) that a large number of the fluorescent colloids are distributed in an amorphous arrangement, but that a number of areas exist with more ordered arrangements (Bar length=25μm)

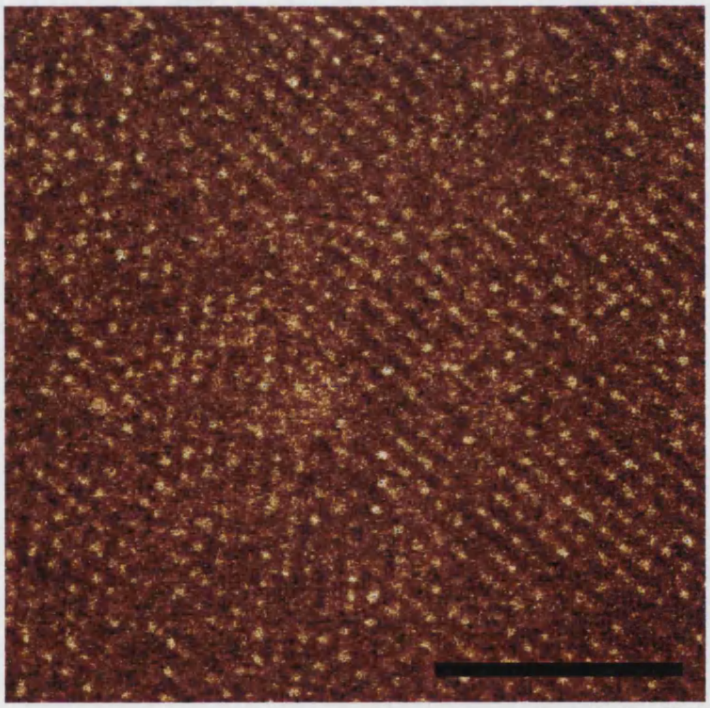

Figure 5.13: Micrograph LE-AB(A)-3 gives a closer view of areas with ordered structure. Although the image is noisy it is apparent that local order exists (Bar length=9μm)

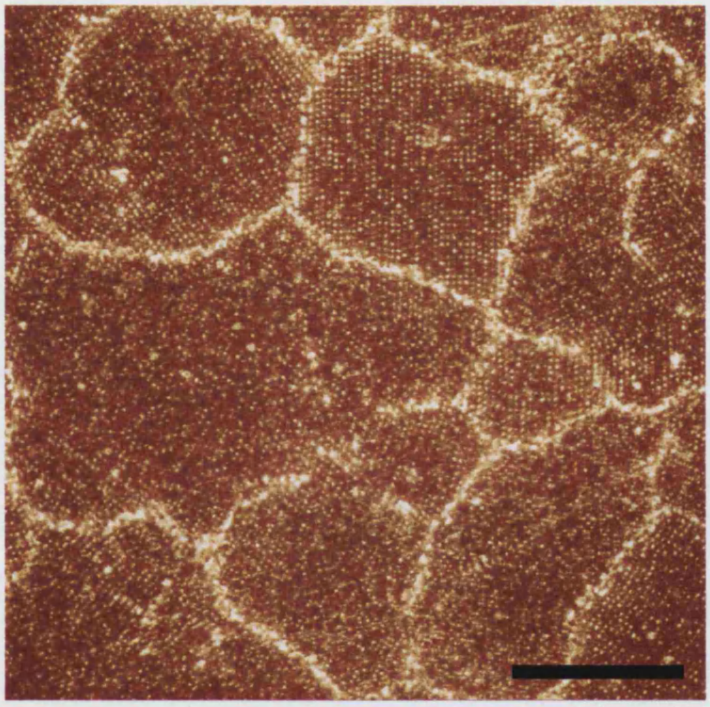

Figure 5.14: Micrograph LE-F1-AB(A)6 shows an inhomogeneous distribution of the smaller fluorescent colloid RSJF1 within the crystalline dispersion. A higher concentration of the fluorescent colloid can be seen in the disordered regions between the grains, which clearly contain ordered structure. A more detailed analysis of the ordered structure within the grains follows in Chapter 6. (Bar length=25μm)

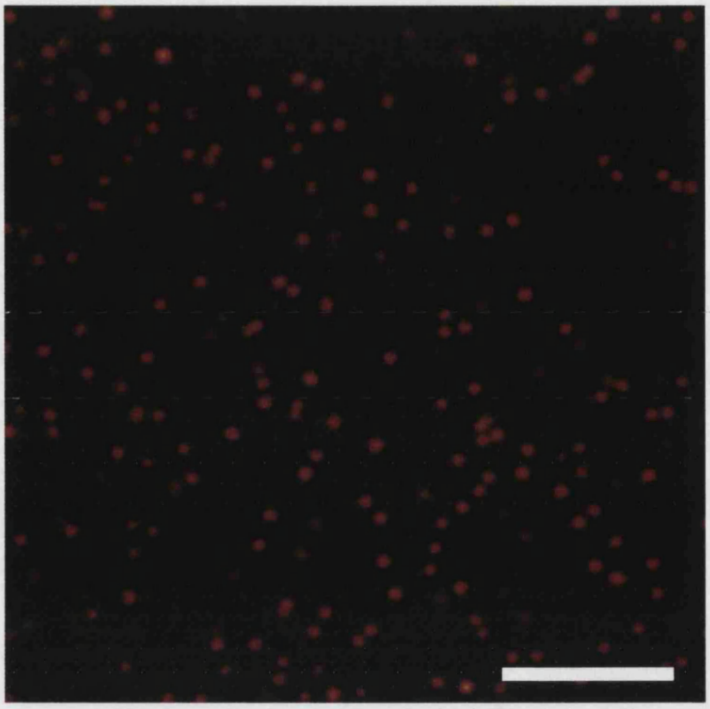

Figure 5.15: This micrograph (LE-F5-AB15(A)-10) contains the fluorescent colloid RSJF5 and demonstrates that the fluorescent dye NBD-MAE used in RSJF5 (see Chapter 3) is as effective for use in LSCM as the polymer-grafted dye NBD-MMA, used in the colloid RSJF1. (Bar length=6μm)

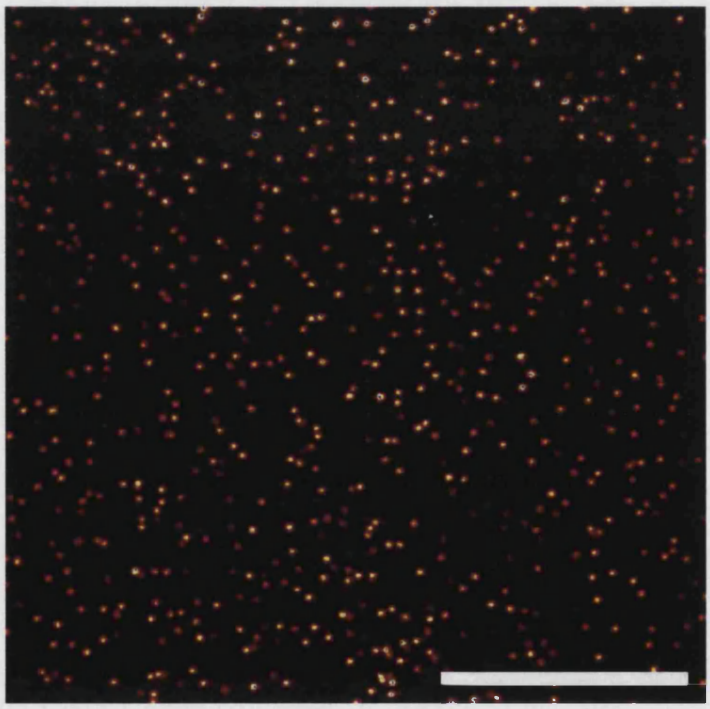

Figure 5.16: Micrographs LE-AB(A)-3 (Figure 5.15) and this micrograph, LE-F5-AB15(A)-1 demonstrate that well separated, large fluorescent colloids are easily resolved using FLSCM. In this example the local structure of the fluorescent colloids is a homogeneous glass. (Bar length=18μm)

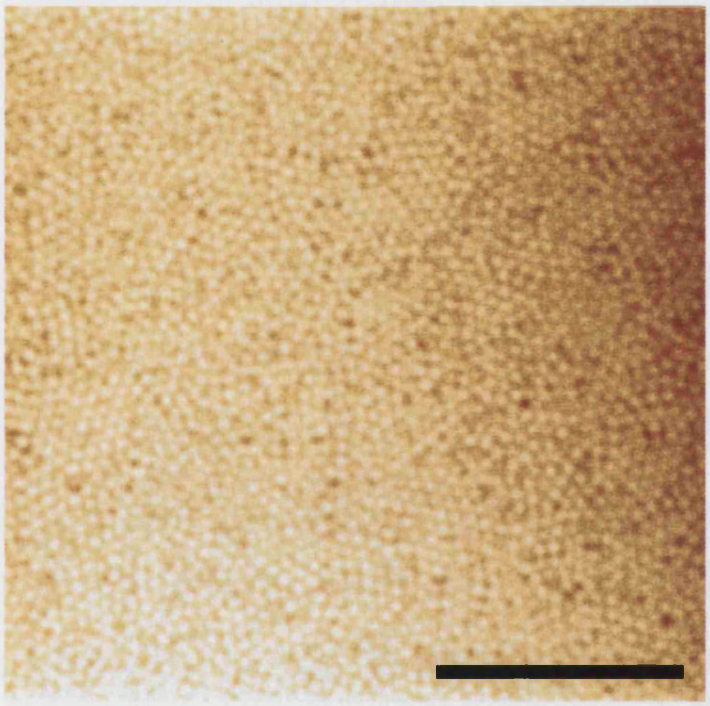

Figure 5.17: Micrograph LE-F5-A-5 demonstrates that even with a sample of fluorescent particles alone where the fluorescent particles are not well separated, individual particles and the local glassy structure can still be distinguished, due to the increased effective axial resolution and increased contrast offered by LSCM. (Bar length=9μm)

Chapter 6

Binary Mixtures of Hard-Sphere PMMA Colloids

An experimental study of the phases and structures formed in concentrated binary mixtures of hard-sphere colloids is presented. Mixtures of colloids with a size ratio of 0.39 are studied and the structures formed are identified by static light scattering studies and fluorescent laser scanning confocal microscopy.

6.1 Introduction

A quantitative analysis of static light scattering from these systems has not been carried out. The structures in these systems were studied using techniques analogous with x-ray powder diffraction techniques. Hence the structures formed were characterized by qualitatively studying the form of experimental scattering profiles and comparing these forms with known results from similar studies or theoretical work. Crystalline structures, for example, can be identified by the number, intensity and location of sharp peaks within the scattering profile.

6.2 Theory

Hard spheres constitute a simple, yet important model within condensed-matter physics [55]. The phase behaviour of hard spheres is determined by minimizing the free energy $F = U - TS$ or, since hard spheres are forbidden to interpenetrate and the internal energy U is a constant, by maximizing the entropy S. It was surprising, given the simplicity of the interactions in hard-spheres, when experiments on colloidal particles [72] demonstrated that hard-spheres of different sizes formed equilibrium structures containing crystalline superlattices. Subsequent computer simulations confirmed that a mixture with a radius ratio $\alpha = R_S/R_L$ of 0.58 formed two binary crystals, with stoichiometries LS_2 and LS_{13} (where L denoted the large particle, S denotes the small). Given the complexity of the structure formed from particles with such a simple interaction, it is worthwhile to try to understand the factors behind the obviously subtle effects of entropy at this ratio. In addition it is interesting to determine what structures may be formed at other ratios. The theoretical phase behaviour of binary hard-sphere mixtures has been investigated, both by the use of computational methods and using molecular

theory. For mixtures with a size ratio in the range $0.85 < \alpha < 1$ the phase behaviour can be thought of in terms of a perturbation of a one-component system, where the large and small spheres, not that different in size, are placed at random on a common close-packed lattice resulting in a substitutionally disordered fcc or hcp structure. Computer simulations, cell theory and density functional theory studies show good agreement over this range [67, 146, 69].

At first sight the idea that entropy, which is normally associated with increasing disorder, might generate complex and highly ordered structures seems counter-intuitive. It is frequently assumed that complex interactions are needed to generate complex phases, but this is incorrect. The physical origin of superlattice formation in hard-sphere suspensions is simple, and of general application to all entropic systems [147]. The resolution of the apparent problem lies in carefully examining entropy over a wider range of space and motions than might initially be examined. The entropy of a system of non-interpenetrating spheres can be thought to be composed of two types of contributions. The *configurational entropy* is associated with the degree of long-range spatial ordering, and the *free volume entropy* is associated with the space available to each particle for local motions. Confining the spheres to the points of a crystalline lattice decreases the configurational entropy compared with a disordered fluid phase, as is intuitively expected. However, the particles within the crystalline lattice have more freedom at small distances than they do within the fluid. Forming a crystal increases the free volume entropy but at the expense of reducing the configurational entropy. At low concentrations, the configurational entropy dominates and the fluid is stable, but with increasing concentration, the gain in free volume entropy on superlattice formation more than compensates for the loss in configuration entropy and stable crystalline structures may be formed. In general, the stability of any particular hard-sphere crystal must depend on three variables, the size

ratio α, the total packing fraction $\phi = \phi_L + \phi_S$, and the relative numbers of large and small spheres n_S/n_L. These concepts have been validated by the accurate entropy calculations from Monte-Carlo simulations [148, 149, 150, 151, 152], density functional theory [153] and cell-model calculations [154, 146].

Although these arguments produce a clear physical explanation of superlattice formation, there is not currently a theory which can predict, *a priori*, the structures formed at any given size ratio. Current methods involve predicting possible structures and analysing these in turn. The problem with this approach is the overwhelming number of possible structures. The work carried out so far however, does suggest that in choosing suitable structures to analyse, one criteria worth examining is the maximum packing density. In particular, if a crystal has a high close-packed density, then at the lower densities where freezing occurs, the particles will have a larger volume in which to access the local degrees of freedom which will contribute to the free volume entropy.

On this basis the free volume entropy of each structure $L_m S_n$ should follow the form of the maximum packing curve $\phi_{cp}(\alpha)$. Such space-filling theories have been explored by Parthe [155] and Sanders [64, 156], who supposed that a superlattice will form only if its maximum packing fraction exceeds that for the pure one-component phase-separated crystals ($\phi_{cp} = \frac{\pi}{\sqrt{18}}$ 0.74). The space filling curves for a small selection of binary crystal structures are shown in Figure 6.1, from which it can clearly be seen that over the range shown only two of the binary structures fill space more efficiently than the one-component structure. This maximum packing theory would therefore predict the stability of the LS_2 crystal at $\alpha =$ 0.58 which has been seen experimentally in colloids [72] and the stability has been confirmed by computer simulation [152]. The maximum packing principle further predicts that an LS structure, with a NaCl or NiAs structure (which are equivalent in terms of packing) is stable, with a maximum packing fraction

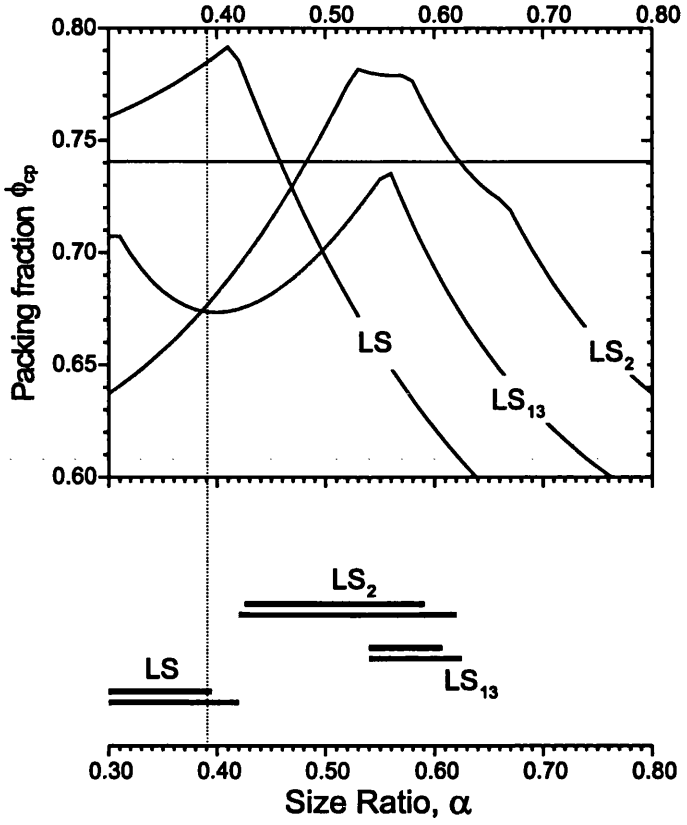

Figure 6.1: The upper section of the figure shows the packing density as a function of size ratio for the LS, LS_2 and LS_{13} structures. The horizontal line at $\phi_{cp} = 0.7405$ shows the close packing limit for a one-component fcc or hcp crystal. The lower section summarizes the regions of stability predicted by computer simulation (grey) [152, 148, 151] and cell calculations (black) [146]. The size ratio studied in this work is given by the dotted line.

of 0.793 at $\alpha = \sqrt{2} - 1(\ 0.414)$. Also shown in Figure 6.1, is the LS_{13} lattice structure which has a close packing limit close to the one-component limit. LS_2 and LS_{13} structures have been observed experimentally in colloidal hard-sphere mixtures, but although a stable NaCl crystal has been predicted by a number of theoretical studies, neither of the LS structures has been observed in experiment. An aim of the present work is to clarify if the NaCl crystal can be observed experimentally, confirming theoretical predictions.

6.3 Experimental Details

The particles used in this chapter are the PMMA spheres characterized in Chapter 4, the details of those particles used in binary mixtures are summarized again in Table 6.1.

The particles were suspended in a near-refractive index matching mixture of *cis*-decahydronapthalene (decalin,n_{488}=1.4847) and carbon disulfide (CS_2, n_{488}=1.6483). Carbon disulfide has a substantial wavelength dependent refractive index and so, in practice, the particles and medium can only be matched at one point in the electromagnetic spectrum. The match was achieved by adding carbon disulfide by eye at a wavelength of approximately λ=568 nm. Choosing to match at this wavelength ensured that the change in refractive index at λ=647 nm, the wavelength used to detect scattering, was sufficient to ensure that the concentrated suspensions exhibited strong single scattering. A total of 25 different samples were prepared over a wide range of volume fractions and compositions (see Table 6.2 and Figure 6.2). The range of sample volume fractions $\phi = \phi_L + \phi_S$, spans the region between the monodisperse freezing volume fraction, $\phi_f = 0.494$, and the glass transition volume fraction $\phi_g = 0.58$, where crystallization is found for one-component suspensions [61]. Samples were prepared at varying n_S/n_L compositions, so as to cover the full extent of the of the fluid-solid transition in

Colloid	R_{xtal} (±5 nm)	R_{DLS} (±5 nm)	σ (±0.01)	ϕ_m (±0.01)
RSJF1 (S)	175	175	0.08	0.548
NH31 (L)	448	458	0.03	0.546

Table 6.1: Particles used in the binary colloidal systems detailed in this chapter. (S) and (L) simply refer to small and large particle, used to simplify structure notation throughout this chapter. R_{xtal},R_{DLS} are the particle radii as determined by static light scattering of the crystal and dynamic light scattering of the particle respectively, σ is the polydispersity and ϕ_m is the scaled melting volume fraction.

the $(\phi, n_s/n_L)$ plane (see Figure 6.2).

Sample	n_S/n_L	ϕ_L	ϕ_S	$\phi_L + \phi_S$	a_{expt} ($\pm$3 nm)
1	0.09	0.5274	0.0023	0.5297	987.20
2	0.10	0.5486	0.0027	0.5513	984.00
3	0.11	0.5682	0.0029	0.5711	990.20
4	0.99	0.5077	0.0243	0.5320	975.51
5	0.95	0.5280	0.0243	0.5522	975.47
6	1.03	0.5419	0.0270	0.5689	974.55
7	4.93	0.4289	0.1025	0.5313	-
8	5.01	0.4331	0.1051	0.5383	-
9	10.04	0.3602	0.1753	0.5355	-
10	10.10	0.3702	0.1812	0.5514	-
11	9.98	0.3838	0.1857	0.5695	-
12	20.02	0.2691	0.2612	0.5303	-
13	20.02	0.2784	0.2702	0.5486	-
14	20.00	0.2930	0.2842	0.5772	-
15	29.95	0.2165	0.3144	0.5309	-
16	30.05	0.2311	0.3367	0.5678	-
17	29.95	0.2322	0.3371	0.5693	-
18	50.12	0.1517	0.3686	0.5203	-
19	50.09	0.1575	0.3824	0.5398	-
20	50.12	0.1635	0.3973	0.5609	-
21	49.89	0.1633	0.3951	0.5585	-
22	200.18	0.0485	0.4704	0.5189	385.34
23	200.13	0.0507	0.4921	0.5428	386.08
24	200.04	0.0523	0.5077	0.5600	383.92
25	200.70	0.0538	0.5236	0.5774	384.13

Table 6.2: Summary of the compositions of binary mixtures prepared at size ratio α=0.39 and the cell lattice parameters of samples containing crystallites as measured by static light scattering.

After preparation, each sample was homogenized by tumbling overnight. Although the samples were index matched, they were not density-matched; the resulting sedimentation can affect the observed behaviour by altering local density, by inducing heterogeneous crystallization for example. To overcome this, each sample was continuously rotated in a vertical plane at a rate of one revolution per day following the methods described by Bartlett *et al.* [48]. The binary samples were sufficiently close to index matched conditions that the first signs of crystallization were most easily observed by eye. The time required to first

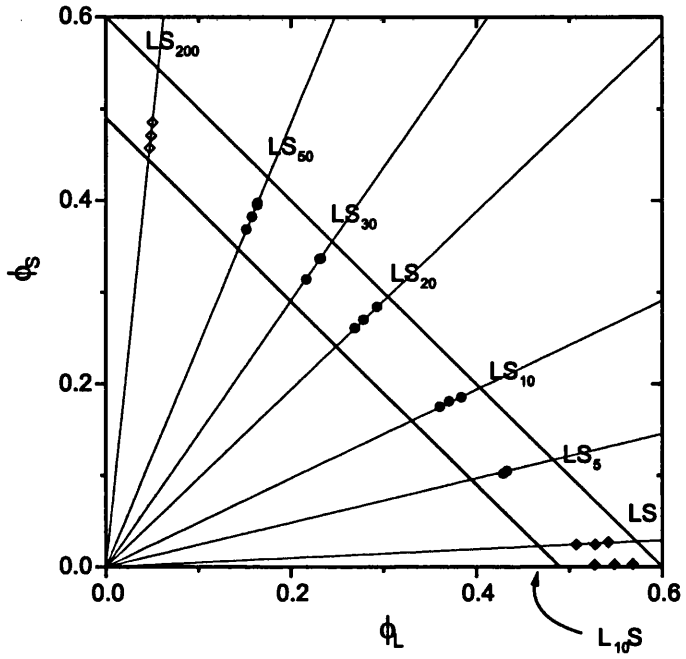

Figure 6.2: Summary of the binary samples prepared at size ratio α=0.39 and the phase behaviour observed. The symbols denote the following; *open diamond*, crystals of small spheres plus fluid; *closed diamond*; crystals of large spheres plus fluid; *closed circle*; amorphous sample. The solid lines correspond to the one-component hard-sphere freezing and melting densities. The dotted lines are guides to indicate the approximate n_S/n_L composition of samples

observe crystals varied considerably but was of the order of weeks. As soon as crystallites appeared the structure and development of the sample were followed with regular static light scattering measurements. Samples were followed for up to a year from preparation.

6.3.1 Static Light Scattering of Binary Colloidal Crystals

As can be seen from Table 6.2 and Figure 6.2, the two regions of fluid-crystal coexistence are extremely narrow with crystallization essentially limited to mixtures with a large proportion of either small or large spheres. It is, however, worth noting that the samples with a composition n_S/n_L=1 do show fluid-crystal coexistence.

In samples 1-6 and 22-25 (see Table 6.2), iridescent specks of nucleating crystallites were observed throughout the cells after a period of days. Over the next few weeks, these crystallites settled under gravity and a sharp crystal-fluid interface was evident. Light scattering measurements on this crystalline layer (see Figure 6.3) revealed powder patterns similar to the distinctive patterns found previously in single component hard-sphere suspensions [113]. The regular positions of the sharp Bragg reflections are consistent with the reflections expected from a random stacking of hexagonal close packed-planes of particles, as described in Section 4.3.1 [157].

Analysis of the scattering from samples 22-25 ($n_S/n_L \sim 200$) reveals close similarity with the scattering from the single-component small hard-sphere crystals, suggesting that the crystallites formed in these suspensions consist of crystals of S alone.

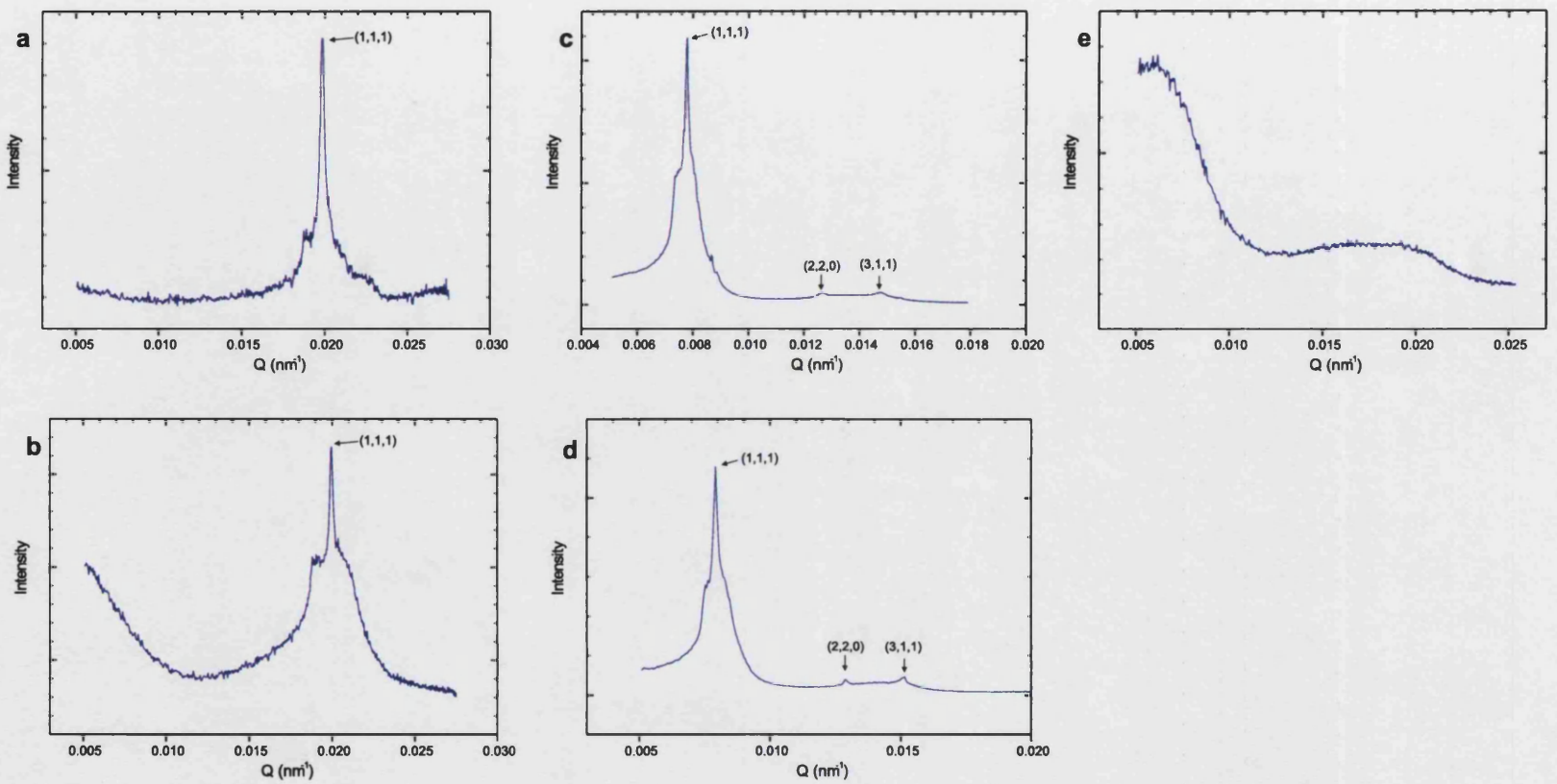

Figure 6.3: The scattering from binary mixtures of colloidal hard-spheres at $\alpha = 0.39$. The samples measured are (see Table 6.2) a) One-component RSJF1, b) Sample 23 (LS_{200}), c) One component NH31, d) Sample 6 (LS), e) Sample 14 (LS_{20}). Patterns a),b),c) and d) show Bragg reflections typical of crystalline phases, and the Bragg peaks are indexed on the rscp basis. Sample e) shows the scattering of a non-crystalline, amorphous sample

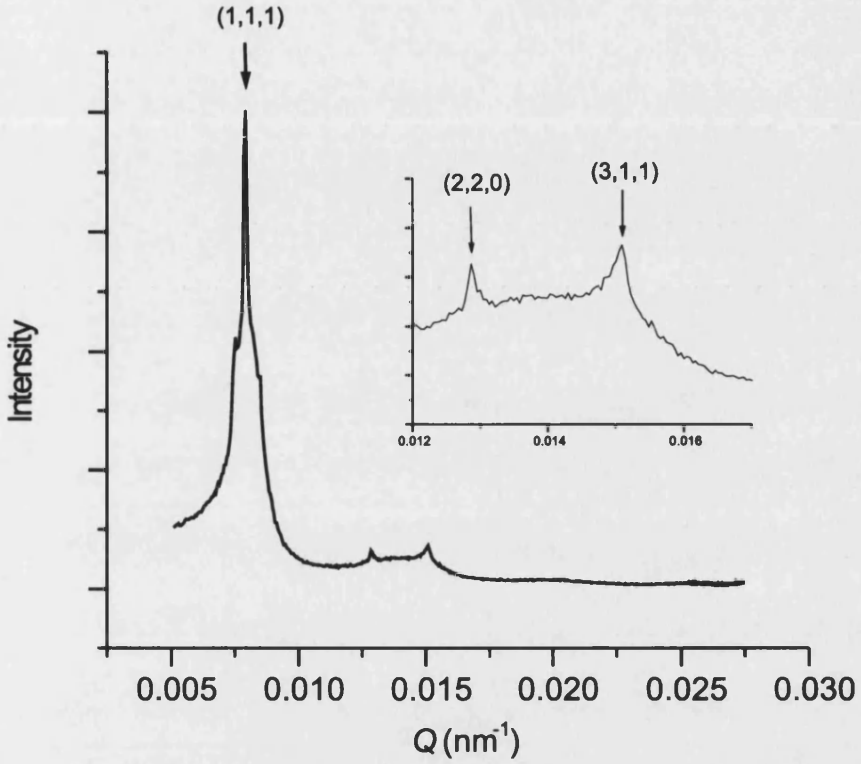

Figure 6.4: A static light scattering pattern from binary colloidal mixture labelled sample 5 in Table 6.2. The peaks correspond to fcc Miller indices as shown in Table 6.3

$Q \cdot 10^{-2}\mathrm{nm}^{-1}$	Miller_{fcc}	a (nm)
0.79	(1,1,1)	974
1.29	(2,2,0)	974
1.51	(3,1,1)	976

Table 6.3: Peak analysis of the static light scattering pattern from binary colloidal mixture labelled sample 5, shown in Figure 6.4, where a is the fcc lattice parameter.

Samples 7-21 ($5 \leq n_S/n_L \leq 50$) remained in a single phase and homogeneous for at least 6 months. Light scattering of these samples revealed amorphous arrangements of particles with no sharp peaks.

Examining the scattering from samples 1-3 ($n_S/n_L \sim 0.1$) and 4-6 ($n_S/n_L \sim 1$) and comparing with the scattering patterns from the one-component crystallites of the large spheres reveals that the scattering from binary mixtures 1-6 closely resembles that of the one-component crystallites. Whilst the evident similarities between the scattering seem to suggest that the crystalline phase found in samples 1-6 is composed of a phase separated crystal of the large particles, a closer study of the scattering technique shows it to be inconclusive. The theoretical calculations outlined in section 6.2 suggest that for α=0.39 LS superlattice phases could be stable. Below we demonstrate that while the scattering from the LS binary structures is in principle different from the one-component large sphere crystals, under the conditions of these experiments the differences are small and consequently, from scattering alone, the nature of the crystals found in samples 1-6 cannot be identified conclusively.

6.3.2 Scattering from LS superlattices

The LS family of superlattices (NaCl, NiAs and random-stacked analogs) consist of a close-packed layer of large spheres with small spheres occupying all of the available octahedral holes in the resulting lattice. To understand why the scattered intensity is insensitive to the differences between these structures, it is advantageous to start from the basic element common to each of these structures, a single hexagonal slice containing both small and large particles. Each of the LS crystals is then generated by stacking many slices together in different orders.

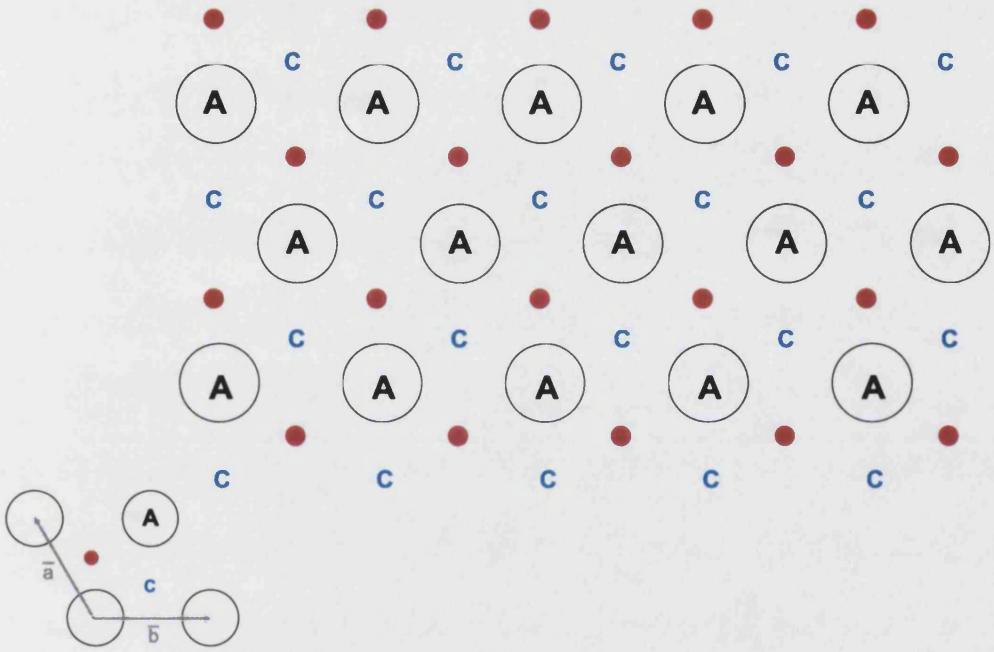

Figure 6.5: The (001) face of the NaCl crystal. The large spheres occupy the positions labelled A. The small spheres occupy the b set of interstitial sites, and the c sites are vacant.

Figure 6.5 shows one such composite slice, together with the hexagonal vectors a and b. The axis c is chosen so that the layer of large spheres lies in the reference plane $c = 0$ and the axis unit length is chosen as equal to the distance between two neighbouring large-sphere layers. The small spheres are positioned above the centre of the equilateral triangle formed by the centres of the three adjacent large spheres in the reference plane. There are two possibilities for placing the layer of small spheres, designated by b and c in Figure 6.5. The position of the b sphere (shown by the filled circle in Figure 6.5), with respect to the reference layer is given by $2a/3+b/3+c/2$, while the c sphere is positioned at $a/3+2b/3+c/2$. The full three dimensional structure is obtained by stacking slices (upper case refers to slices containing large spheres, lower case refers to layers of small spheres). The two simplest periodic arrangements are the NiAs lattice, $AcBcAcBcAcB...$ and the NaCl lattice $AcBaCbAcBaCbAc....$ One component hard-sphere crystal are usually randomly stacked, so similarly we expect that random superlattice structures may occur, such as $AcBaCaBaCbAcB$. Here we show that scattering from any of these structures closely resembles that of the identically stacked large-sphere crystal. In this instance we consider the NaCl lattice, but similar arguments apply to the other structures.

It is clear that for the NaCl structure $AcBaCb...$ or the twin $AbCaBc...$, the periodicity and the symmetry of the small sphere lattice are the same as that of the large-sphere lattice. This is not the case with other superlattice structures, such as LS_2 or LS_{13}. The origin lies in the nature of the NaCl structure where the small spheres occupy the interstitial sites, rather than substitutional sites as in LS_2 and LS_{13}. The three-dimensional arrangement of the larger spheres is not altered by the occupied interstitial sites, so that the Bragg reflection conditions for a NaCl structure are identical to those for a fcc lattice of large-spheres. Although the formation of NaCl does not alter the number of Bragg reflections, it does

modify their intensity. In NaCl, the small-sphere lattice is displaced relative to the large sphere lattice so scattering from the small-spheres is out of phase with the large-sphere scattering and the diffracted intensity is modulated.

The scattered intensity produced by a partially disordered layers has been reviewed by Guinier [114] and Warren [158]. In the NaCl example used here, the scattering intensity is concentrated along hexagonally arranged rods in reciprocal space (see Section 4.3). The intensity along each of the (h, k) rods depends on the stacking sequence of the layers. A general expression for this intensity $I_{hk}(l)$, for a system of N identical slices stacked along the c axis, has been determined by Guinier [114],

$$I_{hk}(l) = \frac{|F|^2}{N} \sum_{m=-N}^{m=N} \left(1 - \frac{|m|}{N}\right) y_m \exp(2\pi i m \Lambda) \tag{6.1}$$

where l is the distance along the rod expressed in units of $c* = 2\pi/c$ and F is defined by

$$F = \sum_p b_p \exp(-2\pi i(hx_p + ky_p + lz_p) \tag{6.2}$$

with b_p the amplitude scattered by each of the p particles contained within the unit cell. The function F is the intensity scattered by a single unit cell, and is called the structure factor in crystallography literature. The function y_m summarizes the degree of correlation between layers.

For the NaCl structure, $AcBaCb$...,we select the reference slice $\bar{A}c$ with a unit cell which contains a large sphere at position A and a small sphere at the interstitial site c. The corresponding cell-form factor, $|F_{Ac}|^2$, is readily calculated from Equation 6.2 and the geometry of Figure reffig:Naclface as

$$|F_{Ac}|^2 = b_L^2 \cos^2 \pi \left(\frac{h-k}{3} + l\right) - 2b_L b_S \cos 2\pi \left(\frac{h-k}{3} - \frac{l}{2}\right) + b_s^2 \qquad (6.3)$$

where b_L and b_S are the amplitudes of scattering from the large and small particles respectively. The position of the $\bar{B}a$ slice is translated by the vector $(2a/3+(b/3)$ relative to the $\bar{A}c$ slice so that the structure factor for a unit cell of slice $\bar{B}a$ is

$$F_{Ba} = F_{Ac} e^{2\pi i[(h-k)/3]} \qquad (6.4)$$

and similarly,

$$F_{Cb} = F_{Ac} e^{-2\pi i[(h-k)/3]} \qquad (6.5)$$

gives the structure factor for slice $\bar{C}b$. Assuming fault-free fcc stacking, the autocorrelation function y_m may be calculated analytically from Equations 6.3 and 6.5 with the result

$$y_m = e^{-2\pi i m(h-k)/3} \qquad (6.6)$$

The intensity along the (h,k) row is then obtained from Equation 6.1 as

$$I_{hk}(l) = \frac{|F_{Ac}|^2}{N} \sum_{m=-N}^{m=N} \left(1 - \frac{|m|}{N}\right) y_m \exp(2\pi i m\Lambda) = |F_{Ac}|^2 \frac{\sin^2 \pi N\Lambda}{\sin^2 \pi\Lambda} \qquad (6.7)$$

where $\Lambda = l - (h-k)/3$. The intensity I_{hk} is a sharply peaked function whose

maximum value is $|F_{Ac}|^2$, for integral values of Λ. As the number of layers increases, $N \to \infty$, so it becomes a δ function. In general, there are two types of Bragg rods. For rods with $(h-k) = 3n$, where n is an integer, there is a succession of nodes at integral values of l. On the other hand, for rods with $(h-k = 3n \pm 1$, the reciprocal-lattice points occur for $l = n \pm 1/3$. All intensity nodes have the same maximum value of $|F_{Ac}|^2$. There is no free energy difference between the sequence $AcBaCb...$ and the symmetric twin structure $AbCaBc...$, so in experiments we expect a superposition of the scattering from both crystals. The scattering from the sequence $AbCaBc...$ may be calculated using the methods described above. The unit cell of the NaCl twin contains a large sphere at A and a small sphere on the b-interstitial site so the cell form factor, $|F_{Ab}|^2$, is

$$|F_{Ab}|^2 = b_L^2 \cos^2 \pi \left(\frac{h-k}{3} - l\right) - 2b_L b_S \cos 2\pi \left(\frac{h-k}{3} + \frac{l}{2}\right) + b_s^2 \qquad (6.8)$$

The layer correlation function is simply $y_m = e^{-2\pi i m(h-k)/3}$. Following Equation 6.7, it can be shown that nodes of intensity $|F_{Ab}|^2$ occur at $l = n \pm 1/3$ along the $(h-k) = 3n$ rods. Consequently, the twinned NaCl crystal $(AcBaCb..., AbCaBc...)$ has reciprocal-lattice points at integral l along the $(h-k) = 3n$ rods and at $l = n \pm 1/3$ along all other rods. The topology of the reciprocal lattice is identical to the lattice of the twinned fcc crystal of large spheres described in Section 4.3.1, so the two structures have identically positioned Bragg reflections. The change in intensity of the Bragg reflections with superlattice formation depends on the relative magnitude of the scattering from large and small particles, b_L/b_S. For a homogeneous particle of radius R, the scattering amplitude is given by the standard expression [159]

$$b(QR) = 4\pi R^3 \Delta n \left(\frac{\sin QR - QR\cos QR}{(QR)^3}\right) \qquad (6.9)$$

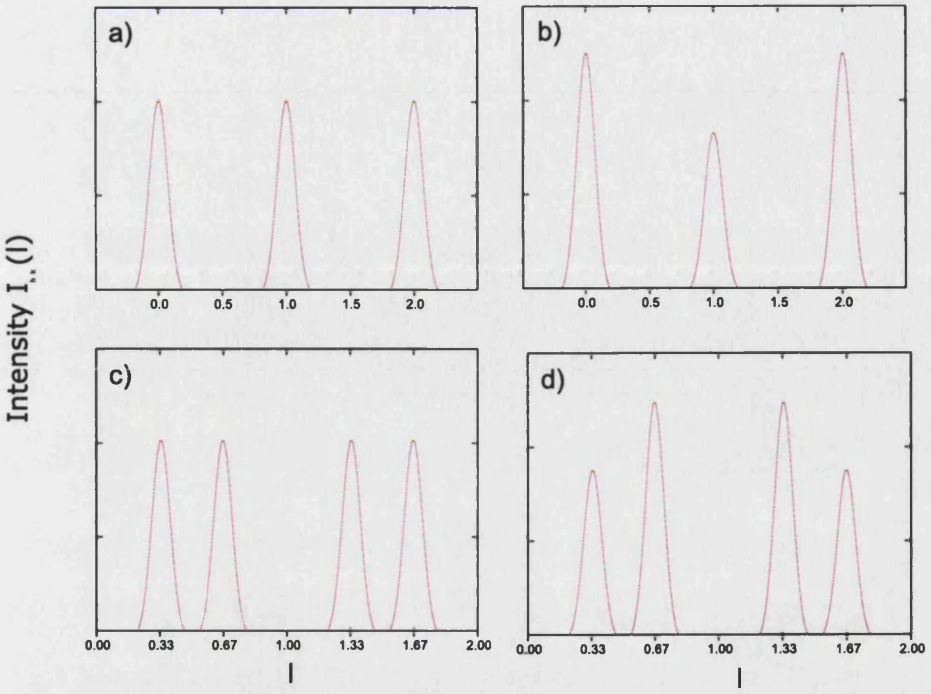

Figure 6.6: The intensity distribution $I_{kh}(l))$ along the (h,k) Bragg rods in reciprocal space for a twinned fcc lattice of large-spheres [a) and c)] and for the twinned NaCl lattice [b) and d)]. The top figures [a) and b)] show $I_{hk}(l)$ along the $(h-k)=3n$ rods and the bottom figures show the corresponding variation along the $(h-k)=3n\pm 1$ rods [160]. The intensity is calculated assuming an amplitude ratio $b_L/b_S = 10$.

where Δn is the refractive index mismatch between particle and medium. The intensity of the scattering depends very strongly on particle size and so in a binary mixture the large particles scatter light much more efficiently than small particles. For instance, for a size ratio of $\alpha \sim 0.4$ and a scattering vector $QR_L \sim 3.5$ (matching the (001) reflection of the twinned NaCl crystal), the ratio b_L/b_S is about 10. Figure 6.6 shows the intensity distribution along the Bragg rods for the twinned fcc lattice of large spheres, calculated for this amplitude ratio. It is clear that although there are changes in the scattering distribution, the effects are small. For polycrystalline samples, the differences are likely to be even less noticeable, since the differences shown in Figure 6.6 have to be distributed over all orientations.

In conclusion it is clear that to identify NaCl crystals from powder light diffraction would demand highly accurate intensity measurements. To aid determination of the structure of the crystals formed in the binary colloidal suspensions, direct imaging methods have also been used.

6.3.3 Imaging of Binary Mixtures

Direct imaging methods have been used to aid determination of the crystal structure. One method commonly used to verify crystalline structures of hard-sphere colloidal suspensions is scanning electron microscopy [SEM]. To prepare samples of crystalline suspensions for SEM the following simple technique was used. The sealant and stopper was removed from the sample cell and the cell was left undisturbed in a fume cupboard for a number of weeks. Once all the solvent had evaporated from the cell, the cell was smashed open, and the fragments of solid dried-crystallite were moved to SEM sample planchette. The planchette and sample were coated in carbon before imaging. The results are shown in Figure 6.7. Although the micrographs clearly show that the crystals are of large spheres, there are small spheres present within the crystal lattice. From the SEMS it is difficult to determine the extent of ordering, if any, of the small spheres. The SEM technique is limited to examining the surface of these crystalline structures and the disturbances to the dispersion required to make samples suitable for SEM would add doubt to any conclusions. To determine unequivocally if a superlattice is formed in these colloidal mixtures, Fluorescence laser-scanning confocal microscopy is used.

To clearly differentiate between a NaCl type superlattice and a crystal purely of large spheres only the small particles in the mixture were fluorescently labelled. The large particles are non-fluorescent and are subsequently not imaged. Fig-

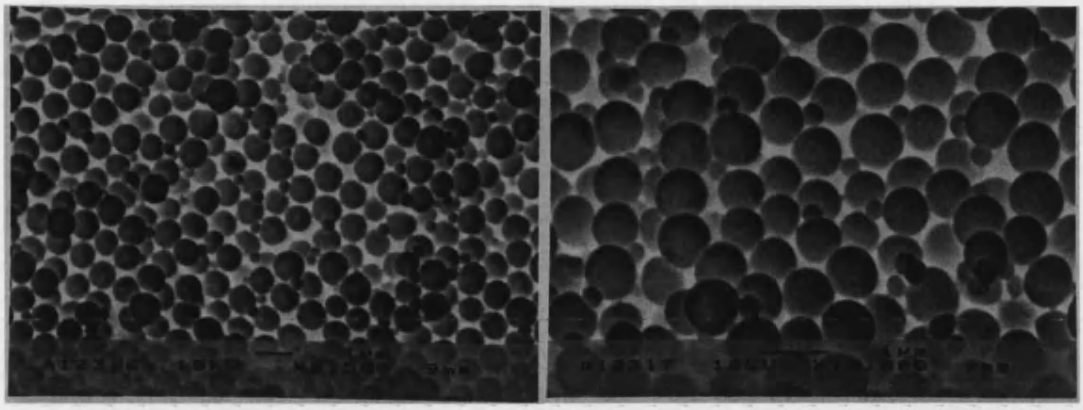

Figure 6.7: Scanning electron micrographs of the binary mixture Sample 4 (see Table 6.2). Although it is clear that small particles are present within the crystalline lattice of large spheres, using SEM it is difficult to determine the number and order of small spheres in the crystal. Micrographs were taken using a JEOL JSM6310

ure 6.8 shows a fluorescent confocal image of a crystalline region formed in a mixture of small NBD-labelled and large unlabelled PMMA particles, dispersed in an index-matched mixture of decalin and CS_2 with composition ${}^{n_S}/_{n_L} = 1$ and a volume fraction, $\phi = 0.532$.

The image was recorded about $15\,\mu$ m below the top glass wall. Although the image is noisy it is apparent that the small fluorescent particles are highly localized within a three-dimensional periodic structure. A careful analysis of the inset portion of the micrograph demonstrates that the crystal consists of small spheres arranged hexagonally in planes. The centre-to-centre distance in the hexagonal plane is 1080 ± 100 nm, which is considerably larger than the diameter of the small spheres ($2R_S = 350$ nm) and comparable to the diameter of the larger particles ($2R_L = 896$ nm) which suggests that the small spheres are separated by the non-fluorescent large particles. From these observations the view in Figure 6.8 can be identified as the (001) plane of the LS superlattice. The crystal is orientated with the close packed (001) plane parallel to the walls of the cuvette. The sphere centre data from the inset image of Figure 6.8 is mapped onto a two dimensional grid scaled in units of 1080 nm in Figure 6.9. Figure 6.10 shows a two dimensional analogue of radial distribution function, $F(\rho)$, where $F(\rho)$ is the

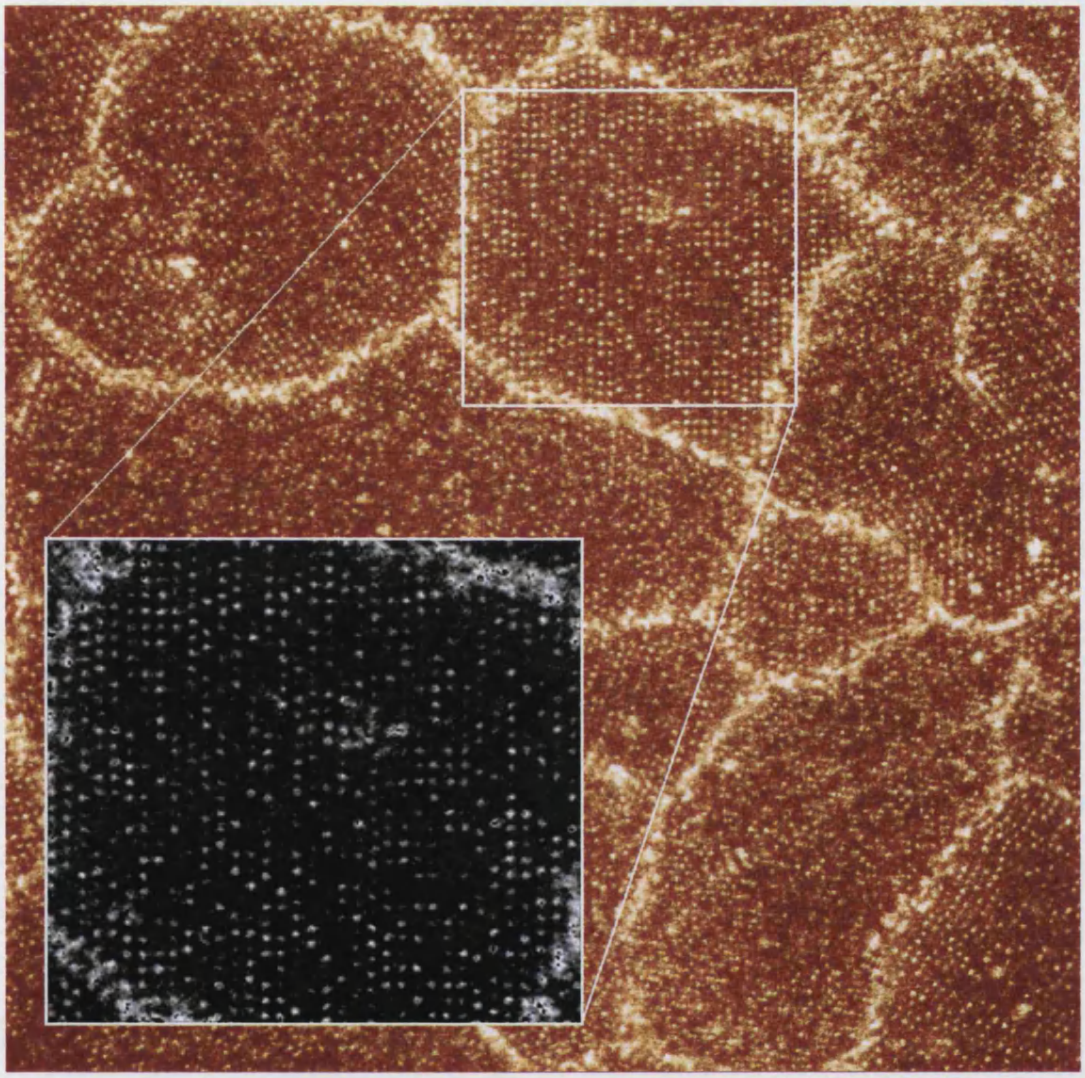

Figure 6.8: Micrograph LE-F1-AB(A)6 shows an inhomogeneous distribution of the smaller fluorescent colloid RSJF1 within the crystalline dispersion. A higher concentration of the fluorescent colloid can be seen in the disordered regions between the grains, which clearly contain ordered structure. One grain is expanded in the inset, and the positions of the colloids within this portion are analysed further

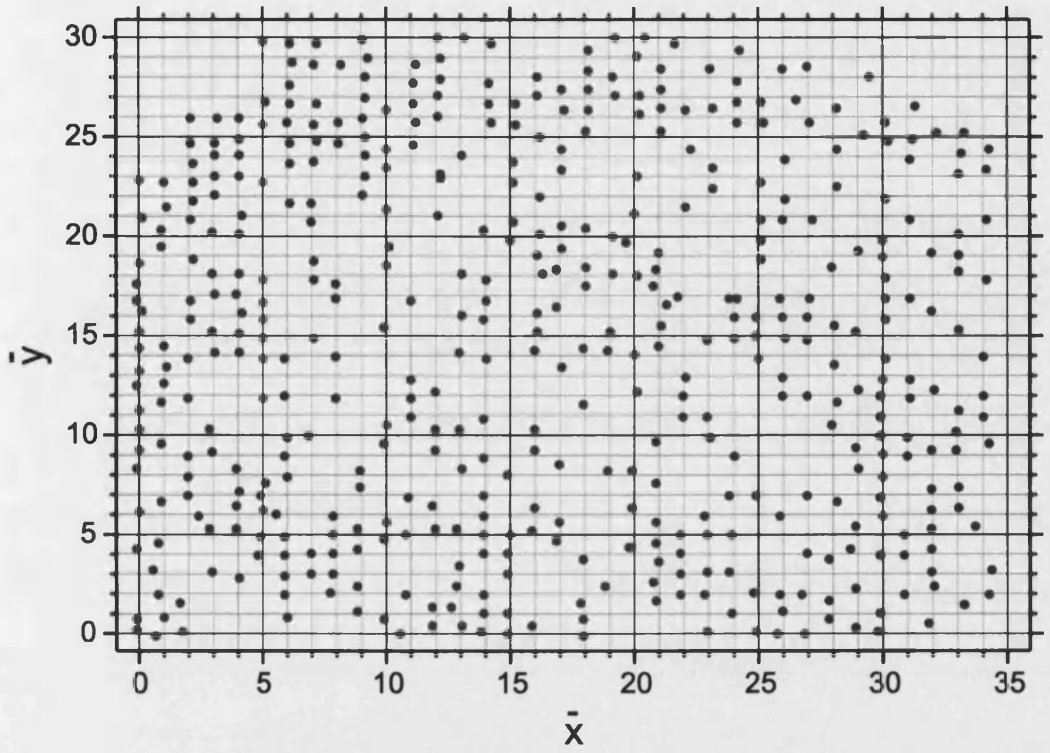

Figure 6.9: Sphere centre data retrieved from Figure 6.8, mapped onto a two dimensional grid. It is clear that the majority of particles are located at the intersections of the underlying square lattice.

probability of finding a second sphere at distance ρ from a first sphere. The peaks at the values of $\rho/2R$= 1, $\sqrt{2}$, 2, $\sqrt{5}$ etc. indicate the presence of small spheres which fit the 2d lattice.

Further conformation for this identification comes from scattering measurements. If a LS structure is formed then the intense first Bragg peak at $q_{(001)} = [7.91 \cdot 10^{-3}]nm^{-1}$ corresponds to a reflection from the (001) planes of the crystal. The interplane spacing is then $c = {}^{2\pi}/_{q_{(001)}} = 794\,\text{nm}$. The hexagonal close packed planes are close packed within the structure so the centre-to-centre separation within the plane is $a = c\sqrt{3/2}$ or 973 nm. This corresponds well to the interparticle spacing measured directly from the micrograph seen in Figure 6.8 of $a = 1080 \pm 100\,\text{nm}$. These results demonstrate that a hexagonal layer of large

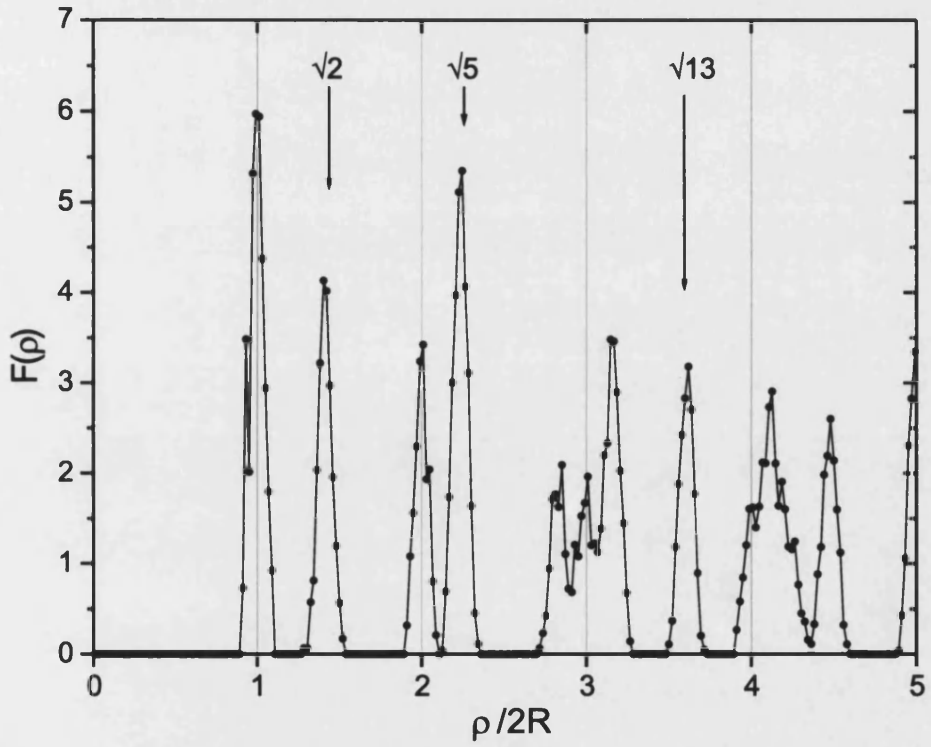

Figure 6.10: 2d radial distribution function from square lattice (5% random displacement 0.46 occupancy)

and small spheres is formed in a binary hard-sphere mixture of $\alpha = 0.39$. In order to distinguish between NaCl, NiAs or a random-stacked crystal it is necessary to determine the stacking sequence of the hexagonal layers. To this end we recorded a series of confocal micrographs,each at the same lateral position in the crystal but separated by unit[0.6]μm in the axial direction. Unfortunately the sample suffered from thermal drift which prevented us from reliably identifying the stacking sequence.

6.4 Conclusions

In this chapter we have presented a comparison between the phase behaviour and structures found in experimental data of binary mixtures of hard-spheres and Monte Carlo and cell model predictions for a mixture of hard spheres. There are substantial differences between the theory and experiment of colloidal mixtures with the size ratio of 0.39 used in this work. The predictions of cell theory [146] are reproduced in Figure 6.11 with the observed experimental data shown by the points. The ratio used is close to the substantial maximum (ϕ_{max}=0.79 at $\alpha = \sqrt{2}-1$) seen in the close packing curve for the NaCl structure (see Figure 6.1).

Consequently, the predicted phase diagram is dominated by the existence of an LS superlattice. The samples which are predicted to lie in the region of two-phase coexistence of LS superlattice and fluid, remain amorphous, and all those samples predicted to lie in on the boundary of the region predicting coexistence between crystals of S, LS and fluid phase separate into crystals of small spheres and fluid phase. The disagreements are most evident in the region where a coexistence between large-sphere crystal and fluid is predicted to exist. The mixture studied by confocal microscopy lies in the middle of this region, yet the

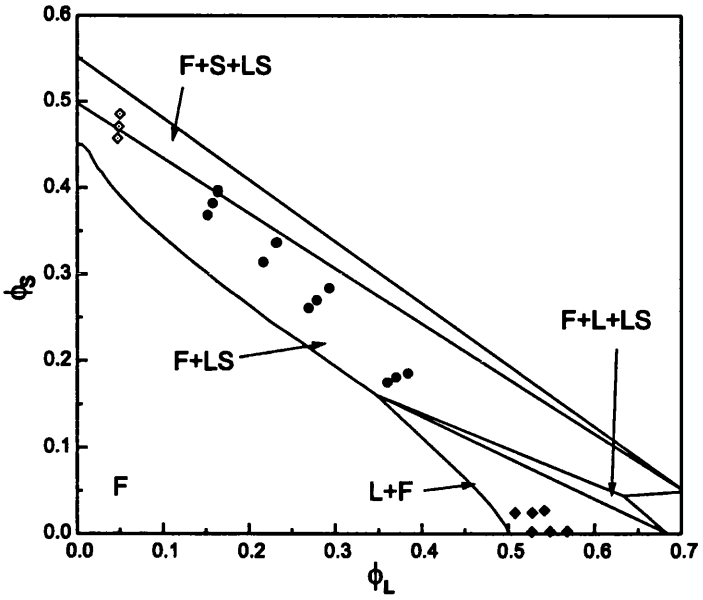

Figure 6.11: Summary of the phase behaviour observed at size ratio α=0.39 and comparison with the predictions of cell-model theory [146]. The symbols denote the following; *open diamond*, crystal of small spheres plus fluid; *closed diamond*; crystal of large spheres plus fluid; *closed circle*; amorphous sample.

data reported above clearly identifies the coexistence of regions of LS superlattices and fluid. These findings are similar to experiments carried out by Hunt at α=0.42 [106], where the experimental phase diagram also contains a substantial region of amorphous behaviour.

A possible factor in the difficulty in forming the LS superlattice is the density at which a structure first becomes stable. Figure 6.12 summarizes the densities at various size ratios, at which a crystal first becomes thermodynamically stable [148, 151].

The two experimentally accessible superlattice structures LS_2 and LS_{13} are stable at substantially lower densities than the LS structure. In addition the densities predicted mirror the difficulty with which each superlattice is nucleated. For example, LS_{13} forms within a few weeks while the LS_2 lattices take several months

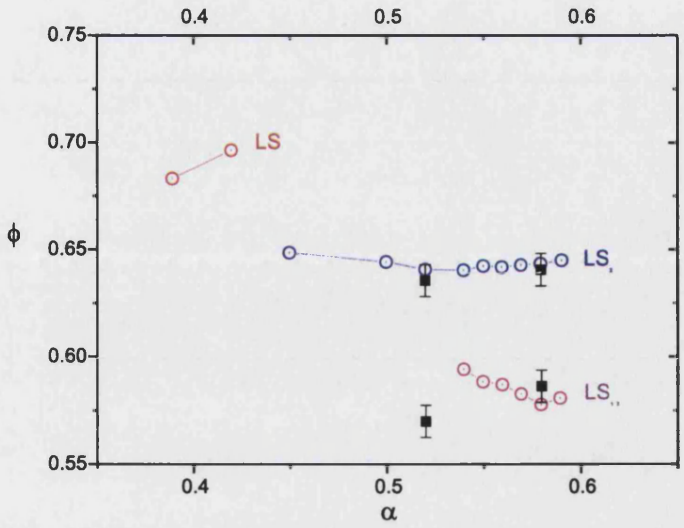

Figure 6.12: The lowest densities (ϕ) for each superlattice in coexistence with a fluid, as a function of size ratio (α). The circles are the simulation predictions of Eldridge *et al.* [148, 151] while the experimental values are shown by the filled squares [160].

to grow, so it is possible that the LS structure takes so long to develop as to be experimentally inaccessible over the years of the experiment. It is probable that the difficulty in nucleating the LS crystal reflects the density dependance of the solid-fluid interfacial tension γ. Little is known about how γ depends on the density mismatch between fluid and crystal, but it seems likely that the interface will become larger as the difference in densities between the two phases increases.

Chapter 7

Mixtures of Hard-Sphere PMMA Colloids and Microemulsion

A novel mixture of colloids and microemulsions with a size ratio of ~0.1 is studied and correlations and ordering of the particles are examined in small-angle neutron scattering experiments. From an analysis of the scattering, the effective pair potential in a highly asymmetric system of spheres is determined.

7.1 Introduction

Many of the industrial and commercial applications of colloids rely on careful control of the effective pair potential. In industrial applications of non-aqueous colloid science it is rare that the system does not involve additions of surfactant or polymer to the mixture. This highly complex situation is of practical interest in many applications today, including paints [14], surface coatings [19], cosmetic preparations [18] and foodstuffs such as mayonnaise [161] and dairy products [162] among the many possible examples.

Frequently the interparticle potential is controlled by the addition of small amounts of non-adsorbing polymer to the colloidal system. This addition is a convenient way to introduce an attractive component to the potential, and in such a system the attractive part of the potential can be controlled by altering the molecular weight and concentration of the polymer added. By altering the potential by small amounts, the properties of these colloid-polymer systems, for example the rheological properties, can be manipulated with a fine-degree of control. The study of attractive potentials in colloidal systems is therefore a topic of considerable interest [163, 164].

Polymer induced depletion attractions were first interpreted theoretically by Asakura and Oosawa [165, 166] and later by Vrij [35] in terms of a simple geometrical model. In this model, the polymer coils are treated as non-additive spheres with a radius equal to the radius of gyration of the polymer. Being non-additive, the polymer spheres interact only with the colloid, and this interaction is assumed to be steeply repulsive at contact. If two colloidal particles move together so that their surface to surface separation is less than the diameter of the radius of gyration of the polymer coil, the polymer molecule is excluded from this region

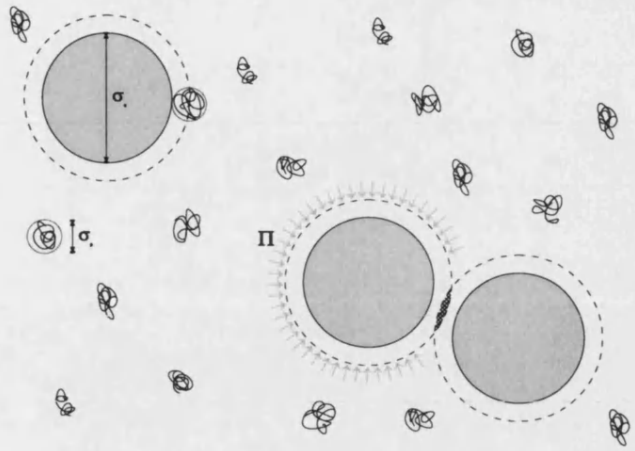

Figure 7.1: Schematic illustrating the Asakura Oosawa [AO] depletion model mechanism. When depletion areas of approaching colloids overlap (*cross-hatched area*), the osmotic pressure experienced by the colloid is anisotropic.

(see Figure 7.1). Polymer molecules outside this region however are still exerting an osmotic pressure on the remainder of the surface of the colloid. This gives rise to an attractive potential between the colloidal particles over a distance equal to twice the radius of gyration of the polymer. The effective potential of such a system, at the limits of low particle concentration, is given by [165, 35];

$$V = -\Pi \begin{cases} \infty & r < D_c \\ V_{overlap} & D_c < r < D_c + D_p \\ 0 & r > D_c + D_p \end{cases} \tag{7.1}$$

where r is the colloid centre-centre separation, D_c is the diameter of the colloidal particle and D_p is twice the radius of gyration of polymer coil. Π is the osmotic pressure exerted by the polymers which is related to the polymer number density, and $V_{overlap}$ is the overlap volume of the depletion zone, given by;

$$V_{overlap} = \frac{4}{3}\pi \bar{D}^3 \left[1 - {}^3\!/_4 \left(\frac{r}{\bar{D}}\right) + {}^1\!/_{16} \left(\frac{r}{\bar{D}}\right)^3\right]$$

where $\bar{D} = 1/2(D_c + D_p)$. The potential can therefore be modified experimentally; the range of the attraction can be tuned by changing the molecular weight of the polymer and the depth of the potential can be modified by altering the concentration of the polymer, which alters the osmotic pressure, Π. These tunable interactions give rise to different forms of phase diagram, many of which have been studied extensively [163, 167, 168]. Particular interest has developed in cases where the attraction is relatively short-range (*e.g.* where $D_p/D_c = 0.08$ [169, 170, 171]). These systems undergo a fluid-crystal phase separation at a certain level of polymer, and non-equilibrium behaviour such as aggregation [172] and transient gelation [173] has also been observed.

Experimental results show that the structure of a mixture of asymmetric PMMA hard spheres can also be understood in terms of depletion interactions [174]. Recently Dijkstra *et al.* have utilized the AO depletion potential to model the behaviour of asymmetric binary hard-sphere mixtures by direct computer simulation [175, 176]. Due to slow equilibration, direct computer simulations of highly asymmetric hard-sphere mixtures using purely hard-sphere potentials are prohibited by the large amounts of computational time that is required to model such a system [175]. By using an effective pairwise potential that is the sum of the hard sphere potential and the AO depletion potential, Dijkstra *et al.* have calculated phase diagrams that agree well with those all-hard-sphere calculations that have so far been computed. The success of this model validates the extension of the depletion model from colloid-polymer mixtures to asymmetric colloidal mixtures.

The range of sizes over which well-defined model hard-sphere colloidal particles can be synthesized restricts the experimental possibilities for examining highly asymmetric mixtures. In this chapter we present experimental results from a novel mixture of highly asymmetric spheres, using PMMA colloidal particles for the large component and an AOT water-in-oil microemulsion [AOT is di-

2-ethylhexylsulfosuccinate] for the small component. To a first approximation the system could be considered a mixture of very-different sized hard spheres, and the nature of depletion forces in such a mixture of spheres can be studied. Mixtures of colloids and microemulsions with a size ratio of ~0.1 are studied and the scattering structure factors are identified by small-angle neutron scattering studies. These scattering profiles are compared with simulated scattering profiles generated by a modified random-phase approximation [RPA] type expression and the potentials from the RPA expressions are interpreted in physical terms.

7.2 Small Angle Neutron Scattering [SANS]

7.2.1 Introduction

One of the most appropriate tools to probe the structures that characterize colloidal materials is the detection of scattered light, as discussed in Chapter 2. Complementary information is provided by the detection of scattering at other wavelengths, in particular from the scattering of neutrons. Two methods used to produce neutrons suitable for scattering experiments are spallation methods and nuclear reactors. Spallation methods involve directing high-energy proton beams at heavy nuclei, the heavy nuclei are thermally excited and decay. An example of a spallation neutron source is the ISIS facility near Oxford, UK [177]. The other method used to produce neutrons is to use a nuclear reactor. Neutrons are released by the fission of uranium-235. Each fission event releases 2 or 3 neutrons, one of which sustains the chain reaction. The most powerful continuous neutron source in the world today is the 58 MW high-flux reactor at the Institute Laue-Langevin [ILL] in Grenoble, France [178].

As produced, neutrons are too energetic for use in scattering experiments, and must be slowed down in a moderator until their kinetic energy is approximately k_BT (thermal neutrons) or less (cold neutrons), at which point their de Broglie wavelengths, $\lambda = \frac{h}{mv}$, are comparable with interatomic distances. Neutron radiation can be produced over a range of wavelengths, typically 0.01-0.3 nm [179]. A fundamental difference between neutron and electromagnetic radiation is the mechanism by which the radiation interacts with matter. Light and X-rays, for example, are scattered by electrons surrounding atomic nuclei, but neutrons are scattered by the nucleus itself. It is often this aspect of neutron scattering that allows the collection of data that is complementary and additional to data retrieved from conventional light scattering experiments. Contrast matching is a technique of which utilizes the difference in scattering properties of various nuclei, frequently by allowing one component of a mixture to be altered so that its average scattering length density matches that of the background medium. The matched component will therefore not contribute to the scattering. Contrast matching therefore allows the scattering to be tuned for specific purposes, but this tuning often does not change the basic chemistry of the system.

To examine detail on a colloidal scale, measurements of scattered neutrons must be made at a very small angle, usually at most a few degrees from the incident radiation. Hence a useful technique commonly used to probe colloidal dispersions is small-angle neutron scattering [SANS]. In this chapter, mixtures of colloid and microemulsion have been probed using the D11 SANS instrument [180] at the ILL, Grenoble. The remainder of this section will give a brief account of the basis of small-angle neutron scattering.

7.2.2 Neutron Scattering Length

In Chapter 2 we described the amplitude of field scattered by a scattering element as

$$E(\mathbf{Q}) = \int_{V_s} f(\mathbf{r}) \exp[i\mathbf{Q} \cdot \mathbf{r}]\, d\mathbf{r} \tag{7.2}$$

where $f(\mathbf{r})$ is the scattering length of the volume element. Investigating the interaction between the neutron and the scattering nuclei we discover that the scattering length varies in an irregular and unpredictable way from one nucleus or isotope to another. The neutron scattering length, conventionally represented with the symbol b, is known with considerable precision for most isotopes, Table 7.1 summarizes neutron scattering lengths for some common nuclei.

The dimensions of b are chosen so that b^2 is the probability that a neutron will be scattered per nucleus, per incident neutron, per solid angle. The probability of the neutron being scattered somewhere in space is thus $4\pi b^2$, and this quantity is named the *cross-section* and is represented by σ.

7.2.3 Coherent and Incoherent Scattering

If there are spatial correlations between nuclei with the same scattering length, then the correlations give rise to structure factors in the detected scattering which characterize these correlations. Scattering which carries information about some structural arrangement within the sample is termed *coherent scattering.* If there are no correlations between the position of a nucleus and the value of its scattering length then there will be a random part to the scattering, termed *incoherent*

scattering. In general coherent scattering arises because materials within the sample have spatial correlations on a scale of the order of the wavelength of the incident neutron beam. Incoherent scattering can arise due to isotopic variation, a sample may contain an occasional isotope having a different scattering length to that of the major isotope. Because, in general, the positions of these isotopic variations are random, the scattering from the isotopic variations cannot carry any structural information and forms a Q-independent background. Incoherent scattering also occurs due to interaction between the spins of nuclei and neutron. When these interactions are taken into account further differences in scattering may arise [181]. In particular hydrogen has two very different scattering lengths depending on its spin state. Since the spin of a nucleus is generally uncorrelated with its position these scattering lengths also give rise to incoherent scattering. Values of coherent and incoherent cross-sections are given in Table 7.1.

7.2.4 Scattering Length Density

A typical SANS experiment is insensitive to details on the atomic scale and the *scattering amplitude density*, β, is a useful average.

Isotope	b_{coh}(fm)	σ_{coh} (barn)	σ_{inc} (barn)	σ_{abs} (barn)
^{1}H	-3.741	1.8	80.3	0.3
^{2}D	+6.671	5.6	2.1	0.0
C	+6.646	5.6	0.0	0.0
N	+9.362	11.0	0.5	1.9
O	+5.803	4.2	0.0	0.0

Table 7.1: The coherent neutron scattering lengths, b_{coh}, of some common nuclei. Where no atomic number is given, the natural isotopic abundance is assumed. σ_{coh}, σ_{inc} and σ_{abs} are the coherent, incoherent and absorption cross section respectively. Note:1 fm=$1{\cdot}10^{-15}$ m and 1 barn= $1{\cdot}10^{-24}$ cm^2

$$\beta = \frac{\sum b}{v} \tag{7.3}$$

The probability of a beam of neutrons being scattered by an assembly of nuclei will be given by the sum of the wavelengths scatted by individual nuclei. If there are nuclei present with different values of b, then these must be averaged before squaring them to obtain the net probability of scattering. A collection of values for relevant molecules is listed in Table 7.2.

7.2.5 The form factor of polydisperse core-shell spheres

Neutron scattering is analogous to light scattering as described in Chapter 2. For scattering from large-scale structures *e.g.* colloids, the scattering can again be usefully divided to distinguish between scattering from volume elements within a particle and radiation scattered by different particles and we return to Equation 2.8

$$E(\mathbf{Q}) = \sum_{i=1}^{N} B_i(\mathbf{Q}) \exp[i\mathbf{Q} \cdot \mathbf{r_i}]$$

Substance	Density (g cm^{-3})	β (10^{10} cm^{-2})
H_2O	0.997	-0.56
D_2O	1.104	+6.38
decane	0.73	-0.49
d-decane	0.84	+6.58
PMMA	1.22	+1.10
d-PMMA	1.22	+7.22

Table 7.2: Scattering length densities of some solvents and polymers are given, along with values for the perdeuterated forms.

The differences between light and neutron scattering can be accounted for in the expression of the particle scattering amplitude, B. The particle scattering amplitude of coherent neutron scattering from an isotropic particle can be written as

$$B_i(Q) = 4\pi \int_0^\infty r^2[\beta_i(r) - \beta_m]\frac{\sin Qr}{Qr}\, dr \tag{7.4}$$

where the scattering profile, $\beta_i(r)$, of particle i, depends only on the radial distance r from the centre of the particle and β_m is the scattering length density of the dispersion medium. Equation 7.4 is analogous to the expression given for light scattering in Equation 2.11.

For a suspension of equal-sized spheres, the average scattered intensity is only a function of Q and again can be written in terms of a form factor and a structure factor i.e.

$$I(Q) = N \cdot P(Q)S(Q) \tag{7.5}$$

where $P(Q)$ and $S(Q)$ are as defined previously in Equations 2.13 and 2.16. $P(Q)$ can be measured by measuring $I(Q)$ for a dilute suspension for which $S(Q) = 1$. We can then obtain the structure factor, $S(Q)$, of a dispersion by measuring $I(Q)$ and dividing by $P(Q)$.

The PMMA-PHSA colloids used in this work may be approximately described by a core-shell model, *i.e.* a PMMA core and an outer shell containing the stabilizer PHSA and solvent, see Figure 7.2

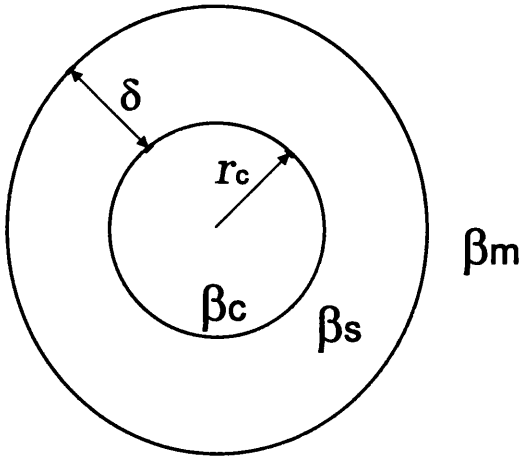

Figure 7.2: Simple core-shell model for a colloidal particle, here consisting of a polydisperse PMMA core with a shell of fixed width. r_c is the core radius, δ is the shell thickness and β_c, β_s and β_m are the coherent scattering length densities of the core, shell and medium respectively

For such a model then the scattering profile has the form

$$\beta_i(r) = \begin{cases} \beta_c & r \leq r_c \\ \beta_s & r_c < r \leq r_c + \delta \end{cases} \tag{7.6}$$

where the spherical core of radius r_c and scattering length density β_c is surrounded by a shell of thickness δ and scattering length density β_s.

The form factor for a homogenous sphere has been discussed earlier in Chapter 2, Equation 2.15;

$$P(Q) = 9\left[\frac{Qr\cos(Qr) - \sin(Qr)}{(Qr)^3}\right]^2$$

The form-factor of a core-shell particle can be derived geometrically from the form-factor of a sphere;

$$\begin{aligned} P(Q) &= (\beta_c - \beta_s)\frac{4\pi r_c^3}{3} \cdot \frac{3(\sin(Qr_c) - Qr\cos(Qr)}{(Qr)^3} \\ &+ \left[(\beta_s - \beta_m)\frac{4\pi(r_c+\delta)^3}{3}\right. \\ &\left. \cdot\frac{3\sin(Q(r_c+\delta)) - Q(r_c+\delta)\cos(Q(r_c+\delta))}{(Q(r_c+\delta))^3}\right] \end{aligned} \tag{7.7}$$

where r_c is the core radius, δ is the shell thickness, and β_c, β_s and β_m are the scattering length densities of the core, shell and solvent respectively. This gives the usual expression for the scattered intensity of a sphere if $\delta = 0$ or if $\beta_s = 0$.

To treat the size polydispersity the particle scattering amplitude can be averaged over a particle size distribution. Here we assume there is a distribution only of the core sizes, whilst the shell thickness is constant for all particles (fixed by the molecular geometry of the grafted stabilizing chains). A common choice for the distribution of sizes in polymer colloidal systems is the Schultz distribution [182], which is mathematically solvable and has a physically realistic skew towards large sizes. The normalized form of the Schultz distribution is given as

$$G(r_c) = \frac{r_c^Z}{\Gamma(Z+1)}\left(\frac{Z+1}{\bar{r}_c}\right)^{Z+1}\exp\left[-\frac{\bar{r}_c^2}{\bar{r}_c^2}(Z+1)\right] \tag{7.8}$$

where $\bar{r}_c$ is the mean core radius, and Z is related to the polydispersity, σ_c, of

the particle core radius distribution by the expression

$$\sigma_c^2 = \left(\frac{\bar{r_c^2}}{\bar{r}_c^2} - 1\right) = \frac{1}{Z+1} \tag{7.9}$$

The size-averaged scattering function for system of a core-shell spheres with a Schultz distribution of sizes can therefore be derived from equations 7.7 and 7.8 and is given in [183]. These expressions are used later in Section 7.4.2 to fit the measured scattering from a PMMA colloid as a function of the scattering length difference $\beta_c - \beta_m$.

7.2.6 Scattering from binary mixtures

In Chapter 2, Equation 2.12;

$$< I(Q) >= \sum_{i=1}^{N}\sum_{j=1}^{N} B_i(Q)B_j(Q) < \exp[i\mathbf{Q}\cdot(\mathbf{r}_i - \mathbf{r}_j)] >$$

was simplified by considering that all B_i were identical. For a mixture of two different species of particles, A and B, the scattering amplitudes are equal to B_A or B_B, and Equation 2.12 can be simplified to

$$\begin{aligned} < I(Q) > \;=\; & B_A^2 \sum_{i}^{N_A}\sum_{j}^{N_A} < \exp[i\mathbf{Q}\cdot(\mathbf{r}_i - \mathbf{r}_j)] > \\ & + B_B^2 \sum_{i}^{N_B}\sum_{j}^{N_B} < \exp[i\mathbf{Q}\cdot(\mathbf{r}_i - \mathbf{r}_j)] > \\ & + 2B_A B_B \sum_{i}^{N_A}\sum_{j}^{N_B} < \exp[i\mathbf{Q}\cdot(\mathbf{r}_i - \mathbf{r}_j)] > \end{aligned} \tag{7.10}$$

or

$$I(Q) = N_A B_A^2 S_{AA}(\mathbf{Q}) + N_B B_B^2 S_{BB}(\mathbf{Q}) + 2\sqrt{N_A N_B} B_A B_B S_{AB}(\mathbf{Q}) \qquad (7.11)$$

where N_A is the number of particles of species A, and S_{AB}, etc. are the *partial structure factors* that describe the average correlations between the centres of the species (*e.g.* S_{AA} describes the averaged correlations between the centres of A type particles, S_{AB} describes the average A-B correlations etc.),

$$S_{AB}(Q) = \frac{1}{\sqrt{N_A N_B}} \sum_i^{N_A} \sum_j^{N_B} < \exp[i\mathbf{Q} \cdot (\mathbf{r}_i - \mathbf{r}_j)] > \qquad (7.12)$$

To determine these structure factors experimentally, contrast variation techniques may be used. If the two components of a binary system have different average scattering densities, then by changing the isotropic composition of one element (most commonly the dispersion medium) it is possible to highlight the correlations between either one of the particle types (see Figure 7.3).

All three partial structure factors could therefore be deduced by using three different compositions. The required procedure would then be to determine each of the single particle form factors using a dilute suspension, then measure the scattering from the binary mixtures, making measurements at three different contrasts before solving the three intensity expressions as in Equation 7.11 to retrieve the three partial structure factors, as discussed below. Only a few such measurements have been made to-date [184, 185, 183] due to the experimental complexity in carrying out this procedure. In this work we have simplified Equation 7.10 by examining the scattering of mixtures where only one-component is scattering, thus removing the cross-terms. For example, considering Equation 7.10, if component B is matched to the scattering length density of the solvent, Equation 7.10

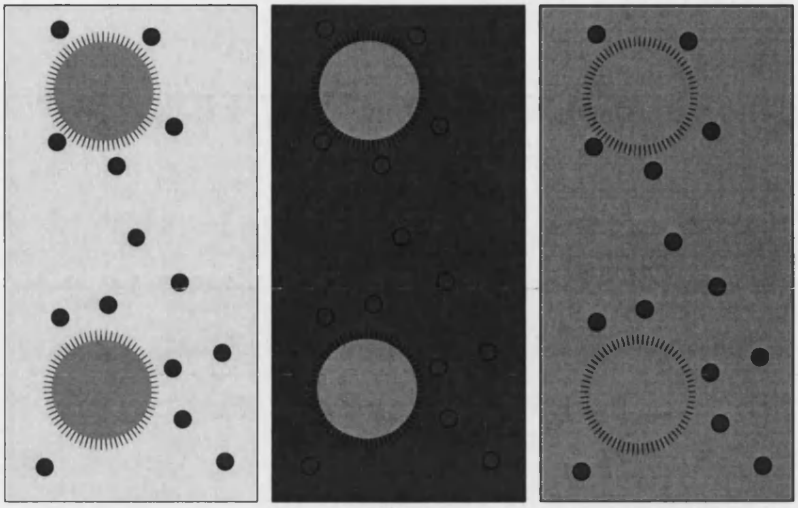

Figure 7.3: Contrast matching technique. Before modification *(a)*, all components in the binary mixture contribute to the scattering. In *(b)* the scattering length density is matched to the small particles and scattering from the large particles dominates, and in *(c)* the small particles dominate scattering

simplifies to

$$< I(Q) >= B_A^2 \sum_i^{N_A} \sum_j^{N_A} < \exp[i\mathbf{Q} \cdot (\mathbf{r}_i - \mathbf{r}_j)] >$$

or

$$I(Q) = N_A B_A^2 S_{AA}(\mathbf{Q}) \tag{7.13}$$

Colloid-colloid and microemulsion-microemulsion partial structure factors are measured in such a way in Section 7.4.

7.3 Experimental Setup and Considerations

7.3.1 Asymmetric System components

Microemulsion component

The small spheres used in the asymmetric system presented here are water-in-oil microemulsion droplets. A microemulsion is defined to be a transparent, homogeneous mixture of two immiscible fluids such as a hydrocarbon and water, stabilized by one or more surfactants, where a phase containing one liquid within the other is formed, usually having domains of one liquid with a characteristic size in the range of 5 nm-50 nm [186]. The AOT-water-oil system [See Figure 7.4, AOT is sodium di-2-ethylhexylsulfosuccinate] is a particularly useful model system since it forms a three-component microemulsion at room temperature and forms a single phase dispersion over a wide range of compositions and temperatures [187].

The single phase AOT-water-decane microemulsion used in this work consists of spherical water cores, each coated with a monolayer of AOT immersed in a continuous oil phase [189, 190, 191, 192]. The size of the droplets remains essentially constant for a fixed water-surfactant ratio [defined as W]. The hydrodynamic radius of such as system is well documented [193] and is given by the linear relationship $r_{\mu e}(/\text{nm}) = 0.70 + 0.136 \cdot W$, therefore for W=40.8 the expected radius is $r_{\mu e} \sim 6.2\,\text{nm}$ [187]. Figure 7.5 shows the temperature/volume-fraction phase diagram of the AOT-water-decane system with a W value of 40.8. Substitution of H_2O by D_2O merely shifts all the phase boundaries upwards by about 2 °C [194, 195]. The 2-phase region consists of two coexisting microemulsion phases, thought analogous to a gas-liquid phase transition [196].

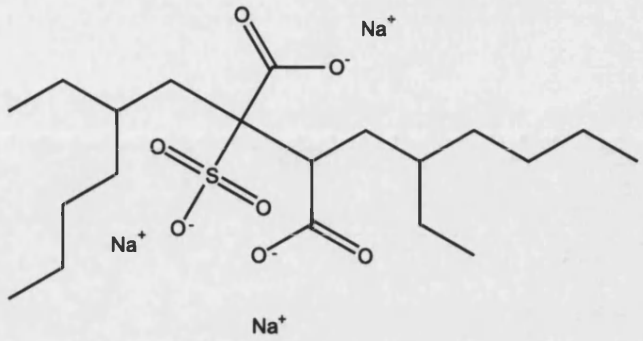

Figure 7.4: Sodium di-2-ethylhexylsulfosuccinate, also known as Aerosol OT or AOT is particularly well suited to forming water-in-oil microemulsions because of its molecular shape. The polar sulfate side surround the water droplet and the hydrocarbon chains extend into the oil [188]

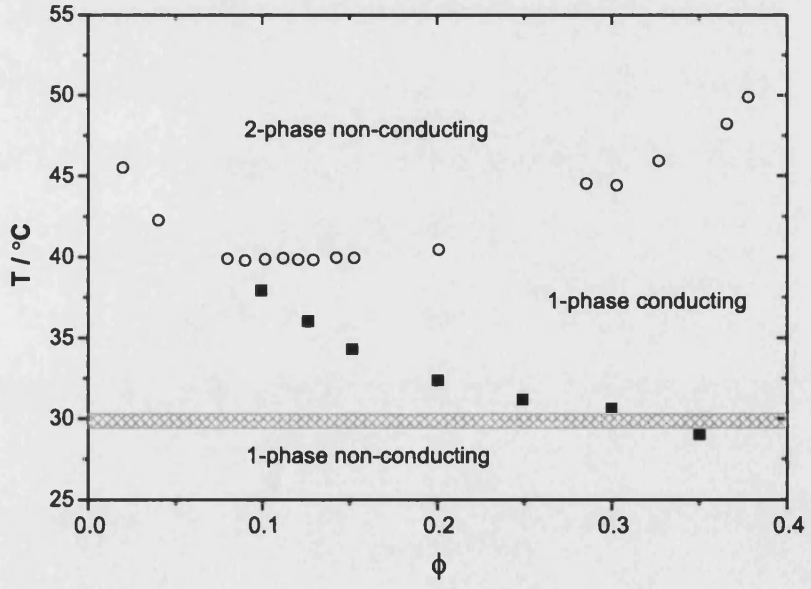

Figure 7.5: The phase diagram of the AOT-water-decane system, at W=40.8 and at atmospheric pressure, where ϕ is the volume fraction of the dispersed phase i.e. AOT+water [194, 195]. All the experiments in this study were undertaken in the within the region marked by the cross-hatched area.

Previous experiments have demonstrated that the interactions between the microemulsion droplets formed in an AOT/water/oil system can be successfully modelled via a hard-sphere potential modified by the addition of a square well attraction [197]. This attraction is thought to be due to the interpenetration of AOT molecules. Although the AOT-AOT interaction is not stronger than the AOT-oil interaction, it is thought that the shape and orientation of AOT molecules allows interaction without a decrease in entropy [197]. Thus one may expect that the interaction between an AOT microemulsion droplet and a PMMA-sphere should be approximately hard-sphere.

Colloidal component

The colloids, which are the large spheres in the asymmetric system, are PMMA colloids with a shell of PHSA based copolymer, the synthesis and characterization of which has been described in chapters 3 and 4. The colloidal dispersions RSJC6-RSJC9 were cleaned into *n*-decane. A stock solution of the colloid was used to prepare the samples detailed in Table 7.3.

Initial results from dynamic light scattering experiments, illustrated in Figure 7.6, showed that the measured hydrodynamic radius of the colloids stayed relatively constant, at varying microemulsion volume fractions and no phase separation was observed, indicating that the presence of microemulsion in the colloidal suspension did not induce any colloidal aggregation.

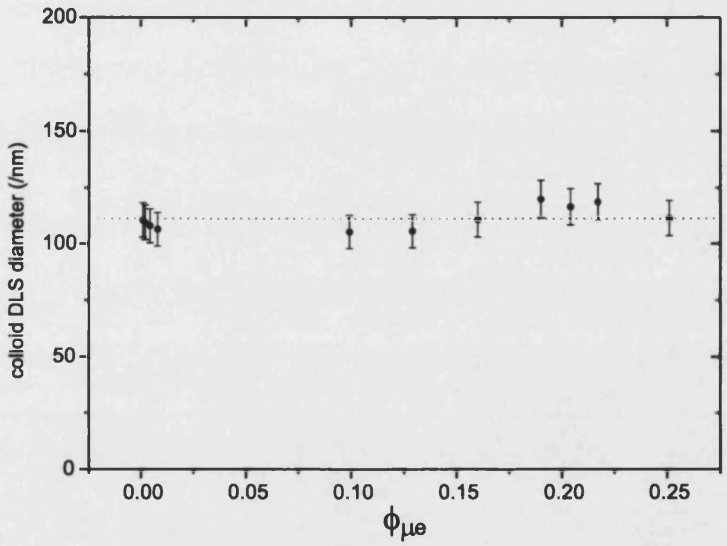

Figure 7.6: Hydrodynamic diameter of PMMA colloid RSJC7 in the presence of varying concentrations of AOT microemulsion, as obtained by dynamic light scattering experiments (taking into account the changing viscosity of the dispersion medium due to the increase in concentration of microemulsion[198]). The dotted line shows the hydrodynamic diameter obtained by DLS measurements on the colloid alone, the solid line indicates the best linear fit to the experimental data.

7.3.2 Sample Preparation

Each microemulsion stock consisted of sodium di-2-ethylhexylsufosuccinate [AOT], a mixture of H_2O and D_2O,and a mixture of *n*-decane and deuterated D_{22} *n*-decane. The *n*-decane (99+%, Aldrich Chemical Co.), D_2O (99.6%, Aldrich) and D_{22} decane were all used as supplied. The H_2O was deionized and filtered. The surfactant, AOT (98+%, Fluka) was purified before use as follows. One part AOT dissolved in three parts methanol was passed through a 0.2 μm filter and dried *in vacuo* at 60 $_o$C. Stock solutions were formulated by mixing the purified AOT with water and decane, such that the molar ratio of water to AOT equals W=40.8. The formulation was gently shaken until the AOT had visibly dissolved. Samples were prepared by adding amounts of the deuterated colloid RSJC8 (see Table 3.3) to produce various sample compositions as detailed in Table 7.3.

7.3.3 The D11 SANS instrument

The small-angle neutron experiments in this work were carried out on the D11 SANS instrument [180] at the Institute-Laue-Langevin [ILL] in Grenoble, France. The D11 is a long, pinhole geometry neutron small angle instrument designed for the study of large-scale structures such as polymers and colloids [180, 199, 200, 201] (see Figure 7.7 for a schematic view of the D11 instrument). The source of neutrons is a 58 MW high flux reactor with a liquid deuterium cold source. The instrument receives neutrons from this vertical cold source, which is situated approximately 100 m from the front of the D11 apparatus, and approximately 140 m from the sample. The detector is therefore in a very low background environment. The beam from the cold source, which is polychromatic, is monochromated by a helical slot velocity selector which selects neutrons of $\pm$10% about a mean

Code	ϕ_C	$\phi_{\mu e}$	$\xi_{\mu e}$	ξ_m
S1	0.080	0.000	-	-0.4881
S2	0.010	0.000	-	-0.4881
S3	0.000	0.249	6.4483	-0.4881
S4	0.083	0.053	-0.4820	-0.4881
S5	0.082	0.150	-0.4820	-0.4881
S6	0.080	0.250	-0.4820	-0.4881
S7	0.080	0.352	-0.4820	-0.4881
S8	0.078	0.452	-0.4820	-0.4881
S9	0.079	0.552	-0.4820	-0.4881
S10	0.079	0.000	-	0.4902
S11	0.008	0.295	6.4483	4.8456
S14	0.009	0.851	-0.4873	-0.4881
S15	0.008	0.325	6.4483	5.1574
S16	0.079	0.209	-0.4820	-0.4881
S17	0.081	0.174	-0.4820	-0.4881
S18	0.079	0.224	-0.4820	-0.4881
S19	0.079	0.105	-0.4820	-0.4881
S20	0.077	0.048	6.4483	0.5086
S21	0.080	0.025	-0.4820	-0.4881
S22	0.079	0.201	6.4483	0.5532
S23	0.079	0.000	-	0.7524
S24	0.080	0.000	-	0.9242
S25	0.081	0.010	-0.4820	-0.4881
S26	0.080	0.005	-0.4820	-0.4881
S27	0.000	0.050	6.4483	-0.4881
S28	0.000	0.147	6.4483	-0.4881
S29	0.000	0.200	-0.4820	-0.4881

Table 7.3: Details of samples prepared, ϕ_C is the volume fraction of colloid, $\phi_{\mu e}$ is the total volume fraction of microemulsion, $\xi_{\mu e}$ is the scattering length density of the microemulsion core and ξ_m is the scattering length density of the decane medium.

Code	ϕ_C	$\phi_{\mu e}$	$\xi_{\mu e}$	ξ_m
S30	0.080	0.000	-	1.0730
S31	0.084	0.005	6.4483	0.9125
S32	0.079	0.227	6.4483	0.9051
S33	0.081	0.275	-0.4820	-0.4881
S50	0.0807	0.0000	-	-0.4881
S51	0.0808	0.0022	-0.4853	-0.4881
S52	0.0812	0.0073	-0.4853	-0.4881
S53	0.0800	0.0125	-0.4853	-0.4881
S54	0.0800	0.0176	-0.4853	-0.4881
S55	0.0814	0.0023	6.4483	0.9355
S56	0.0792	0.0076	6.4483	0.9126
S57	0.0784	0.0123	6.4483	0.9094
S58	0.0789	0.0178	6.4483	0.9057
S59	0.0000	0.4085	6.4483	-0.4881
S60	0.0206	0.0000	-	-0.4881
S61	0.1593	0.0000	-	-0.4881
S62	0.1589	0.1483	-0.4845	-0.4881
S63	0.1578	0.1754	-0.4845	-0.4881
S64	0.1596	0.1929	-0.4845	-0.4881
S65	0.1614	0.2185	-0.4845	-0.4881
S67	0.0000	0.0990	6.4483	-0.4881
S68	0.0000	0.1503	6.4483	-0.4881
S69	0.0000	0.1975	6.4483	-0.4881
S70	0.0000	0.2468	6.4483	-0.4881
S71	0.0000	0.3018	6.4483	-0.4881
S72	0.0000	0.0300	6.4483	-0.4881

Table 7.3 continued: Details of samples prepared, ϕ_C is the volume fraction of colloid, $\phi_{\mu e}$ is the total volume fraction of microemulsion, $\xi_{\mu e}$ is the scattering length density of the microemulsion core and ξ_m is the scattering length density of the decane medium.

wavelength determined by the rotation speed of the drum. The neutrons are then collimated by a series of movable neutron guides. Guide sections are inserted or removed from the beam by computer control, to achieve the incident beam divergence required. The sample zone, situated 40m down-stream from the velocity selector, may be equipped with numerous sample environments such as a temperature controlled sample changer, cryostat, magnet, shearing cell, etc. to allow experiments to take place in a wide variety of environments, for example alternating magnetic or electric fields [202, 203] Neutrons scattered from the sample are detected on a 64 cm x 64 cm LETI BF3 multi-detector mounted on a computer controlled platform within the evacuated detector tube. The detector may be placed at any distance between 1.1 m and 35.7 m from the sample position giving an accessible Q range of $5x10^{-4}$Å^{-1} to 0.3Å^{-1}.

7.3.4 Collection of SANS Data

Measurements were taken at 2.5 m, 5.0 m, 8.0 m and 35.7 m on the D11 instrument. All experiments were carried out using an incident neutron beam wavelength of 0.8 nm. Wavelength divergence was approximately 10% (at full-width half-maximum). All samples were sealed into carefully cleaned, optical quality rectangular quartz cells with a path length of 1 mm, the cells were held in a thermostatically controlled sample holder at 25°C.

The experiments consist of taking a sequence of measurements, which are subsequently reduced one to the other. The term data reduction is here applied to those procedures which are involved in arriving at a set of scattering data which is free from instrumental artefacts, including detector efficiencies, background etc. using conventional procedures [204]. The term data analysis is used later and refers to the process of interpreting the data, *e.g.* fitting models to data etc.

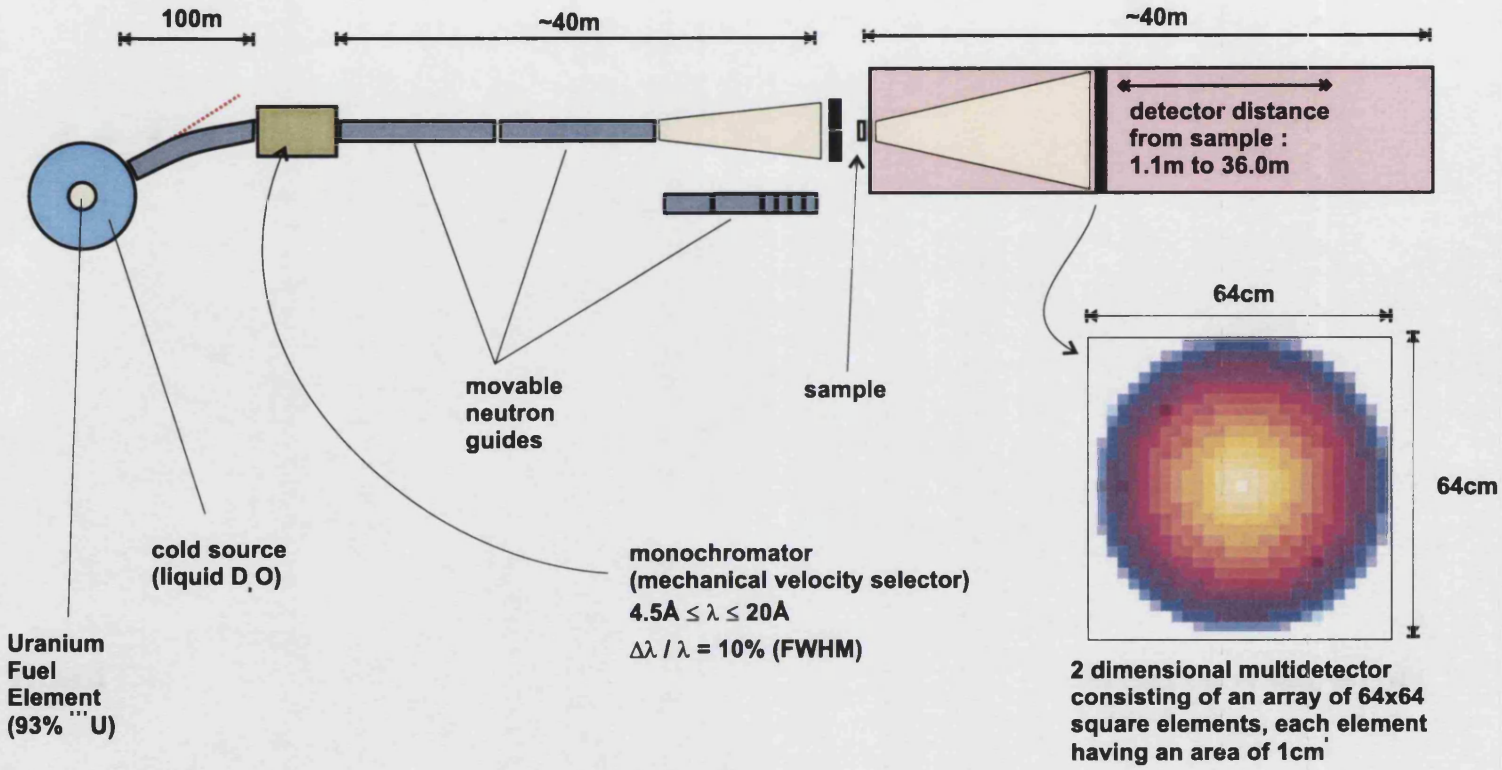

Figure 7.7: Schematic Illustration of the D11 SANS machine at the ILL, Grenoble.

As a first step the counts on the detector are correlated to the reaction flux, this is achieved by simultaneously recording the counts from a monitor, permanently placed in the reaction beam. The electronic background was measured by stopping the beam at the sample position. Transmission is estimated as the ratio of intensities of the beam transmitted through sample or cell with respect to that of the empty holder, in this case all samples were all held in a temperature controlled cell holder. The transmission measurements are made by attenuating the beam intensity and using the main detector with the beam stop removed. Simple summations over the central area of the detector are used to obtain the intensity. Each transmission measurement was carried out for a length of time sufficient to yield an integrated total neutron count of at least 100000. Transmission measurements are made for the empty holder, the empty quartz cell, a water sample, and for each sample. Once the transmission measurements have been made, the small angle scattering data may be gathered by removing the attenuation and introducing the beam-stop which masks the detector from the direct high intensity beam. Small angle scattering measurements were made on the empty quartz cell, on the water sample, and for each sample. Measurements can be made at varying detector distances and at various wavelengths, at each configuration scattering measurements for the empty quartz cells and the water sample must be taken. Four detector distances were used to provide measurements over a range of Q values, 2.5 m, 5.0 m,8.0 m and 35.7 m. Masking is then performed on the data by marking as insignificant those cells which were obscured or partially obscured by the beam stop. Once masked the scattering data is briefly checked to ensure that the scattering is isotropic. All the scattering from samples detailed in this work was radially isotropic, hence the 2-dimensional map of data collected by the detector can be radially averaged to regroup the data as a function of Q.

7.3.5 Reduction of SANS data

Data reduction, the process of removing all instrumental artefacts from the scattering is described here. Two steps toward data reduction which should be taken before any structural data can be retrieved are normalization and removal of incoherent background. The measured intensity $I_m(\mathbf{Q})$ is related to the differential cross-section per unit sample volume $(\delta\sigma/\delta\Omega)_v$.

$$I_m(\mathbf{Q}) = I_0\Omega_0\epsilon AdT(\delta\sigma/\delta\Omega)_v \tag{7.14}$$

where I_0 is the incident neutron flux, Ω_0 is the solid angle of acceptance of the detector, ϵ is the detector efficiency, A is the area of the beam, d is the sample thickness and T is the transmission of the sample. To correct for detector efficiency it was necessary to measure the scattering from a substance that scatters entirely incoherently over the Q range of the experiment, water was used for this purpose in these experiments. The scattering from a standard incoherent scatterer such as water, can be described by

$$I_m(Q)_S = I_0\Omega_0\epsilon Ad_S T_S(\delta\sigma/\delta\Omega)_{i,S} \tag{7.15}$$

where the subscript S refers to the standard. For an incoherent scatterer, the scattered intensity is spread uniformly over 4π steradians.

The detector corrections are calculated using;

$$V_f = H_2O - C - \frac{T_{H_2O}}{T_{Qz}} \cdot (Qz - C) \tag{7.16}$$

where C is the electronic background, H_2O is the scattering from the water sample (i.e. includes scattering from the water plus the quartz cell), Qz is the scattering from the empty quartz cell, and T_{H_2O} and T_{Qz} are the transmissions of the water sample and the empty quartz cell respectively.

The sample holder scattering is then subtracted from the sample scattering;

$$S' = S - C - \frac{T_S}{T_{Qz}} \cdot (Qz - C) \tag{7.17}$$

where S is the scattering from the sample, and T_S is the transmission of the sample.

Normalization of the data is then performed against the water standard sample using [205];

$$S_f = \frac{S}{V_f} \cdot \frac{T_{H_2O}}{T_S} \cdot \frac{N_{H_2O}}{N_S} \cdot \frac{d\sigma_{H_2O}}{d\Omega} \tag{7.18}$$

These normalization procedures are performed using the standard ILL procedure via the computer program SPOLLY [180].

To summarize, collection and reduction of the data is performed as follows;

- Transmission measurements are performed on the empty holder,the empty quartz cell, a quartz cell containing water and all samples

- The scattering is measured from; an empty quartz cell, a cell containing water, and all samples at various detector distances.
- Those cells affected by the beam-stop from the data are removed from further analysis by masking
- The isotropic scattering data is radially averaged as a function of Q
- Any detector corrections required are calculated
- The sample holder scattering is subtracted from the scattering from each sample
- The sample scattering data is them normalized with the water standard to convert to an absolute scale and account for detector efficiencies

7.4 Results and Data Analysis

7.4.1 Contrast Match Determination

At zero scattering angle i.e. $Q = 0$, the particle form factor $P(Q)$, is unity and we can use this to determine the neutron scattering length of particles;

$$I(0) = A(\beta_p - \beta_m)^2 \tag{7.19}$$

where A is an constant and β_p and β_m are the scattering length density of the particle and the medium respectively.

SANS measurements were made on dilute ($\varphi \leq 0.08$) suspensions of the deuter-

ated spheres (d-RSJC8) at various scattering length densities, β_m between β_m=-0.4881 10^{-6}Å^{-2} and 1.073 10^{-6}Å^{-2}.

At low concentrations interactions can be neglected and plotting $\log[I(Q)]$ as a function of Q^2 using the Guinier method [114] one can write;

$$\log I(Q) = \log I(0) - Q^2 \frac{\bar{R}_g^2}{3} + ... \tag{7.20}$$

where R_g is the radius of gyration, and for a sphere of radius r, $\bar{R}_g^2 = {}^3/_5 r^2$. The Guinier plot is only valid over a limited Q range, where $Qr \ll 1$, but over this range the initial part of the plot is a straight line, allowing the extrapolation of the measured intensity to $Q = 0$.

By plotting the square root of the intensity at $Q = 0$, against the scattering length density of the medium, we obtain a straight line. The intersection of this line with the x-axis gives the mean colloid scattering length density. The results are plotted in Figure 7.8. The match point for the colloids is at approximately $\beta_{coll} = \beta_m \sim 0.951 \pm 0.013 10^{-6}$Å^{-2}.

7.4.2 Fitting colloid only form-factors

An understanding of the dependance of the polydisperse particle form factors on the medium contrast is the essential first step to determining the partial structure factors. For a single-component with a sufficiently low number density that interparticle interactions become negligible, the measured scattered intensity is simply proportional to the particle form factor $P(Q)$. This presents an experimental difficulty however, as at sufficiently low concentrations the scattering of

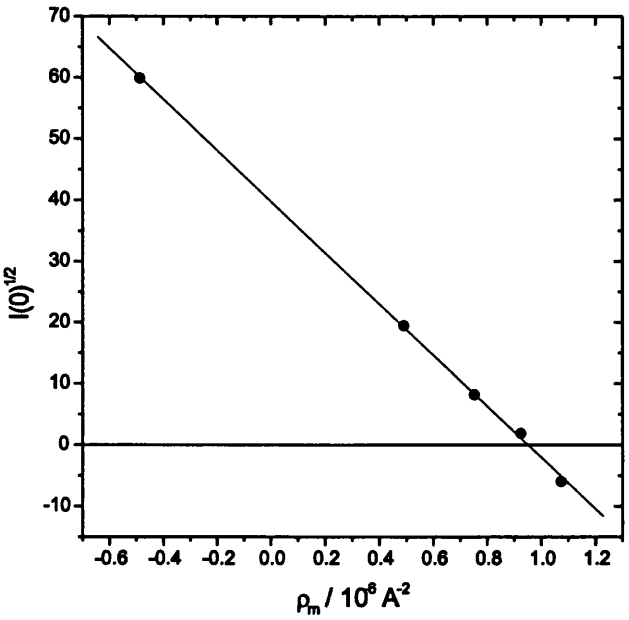

Figure 7.8: Graph showing the dependence of scattered intensity at Q=0 for ϕ_c=0.08 as the scattering length density of the dispersion medium (h/d-decane) is altered. The match point β_{coll} is at $0.951 \pm 0.013 \cdot 10^{-6} A^{-2}$

the colloidal suspensions is weak, particularly around the match point. To overcome this measurements were made on one very dilute sample (ϕ_c=0.01) a long way from the match point, and this sample was compared with a more concentrated sample (ϕ_c=0.08) under otherwise identical conditions. The experimental structure factor was then recovered.

One component samples were prepared containing only the PMMA colloid, at constant concentrations of ϕ_c=0.08, in a decane medium at varying medium scattering length densities and SANS measurements were taken. The corrected intensity was obtained by applying the standard corrections as detailed in section 7.3.5 and the measured structure factor was removed. This set of data was then fitted using one polydisperse core-shell form-factor model as described in section 7.2.5 with the core scattering length density, β_c, and the polydispersity, σ, fixed, and the core radius r_c, the shell thickness δ and the scattering length density of the shell, β_s, floated. The results are tabulated in Table 7.4 and the

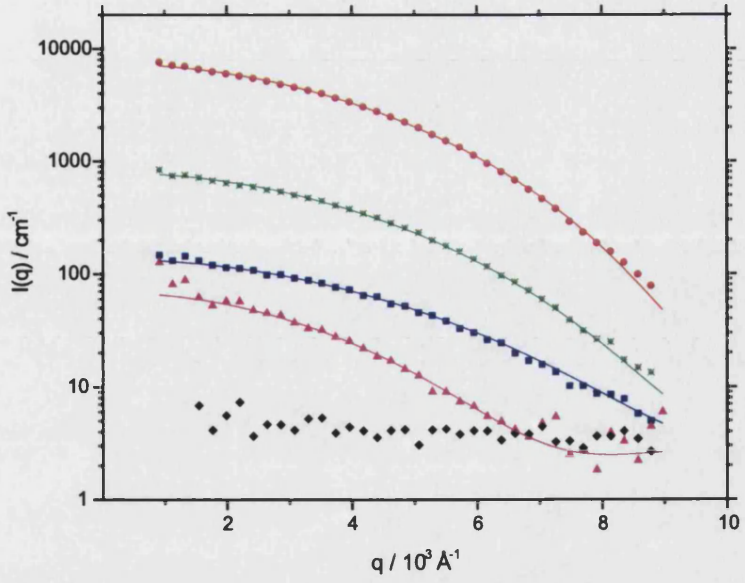

Figure 7.9: Graph showing the changing intensity of scattered from colloids as the scattering density of the dispersion medium is altered. The densities are as follows; *circle* β_m=-0.49; *cross* β_m=0.49;*square* β_m=0.75;*diamond* β_m=0.92;*triangle* β_m=1.07. The fits are obtained using a polydisperse core-shell form-factor, the parameters of which are tabulated in Table 7.4

data and fits are plotted in Figure 7.9.

Fits to the experimental form factors gave the mean core radii as 396±20 nmÅ with a shell thickness of 146.21 ±0.2 Å. The observation that the fitted values of β_s are not constant, but vary with the medium contrast, β_m, strongly supports the hypothesis that the shell contains solvated stabilizing chains. The relationship between the scattering length density of the shell and the scattering length density

Sample	r_c	σ	δ	β_s	β_c	β_m
S1	396.86	0.10	146.21	-0.1144	0.9991	-0.488
S10	396.86	0.10	146.21	0.5790	0.9991	0.490
S23	396.86	0.10	146.21	0.7708	0.9991	0.752
S30	396.86	0.10	146.21	0.9916	0.9991	1.073

Table 7.4: Details of polydisperse core-shell form-factor fits as plotted in Figure 7.9 where r_c is the radius of the core (/Å),σ is the polydispersity of the core, δ is the thickness of the shell (/Å), and $\beta_c, \beta_s, \beta_m$ are the scattering length density of the core, shell and medium respectively ($/10^{-6}$Å^{-2})

Sample	r_c(/Å)	σ	δ(/Å)	ϕ_{hs}	β_s	β_c
S50	397	0.1	106	0.10	-0.1144	0.9991
S61	397	0.1	106	0.22	-0.1144	0.9991

Table 7.5: Details of polydisperse hard-sphere structure factor fits. r_c is the core radius, σ is the polydispersity of the core, δ is the shell thickness, ϕ_{hs} is the hard-sphere volume fraction, β_s and β_c are the scattering length densities used for the shell, and core respectively.

of the medium is complex and suggests that there is partitioning of the deuterated solvent into the stabilizing layer.

7.4.3 Fitting of one-component colloidal structure factors

Once the colloid form-factor has been determined, for the one-component samples, retrieval of the colloidal structure factor is possible. Samples containing only colloid were prepared at varying concentrations and SANS measurements were performed. The corrected intensity was obtained by applying the standard corrections as detailed in section 7.3.5. The data was fitted using the theoretical calculations of the scattering from a system of polydisperse hard-spheres given by Vrij [206, 207] for the scattering functions of polydisperse hard-spheres within the Percus-Yevick [PY] approximation [208].

The results are tabulated in Table 7.5 and the data and fits are plotted in Figures 7.10 and 7.11. The PY model is a good fit for the colloid only mixtures, indicating that the colloidal samples show a structure which is well explained by the PY polydisperse hard-sphere model.

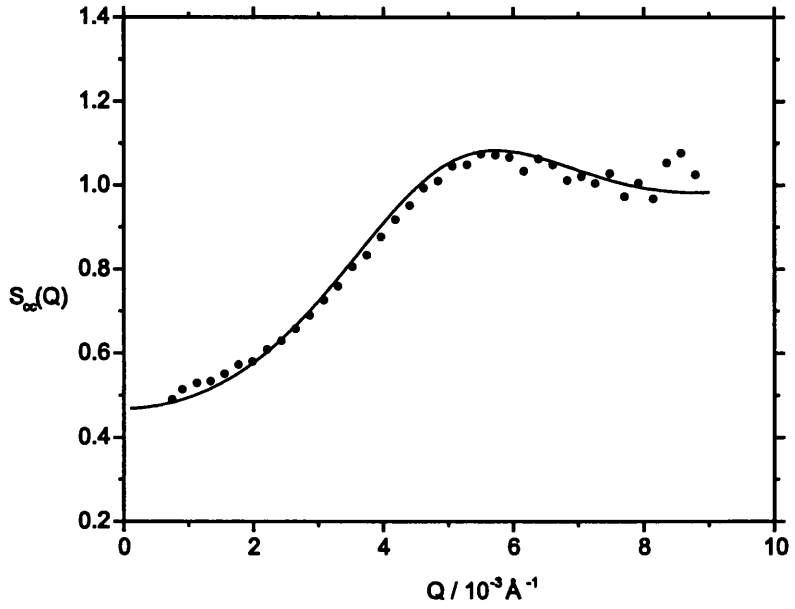

Figure 7.10: The structure factor for Sample S50 is plotted (circles) along with the polydisperse hard-sphere fit (line) for ϕ_{hs}=0.10 as described in Table 7.5. The fit has a maximum at $Q = 5.8 \cdot 10^{-3}$Å^{-1}

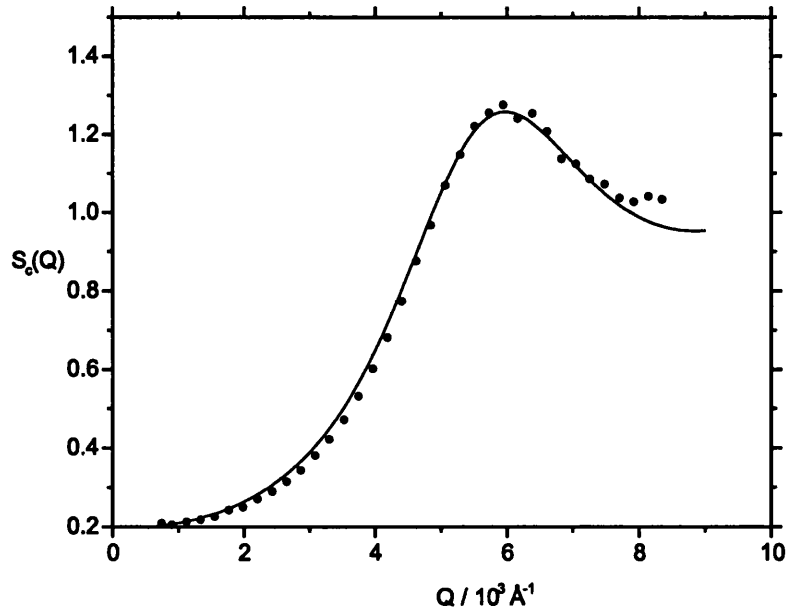

Figure 7.11: The structure factor for Sample S50 is plotted (circles) along with the polydisperse hard-sphere fit (line) for ϕ_{hs}=0.22 as described in Table 7.5. The fit has a maximum at $Q = 5.8 \cdot 10^{-3}$Å^{-1}

7.4.4 Examining colloid-colloid structure factors in binary mixtures

Once the form-factor model is established, the scattering from the binary mixtures can be interpreted. In this case the scattering from binary mixtures is considerably simplified by contrast matching. The microemulsion contains a mixture of D_20 and H_20, such that the scattering length density of the microemulsion droplets is almost identical to the scattering length density of the solvent, hence the microemulsion will not contribute to the scattering and the colloid-colloid correlations in the presence of the microemulsion can be determined from the scattering;

$$I(Q) = P(Q) \cdot S_{cc}(Q)$$

By dividing the measured intensity by the form-factor model, the colloid-colloid partial structure factor is thus revealed.

The structure factors for samples containing varying fractions of microemulsion were measured as detailed above. The sample details are plotted in Figures 7.12 and 7.13.

The scattering from the three samples with the lowest concentration of microemulsion is plotted in Figure 7.12. As is evident from the lack of any steep rise in the very low-Q scattering, and from visual inspection of the samples, the addition of microemulsion to the colloidal species does not cause flocculation. A number of additional points can be noted from Figure 7.12. Most noticeable is that addition of even a small quantity of microemulsion has a dramatic effect on

the colloidal interactions. The strong correlation peak at 5.8 x 10-3 $Å^{-1}$ which is observed in the absence of added microemulsion shifts to lower-Q with increasing microemulsion content. At $\phi_{\mu e} = 0.0125$ the position of the peak is reduced to $4.5 \cdot 10^{-3} Å^{-1}$. Also of note is the behaviour of the structure factor at very low Q. The low Q structure factor drops dramatically with the introduction of the microemulsion at very low concentrations until a point, after which the structure factor rises.

The scattering from the remainder of the samples is plotted in Figure 7.13. In these samples the opposite behaviour is observed, that is, with increasing microemulsion volume fraction, the scattering at $Q = 0$ increases and the peak in the scattering can be seen to shift to increasing values of Q.

Low Q Scattering

It is useful to examine the low Q scattering, to enable some simple interpretation of the partial structure factors. This may help to gain further understanding of the processes happening within the sample, so that a suitable model may be defined.

$S(Q)$ is proportional to the to the susceptibility, $\hat{\chi}(Q)$, which characterizes the density response of the system to an external perturbation of spatial frequency Q or wavelength $\lambda = 2\pi/Q$. As $Q \to \infty$ the wavelength will become much smaller than the particle spacing and there will be no local correlations in the density in response to such a perturbation, hence as $Q \to \infty$, $S(Q) \to 1$. At intermediate values of Q the structure factor is an oscillatory function, expressing the susceptibility to density fluctuations at the relevant scale, determined mainly by excluded volume effects. The $Q \to 0$ limit of the partial structure factor is of

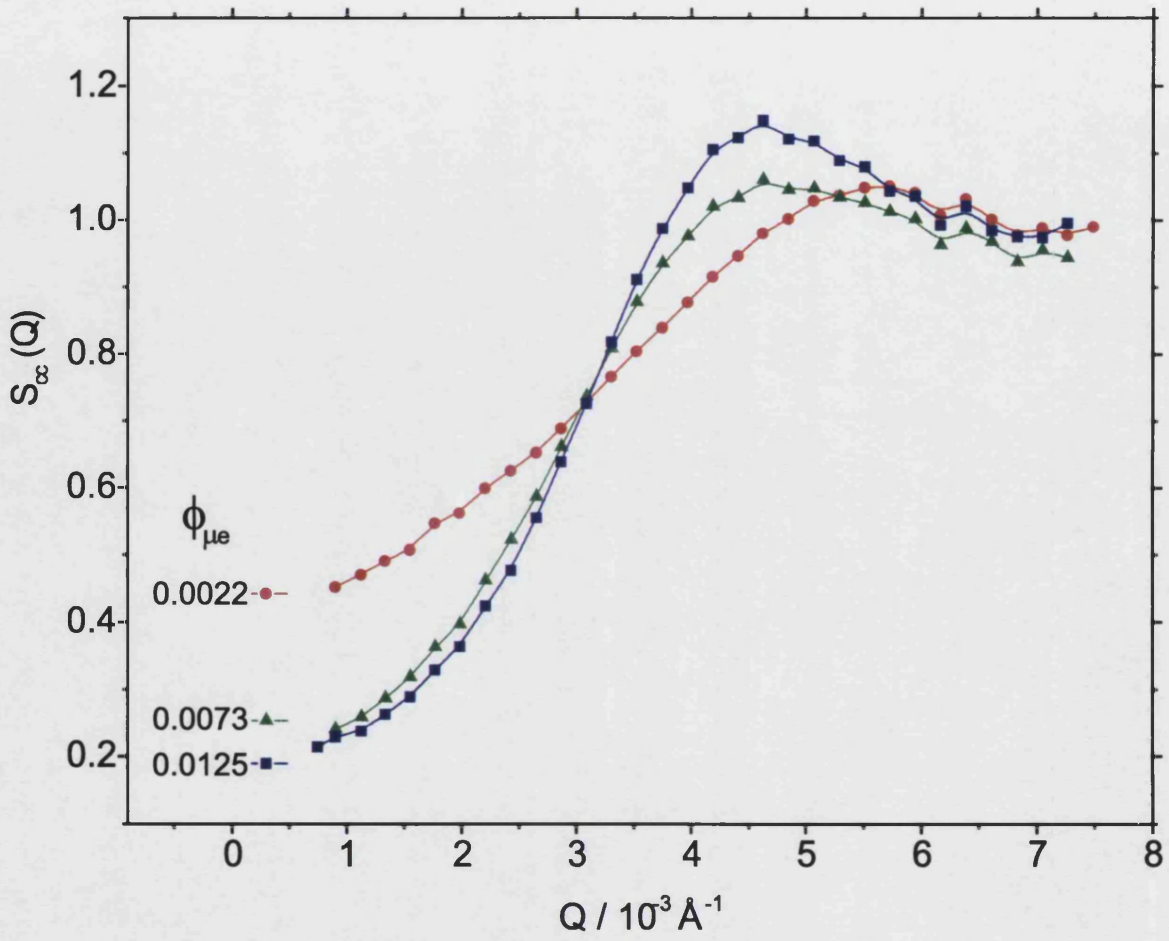

Figure 7.12: Colloid-colloid structure factors at very low concentrations of microemulsion. The partial colloid structure factors are plotted (the lines are simply guides for the eye). Of note is the decrease in scattering at $Q = 0$ as the concentration of microemulsion is increased and the movement of the peak in the structure factors to lower Q values.

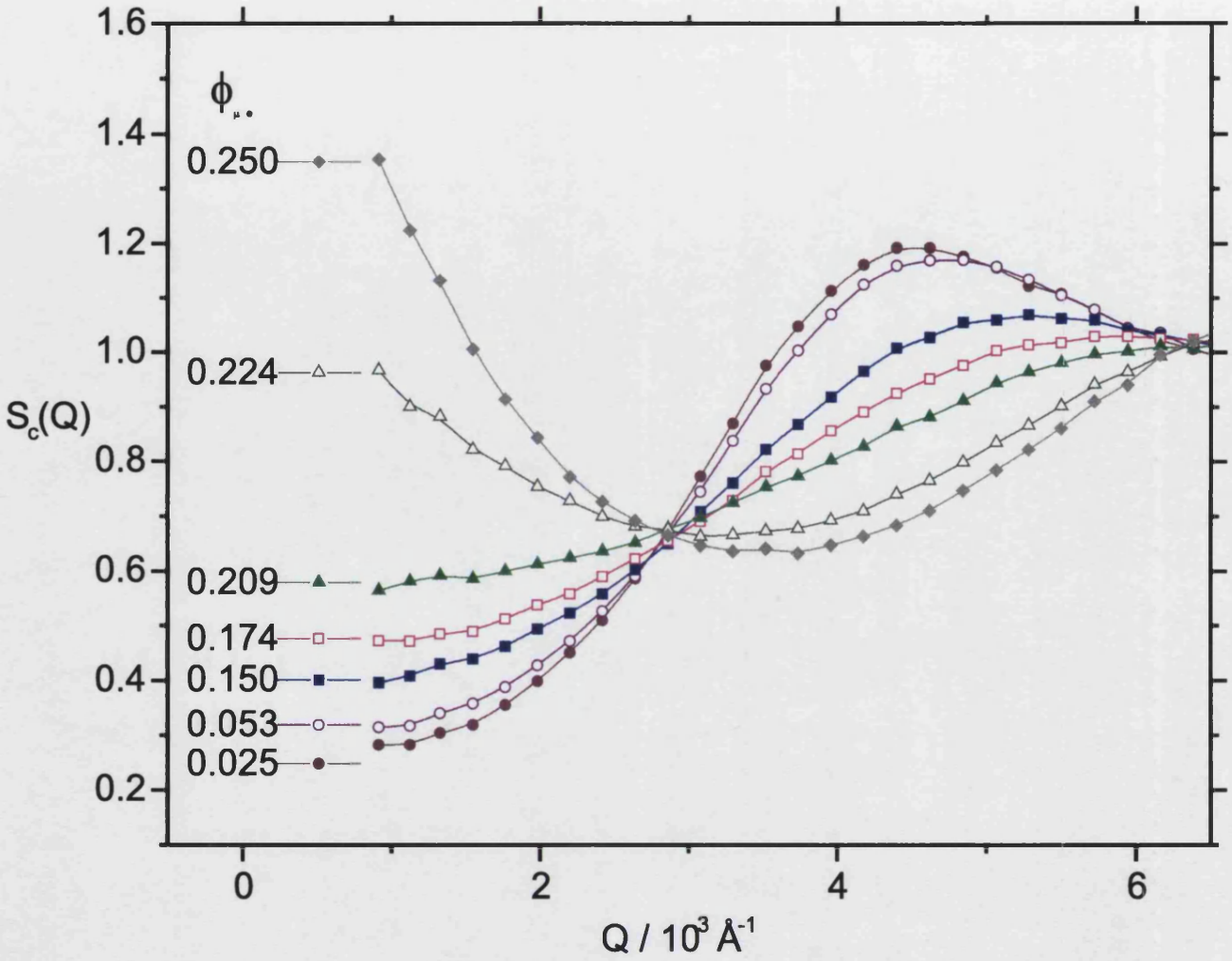

Figure 7.13: Colloid-colloid structure factors of microemulsion. The colloidal structure factor at varying volume fractions of microemulsion, ($\phi_{\mu e}$). Points to note are the increasing values of S_{cc} at $Q = 0$ with increasing microemulsion volume fraction, the movement of the structure factor maximum to higher Q values with increasing ϕ_{ue}, and the presence of two isobestic points

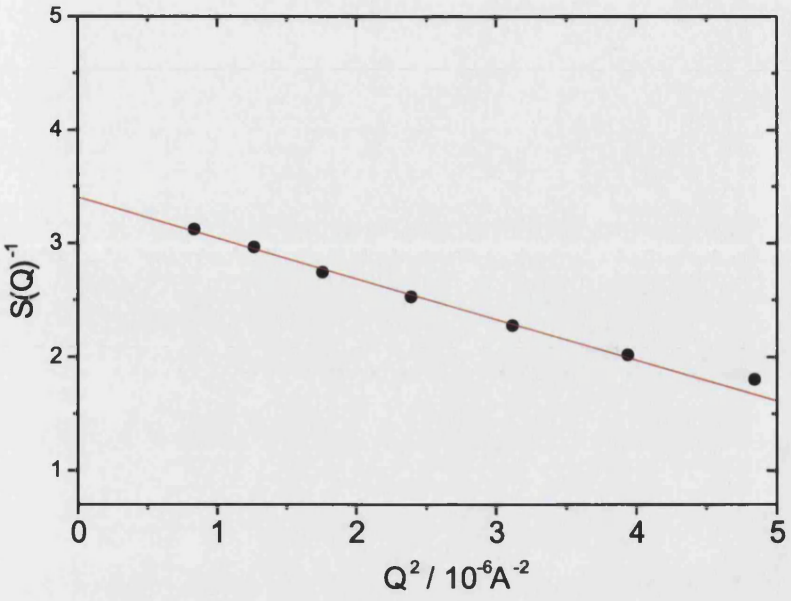

Figure 7.14: Results from fitting the measured structure factor at small Q values (In this case for Sample 26).

special interest, and yields the *isothermal compressibility.* This quantity has been extensively studied by Ottewill and coworkers [209]. Extrapolating the structure factor to $Q = 0$ will yield a measure of this compressibility of the system which in turn gives an indication of the sign of the mean interparticle potential. If the effective interaction becomes more repulsive the compressibility diminishes, more attractive and the compressibility increases. The extrapolation of the structure factor at low Q is shown in Figure 7.14.

Figure 7.15 plots the behaviour of $S_{cc}(0)$ at differing concentrations of microemulsion. A sharp drop in the structure factor at $Q = 0$ at low concentrations of microemulsion indicates the presence of a repulsive potential. This is followed, as the concentration of microemulsion increases, by a gradual rise in the structure factor at $Q = 0$, indicating the presence of an attractive force. At a microemulsion volume fraction of 0.2 the structure factor at $Q = 0$ rises sharply, indicating a strong attractive force.

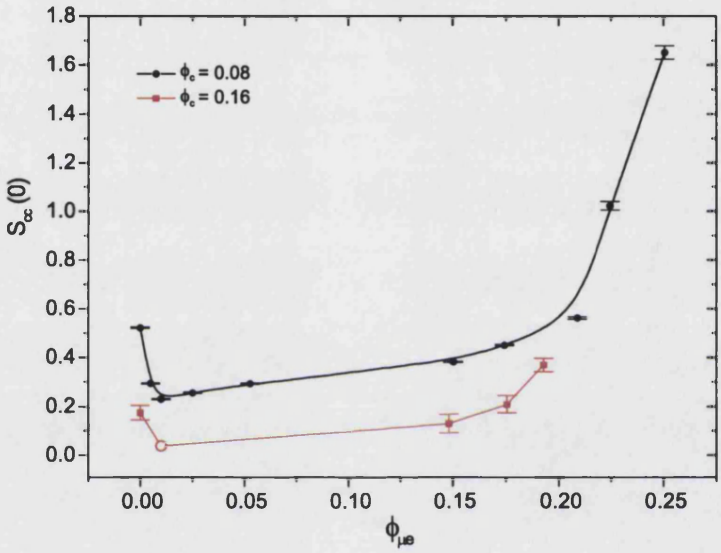

Figure 7.15: The behaviour of $S_{cc}(0)$ at differing concentrations of microemulsion. At low concentrations of microemulsion, $S_{cc}(0)$ decreases, indicating the presence of a repulsive potential. A gradual rise follows, indicating the presence of an attractive force after the initial repulsion. At a microemulsion volume fraction of 0.2 the structure factor at $Q = 0$ rises sharply, indicating a strong attractive force.

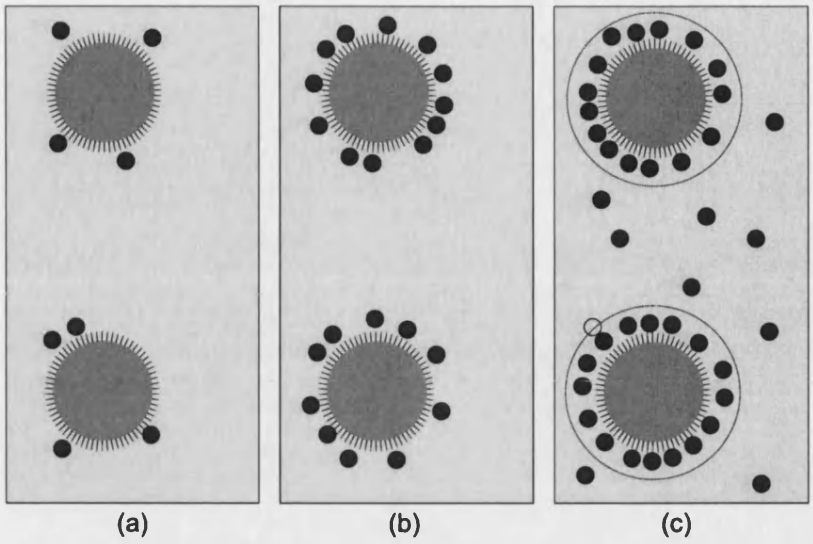

Figure 7.16: Stages of colloid-microemulsion interaction. *(a)* Initially there is an attractive force between the microemulsion and the surface of the colloid.*(b)* The colloid surface gradually becomes saturated with microemulsion droplets. *(c)* When colloid surfaces are saturated there is no longer an attractive force between colloid and microemulsion, but the microemulsion contributes to an attractive force between colloids via a depletion mechanism

One possible physical explanation for the changes in isothermal compressibility outlined above is illustrated in Figure 7.16.

At small concentrations of microemulsion, where the structure factor at $Q = 0$ decreases, the microemulsion is becoming adsorbed to the surface of the colloid, effectively therefore just increasing the excluded volume and thus decreasing the compressibility. At a certain concentration of microemulsion, the microemulsion droplets no longer become adsorbed to the surface of the colloid, and instead move freely within the solvent. This results in a depletion attraction between colloids in a similar way to the mechanism explaining colloid-polymer depletion mentioned at the beginning of this chapter. The sharp rise would then indicate a phase boundary induced by the depletion forces.

To test this theory the microemulsion-microemulsion partial structure factor was measured, by eliminating the colloid from scattering by matching the neutron

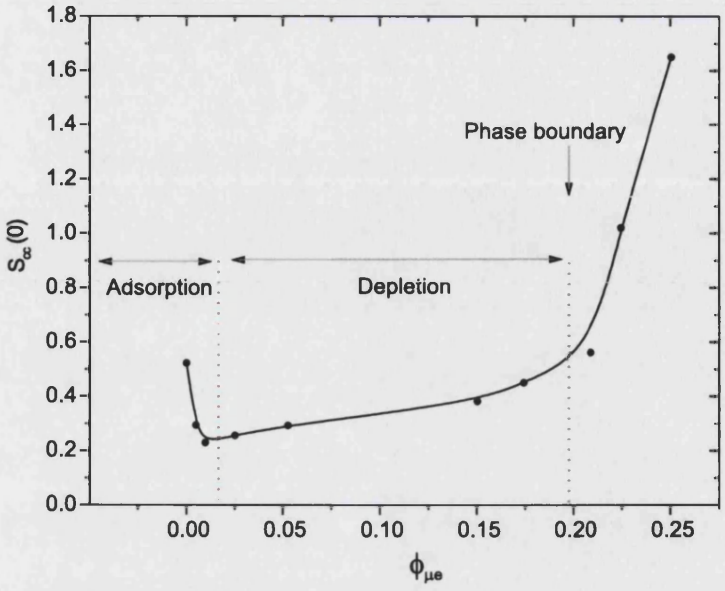

Figure 7.17: Explaining the changes in the scattering structure factor at $Q = 0$.

scattering length density of the solvent to match the colloid.

7.4.5 Fitting of one-component Microemulsion structure factors

Binary samples were prepared with the scattering length density of the decane solvent matched to the colloid match point determined above. The contrast between the AOT drops and the rest of the mixture was further increased by using D_2O. SANS measurements were taken and the corrected intensity was obtained by applying the standard corrections as detailed in section 7.3.5 and. The data is plotted in Figure 7.18.

Over the range of scattering studied, the scattering from the microemulsion drops

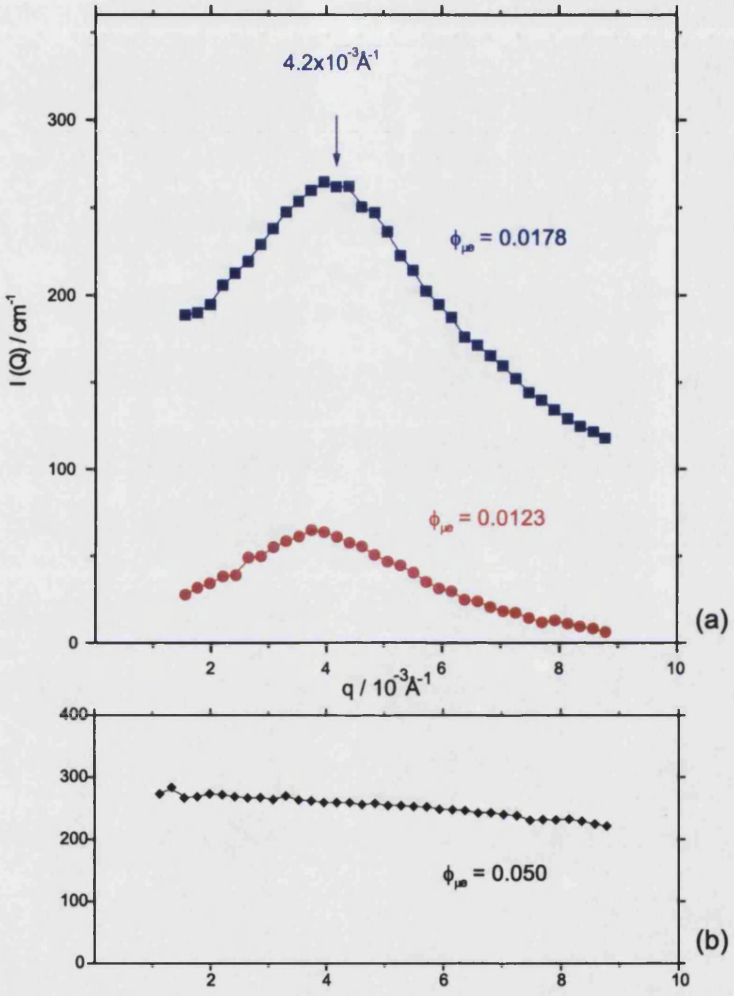

Figure 7.18: Graph showing the scattered intensity from AOT microemulsion droplets in a binary mixture of PMMA colloid and microemulsion. a) shows the scattering from samples S57 and S58 containing low concentrations of microemulsion in the presence of a fixed volume fraction of colloid $\phi_c = 0.08$. A peak is evident at $Q = 4.2 \cdot 10^{-3}\text{Å}^{-1}$, indicating formation of structure in the microemulsion on a scale comparable with the size of the colloid. b) Scattering from Sample 27 shows the relatively flat scattering typical of the scattering from all the samples of microemulsion alone.

in the absence of colloid (seen in Figure 7.18b) is almost constant, as expected . Yet when colloidal particles are present (seen in Figure 7.18a) the scattering $I(Q)$ contains a peak at $Q = 4.2 \cdot 10^{-3}\text{Å}^{-1}$, close to that seen in the colloid structure factor $S_{cc}(Q)$. This strongly suggests correlation of the microemulsion drops on a colloidal scale. A simple explanation for this is that the microemulsion drops are adsorbed onto the surface of the colloidal particles. These microemulsion-microemulsion scattering results can be seen to support the adsorption part of the adsorption/depletion theory suggested by the low Q colloid-colloid scattering. To further probe the theory outlined above interpretation of the entire structure factors is attempted, by modelling a possible colloid-colloid potential for the colloid-microemulsion system described above, and comparing the calculated scattering from the model system with the experimental results.

7.4.6 Modelling colloid-colloid structure factors in binary mixtures

In this section an effective colloid-colloid potential is postulated, based on the adsoprtion/depletion description of the binary system as detailed above. From this model pair potential the scattering is calculated using a random-phase approximation [RPA] and compared with the experimental results.

Relating potential to structure

The relationship between the interparticle potential and the sample structure is a complex one. In principle, given the entire structure factor, $S(Q)$, it is possible to retrieve the particle pair correlation function, $g(r)$. Unfortunately the necessary inversion process involves serious technical and numerical complications [78].

Here the aim is to simplify the relationship between potential and structure to enable further interpretation of scattering profiles. In this context, the most useful approaches all derive from the equations of Ornstein and Zernike [210]. Based on the concept that the total average force between two particles is made up of a direct force, due to the intermolecular potential and an indirect force, due to the presence of other particles, the Ornstein-Zernike [OZ] equations essentially define the direct correlation function, $c(r)$ in terms of the total correlation function $h(r) = g(r) - 1$. Using a formal density expansion of the potential of mean force in powers of the density [56], it is possible to describe $c(r)$ in terms of the intermolecular potential, the temperature density and total correlation function, $h(r)$, but the expression for $c(r)$ cannot be written down in closed form. However, by omitting unmanageable terms, an approximate expression for $c(r)$ can be obtained. This leads to a class of approximations with names such as the Hypernetted-Chain [HNC], the Mean-Spherical Approximation [MSA] and the Percus-Yevick [PY]. The Percus-Yevick approximation [208] is equivalent to assuming that

$$[h(r) - c(r)] < 1 \tag{7.21}$$

which gives

$$g(r) = \exp(-u(r)/kT[1 + h(r) - c(r)] \tag{7.22}$$

For hard sphere fluids the PY approximation turns out to be quite accurate and is solvable analytically. A common approximation used to treat non hard-sphere fluids is to relate the properties of the system to a hard-sphere reference system, with other parts of the potential treated as perturbations. One such approximation is known as the random-phase approximation [RPA] [211]. Using the RPA we find that the structure factor of the system of interest is related to the structure factor of a hard-sphere reference system by

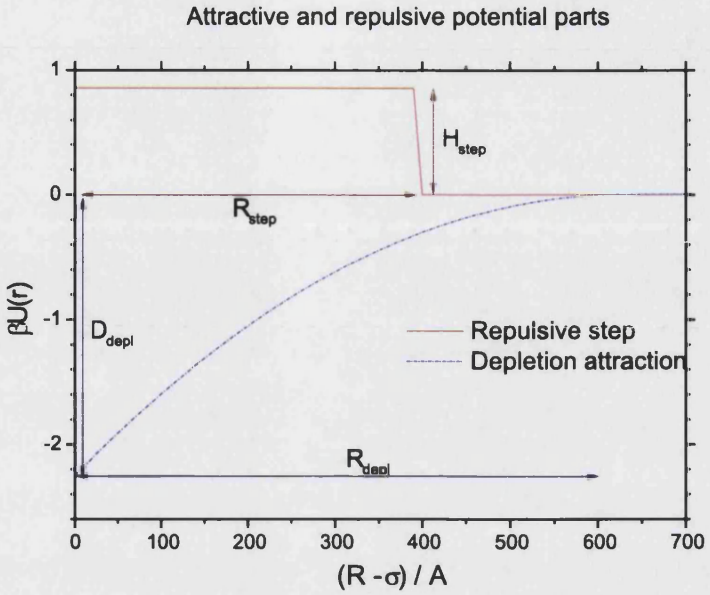

Figure 7.19: The perturbation potential used is composed of two parts, an attractive part based on the AO model for depletion, and a repulsive part to account for the adsorption, modelled simply as a repulsive step. There are 4 parameters, the depth, D_{depl}, and effective range, R_{depl}, of the depletion induced attraction, and the height, H_{step}, and effective range, R_{step}, of the step. The form of the resultant potential is shown in Figure 7.20.

$$S(Q) = \frac{S_o(Q)}{1 + \beta\rho S_o(Q)\hat{w}(Q)} \tag{7.23}$$

where $S_o(Q)$ is the hard-sphere structure factor and $\hat{w}(Q)$ is the Fourier transform of the perturbation potential.

To model the effective potential between the colloids in the presence of the microemulsions, a RPA approach is used, based on a hard-sphere potential, with the perturbation potential being composed of two distinct parts, an attractive part based on the AO model for depletion, and a repulsive part, modelled simply as a repulsive step to account for the adsorption as shown in Figure 7.19. The form of the resulting potential is illustrated in Figure 7.20.

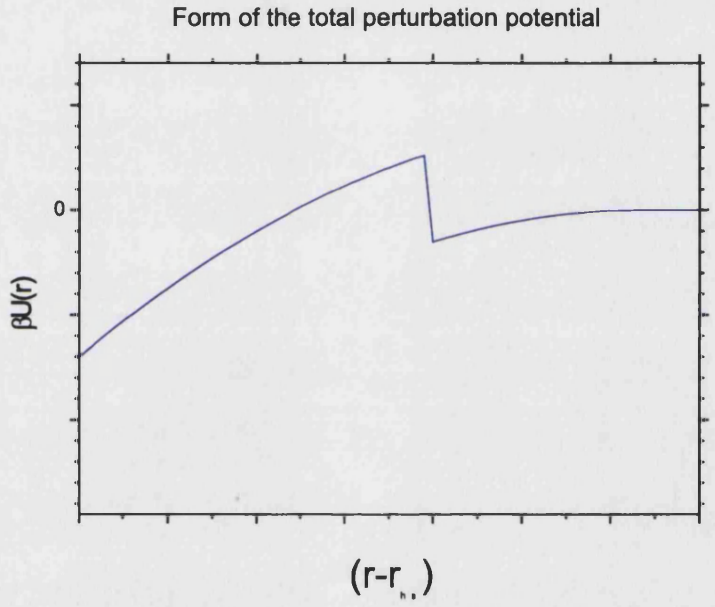

Figure 7.20: The form of the model potential used to calculate colloid-colloid structure factors for binary mixtures of colloid and microemulsion, using the RPA approximation.

Sample	$\phi_{\mu e}$	R_{step}	H_{step}	D_{depl}	R_{depl}
S21	0.025	397.5	0.832	0	0
S5	0.150	397.5	0.832	-0.94	0.80
S17	0.174	397.5	0.832	-1.50	0.69
S16	0.209	397.5	0.832	-2.25	0.61
S18	0.224	397.5	0.832	-4.72	0.50
S6	0.250	397.5	0.832	-6.49	0.47

Table 7.6: The effective model potential parameters for the AO-step potential. The potentials are plotted in Figure 7.21 and the scattering, calculated from the potentials using a random-phase approximation approach, is plotted in Figure 7.22

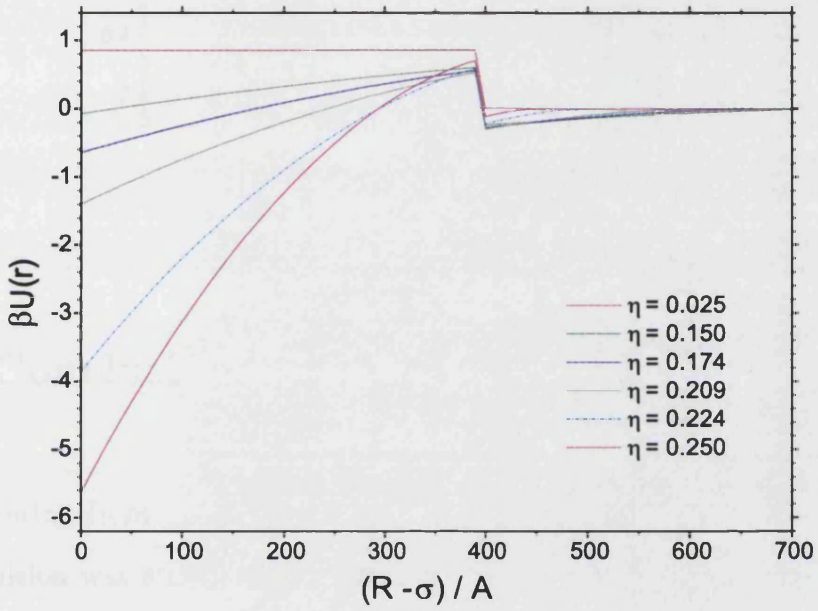

Figure 7.21:

The experimental colloid-colloid structure factors were fitted as follows; The form of the potential was assumed, as described in Figure 7.20. The Fourier transform of the perturbation potential was calculated, the required structure factor was calculated and the potential parameters were adjusted to give the best fit to the measured structure factors.

The results are shown in Table 7.6 and Figures 7.21 and 7.22.

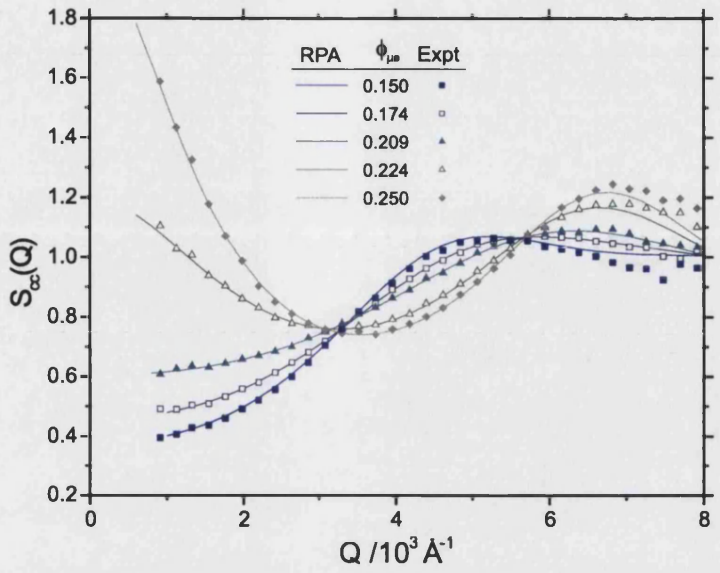

Figure 7.22:

7.5 Conclusions

The scattering from colloidal particles dispersed within a droplet water-in-oil microemulsion was studied. The colloidal particles consisted of a core of poly (methyl methacrylate) and a chemical grafted layer of poly (12-hydroxy stearic acid) with an overall radius of 503 Å and a polydispersity of 10%. The particles were suspended in a inverse microemulsion formed by AOT/(H_20,D_20)/n-decane. The relative composition of AOT and H_20/D_20 was fixed at the ratio $W = \frac{[H_20]+[D_20]}{[AOT]} = 40.8$. Under these conditions the microemulsion exists as a single inverse phase of small (radius$\sim$ 88 Å) water-in-oil droplets.

Both the colloid-colloid structure factor $S_{cc}(Q)$ and the microemulsion structure factor, $S_{mm}(Q)$, were measured. Data was collected under conditions of microemulsion match (so as to obtain $S_{cc}(Q)$) and at a coherent scattering length density of $0.92 \cdot 10^{-6}$Å^{-2} where the PMMA colloidal particles are matched (to

obtain $I_{mm}(Q)$).

Addition of even a small quantity of microemulsion has a dramatic effect on the colloidal interactions. The strong correlation peak at 5.8 x 10-3 $Å^{-1}$ which is observed in the absence of added microemulsion shifts to lower-Q with increasing microemulsion content. At $\phi_{\mu e} = 0.0125$ the position of the peak is reduced to $4.5 \cdot 10^{-3} Å^{-1}$.

A sharp drop in the structure factor at low Q at small quantities of microemulsion is also observed, indicating the presence of a repulsive potential. This is followed, as the concentration of microemulsion increases above $\phi_{\mu e} = 0.025$, by a gradual rise in the structure factor at $Q = 0$, indicating the presence of an attractive force. At a microemulsion volume fraction of 0.2 the structure factor at $Q = 0$ rises sharply, indicating a strong attractive force.

The reason for the peak shift and low Q scattering is most dramatically revealed by measurements when the colloidal particles are matched and only the microemulsion drops contribute to the measured intensity. Over the range of scattering vector studied the scattering from the microemulsion drops in the absence of colloid is almost constant. Yet when colloidal particles are present the scattering $I(Q)$ reveals a strong correlation peak at $Q = 4.2 \cdot 10^{-3} Å^{-1}$, close to that seen in the colloid structure factor $S_{cc}(Q)$. This strongly suggests that microemulsion drops are adsorbed onto the surface of the colloidal particles. But as is evident from the lack of any steep rise in the low-Q scattering of the colloidal species the adsorption does not result in bridging flocculation. The microemulsion decorated colloidal particles are stable.

The colloid structure factor $S_{cc}(Q)$ measured for $\phi_{\mu e} = 0.025$ to $\phi_{\mu e} = 0.250$ can be described by a potential hard-sphere model which is modified to include an

Asakura-Oosawa depletion attraction and a simple repulsive step. The scattering expected from particles having this potential was calculated, using a random-phase approximation approach to model the additional attractive and repulsive parts as perturbations to the original hard-sphere calculations. The calculated scattering is a good fit to the experimental data over $Q > 6 \cdot 10^{-3}$ Å^{-1} and demonstrates the shift of the correlation peak as well as the gradual rise in the structure factor at $Q = 0$.

References

[1] J. K. G. Dhont. *An Introduction to Dynamics of Colloids.* Elsevier, Amsterdam, (1996).

[2] B. J. Ford. Brownian movement in Clarkia pollen: A reprise of the first observations. *The Microscope*, **40**(4),235–241, (1992).

[3] A. Einstein. Zur elektrodynamik bewegter Korper. *Annal of Physics (Leipzig)*, **17**,891, (1905).

[4] A. Einstein. Zur Theorie der Brownschen Bewegung. *Annal of Physics (Leipzig)*, **19**,371, (1906).

[5] M. P. Langevin. *Comptes Rendus des Sciences de l'academie*, **146**,530, (1908).

[6] L. Onsager. Theories of concentrated electrolytes. *Chemistry Review*, **13**,73–89, (1933).

[7] D. H. Everett. *IUPAC Manual of Symbols and Terminology for Physiochemical Quantities and Units. (Appendix 2, Part 1).* Butterworth and Company, London, (1972).

[8] P. N. Segre, S. P. Meeker, P. N. Pusey, and W. C. K. Poon. viscosity

and structural relaxation in suspensions of hard-sphere colloids. *Physical Review Letters*, **75**(5),958–961, (1995).

[9] P. N. Pusey and R. J. A. Tough. Particle Interactions. In R. Pecora, editor, *Dynamic Light Scattering. Applications of Photon Correlation Spectroscopy*, chapter 4, pages 85–180. Plenum Press, New York, (1985).

[10] P. N. Pusey. Colloidal Suspensions. In *Liquids, Freezing and Glass Transition*, chapter 10, pages 765–942. Elsevier Science, Amsterdam, (1989).

[11] W. C. K. Poon, P. N. Pusey, and H. Lekkerkerker. Colloids in suspense. *Physics World*, pages 27–32, (1996).

[12] Y. S. Lipatov. *Colloid Chemistry of Polymers.* Elsevier Science, Amsterdam, (1988).

[13] R. J. Hunter. *Foundations of Colloid Science.* Clarendon Press, Oxford, (1986).

[14] R. A. Prior, W. R. Hinson, O. W. Smith, and D. R. Bassett. Statistical studies of branched ester latex and paint properties. *Progress in Organic Coatings*, **29**,209–224, (1996).

[15] T. Fujitani. Stability of pigment and resin dispersions in waterborne paint. *Progress in Organic Coatings*, **29**,97–105, (1996).

[16] H. Douglas Goff. Colloidal Aspects of Ice Cream: A review. *International Dairy Journal*, **7**,363–373, (1997).

[17] H. de Jonge, O. H. Jacobsen, L. W. de Jonge, and P. Moldrup. Colloid-facilitated transport of pesticide in undisturbed soil columns. *Physical Chemistry of Earth*, **23**(2),187–191, (1998).

[18] T. Cosgrove. The use of block copolymer stabilizers for controlling dispersion stability. *International Journal of Cosmetic Science*, **19**(4),157–166, (1997).

[19] M. Colic and D. W. Fuerstenau. The influence of surfactant impurities on colloid stability and dispersion of powders in aqueous suspensions. *Powder Technology*, **97**,129–138, (1998).

[20] W. B. Hardy. *Proceedings of the Royal Society of London A*, **66**,110, (1900).

[21] J. N. Israelachvili. *Intermolecular and Surface Forces.* Academic Press, London, (1985).

[22] E. J. W. Verwey and J. T. C. Overbeek. *Theory of Stability of Lyophobic Colloids.* Elsevier, Amsterdam, (1948).

[23] J. P. Hansen and I. R. McDonald. *Theory of Simple Liquids.* Academic Press, London, (1986).

[24] E. M. Lifschitz. *Soviet Physics JETP*, **2**,873, (1956).

[25] N. V. Churaev. The DVLO theory in Russian colloid science. *Advances in Colloid and Interface Science*, **83**,19–32, (1999).

[26] R. H. Ottewil and R. Buscall. *Colloid Science: Specialist Report No.2.* Royal Society of Chemistry, London, (1975).

[27] J. N. Israelachvilli. *Intermolecular and Surface Forces.* Academic Press, London, (1985).

[28] G. Toikka and R. A. Hayes. Direct measurementof Colloidal forces between mica and silica in aqueous electrolyte. *Journal of Colloid and Interface Science*, **191**,102–109, (1997).

[29] R. H. Ottewill. Colloid stability and instability: Order disorder. *Langmuir*, **5**,4–9, (1989).

[30] W. A. Ducker, T. J. Senden, and R. M. Pashley. Direct measurement of colloidal forces using an atomic force microscope. *Nature*, **353**,239–241, (1991).

[31] H. J. Butt. Measuring electrostatic, van der Waals and hydration forces in electrolyte-solutions with an atomic force microscope. *Biophysical Journal*, **60**(6),1438:1444, (1991).

[32] W. A. Ducker, T. J. Senden, and R. M. Pashley. Measurement of forces in liquids using a force microscope. *Langmuir*, **8**(7),1831–1836, (1992).

[33] D. H. Napper. Polymeric Stabilization. In J. W. Goodwin, editor, *Colloidal Dispersions*, chapter 5, pages 99–128. The Royal Society of Chemistry, London, (1982).

[34] D. H. Napper. *Polymeric Stabilization of Colloidal Particles.* Academic, London, (1983).

[35] A. Vrij. Polymers at interfaces and the interactions in colloidal dispersions. *Pure and Applied Chemistry*, **48**,471–483, (1976).

[36] M. D. Croucher and M. L. Hair. In R. M. Fitch, editor, *Polymer Colloids II.* Plenum Press, New York, (1980).

[37] S. T. Milner. Polymer Brushes. *Science*, **251**,905–914, (1991).

[38] M. G. Saphiannikova, V. A. Pryamitsyn, and T. Cosgrove. Self-consistent Brownian dynamics simulation of polymer brushes under shear. *Macromolecules*, **31**,6662–6668, (1998).

[39] D. G. Grier. Optical tweezers in colloid and interface science. *Current Opinions in Colloid and Interface Science*, **2**,264–270, (1997).

[40] C. Mio and D. W. M. Marr. Optical trapping for the manipulation of colloidal particles. *Advanced Materials*, **12**(12),917–920, (2000).

[41] J. W. Goodwin, J. Hearn, C. C. Ho, and R. H. Ottewill. Preparation and characterization of polymer latices in the absence of surface active groups. *British Polymer Journal*, **5**,347–362, (1973).

[42] R. K. Iler. *The Chemistry of Silica.* J.Wiley, (1979).

[43] W. Stober, A. Fink, and E. Bohn. Controlled growth of monodisperse silica spheres in the micron size range. *Journal of Colloid and Interface Science*, **26**(1),62–69, (1968).

[44] M. E. Thies-Weesie, A. P. Philipse, and H. N. W. Lerkerkerker. Sedimentation of bidisperse, uncharged coloidal sphere suspensions: Influence of viscosity and irregular surfaces. *Journal of Colloid and Interface Science*, pages 427–438, (1996).

[45] K. E. J. Barrett. *Dispersion Polymerization in Organic Media.* Wiley Interscience, London, (1975).

[46] L. Antl, J. W. Goodwin, R. D. Hill, R. H. Ottewill, S. M. Owens, S. Papworth, and J. A. Waters. The preparation of poly(methyl methacrylate) latices in non-aqueous media. *Colloids and Surfaces*, **17**,67–78, (1986).

[47] R. H. Ottewill and I. Livsey. The imbibition of carbon disulphide by poly(methyl methacrylate) latex particles. *Polymer*, **28**,109, (1987).

[48] P. Bartlett, P. N. Pusey, and R. H. Ottewill. Colloidal crystallization under time-averaged zero gravity. *Langmuir*, **7**(2),213–215, (1991).

[49] C. T. Lant, A. E. Smart, D. S. Cannell, W. V. Meyer, and M. P. Doherty. Physics of hard spheres experiment: A general-purpose light scattering instrument. *Applied Optics*, **36**(30),7501–7507, (1997).

[50] P. Ball. Crystal gazing. *New Scientist*, **November**,40–44, (1997).

[51] P. N. Pusey and W. van Megan. Phase behaviour of concentrated suspensions of nearly hard colloidal spheres. *Nature*, **320**,340–342, (1986).

[52] S. E. Paulin and B. J. Ackerson. Observation af a phase transition in the sedimentation velocity of hard spheres. *Physical Review Letters*, **64**,2663, (1990).

[53] S. M. Underwood, J. R. Taylor, and W. van Megen. Sterically stabilized colloidal particles as model hard spheres. *Langmuir*, **10**(10),3550–3554, (1994).

[54] B. Vincent, J. Edwards, S. Emmet, and R. Croot. Phase-separation in dispersions of weakly interacting particles in solutions of non-adsorbing polymer. *Colloids and Surfaces*, **31**,267–298, (1988).

[55] P. M. Chaikin and T. C. Lubensky. *Principles of Condensed Matter Physics.* Cambridge University Press, Cambridge, 1st edition, (1995).

[56] J. P. Hansen and I. R. McDonald. *Theory of Simple Liquids.* Academic, New York, (1976).

[57] P. Bartlett, P. A. Madden, and P. N. Pusey. self-organisation of colloids. (?).

[58] B. J. Alder and T. E. Wainwright. Phase transitions for a hard sphere system. *Journal of Chemical Physics*, **27**,1208–1209, (1957).

[59] W. G. Hoover and F. H. Ree. Melting transition and communal entropy for hard spheres. *Journal of Chemical Physics*, **49**,3609, (1968).

[60] A. Kose and S. Hachisu. Kirkwood-Alder Transition in Monodisperse Latexes: Nonaqueous Systems. *Journal of Colloid and Interface Science*, **46**(3),460–469, (1974).

[61] P. N. Pusey and W. van Megen. Phase Behaviour of concentrated suspensions of nearly hard colloidal spheres. *Nature*, **320**,340–342, (1986).

[62] P. Pusey and W. van Megan. Dynamic light scattering by non-ergodic media. *Physica A*, **157**,705–741, (1989).

[63] P. Pieranski. Colloidal Crystals. *Contempory Physics*, **24**(1),25–73, (1983).

[64] J. V. Sanders. Close-packed structures of spheres of two different sizes: I. Observation on natural opal. *Philosophical Magazine A*, **42**(6),705–720, (1980).

[65] M. S. Elliot, B. T. F. Bristol, and W. C. K. Poon. Direct measurement of stacking disorder in hard-sphere colloidal crystals. *Physica A*, **235**,216–223, (1997).

[66] N. A. M. Verhaegh, J. S. van Duijneveldt, A. van Blaaderen, and H. N. W. Lekkerkerker. Direct observation of stacking disorder in a colloidal crystal. *Journal of Chemical Physics*, **102**(3),1416, (1995).

[67] W. G. T. Kranendonk and D. Frenkel. Computer simulation of solid-liquid coexistence in binary hard sphere mixtures. *Molecular Physics*, **72**(3),679–697, (1991).

[68] T. Biben, J. P. Hansen, and J. L. Barrat. Density profiles of concentrated colloidal suspensions in sedimentation equilibrium. *Journal of Chemical Physics*, **98**(9),7330–7344, (1993).

[69] X. C. Zeng and D. W. Oxtoby. Density functional theory for freezing of a binary hard sphere liquid. *Journal of Chemical Physics*, **93**,4357–4363, (1990).

[70] P. Bartlett and W. van Megan. Physics of Hard-Sphere Colloidal Suspensions. In A. Mehta, editor, *Granular Matter: An Interdisciplinary Approach*, chapter 7, pages 195–257. Springer-Verlag, New York, (1994).

[71] P. N. Pusey, W. C. K. Poon, S. M. Ilett, and P. Bartlett. Phase behaviour and structure of colloidal suspensions. *Journal of Physics: Condensed Matter*, **6**,A29–A36, (1994).

[72] P. Bartlett, R. H. Ottewill, and P. N. Pusey. Superlattice formation in binary mixtures of hard-sphere colloids. *Physical Review Letters*, **68**(25),3801–3804, (1992).

[73] M. Kerker. *The Scattering of Light and Other Electromagnetic Radiation.* Academic Press, London, (1969).

[74] B. Chu. *Laser Light Scattering.* Academic, New York, (1974).

[75] P. N. Pusey and J. M. Vaughan. Light Scattering and Intensity Fluctuation Spectroscopy. In *Dielectric and Related Molecular Processes*, chapter 2, pages 48–105. (1975).

[76] I. L. Fabelinsky. *Molecular Scattering of Light.* Plenum, New York, (1967).

[77] B. Berne and R. Pecora. *Dynamic Light Scattering.* Wiley and Sons, New York, (1976).

[78] C. J. Pings. Structure of Simple Fluids By X-Ray Diffraction. In H. N. V. Temperly, J. S. Rowlinson, and G. S. Rushbrooke, editors, *Physics of Simple Fluids*, chapter 10, pages 387–445. North-Holland, Amsterdam, (1968).

[79] L. Brillouin. Uber die fortpflanzung des lichts in dispergierenden medien. *Comptes Rendus des Sciences de l'academie*, **44**,203, (1914).

[80] H. Z. Cummins, N. Knable, and Y. Yeh. Observation of diffusion broadening of Rayleigh scattered light. *Physical Review Letters*, **12**,150, (1964).

[81] A. J. F. Siegert. *MIT Radiation Laboratory*, **Report Number 465**, (1943).

[82] P. N. Pusey, H. M. Fijnaut, and A. Vrij. Mode amplitudes in dynamic light scattering by concentrated liquid suspensions of polydisperse hard spheres. *Journal of Chemical Physics*, **77**(9),4270–4281, (1982).

[83] F. Reif. *Fundamentals of Statistical and Thermal Physics.* McGraw-Hill, New York, (1965).

[84] B. Chu. *Laser Light Scattering: Basic Principles and Practice.* Academic Press, London, 2nd edition, (1991).

[85] S. W. Provencher. *Proceeding of the 5th International Conference On Photon Correlation Techniques in Fluid Mechanics.* Springer-Verlag, Berlin, (1983).

[86] D. E. Koppel. Analysis of macromolecular polydispersity in intensity correlation spectroscopy: The method of cumulants. *Journal of Chemical Physics*, **57**(11),4814–4820, (1972).

[87] G. Bryant and J. C. Thomas. Improved particle size distribution measurements using multiangle dynamic light scattering. *Langmuir*, **11**,2480–2485, (1995).

[88] P. N. Pusey and W. van Megan. Detection of small polydispersities by photon correlation spectroscopy. *Journal of Chemical Physics*, **80**(8),3513–3520, (1984).

[89] P. N. Pusey and W. van Megen. Detection of small polydispersities by photon correlation spectroscopy. *Journal of Chemical Physics*, **80**(8),3513–3520, (1984).

[90] G. V. Schultz. *Z.Phys.chem*, **43**,25, (1935).

[91] S. R. Aragn and R. Pecora. Theory of dynamic light scattering from polydisperse systems. *Journal of Chemical Physics*, **64**(6),2395–2404, (1976).

[92] W. D. Harkins. A general theory of the mechanism of emulsion polymerization. *Journal of the American Chemical Society*, **69**,1428–1444, (1947).

[93] D. C. Blackley. *Emulsion Polymerization.* John Wiley & Sons, New York, (1975).

[94] R. J. R. Cairns, R. H. Ottewill, D. W. J. Osmond, and I. Wagstaff. Studies on the preparation and properties of latices in nonpolar media. *Journal of Colloid and Interface Science*, **54**(1),45–51, (1976).

[95] S. A. Srinavasan, J. L. Hedrick, D. R. McKean, R. D. Miller, and J. G. Hilborn. Preparation of thermally labile PMMA particlesby combined non-aqueous dispersion polymerization and chain transfer. *Polymer*, **39**(6-7),1497–1501, (1998).

[96] J. Davoust, P. Devaux, and L. Leger. Fringe pattern photobleaching, A new method for the measurement of transport-coefficients of biological macromoleclues. *EMBO journal*, **1**,1233, (1982).

[97] P. N. Pusey and M. Drewel. Number Fluctuation Spectroscopy in Standing-Wave Fringes. *Optica Acta*, **30**(10),1483–1500, (1983).

[98] J. Ricka and T. Binkert. Direct measurement of a distinct correlation function by fluorescence cross-correlation. *Physical Review A*, **39**,2646–2652, (1989).

[99] T. Wilson. *Confocal Microscopy.* Academic Press, London, (1990).

[100] M. D. Croucher and M. A. Winnik. Preparation of Polymer Particles By Dispersion Polymerization. In F. Candau and R. H. Ottewill, editors, *Sci-*

entific Methods for the Study of Polymer Colloids and Their Applications, pages 35–72. Kluwer, Dordrecht, (1990).

[101] B. R. Morrison. B.Sc. Thesis, University of Sydney, (1987).

[102] C. Pathmamanoharan, C. Slob, and H. N. W. Lerkerkerker. Preparation of polymethylmethacrylate latices in non-polar media. *Colloid and Polymer Science*, **267**,448–450, (1989).

[103] B. Williamson, R. Lukas, M. A. Winnik, and M. D. Croucher. The preparation of micron-size polymer particles in nonpolar media. *Journal of Colloid and Interface Science*, **119**(2),559–564, (1987).

[104] J. W. Goodwin, R. H. Ottewill, J. Hearn, and C. C. Ho. Preparation and characterization of polymer latices in the absence of surface active groups. *British Polymer Journal*, **5**,347, (1973).

[105] D. W. J. Osmond and D. J. Walbridge. Steric stabilization of polymer-suspensions in hydrocarbon media by adsorbed layers of graft copolymers. *Journal of Polymer Science: Part C*, **30**,381–391, (1970).

[106] N. Hunt. *A Study of the Freezing of Binary Mixtures of Hard Colloidal Spheres.* Ph.D. Thesis, University of Bath, (1999).

[107] F. H. Kasten. Introduction to Fluorescent Probes: Properties, History and Applications. In W. T. Mason, editor, *Fluorescent and Luminescent Probes for Biological Activity*, pages 12–33. Academic Press, London, (1993).

[108] J. W. Kok and D. Hoekstra. Fluorescent Lipid Analogues. In W. T. Mason, editor, *Fluorescent and Luminescent Probes for Biological Activity*, pages 101–119. Academic Press, London, (1993).

[109] J. A. Monti, S. T. Christian, W. A. Shaw, and W. H. Finley. Synthesis and

properties of a fluorescent derivative of phosphatidylcholine. *Life Sciences*, **21**,345–356, (1977).

[110] D. H. Everett and J. F. Stageman. Preparation and stability of novel polymer colloids in a range of simple liquids. *Faraday Discussions of the Chemical Society*, **65**,230–241, (1978).

[111] B. J. Alder and T. E. Wainwright. Studies in molecular dynamics. Behaviour of a small number of elastic spheres. *Journal of Chemical Physics*, **33**,1439–1451, (1960).

[112] W.Gotze. Aspects of Structural Glass Transitions. In *Liquids, Freezing and Glass Transition: Les Houches*, chapter 5. North-Holland, Amsterdam, (1991).

[113] P. N. Pusey, W. van Megen, P. Bartlett, B. J. Ackerson, and Rarity. Structure of crystals of hard colloidal spheres. *Physical Review Letters*, **63**(25),2753–2756, (1989).

[114] A. Guinier. *X-Ray Diffraction.* Freeman, New York, (1963).

[115] A. J. C. Wilson. *Proceedings of the Royal Society of London A*, **180**,277, (1942).

[116] S. B. Hendricks and E. Teller. *Journal of Chemical Physics*, **10**,147–167, (1942).

[117] M. H. Blees and J. C. Leyte. The effective translational self-diffusion coefficient of small molecules in colloidal crystals of spherical particles. *Journal of Colloid and Interface Science*, **166**,118–127, (1994).

[118] A. H. Marcus and S. A. Rice. Phase transitions in a confined quasi-two-dimensional colloid suspension. *Physical Review E*, **55**(1),637–656, (1997).

[119] Y. He, B. Olivier, and B. J. Ackerson. Morphology of crystals made of hard spheres. *Langmuir*, **13**,1408–1412, (1997).

[120] A. Kose, M. Ozaki, K. Takano, Y. Kobayashi, and S. Hachisu. Direct observation of ordered latex suspension by metallurgical microscope. *Journal of Colloid and Interface Science*, **44**(2),330–338, (1973).

[121] N. Ise, T. Okubo, S. Dosho, and I. Sogami. Ordered Structure in Dilute Suspensions of Highly Charged Polymer Latices as Studied by Microscopy. 2. The Influence of Ionic Strength, Dielectric Constant, Temperature, and Viscosity. *Journal of the American Chemical Society*, **107**(26),8074–8077, (1985).

[122] N. Ise, T. Okubo, M. Sugimura, K. Ito, and H. J. Nolte. Ordered structure in dilute solutions of highly charged polymer lattices as studied by microscopy. I. Interparticle distance as a function of latex concentration. *Journal of Chemical Physics*, **78**(1),536–540, (1983).

[123] K. Ito, H. Nakamura, and N. Ise. Ordered structure in dilute suspensions of charged polymer lattices as observed in the vertical planes and in mixtures of heavy and light waters. *Journal of Chemical Physics*, **85**,6136–6142, (1986).

[124] S. Dosho, N. Ise, K. Ito, S. Iwai, H. Kitano, H. Matsuoka, H. Nakmura, H. Okumura, T. Ono, I. S. Sogami, Y. Ueno, H. Yoshida, and T. Yoshiyama. Recent study of polymer latex dispersions. *Langmuir*, **9**,394–411, (1993).

[125] N. A. M. Verhaegh and A. van Blaaderen. Dispersions of Rhodamine-labeled Silica Spheres: Synthesis, Characterization, and Fluorescence Confocal Scanning Laser Microscopy. *Langmuir*, **10**,1427–1438, (1994).

[126] A. van Blaaderen and P. Wiltzius. Real-space structure of colloidal hard-sphere glasses. *Science*, **270**,1177–1179, (1900).

[127] A. van Blaaderen, R. Ruel, and P. Wiltzius. Template directed colloidal crystallization. *Nature*, **385**,321–323, (1997).

[128] A. van Blaaderen and P. Wiltzius. Growing large, well-oriented colloidal crystals. *Advanced Materials*, **9**(10),833–835, (1997).

[129] E. Abbe. Note on the proper definition of the amplifying power of a lens or a lens-system. *Journal of the Royal Microscopy Society*, **4**,348–351, (1884).

[130] E. H. Linfoot and E. Wolf. Phase distribution near focus in an aberration-free diffraction image. *Proceedings of the Physics Society*, **B69**,823–832, (1956).

[131] M. Born and E. Wolf. *Principles of Optics.* Pergamon Press, Oxford, (1980).

[132] M. Berek. Grundlagen der Tiefenwahrnehmung im Mikroscop. *Markburg Sitzungs Ber.*, **62**,189–223, (1927).

[133] H. Ernst Keller. Objective Lenses for Confocal Microscopy. In J. B. Pawley, editor, *Handbook of Biological Confocal Microscopy*, chapter 7, pages 111–126. plenum press, New York, (1995).

[134] J. B. Pawley. *Handbook of Biological Confocal Microscopy.* Plenum, New York, 2nd edition, (1995).

[135] G. S. Kino and T. R. Corle. Confocal scanning optical microscopy. *Physics Today*, **9**,55–62, (1989).

[136] R. H. Webb. Confocal optical microscopy. *Reports on Progress in Physics*, **59**,427–471, (1996).

[137] G. J. Brakenhoff and H. T. M. van der Voort. 3-D image formation in high-aperture fluorescence confocal microscopy: A numerical analysis. *Journal of Microscopy*, **158**(1),43–54, (1990).

[138] J. B. Pawley. Fundamental and practical limits in confocal light microscopy. *Scanning*, **13**,184–198, (1991).

[139] C. J. R. Sheppard. Aberrations in high aperture conventional and confocal imaging systems. *Applied Optics*, **27**(22),4782–4786, (1988).

[140] G. J. Brakenhoff, P. Blom, and P. Barends. Confocal scanning light microscopy with high aperture immersion lenses. *Journal of Microscopy*, **117**(2),219–232, (1979).

[141] M. Minsky. Memoir on inventing the confocal scanning microscope. *Scanning*, **10**,128–138, (1988).

[142] E. Gratton and M. vandeVen. Laser Sources for Confocal Microscopy. In J. B. Pawley, editor, *Handbook of Biological Confocal Microscopy*, chapter 5, pages 69–90. Plenum Press, New York, (1995).

[143] H. M. Shapiro. Laser Noise. *Cytometry*, **8**,248–250, (1987).

[144] J. Art. Photon Detectors for Confocal Microscopy. In J. B. Pawley, editor, *Handbook of Biological Confocal Microscopy*, chapter 12, pages 183–196. Plenum Press, New York, (1995).

[145] W. Engelhardt and W. Knebel. *Leica Scientific and Technical Information*, **X**(5),159–168, (1993).

[146] X. Cottin and P. A. Monson. A cell theory for solid solutions: Application to hard sphere mixtures. *Journal of Chemical Physics*, **99**(11),8914–8921, (1993).

[147] B. J. Ackerson. When order is disordered. *Nature*, **365**(6441),11–12, (1993).

[148] M. D. Eldridge, P. A. Madden, P. N. Pusey, and P. Bartlett. Binary hard-sphere mixtures: A comparison between computer simulation and experiment. *Molecular Physics*, **84**,395–420, (1995).

[149] D. Frenkel, M. Dijkstra, and J. P. Hansen. Phase separation in binary hard-core mixtures. *Journal of Chemical Physics*, **101**(4),3179–3189, (1994).

[150] P. G. Bolhuis and D. A. Kofke. A Monte Carlo study of freezing of polydisperse hard spheres. *Physical Review E*, **54**(1),634–643, (1996).

[151] E. Trizac, M. D. Eldridge, and P. A. Madden. Stability of the AB crystal for asymmetric binary hard sphere mixtures. *Molecular Physics*, **90**(4),675–678, (1997).

[152] M. D. Eldridge, P. A. Madden, and D. Frenkel. Entropy-driven formation of a superlattice in a hard-sphere binary mixture. *Nature*, **365**,35–37, (1993).

[153] H. Xu and M. Baus. A density functional study of superlattice formation in binary hard-sphere mixtures. *Journal of Physics: Condensed Matter*, **4**,663–668, (1992).

[154] X. Cottin and P. A. Monson. Substitutionally ordered solid solutions of hard spheres. *Journal of Chemical Physics*, **102**(8),3354–3360, (1995).

[155] E. Parthe. Space filling of crystal structures: A contribution to the graphical presentation of geometrical relationships in simple crystal structures. *Zeitschrift fr Kristallographie*, **115**,52–79, (1961).

[156] J. V. Sanders and M. J. Murray. Close-packed structures of spheres of two different sizes: 2. The packing densities of likely arrangements. *Philosophical Magazine A*, **42**(6),721–740, (1980).

[157] P. N. Pusey, W. van Megan, P. Bartlett, B. J. Ackerson, J. G. Rarity, and S. M. Underwood. Structure of crystals of hard colloidal spheres. *Physical Review Letters*, **63**(25),2753–2756, (1989).

[158] B. E. Warren. *X-Ray Diffraction.* Addison-Wesley, Reading, MA, (1969).

[159] P. N. Pusey. Colloidal Suspensions. In J. P. Hansen, D. Levesque, and J. Zinn-Justin, editors, *Liquids, Freezing and the Glass Transistion*, pages 763–942. North-Holland, Amsterdam, (1981).

[160] R. Jardine, P. Hunt, and P. Bartlett. Superlattice formation in mixtures of hard-sphere colloids. *Physical Review E*, **62**(1),900–913, (2000).

[161] P. Manoj, A. J. Fillery-Travis, A. D. Watson, D. J. Hibberd, and M. M. Robins. Creaming Behaviour. *Journal of Colloid and Interface Science*, **207**(2),283–293, (1998).

[162] E. Dickinson. Caseins in emulsions: Interfacila properties and interactions. *International Dairy Journal*, **9**,305–312, (1999).

[163] H. N. W. Lekkerkerker, W. C. K. Poon, P. N. Pusey, A. Stroobants, and P. B. Warren. Phase behaviour of colloid and polymer mixtures. *Europhysics Letters*, **20**(6),559–564, (1992).

[164] Y. Mao, M. E. Cates, and H. N. W. Lerkerkerker. Depletion forces in colloidal systems. *Physica A*, **222**,10–24, (1995).

[165] S. Asakura and F. Oosawa. On the interaction between two bodies immersed in a solution of macromolecules. *Journal of Chemical Physics*, **22**,1255–1256, (1954).

[166] S. Asakura and F. Oosawa. Interaction between particles suspended in solutions of macromolecules. *Journal of Polymer Science*, **33**,183–192, (1958).

[167] A. P. Gast, C. K. Hall, and W. B. Russel. Polymer-induced phase separations in non-aqueous colloidal suspensions. *Journal of Colloid and Interface Science*, **96**,251, (1983).

[168] N. A. M. Verhaegh, J. K. G. Dhont, H. N. W. Lekkerkerker, and J. S. van Duijneveldt. Fluid-fluid phase separation in colloid-polymer mixtures

studied with small angle light scattering and light microscopy. *Physica A*, **230**,409–436, (1996).

[169] P. N. Pusey, A. D. Pirie, and W. C. K. Poon. Dynamics of colloid polymer mixtures. *Physica A*, **201**,322, (1993).

[170] W. C. K. Poon, A. D. Pirie, and P. N. Pusey. Gelation in colloid-polymer mixtures. *Faraday Discussions of the Chemical Society*, **101**,65–76, (1995).

[171] W. C. K. Poon, A. D. Pirie, M. D. Haw, and P. N. Pusey. Non-equilibrium behaviour of colloid-polymer mixture. *Physica A*, **235**,110–119, (1997).

[172] W. C. K. Poon, A. D. Pirie, M. D. Haw, and P. N. Pusey. Non-equilibrium behaviour of colloid-polymer mixtures. *Physica A*, **235**,110–119, (1997).

[173] N. A. M. Verhaegh, D. Asnaghi, and H. N. W. Lekkerkerker. Transient gels in colloid-polymer mixtures studied with fluorescence confocal scanning laser microscopy. *Physica A*, **264**,64–74, (1999).

[174] P. Bartlett and R. H. Ottewill. geometric interactions in binary colloidal dispersions. *Langmuir*, **8**,1919–1925, (1992).

[175] M. Dijkstra, R. van Roij, and R. Evans. Phase behaviour and structure of binary hard-sphere mixtures. *Physical Review Letters*, **81**(11),2268–2271, (1998).

[176] M. Dijkstra, R. Roij, and R. Evans. Direct simulation of the phase behaviour of binary hard-sphere mixtures: Test of the depletion potential description. *Physical Review Letters*, **82**(1),117–120, (1999).

[177] C. C. Wilson. ISIS, the UK spallation neutron source - A guided tour. *Neutron News*, **1**(14), (1990).

[178] K. Ibel. *Guide to Neutron Research Facilities At the ILL*. Scientific Coordination Office, ILL, Grenoble, (1994).

[179] S. King. Small Angle Neutron Scattering. In R. A. Pethrick and J. V. Dawkins, editors, *Modern Techniques for Polymer Characterisation*, chapter 7. John Wiley and Sons, New York, (1999).

[180] P. Linder, R. P. May, and P. Timmins. Upgrading of the SANS instrument D11 at the ILL. *Physica B*, **180**,967–972, (1992).

[181] J. S. Higgins and H. C. Benoit. Theoretical Basis of Scattering. In *Polymers and Neutron Scattering*, chapter 4, pages 81–115. Clarendon Press, Oxford, (1994).

[182] B. H. Zimm. *Journal of Chemical Physics*, **16**,1099, (1948).

[183] P. Bartlett and R. H. Ottewill. A neutron scattering study of the structure of a bimodal colloidal crystal. *Journal of Chemical Physics*, **96**(4),3306–3318, (1992).

[184] M. H. G. Duits, R. P. May, A. Vrij, and C. G. de Kruif. Partial structure factors in colloidal silica mixtures determined with small-angle neutron scattering contrast variation. *Journal of Chemical Physics*, **94**,4521–4531, (1991).

[185] P. Lindner, H. J. M. Hanley, and G. C. Straty. Order in a simple colloidal mixture suspension. *Physica A*, **174**,60–73, (1991).

[186] J. S. Huang and M. W. Kim. Critical behaviour of a microemulsion. *Physical Review Letters*, **47**(20),1462–1465, (1981).

[187] M. Kotlarchyk, S. H. Chen, J. S. Huang, and M. W. Kim. Structure of three-component microemulsions in the critical region determined by small-angle neutron scattering. *Physical Review A*, **29**(4),2054–2069, (1984).

[188] D. J. Cebula, R. H. Ottewill, and J. Ralston. Investigations of microemulsions by light scattering and neutron scattering. *Journal of the Chemical Society Faraday Transactions*, **77**,2582–2612, (1981).

[189] C. Cabos and P. Delord. Etude d'un systeme micellaire de type inverse par diffusion centrale des neutrons. *Journal of Applied Crystallography*, **12**,502, (1979).

[190] M. Kotlarchyk, S. H. Chen, and J. S. Huang. Temperature-dependence of size and polydispersity in a 3-component micro-emulsion by small-angle neutron-scattering. *Journal of Physical Chemistry*, **86**,3273–3276, (1982).

[191] T. Assih, F. Larche, and P. Delord. Evolution of the radius of the inverse micelles at high dilution in the aerosol-OT/water/normal-decane system. *Journal of Colloid and Interface Science*, **89**,35, (1982).

[192] M. Zulauf and H. F. Eicke. Inverted micelles and microemulsions in the ternary system water/Aerosol OT/isooctane as studied by photon correlation spectroscopy. *Journal of Physical Chemistry*, **83**,480–486, (1979).

[193] U. Batra, W. B. Russel, M. Pitsikalis, S. Sioula, J. W. Mays, and J. S. Huang. Phase behaviour and viscoelasticity of AOT microemulsions containing triblock copolymers. *Macromolecules*, **30**,6120–6126, (1997).

[194] S. H. Chen, J. Rouch, F. Sciortino, and P. Tartaglia. Static and dynamic properties of water-in-oil microemulsions near the critical and percolation points. *Journal of Physics: Condensed Matter*, **6**,10855–10883, (1994).

[195] C. Cametti, P. Codastefano, P. Tartaglia, J. Rouch, and S. H. Chen. Theory and experiement of electrical conductivity and percolation locus in water-in-oil microemulsions. *Physical Review Letters*, **64**(12),1461–1464, (1990).

[196] J. Bergenholtz, A. A. Romagnoli, and N. J. Wagner. Viscosity, microstructure, and interparticle potential of AOT/H*2*0/n-decane inverse microemulsions. *Langmuir*, **11**,1559–1570, (1995).

[197] J. S. Huang. Surfactant interactions in oil continuous microemulsions. *Journal of Chemical Physics*, **82**(1),480–484, (1985).

[198] D. Majolino, F. Mallamace, and N. Micali. Viscosity measurements in dense microemulsions, evidence of aggregation process. *Solid State Communications*, **74**(6),465–468, (1990).

[199] K. Ibel. The Neutron Small-Angle Camera D11 at the High-Flux Reactor, Grenoble. *Journal of Applied Crystallography*, **9**,296–309, (1976).

[200] K. Ibel, W. Schmatz, and T. Springer. Theory of a Velocity Focusing Instrument for Neutron Small Angle Scattering. *Atomkernenergie*, **17**,1518, (1971).

[201] R. P. May, K. Ibel, and J. Haas. The Forward Scattering of Cold Neutrons by Mixtures of Light and Heavy Water. *Journal of Applied Crystallography*, **9**,296–309, (1982).

[202] M. Wurth and T. Palberg. elastic and plastic response of colloidal crystals subjected to alternating inhomogeneous electric fields. *Journal of Colloid and Interface Science*, **167**,221–223, (1994).

[203] R. H. Ottewill, A. R. Rennie, and A. Schofield. The effect of electric fields on nonaqueous dispersions. *Progress in Colloid and Polymer Science*, **81**,1–5, (1990).

[204] J. P. Cotton. *Neutron, X-Ray and Light Scattering: Introduction to an Investigative Tool for Colloidal and Polymeric Systems.* North-Holland, Amsterdam, (1991).

[205] G. D. Wignall and F. S. Bates. Absolute calibration of small-angle neutron scattering data. *Journal of Applied Crystallography*, **20**,28–40, (1986).

[206] A. Vrij. *Journal of Chemical Physics*, **69**,1742, (1978).

[207] A. Vrij. *Journal of Chemical Physics*, **71**,3267, (1979).

[208] J. K. Percus and G. J. Yevick. Analysis of classical statistical mechanics by means of collective coordinates. *Physical Review*, **110**,1–13, (1958).

[209] R. H. Ottewill. Concentrated Dispersions. In J. W. Goodwin, editor, *Colloidal Dispersions*, chapter 9, pages 197–217. Royal Society of Chemistry, London, (1982).

[210] L. S. Ornstein and F. Zernike. *Proc.Acad.Sci (Amsterdam)*, **17**,793, (1914).

[211] P. G. de Gennes. *Scaling Concepts in Polymer Physics.* Cornell University Press, Ithaca, (1979).

PHYSICAL REVIEW E VOLUME 62, NUMBER 1 JULY 2000

Superlattice formation in mixtures of hard-sphere colloids

Neil Hunt, Roger Jardine, and Paul Bartlett*
Department of Chemistry, University of Bath, Bath BA2 7AY, United Kingdom
(Received 4 February 2000)

We report a detailed experimental study of the superlattice structures formed in dense binary mixtures of hard-sphere colloids. The phase diagrams observed depend sensitively on the ratio $\alpha = R_S/R_L$ of the radii of the small (S) and large (L) components. Mixtures of size ratio $\alpha = 0.72$, 0.52, 0.42, and 0.39 are studied. The structures of the colloidal phases formed were identified using a combination of light-scattering techniques and confocal fluorescent microscopy. At $\alpha = 0.39$, ordered binary crystals are formed in suspensions containing an equal number of large and small spheres which microscopy shows have a three-dimensional structure similar to either NaCl or NiAs. At the larger size ratio, $\alpha = 0.52$, we observe LS_2 and LS_{13} superlattices, isostructural to the molecular compounds AlB_2 and $NaZn_{13}$, while at $\alpha = 0.72$ the two components are immiscible in the solid state and no superlattice structures are found. These experimental observations are compared with the predictions of Monte Carlo simulations and cell model theories.

PACS number(s): 82.70.Dd, 64.70.Dv, 64.75.+g

I. INTRODUCTION

Hard spheres constitute probably the simplest yet also one of the most important models of condensed-matter physics [1]. The phase behavior of hard spheres is determined by minimizing the free energy $F = U - TS$ or, since hard spheres are forbidden to interpenetrate and the internal energy U is a constant, by maximizing the entropy S. It was highly surprising, therefore, given the simplicity of the interactions in hard spheres, when experiments on colloidal particles [2] demonstrated that hard spheres of different sizes form equilibrium crystalline superlattices with large and highly complicated unit cells. Subsequent computer simulations [3] confirmed that a mixture with a radius ratio $\alpha = R_S/R_L$ of 0.58 formed two binary crystals, with stiochiometries LS_2 and LS_{13} (where L denotes the large particle). Clearly, given the subtlety of entropic effects at this size ratio, it is interesting to ask what structures might be stable at other size ratios. In general, the stability of a binary crystal, L_mS_n, depends on three variables, namely the size ratio α, the total packing fraction $\phi = \phi_L + \phi_S$, and the relative numbers of small and large spheres n_S/n_L. Clearly a determination of the phase behavior as a function of these three variables, α, ϕ, and n_S/n_L, represents a formidable task.

The present paper presents a first step in this direction where we report a comprehensive experimental study of the phase behavior of hard-sphere mixtures at size ratios $\alpha = 0.72$, 0.52, 0.42, and 0.39. Our motivation is threefold. First, while the stability of superlattice phases at size ratios *other* than $\alpha = 0.58$ has attracted considerable theoretical interest in recent years [4,5], there has been little experimental work that critically tests these theories. In the current paper we use a sterically stabilized colloidal system which other studies have demonstrated [6] provides a close experimental realization of classical hard spheres. Our experiments therefore model accurately a mixture of hard spheres. Second, the statistical properties of mescoscopic systems of particles are frequently dominated by entropic as opposed to enthalpic interactions. Consequently, the phase behavior of many colloidal systems can be appropriately mapped onto an effective hard-sphere system. Thus, for instance, LS_2 and LS_{13} structures have been observed in a range of mesoscopic systems including mixtures of charge-stabilized polystyrene spheres [7], two-dimensional arrays of gold clusters [8], and gem opals [9,10] in which the interactions are far from hard-sphere-like. Experiments on colloidal hard-sphere mixtures are important therefore as a simple reference case. Third, colloidal superlattices provide examples of three-dimensional photonic crystals with lattice parameters of the order of the wavelength of visible light and a range of different lattice symmetries. Such crystals could be used to create photonic band gaps (frequency ranges where light will not propagate because of multiple Bragg reflections) which are predicted to have unique and highly useful optical properties [11,12].

The paper is organized as follows. In Sec. II we summarize the current theoretical predictions for freezing in binary hard-sphere mixtures. The colloidal mixtures used are outlined in Sec. III and our detailed observations of the phase behavior are presented in Sec. IV. We then describe the scattering from a random-stacked LS superlattice in Sec. V and its microscopy in Sec. VI. Finally, we compare our results with theoretical predictions in Sec. VII and we collect our conclusions in Sec. VIII.

II. BINARY MIXTURES

At first sight the idea that entropy, which is normally taken to be a force-favoring disorder, should generate complex superlattice structures seems counterintuitive. It is frequently assumed, for instance, incorrectly, that complex interactions between particles are needed to generate complex phases. However, the physical origin of superlattice formation in hard-particle suspensions is both extremely simple and general [13]. The resolution of this paradox relies on distinguishing two components to the total entropy. The entropy of a system of spheres is composed of contributions

*Corresponding author.

associated with the degree of spatial ordering (the "configurational" entropy) and that associated with the space available to each particle for local motions (the "free volume" entropy). Confining the spheres of a binary suspension to the lattice cells of a superlattice structure decreases the configurational entropy compared with a disordered fluid phase. However, the particles within a superlattice have more local free volume in which to move than they do in the fluid, provided the superlattice fills space more efficiently than the fluid. Forming a superlattice increases the free volume entropy but at the expense of lowering the configurational entropy. At low concentrations, the configurational entropy dominates and the fluid is stable but with increasing concentration, the gain in free volume entropy on superlattice formation more than compensates for the loss of configurational entropy, and a stable superlattice is formed. These ideas have been confirmed by accurate calculations of the entropy from Monte Carlo simulations [3,4,14], density-functional theory [15], and cell-model calculations [5].

While the physical picture for superlattice formation is clear, there is as yet no theory which predicts *a priori*, given the size ratio, which structures are stable. All the current methods essentially go through a list of possible structures and analyze each in turn. The difficulty is the sheer number of potential candidates. The arguments given above do, however, suggest that one simple way to select feasible candidate structures is to use packing arguments. In particular, if a crystal structure has a high *close-packed* density (ϕ_{cp}), then, at the lower densities where freezing occurs, the constituent particles will have a large volume in which to move and a correspondingly higher free volume contribution to the entropy. On this basis, the entropy of each structure L_mS_n should mirror the maximum packing curve $\phi_{cp}(\alpha)$. Such space-filling arguments have been explored in detail by Sanders [9], who postulated that a superlattice will form only if its maximum packing fraction exceeds that for the pure one-component phase-separated crystals ($\phi_{cp}=\pi/\sqrt{18}$ ~ 0.74).

The space-filling curves for a few selected binary structures are reproduced in Fig. 1, from which it is clear that over the range $0.3<\alpha<0.8$ only two structures, LS_2 and LS, fill space more efficiently than the fcc or hcp limit. The maximum packing principle accounts for the stability of the LS_2 crystal already seen in experiments at $\alpha=0.58$ and predicts furthermore that an LS compound, with a NaCl or a NiAs structure (both have identical values of ϕ_{cp}), should be stable around $\alpha=\sqrt{2}-1\sim 0.414$, for which the packing limit ($\phi_{max}=0.793$) is substantially above the uniform hard-sphere limit ($\phi_{cp}=0.7405$). A detailed study of Fig. 1 shows two further structures, the LS_{13} lattice ($\phi_{cp}=0.738$ at $\alpha=0.557$) and the CsCl structure ($\phi_{cp}=0.729$ at $\alpha=0.732$), which have packing limits close to, although slightly below, the monodisperse limit. While these structures should be unstable according to Sanders, their proximity to the fcc limit suggests they should be included in more detailed approaches.

Guided by maximum packing arguments, five different crystals have been suggested as possible equilibrium structures in mixtures of hard spheres.

(i) Substitutionally disordered fcc or hcp structure. In this crystal the large and small spheres are placed at random on a common fcc or hcp lattice. In the limit where the spheres have the same size, $\alpha\rightarrow 1$, we recover the single-component hard-sphere crystal. Computer simulations [16] predict that this structure is mechanically stable only if the sizes of the two particles are comparable, $\alpha>0.85$.

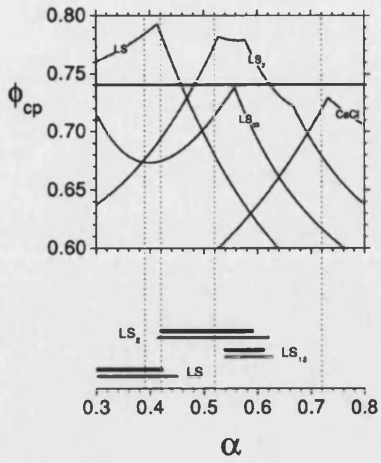

FIG. 1. The close-packing density (ϕ_{cp}) as a function of the size ratio α for the CsCl, LS_2, LS_{13}, and LS (NaCl or NiAs) structures. The packing limit of a fcc or hcp crystal of monodisperse spheres is shown by the horizontal line at $\phi_{cp}=0.7405$. The lower chart summarizes the regions of stability predicted by computer simulation (gray) [3,4,14] and cell calculations (black) [5,35]. The size ratios studied in the current work are shown dotted.

(ii) Ordered CsCl structure. This crystal consists of two interpenetrating simple-cubic lattices, one for each species. The structure has not been observed experimentally in colloidal hard-sphere mixtures, although it has been found in suspensions with a cross-attraction between large and small spheres [17]. Early density-functional calculations [18,19] predicted that CsCl should be stable in equimolar hard-sphere mixtures, but more recent and extensive simulation [14] and cell-model calculations [5] have not located a stable CsCl solid.

(iii) Ordered LS_2 structure. This crystal, which is isostructural with the alloy AlB_2, consists of a simple hexagonal crystal of large spheres with smaller particles filling all the trigonal cavities between the L layers. The structure has been observed [2] in mixtures of colloids with $\alpha=0.58$ and its stability confirmed by computer simulation [3].

(iv) Ordered LS_{13} structure. In the LS_{13} structure the large particles form a simple cubic lattice; each cubic subcell contains thirteen small particles, one at the body center and the remaining twelve on the vertices of an icosahedron surrounding the central particle. The icosahedra are rotated by 90° between adjacent subcells so that the full unit cell contains eight subcells and a total of 112 particles. The LS_{13} crystal has been seen in colloidal hard-sphere mixtures at $\alpha=0.58$ and 0.62 [2,20] and its stability was investigated by simulation [3].

(v) Ordered NaCl or NiAs structures (stiochiometry LS). The NaCl structure consists of a fcc lattice of large spheres with small spheres located on the octahedral interstitial sites, generating a second interpenetrating fcc lattice. The NiAs crystal is an analogous structure in which the large spheres are arranged in a hcp as opposed to a fcc lattice. The small

spheres still occupy octahedral sites but are now sited in a simple cubic rather than a fcc sublattice. Neither structure has been observed in experiments, although a stable NaCl crystal has been predicted by a number of theoretical studies [4,5,18,19].

The relative stability of these crystals depends on the density and composition of the mixture as well as the ratio of the sizes of the spheres. The most extensive analysis of the stability of hard-sphere mixtures has been performed using Monte Carlo simulation techniques [3,4,14,21,22] and a simple but reliable cell model developed by Cottin and Monson [5]. Density-functional theory has also been used to test the stability of different phases but only for *fixed* compositions. This restriction is not appropriate for our experiments so we shall not discuss these predictions further. Computer simulation and cell-model calculations, although based on very different approximations, reach essentially identical conclusions. For the size ratio range $0.3<\alpha<0.85$ these theories predict three stable superlattices: the LS_2 and LS_{13} lattices seen in experiments [2] at $\alpha=0.58$ and an LS compound with the NaCl (or NiAs [23]) structure. The range of size ratios over which each structure is stable is summarized at the bottom of Fig. 1. Very similar results were found using the cell model, although the widths of the stability domain predicted for LS_2 and LS_{13} are somewhat smaller [5]. Finally, both studies considered the stability of the CsCl lattice [5,14] but the crystal was predicted to be unstable with respect to phase separation into two pure solid phases.

The purpose of the present work is to compare these theoretical predictions with systematic experimental measurements on colloidal hard-sphere mixtures. The experimental system used in the current work is similar to the earlier work reported [2] at $\alpha=0.58$, but here we report data for a more extensive set of mixtures, extending the previous results to lower size ratios. In particular, we set out to address three questions. First, we study mixtures with size ratios $\alpha\sim0.4$ to clarify if the NaCl structure predicted is indeed observed experimentally. Second, we make measurements on systems with $\alpha=0.52$ with the aim of checking the theoretical prediction that this value of α marks the lower stability boundary of the LS_{13} superlattice. And finally, we explore the phase behavior at $\alpha=0.72$, close to the peak in the maximum packing curve for CsCl, where the formation of CsCl seems most likely.

III. EXPERIMENTAL DETAILS

The particles used in this study consisted of poly-(methyl methacrylate) (PMMA) spheres stabilized sterically by a thin (~10 nm thick) chemically grafted comblike layer of poly-(12-hydroxy stearic acid) (PHSA) chains. They were synthesized by a nonaqueous dispersion polymerization of a mixture of 98% methyl methacrylate (MMA) and 2% (by weight) methacrylic acid with a comb copolymer of PHSA and PMMA added as a stabilizer. Four different-sized particles (labeled $B-E$ in Table I) were prepared by changing the total monomer content following the methods described by Antl *et al.* [24]. Dye-labeled particles were made by repeating this synthesis using a mixture of methyl methacrylate (MMA), methacrylic acid, and 0.22 wt. % of the fluorescent monomer 2-(methyl-(8-nitro-benzo [1,2,5] oxadiazol-1-yl)-amino) methyl methacrylate (NBD-MMA) [25] as the constituent monomers. The resulting particles, labeled A in Table I, consisted of a fluorescent core and a nonfluorescent stabilizing layer of PHSA. The NBD-containing core absorbed at $\lambda=488$ nm and fluoresced intensely in a broadband of wavelengths centered around $\lambda\sim519$ nm. The particle radii and polydispersities [26] were determined from dynamic light-scattering measurements on dilute samples in *cis*-decahydronaphthalene (see Table I). Polydispersities of the nonfluorescent particles were of the order of 4%, while the fluorescent colloid A had a larger polydispersity of about 8%. Although polydispersities of this order affect the position of the freezing transition, the fact that all of our particles, including the fluorescent spheres, crystallize suggests that to a first approximation it is reasonable to neglect polydispersity.

TABLE I. Particles used in this work.

Colloid	Radius (nm)[a] R (±3 nm)	R_{DLS} (±5 nm)	σ (±0.01)[b]	ϕ_m (±0.003)[c]
A[d]	175	175	~0.08	0.548
B	188	199	0.04	0.548
C	231	233	0.03	0.557
D	321	327	0.03	0.546
E	448	458	0.03	0.546

[a]Determined from crystallography and dynamic light scattering (DLS).

[b]Polydispersity $\sigma=\sqrt{\langle R^2\rangle}/\langle R\rangle$ determined by dynamic light scattering [26].

[c]Melting volume fraction. Computer simulation [27] gives $\phi_m=0.545$ for monodisperse hard spheres.

[d]Particle fluorescently labeled with NBD-MMA.

The particles were suspended in a near-refractive index-matching mixture of *cis*-decahydronapthalene (decalin, $n_{488}=1.4847$) and carbon disulphide (CS_2, $n_{488}=1.6483$). Carbon disulfide, in particular, has a substantial wavelength-dependent refractive index so, in practice, the particles and medium can be precisely matched only at one precise wavelength. We adjusted the proportions of the two solvents to minimize the scattering at $\lambda=568$ nm. With this choice, the change in refractive indices at the other laser wavelengths available to us, 488 and 647 nm, was sufficient to ensure that concentrated suspensions exhibited strong single scattering and little or no multiple scattering. Carbon disulfide is a good solvent for PMMA and swells the particles. However, the increase in size is small. Dynamic light-scattering measurements on dilute dispersions in pure CS_2 showed that equilibrium swelling is achieved within a few hours of contact with CS_2 and the resulting increase in the radius is <2%. Index matching as well as making the scattering measurements feasible also suppresses the van der Waals forces. Indeed, previous studies have established that for suspensions of this type, the interparticle potential is steep, purely repulsive, and well approximated by a hard-sphere interaction. We confirmed that our particles behaved like hard spheres by observing the position of the fluid-crystal transition [6]. A series of one-component suspensions were prepared at concentrations which spanned the transition by centrifuging a stock solution and removing a known mass of solvent. The

samples were tumbled overnight to homogeneously mix the particles and solvent and were then left to stand undisturbed for observation. The heights of the fluid and crystalline phases were measured with a traveling microscope as a function of time. The linear dependence found for the height of each phase with time was extrapolated back to the start of the experiment to remove the effects of sedimentation and the equilibrium phase diagram determined. The melting point ϕ_m was found from linear regression through points in the coexistence region. Values for ϕ_m for each of the five colloids used are detailed in Table I. The close agreement seen between the experimental data and the value found from computer simulation [27] for the hard-sphere melting density, $\phi_m = 0.545$, confirms that the interparticle potential is close to hard sphere.

The structures of the crystals formed were studied using optical powder-diffraction techniques. Suspensions within the coexistence region were sealed inside optical quality 1 cm^2 rectangular glass cuvettes. The cuvette was placed at the center of an 150 mm diameter cylindrical bath filled with an index-matching mixture of 1, 2, 3, 4-tetrahydronapthalene (tetralin) and decalin. A parallel expanded beam from a krypton-argon laser ($\lambda = 647$ nm), approximately 15 mm in diameter, illuminated the sample through an optically flat window glued to the surface of the bath. The large scattering volume ensured that the intensity measured was a proper orientational average of the scattering from a powder of crystallites [28]. The index bath acted as a cylindrical lens, focusing scattered radiation onto a vertical slit which was placed in front of a photomultiplier tube. The collection optics were mounted on a computer-controlled turntable so that scattered intensities I could be measured over a range of angles from $\theta = 20°$ to 140° with a resolution of about 0.05°. With the laser beam perpendicular to the axis of rotation, the magnitude of the scattering vector, defined as $q = |k_i - k_s|$, is $q = (4\pi n/\lambda)\sin\theta/2$, where k_i and k_s are the incident and scattered wave vectors, n is the refractive index of the sample, and λ the laser wavelength.

The scattered intensity $I(q)$ measured from the pure one-component crystals showed the random-stacked close packed (rscp) powder pattern seen previously [28]. For samples in the coexistence region, the position q_{001} of the intense central peak [indexed to the (001) line in the reduced hexagonal basis of Sec. IV A] was used to obtain an accurate estimate of the effective hard-sphere radius from the identity $Rq_{001} = 3(\pi^2\phi_m/\sqrt{12})^{1/3} \sim 3.47$. The corresponding hard-sphere radii R are listed in Table I. The close agreement seen with the values obtained from dynamic light-scattering measurements (R_{DLS}) confirms the hard-sphere nature of these suspensions.

Binary suspensions were prepared by mixing stock solutions of the different-sized PMMA particles. Samples were concentrated by centrifugation. Four different particle combinations were studied (see Table II) with size ratios $\alpha = R_S/R_L$, calculated from the hard-sphere radii, of 0.39, 0.42, 0.52, and 0.72. At each α, samples were prepared at a number of volume fractions, $\phi = \phi_L + \phi_S$, which spanned the region between the monodisperse freezing $\phi_f = 0.494$ and glass transitions $\phi_g = 0.58$ where rapid crystallization is found for one-component suspensions [6]. Samples were prepared with a wide range of compositions, n_S/n_L, so as to cover the full extent of the fluid-solid transition in the $(\phi, n_S/n_L)$ plane. After preparation, each sample was homogenized by tumbling overnight and then inspected visually at regular intervals. While the samples were index-matched, they were not density-matched; the resulting sedimentation can dramatically affect the observed phase behavior in binary suspensions by altering the local density and composition within the sample. To prevent this gravity-induced separation, each sample was continuously rotated in a vertical plane at a rate of one revolution per day. Over one complete revolution, the effective sedimentation force averaged to zero and suspensions showed no signs of sedimentation [29]. The binary samples were sufficiently close to index-matched conditions that the first signs of crystallization were most easily detected by eye. The time required to first observe crystals from an initially homogenized suspension varied considerably but was on the order of weeks. As soon as crystallites could be seen, the structure and development of the sample were followed with regular powder-diffraction measurements. Samples were followed for up to a year from preparation.

TABLE II. Binary mixtures studied in this work. Size ratios determined by crystallography and dynamic light scattering (DLS).

Colloid combination (S-L)	Radius ratio $\alpha = R_S/R_L$ $\alpha \pm 0.01$	$\alpha_{DLS} \pm 0.02$
A-E	0.39	0.36
B-E	0.42	0.43
C-E	0.52	0.51
D-C	0.72	0.71

The crystal structure in a couple of binary suspensions was also examined using confocal scanning laser microscopy (CSLM). Confocal images were collected on 100 μm thick, highly transparent PMMA suspensions with an index-matched solvent mixture of decalin and CS_2. The concentrated suspensions were stored in flat capillaries (2 mm wide, 5 cm long, 100 μm thick, with 170 μm thick walls) and sealed with araldite to prevent solvent evaporation. Although we made no quantitative measurements, binary suspensions crystallized noticeably faster in the thin capillary cells than the 1 cm path length optical cuvettes. Confocal micrographs of the colloidal crystals formed were obtained with an upright Leica TC NT microscope and the 488 nm line of an argon ion laser. We used a 100× 1.3 NA oil immersion objective lens and a filter block which detected the fluorescence above 515 nm. Micrographs of 512 by 512 pixels were obtained in about 1 s by beam scanning.

IV. DETAILED OBSERVATIONS OF THE PHASE BEHAVIOR

The final phases observed in colloidal mixtures, with radius ratios of $\alpha = 0.72$, 0.52, 0.42, and 0.39, are summarized in Figs. 2(a)–2(d). The sequence of events after mixing depends sensitively on the radius ratio α and the relative numbers n_S/n_L or volume fractions ϕ_S/ϕ_L of small and large particles. Below, we describe our detailed observations.

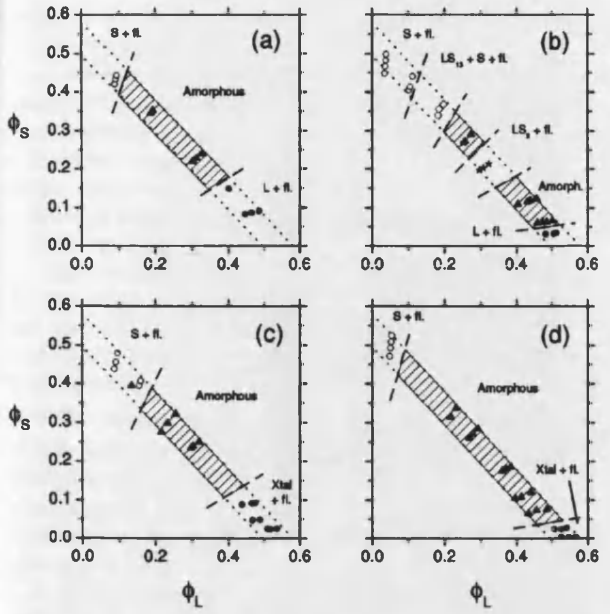

FIG. 2. Summary of final phase behavior observed for size ratios $\alpha=0.72$ (a), 0.52 (b), 0.42 (c), and 0.39 (d). The symbols denote the following: open circle, crystal of small spheres plus fluid; diamond, three-phase coexistence of LS_{13} crystal, crystal of large spheres, and fluid; triangle, glass; star, LS_2 crystal plus fluid; filled circle, crystal of large spheres plus fluid (for $\alpha=0.72$ and 0.52) or crystal (probably with defective NaCl structure—see text) plus fluid (for $\alpha=0.42$ and 0.39). The half-filled circle in (d) identifies the two-phase sample studied by confocal microscopy. The dashed lines correspond to the one-component hard-sphere freezing ($\phi_f=0.494$) and melting densities ($\phi_m=0.545$). All other lines are drawn in as guides to the eye.

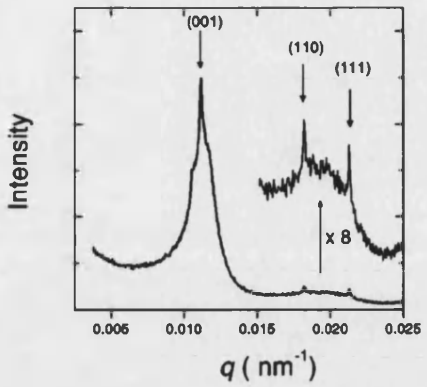

FIG. 3. Scattered light intensity from the coexisting crystalline phase formed in a binary mixture with size ratio $\alpha=0.72$, composition $n_S/n_L=0.5$ ($\phi_S/\phi_L=0.19$), and overall volume fraction $\phi_L+\phi_S=0.529$. The sharp Bragg peaks are indexed using the hexagonal rscp basis described in the text. The lattice constant (equal to the nearest-neighbor separation) is $a=671\pm6$ nm, which equates to a crystal density of $\phi_L=(8\pi/3\sqrt{2})(R_L/a)^3=0.65\pm0.02$.

A. Size ratio $\alpha=0.72$

Mixtures with a size ratio of $\alpha=0.72\pm0.01$ were prepared by combining large particles of colloid $D(R_L=321\pm3$ nm) with the smaller particles of colloid $C(R_S=232\pm3$ nm). A total of thirteen different mixtures was prepared, at five different number ratios, with total volume fractions in the range $0.507\leq\phi_L+\phi_S\leq0.576$. Three different classes of phase behavior were observed depending on the ratio of small to large spheres. Our observations are summarized in Fig. 2(a).

In samples with a large proportion of either the large or small species, colloidal fluid-crystal coexistence was observed. Small colloidal crystallites first appeared a few days after mixing. Nucleation appeared to be homogeneous with crystals appearing throughout the bulk of the sample. Over the next couple of weeks, these crystallites settled under gravity so that after 19 days a sharp interface was evident between an iridescent polycrystalline lower region and a slightly turbid colloidal fluid at the top. Light-scattering measurements, shown in Fig. 3, on the lower polycrystalline phase revealed a powder pattern profile similar to the distinctive patterns found previously in single-component hard-sphere suspensions [28].

The scattering from a pure hard-sphere system shows sharp Bragg peaks on top of a diffuse background. This distinctive powder pattern can be understood in terms of a random stacking of hexagonal close-packed planes of particles [28]. Starting with a single hexagonal close-packed plane (position *A*), there are two choices for the position of the next registered layer, *B* or *C*. Both of these possibilities lead to a close-packed structure. So, for instance, a fcc crystal can be built up from the stacking sequence *ABCABC*... or the symmetric twinned structure *ACBACB*..., while the sequence *ABABAB*... generates the corresponding three-dimensional hcp crystal. For the case of a purely random-stacked close-packed (rscp) sequence (*ABCBCA*...), the scattering is most conveniently described using a hexagonal layer of spheres as the basic structural unit.

The reciprocal space of a hexagonal layer with lattice constant a is a system of hexagonally arranged Bragg rods with a rod spacing in reciprocal space of $a^*=4\pi/a\sqrt{3}$ [30]. With a spacing between two close-packed layers of $c=a\sqrt{2/3}$, the unit vector in reciprocal space along the rods is of length $c^*=2\pi/c$ [31]. The intensity distribution along each of the Bragg rods with indices (h,k) depends on the stacking sequence of the hexagonal layers. When the layers are close-packed (consecutive layers occupy different lateral positions *A*, *B*, or *C*), the rods split into two distinct groups which are affected differently by randomness in the stacking sequence. For rods with $(h-k)=3n$, where n is an integer, the scattering intensity is always concentrated at the points (h, k, l), with l an integral, independent of the exact stacking order (provided it remains close-packed). On the other hand, if $(h-k)\neq3n$, the intensity distribution depends on the stacking sequence. For the twinned fcc structures, *ABCABC*... or *ACBACB*..., reciprocal-lattice points occur at $l=m\pm1/3$ with m an integral. For hcp, *ABABAB*... or *ACACAC*..., nodes occur at $l=m\pm1/2$. If stacking faults occur, the intensity maximum is broadened and spread along the rods. For randomly stacked layers, the intensity is continuously distributed along these rods with a maximum at $l=m\pm1/2$ and a minimum at $l=m$ with an intensity ratio of 9:1. The two sets of rods contribute in a qualitatively different manner to the observed powder-diffraction pattern. The high-intensity spots along the $(h-k)=3n$ rods, when orien-

tationally averaged, generate sharp Bragg peaks in the powder pattern. Conversely, the continuous intensity distribution along the $(h-k)=3n\pm1$ rods results in a broad, relatively featureless scattering peak in the powder spectrum. The rscp powder pattern of colloidal hard spheres consequently shows a distinctive combination of sharp Bragg peaks and broad diffuse regions of scattering.

Both of these features can be clearly identified in Fig. 3. Indeed, the close similarity between Fig. 3 and the results for the single-component hard-sphere crystals [28] suggests that the crystallites formed in this binary suspension are fractionated and consist of just one of the two species. The three sharp Bragg peaks visible in the powder pattern (Fig. 3) arise from scattering from the unbroadened (00) and (11) rods [and the equivalent rods $(2,\bar{1})$, $(1,\bar{2})$, $(\bar{1},\bar{1})$, $(\bar{2},1)$, and $(\bar{1},2)$]. Indexing these lines as the (001), (110), and (111) reflections gives a lattice parameter of $a=671\pm6$ nm. This is comparable to the diameter of the larger particle ($2R_L=642$ nm) so the crystal formed in this binary mixture must consist of a rscp crystal of large spheres.

A similar analysis of the scattering from all samples in the region $n_S/n_L\leq1.0$ or $\phi_S/\phi_L\leq0.4$ [represented by the filled circles in Fig. 2(a)] confirms fluid-crystal L coexistence. The crystals formed in the coexisting region of the phase diagram are strongly compressed in comparison with the melting density for one-component hard spheres of $\phi_m=0.545$. Measurements of the positions of the Bragg reflections revealed coexisting crystal densities as high as 0.65 in this region. Samples where there was an excess of small particles showed an analogous behavior. In the region $n_S/n_L\geq13(\phi_S/\phi_L\geq5)$, light crystallography confirmed the coexistence of a fluid and a crystalline phase, comprised of small spheres [indicated by the open circles in Fig. 2(a)]. Noticeably, however, the densities of the crystallites, as estimated from the positions of the Bragg peaks, were not as high as those found where large spheres were in excess with densities $\phi_S\sim0.54$, comparable to ϕ_m.

The most dramatic observation was in samples which contained sizable concentrations of both large and small species. Samples with compositions in the range $1.0<n_S/n_L<13.0$ $(0.4<\phi_S/\phi_L<5)$ remained single phase and homogeneous for at least six months. Light scattering revealed a "fluidlike" amorphous arrangements of particles.

B. Size ratio $\alpha=0.52$

Reducing the radius ratio to $\alpha=0.52\pm0.01$ significantly changed the observed pattern of behavior. Our findings are summarized in Fig. 2(b). Twenty-eight mixtures were prepared by combining large spheres ($R_L=448$ nm) of suspension E with small spheres of colloid $C(R_S=231$ nm) at eight different number ratios with volume fractions in the range $0.494\leq\phi_L+\phi_S\leq0.581$.

The most dramatic difference from the experiments at $\alpha=0.72$ is the formation of mixed binary or superlattice crystals. Superlattice colloidal crystals were found in mixtures with composition $n_S/n_L=14$ $(\phi_S/\phi_L=2)$. The superlattice phase appeared in coexistence with a second crystalline phase of pure small crystals and a fluid phase [the open diamonds in Fig. 2(b)]. Formation was exceedingly slow. A few days after mixing, iridescent specks of nucleating crystallites

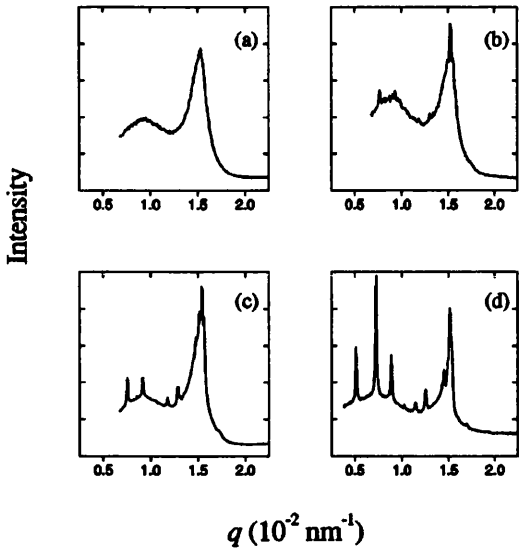

FIG. 4. The scattering from the bottom iridescent layer formed in mixture with $\alpha=0.52$, $n_S/n_L=14$ $(\phi_S/\phi_L=2)$, and $\phi=0.521$ measured (a) 107, (b) 116, (c) 130, and (d) 198 days after mixing. Pattern (a) shows that the first-formed crystalline phase consists of small (diffraction-broadened) crystallites of small spheres ($a=506$ nm, $\phi_S=0.56$). After ~110 days the low-q reflections of the LS_{13} superlattice become visible. The proportion of LS_{13} in the crystalline phase increases with time. The Bragg peaks in (d) are, in order of increasing q, the (200), (220), (222), (400), (420), (422), and (440) reflections of the LS_{13} structure, which gives a cubic lattice constant of $a=2460$ nm and a crystal density of $\phi=32\pi(R_L^3+13R_S^3)/(3a^3)=0.56$.

appeared throughout the samples and sedimented to form a polycrystalline layer. Light-scattering measurements revealed [Fig. 4(a)] that this crystalline layer consisted of a random close-packed crystal of small spheres. Only after four months did features first appear in the scattering profile characteristic of a superlattice structure [see Fig. 4(b)]. The intensity of the superlattice peaks grew rapidly over the next four weeks and then remained essentially unchanged for three months of observation. The regular positions of the sharp Bragg reflections evident in Fig. 4(d) are consistent with the formation of a cubic structure. Fitting the peak positions to $q_{hkl}=(2\pi/a)\sqrt{h^2+k^2+l^2}$ gives a cubic lattice constant a of 2460 ± 6 nm. The large lattice constant and the similarity of the scattering seen in Fig. 4(d) to previous measurements made on mixtures of $\alpha=0.58$ suggest that the structure formed is the cubic LS_{13} phase. Assuming an LS_{13} structure, the experimentally determined lattice constant gives a crystal density of $\phi_L+\phi_S=0.56$, which compares favorably with the overall density of the suspension $\phi=0.521$.

A second superlattice phase appeared in mixtures [marked by stars in Fig. 2(b)] with composition $n_S/n_L=5$ and 8 $(\phi_S/\phi_L=0.7$ and 1.1). The rate of crystallization was again slow with full crystallization taking about 80 days for $n_S/n_L=5$ $(\phi_S/\phi_L=0.7)$ and over 200 days for mixtures with $n_S/n_L=8$ $(\phi_S/\phi_L=1.1)$. Crystals were observed visually first in a narrow layer at the center of the sample cuvette. Analysis by powder light crystallography showed three relatively weak but sharp Bragg peaks superimposed on a broad

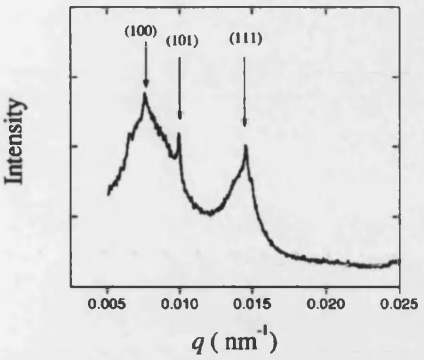

FIG. 5. The scattering from the bottom iridescent layer formed in a mixture of size ratio $\alpha=0.52$, composition $n_S/n_L=5(\phi_S/\phi_L=0.7)$, and volume fraction $\phi=0.509$. The Bragg reflections index on the hexagonal unit cell of the LS_2 superlattice. The featureless background scattering present indicates that the lower phase also probably contains amorphous material.

diffuse background (Fig. 5). The reflections measured from four different mixtures indexed on a hexagonal lattice, $q_{hkl}^2/4\pi^2=(4/3a^2)(h^2+k^2+hk)+(l^2/c^2)$, with a mean hexagonal interlayer spacing of $c/a=1.041\pm0.001$ and a mean lattice parameter of $a=950\pm2$ nm. The most plausible structure for the observed phase is the LS_2 lattice. Strong evidence for the formation of this structure in mixtures with $\alpha=0.52$ comes from a comparison with earlier data. The experimental c/a ratio differs by less than 0.4% from that found previously [2] and the crystal density, $\phi=0.622\pm0.004$, is similar to the values quoted in Ref. [14].

The two regions of superlattice formation were separated by a central band of compositions where samples remained amorphous ($n_S/n_L=8$ or $\phi_S/\phi_L=1.1$). In this region, crystallization was totally suppressed and mixtures remained amorphous during the year-long duration of our observations. Similar behavior was also observed in the second region of amorphous behavior for compositions $0.5<n_S/n_L<4$ $(0.07<\phi_S/\phi_L<0.6)$. Finally, close to the two axes the phase behavior is similar to that observed in the $\alpha=0.72$ system. So, for instance, two-phase coexistence of random-packed L crystals and fluid is found for $n_S/n_L\leq0.5$ $(\phi_S/\phi_L=0.07)$, while for $n_S/n_L\geq30$ $(\phi_S/\phi_L\geq4)$ the stable phase are crystals of small spheres and fluid.

It is instructive to compare the current observations for $\alpha=0.52$ with the experimental results obtained previously [14] for $\alpha=0.58$ and 0.62 (Fig. 6). It is clear that there are striking differences between these closely spaced sets of mixtures. First, the superlattice regions in the $\alpha=0.52$ phase diagram are narrow in extent in comparison with the well developed region of superlattice formation found for the $\alpha=0.58$ mixture. Second, there is a marked slowing-down in the rate of nucleation and growth of the LS_2 and LS_{13} phases as α is reduced towards 0.52. In the $\alpha=0.58$ mixture, crystallites of LS_{13} appeared within three days, with LS_2 formation taking about five weeks. In comparison, at $\alpha=0.52$, growth of LS_2 and LS_{13} required over three months. Finally, the phase diagram at $\alpha=0.52$ is more complicated than either the $\alpha=0.58$ or 0.62 diagrams. In particular, the two regions of superlattice coexistence are separated in the $\alpha=0.52$ system by an intervening amorphous region not

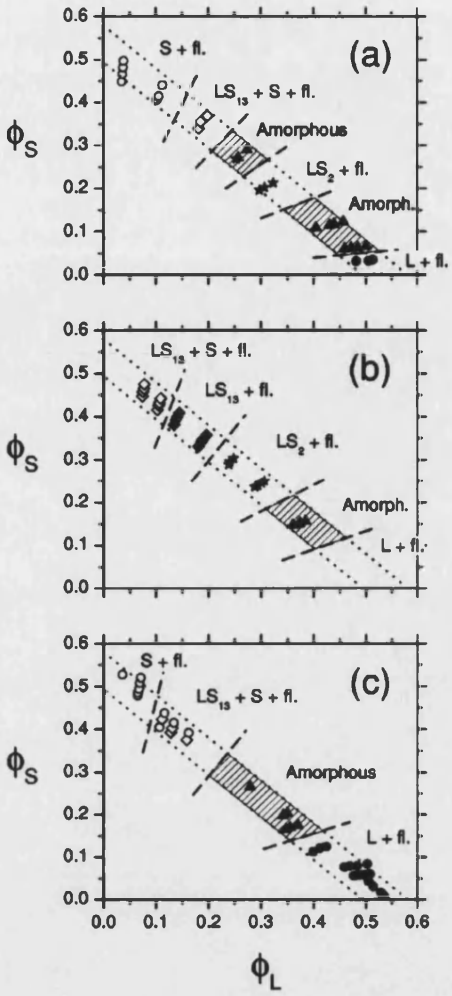

FIG. 6. A comparison of the experimental phase behavior seen in mixtures of size ratio (a) $\alpha=0.52$, (b) 0.58 and, (c) 0.62. The meaning of the symbols is the same as in Fig. 2. The regions of amorphous phases are shown shaded. The dashed lines correspond to the one-component hard-sphere freezing ($\phi_f=0.494$) and melting densities ($\phi_m=0.545$). All other lines are drawn as guides to the eye.

present for $\alpha=0.58$. These changes suggest that the LS_2 and LS_{13} phases are becoming increasingly less stable as the size ratio α is reduced.

C. Size ratio $\alpha=0.42$

Binary mixtures with radius ratios of $\alpha=0.42$ showed substantially different behavior from the $\alpha=0.52$ mixtures studied above. The most striking difference was observed in mixtures with sizeable number densities of each species. In the $\alpha=0.52$ system, these central compositions form superlattice phases. Reducing the radius ratio to $\alpha=0.42$ seemed to destabilize all crystalline phases. Those compositions which crystallized in the $\alpha=0.52$ system now remained totally amorphous. Our findings are summarized in Fig. 2(c). Twenty-one mixtures of radius ratio $\alpha=0.42\pm0.01$, at five different number ratios, were made by combining large colloidal particles from batch $E(R_L=448$ nm) with smaller par-

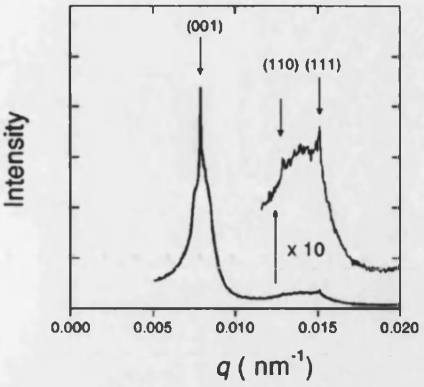

FIG. 7. Scattering from the crystalline layer formed in a suspension of ratio $\alpha=0.42$, $n_S/n_L=1(\phi_S/\phi_L=0.07)$, and $\phi=0.537$. The Bragg peaks are indexed on the rscp basis.

ticles from batch $B(R_S=188\,\text{nm})$ to give volume fractions in the range $0.525\leq\phi_L+\phi_S\leq0.565$. In a one-component system, suspensions with volume fractions in this range crystallize rapidly.

The sequence of behavior observed resembles, at least superficially, that reported above for the $\alpha=0.72$ system. So, for instance, in samples with an excess, by volume, of large spheres ($n_S/n_L=0.5$, 1, or 2), the final equilibrium state corresponded to a fluid-crystal coexistence. However, in comparison with the $\alpha=0.72$ system, crystallization was noticeably slower. For instance, $\alpha=0.72$ mixtures with $n_S/n_L=0.5$ formed small crystallites, just visible by eye (estimated size 10–15 μm), within two days of mixing. In the $\alpha=0.42$ system, mixtures with the same composition and total density took approximately 20 days for crystals to be observable. Over a couple of days, these small crystallites sank to the bottom of the sample cell and formed an iridescent crystalline layer. Figure 7 shows the powder-diffraction profile measured from the crystalline layer formed in a suspension with an equal number of large and small spheres and a total density of $\phi=0.537$. As is clear from a comparison between Fig. 7 and Fig. 3, the measured scattering profile resembles closely the scattering seen from a rscp crystal of large spheres.

While the evident similarities between the scattering observed in this region and that from a rscp crystal of large spheres seem, at first sight, to suggest that the crystalline phase is composed of a phase-separated crystal of large spheres, a closer study of the scattering data shows it to be inconclusive. The theoretical calculations outlined in Sec. II suggest that for $\alpha=0.42$ any one of a family of close-packed superlattice phases which includes NaCl and NiAs could be stable. Below we demonstrate that while the scattering from each of these structures is in principle different from each other and from the fractionated large-sphere crystal phases, under the conditions of our experiments the differences are small. To distinguish between the different superlattice structures and a rscp crystal of large spheres requires careful intensity measurements. Because of the high sensitivity of the particle scattering near index-match, these experiments are very demanding. Consequently, from scattering alone, we cannot identify the nature of the crystal seen in Fig. 7. We shall return to this point in Sec. VI.

Increasing the proportion of small spheres further reduced the rate of crystallization. In suspensions with $n_S/n_L=8$ ($\phi_S/\phi_L=0.6$), crystals were observed but only in the lowest volume fraction sample ($\phi=0.532$). Even in this sample the crystallites were sufficiently small that efforts to measure the scattering from the small proportion of crystalline material present were unsuccessful. With larger proportions of small spheres, $n_S/n_L=13$ or 25 ($\phi_S/\phi_L=1$ or 2), crystallization was totally suppressed and remained totally amorphous during our observations. Very large proportions of small spheres ($n_S/n_L=52, \phi_S/\phi_L=4$) gave mixtures which, once again, displayed two-phase coexistence. In these samples, flecks of colloidal crystallites appeared throughout the sample within about 30 days of mixing. The crystallites rapidly sedimented into an iridescent layer at the bottom of the cuvette. Powder-diffraction measurements gave results which were almost identical to the scattering from crystals of the small spheres alone. In this case there is no possibility of confusion between a crystal of small spheres and a NaCl-type superlattice, so we can confidently identify the crystalline phase formed in the mixture as a random-stacked crystal of small spheres.

D. Size ratio $\alpha=0.39$

To clarify, if the NaCl-type superlattice is formed at $\alpha\sim0.4$, the experiments detailed in Sec. IV C were repeated but with a mixture of fluorescent and nonfluorescent particles. The real-space structure of the crystals formed was studied using fluorescent confocal scanning laser microscopy (CSLM) and is discussed below in Sec. VI. Here we summarize the observed phase behavior.

Twenty-four binary mixtures were prepared by combining small fluorescent particles from batch A ($R_S=175\,\text{nm}$) with larger, nonfluorescent spheres of colloid $E(R_L=448\,\text{nm})$ to give a size ratio of $\alpha=0.39\pm0.01$. The mixtures studied are detailed in Fig. 2(d) together with a summary of the phase behavior found. The small particles were fluorescently labeled by incorporating the monomer 2-(methyl-(8-nitrobenzo [1,2,5] oxadiazol-1-yl)-amino) methyl methacrylate (NBD-MMA) into the core of the colloidal particle. The dye is absent from the surface of the particle so the interaction potential and the phase behavior of the small spheres ought not to be affected by labeling. Experiments confirm this prediction with suspensions of pure fluorescently labeled particles crystallizing rapidly with a melting density of $\phi_m=0.548$, which is close to the value expected for hard spheres ($\phi_m=0.545$). Furthermore, measurements of the scattered light intensity from the crystals, at long wavelengths ($\lambda=647\,\text{nm}$) where the particles do not fluoresce, reveal that the crystal has the rscp structure expected for colloidal hard spheres. Consequently, the differences observed between the phase diagrams of the fluorescent $\alpha=0.39$ and nonfluorescent $\alpha=0.42$ mixtures may be attributed to a change in the size ratio α and not to labeling.

Comparison of the two phase diagrams shows that reducing α from 0.42 to 0.39 broadens the extent of the amorphous region. So while for $\alpha=0.42$ the amorphous region extended over compositions from $8<n_S/n_L<25$ ($0.6<\phi_S/\phi_L<1.9$), the range has expanded to $2<n_S/n_L<50$ ($0.1<\phi_S/\phi_L<3.0$) by $\alpha=0.39$. In the $\alpha=0.39$ mixture, the

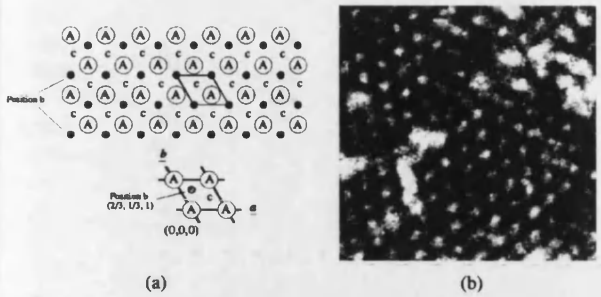

FIG. 8. (a) The (001) face of the NaCl crystal. The positions of the large spheres are labeled "*A*." The small spheres (shown in bold) occupy the "*b*" set of interstitial sites while the "*c*" sites are vacant. The unit cell of the hexagonal layer is shown in bold. (b) CSLM image of ordered binary crystal formed in a suspension of size ratio $\alpha=0.39$, composition $n_L/n_S=1$ ($\phi_S/\phi_L=0.06$), and volume fraction $\phi=0.532$. The picture was taken with a 100 $\times$ 1.3 NA oil immersion lens and is 12.5 μm square. The hexagonal order of the small fluorescent particles is clearly visible.

two regions of fluid-crystal coexistence are extremely narrow and crystallization is essentially limited to mixtures very rich in either large or small spheres. Outside these compositions, mixtures remained amorphous on the time scale of the experiments. Finally, we note that samples containing an equal number of big and small spheres, $n_S/n_L=1$ ($\phi_S/\phi_L=0.06$), show fluid-crystal coexistence.

V. SCATTERING FROM *LS* SUPERLATTICES

The *LS* family of superlattices (NaCl, NiAs, and random-stacked analogs) consists of a close-packed layer of large spheres with small spheres occupying all the available octahedral interstitial sites in the resulting lattice. To understand why the scattered intensity is insensitive to the differences between these structures, it is advantageous to start from the basic element common to each of these structures—a single hexagonal slice containing both large and small particles. Each of the *LS* crystals is generated by stacking these slices in a different order. Figure 8(a) shows one such composite slice together with the conventionally defined hexagonal basis vectors **a** and **b**. The axis c is chosen as equal to the distance between two neighboring large-sphere layers and is set so that the layer of large spheres lies in the reference plane $c=0$. The slice consists of a hexagonal layer of large spheres with a further layer of small spheres situated in the plane $c=1/2$. The small spheres are positioned above the center of the equilateral triangle formed by the centers of the three adjoining large spheres in the $c=0$ reference plane. There are two ways in which the layer of small spheres may be placed on the reference layer *A* of large spheres, which are designated by *b* and *c* in Fig. 8(a). The position of the *b* sphere [shown in black in Fig. 8(a)] with respect to the large spheres in layer *A* is given by the vector $2\mathbf{a}/3+\mathbf{b}/3+\mathbf{c}/2$, while the *c* sphere is located at $\mathbf{a}/3+2\mathbf{b}/3+\mathbf{c}/2$. The full three-dimensional structure is obtained by stacking slices repeatedly on top of the slice shown in Fig. 8(a). The projection of each large-sphere layer on the reference plane ($c=0$) can take only one of three different positions—*A*, *B*, or *C*—if the structure is to be close-packed. In position *B* (or *C*), the large sphere in the second slice is placed above a vacant interstitial *b* (or *c*) site in the first slice.

The two simplest arrangements which are periodic are the NiAs lattice, consisting of a close-packed hexagonal stacking of large spheres (upper case) with small spheres (lower case) organized in vertical columns, *AcBcAcBcAcBc*, and the NaCl lattice where the arrangement of the large-sphere layers is fcc and the layers of small spheres generate a second interlocking fcc lattice, *AcBaCbAcBaCbAc*. One-component colloidal crystals are nearly always randomly stacked (with stacking sequences such as *ABCBCAB*... or *ACBABC*... rather than pure fcc or hcp) so similarly we expect that random superlattice structures such as *AcBaCaBaCbAcB* may occur. Here we show that the scattering from any of these structures closely resembles that of the identically stacked large-sphere crystal. To that end we shall consider in detail just one of the possible superlattice structures—namely the NaCl lattice. This is the most straightforward case to analyze but our arguments are readily extended to treat the other structures.

It is clear that for the NaCl structure *AcBaCb*... or its twin *AbCaBc*..., the periodicity and symmetry of the small-sphere lattice are the same as that of the large-sphere lattice (although displaced by $\Delta c=1/2$). This is very different from the behavior observed when either LS_{13} or LS_2 form, where the superlattice structures have a new symmetry and periodicity that is not shared with the one-component crystal. The origin of this difference lies in the nature of the NaCl structure, where the small spheres occupy interstitial sites rather than substitutional sites as in LS_2 or LS_{13}. Occupying interstitial sites does not alter the three-dimensional arrangement of the larger spheres so that the Bragg reflection conditions for the NaCl structure are identical to those for a fcc lattice of large spheres. Although the formation of NaCl does not alter the number of Bragg reflections, it does modify their intensity. In NaCl, the small-sphere lattice is displaced relative to the large-sphere lattice so that scattering from the small spheres is out-of-phase compared with the large-sphere scattering and the diffracted intensity is modulated.

The scattered intensity produced by a phase of partially disordered layers has been addressed by a number of authors. Excellent reviews are available in the textbooks on x-ray diffraction by Guinier [30] and Warren [32]. In the systems of interest to us, the three-dimensional (3D) close-packed structures are built up from 2D hexagonal slices and the intensity scattered by the crystal is concentrated along hexagonally arranged rods in reciprocal space (see Sec. IV A). The intensity along each of the (h,k) rods is determined by the stacking sequence of the layers. A general expression for this intensity $I_{hk}(l)$, for a system of N identical slices stacked along the c axis, has been derived by Guinier [30],

$$I_{hk}(l)=\frac{|F|^2}{N}\sum_{m=-N}^{m=N}\left(1-\frac{|m|}{N}\right)y_m\exp(2\pi ilm), \qquad (1)$$

where l is the distance along the rod expressed in units of $c^*=2\pi/c$ and F is defined by

$$F=\sum_p b_p e^{-2\pi i(hx_p+ky_p+lz_p)}, \qquad (2)$$

with b_p the amplitude scattered by each of the p particles contained within the unit cell. The function F is called, rather confusingly, the structure factor in the crystallography literature, although $|F|^2$ is actually the intensity scattered by a single unit cell and so is best thought of as a cell form factor. The function y_m summarizes the degree of correlation between layers. In detail, $|F|^2 y_m$ is the ensemble average $\langle F_n F^*_{n+m}\rangle$ of the product of the amplitudes scattered by two unit cells separated by a vertical distance mc along the c axis.

For the NaCl structure, *AcBaCb*..., we select the reference slice as $\overline{Ac}$ with a unit cell which contains a large sphere at position A and a second (small) sphere on the interstitial site c. The corresponding cell form factor, $|F_{Ac}|^2$, is readily calculated from Eq. (2) and the geometry of Fig. 8(a) as

$$|F_{Ac}|^2 = b_L^2 \cos^2 \pi\left(\frac{h-k}{3}+l\right) - 2b_L b_S \cos 2\pi\left(\frac{h-k}{3}-l/2\right)+b_S^2, \tag{3}$$

where b_L and b_S are the amplitudes of scattering from the large and small particles, respectively. The position of the $\overline{Ba}$ slice is translated by the vector $(2\mathbf{a}/3)+(\mathbf{b}/3)$ relative to the $\overline{Ac}$ slice so that the structure factor for a unit cell of slice $\overline{Ba}$ is

$$F_{Ba} = F_{Ac} e^{2\pi i[(h-k)/3]}. \tag{4}$$

Similarly,

$$F_{Cb} = F_{Ac} e^{-2\pi i[(h-k)/3]} \tag{5}$$

for the slice $\overline{Cb}$. Assuming fault-free fcc stacking, the autocorrelation function y_m may be calculated analytically from Eqs. (4) and (5) with the result $y_m = e^{-2\pi i m(h-k)/3}$. The intensity along the (h,k) row is then obtained from Eq. (1) as

$$I_{hk}(l) = \frac{|F_{Ac}|^2}{N}\sum_{m=-N}^{m=N}\left(1-\frac{|m|}{N}\right) y_m \exp(2\pi i m\Lambda) = |F_{Ac}|^2 \frac{\sin^2 \pi N\Lambda}{\sin^2 \pi\Lambda}, \tag{6}$$

where $\Lambda = l-(h-k)/3$. The intensity I_{hk} is a sharply peaked function whose maximum value is $|F_{Ac}|^2$, for integral values of Λ. As the number of layers increases, $N\to\infty$, it becomes a δ function. In general, there are two types of Bragg rods. For rods with $(h-k)=3n$, where n is an integer, there is a succession of nodes at integral values of l. On the other hand, for rods with $(h-k)=3n\pm 1$, the reciprocal-lattice points occur for $l=n\pm 1/3$. All intensity nodes have the same maximum value of $|F_{Ac}|^2$.

There is no free-energy difference between the sequence *AcBaCb*... and the symmetric twin structure *AbCaBc*..., so in experiments we expect a superposition of the scattering from both crystals. The scattering from the sequence *AbCaBc*... may be calculated using the methods of the preceding paragraph. The unit cell of the NaCl twin contains a large sphere at A and a small sphere on the b-interstitial site so the cell form factor, $|F_{Ab}|^2$, is

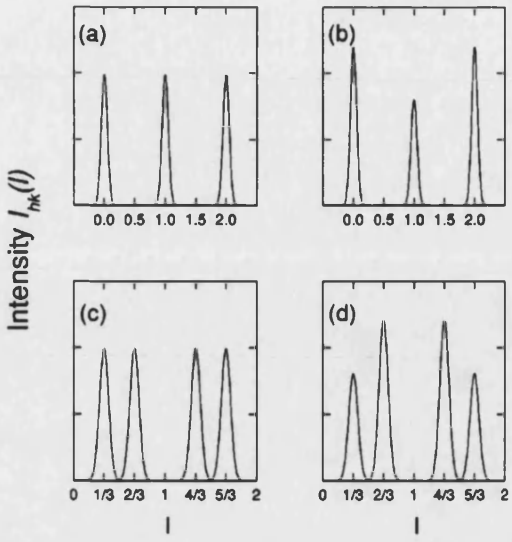

FIG. 9. The intensity distribution $I_{hk}(l)$ along the (h,k) Bragg rods in reciprocal space for a twinned fcc lattice of large spheres [(a) and (c)] and for the twinned NaCl lattice [(b) and (d)]. The top figures [(a) and (b)] show $I_{hk}(l)$ along $(h-k)=3n$ rods while the bottom set [(c) and (d)] shows the corresponding variation along the $(h-k)=3n\pm 1$ rods. The intensity is calculated assuming an amplitude ratio $b_L/b_S=10$.

$$|F_{Ab}|^2 = b_L^2 \cos^2 \pi\left(\frac{h-k}{3}-l\right) - 2b_L b_s \cos 2\pi\left(\frac{h-k}{3}+l/2\right)+b_s^2. \tag{7}$$

The layer correlation function is simply $y_m = e^{2\pi i m(h-k)/3}$. Following Eq. (6), it is easily shown that nodes of intensity $|F_{Ab}|^2$ occur at $l=n\pm 1/3$ along the $(h-k)=3n\mp 1$ rods and for integral l along the $(h-k)=3n$ rods. Consequently, the twinned NaCl crystal (*AcBaCb*..., *AbCaBc*...) has reciprocal-lattice points at integral l along the $(h-k)=3n$ rods and at $l=n\pm 1/3$ along all other rods. The topology of the reciprocal lattice is identical to the lattice of the twinned fcc crystal of large spheres, outlined in Sec. IV A, so the two structures have identically positioned Bragg reflections.

The change in intensity of the Bragg reflections with superlattice formation depends upon the relative magnitude, b_L/b_S, of the scattering from large and small particles. For a homogeneous particle of radius R, the scattering amplitude is given by the standard expression [33]

$$b(qR) = 4\pi R^3 \Delta n\left(\frac{\sin qR - qR\cos qR}{(qR)^3}\right), \tag{8}$$

where Δn is the refractive index mismatch between particle and medium. The intensity of scattering depends very strongly upon the particle size and so in a binary mixture the large particles scatter light much more efficiently than small particles. For instance, for a size ratio of $\alpha=0.42$ and a scattering vector $qR_L\sim 3.5$ [matching the (001) reflection of the twinned NaCl crystal], the ratio b_L/b_S is about 10. Figure 9 shows the intensity distribution along the Bragg rods

for the twinned NaCl and for the twinned fcc lattice of large spheres, calculated for this amplitude ratio. It is clear that although there are changes in the scattering distribution, the effects are small. For polycrystalline samples, the differences are likely to be even less noticeable since the results in Fig. 9 have to be averaged over all orientations. In conclusion, it is clear that identifying the NaCl superlattice from powder diffraction demands accurate intensity measurements.

VI. CONFOCAL MICROSCOPY

To determine unequivocally if a superlattice is formed in colloidal mixtures of size ratio $\alpha=0.39$, we have used direct imaging methods. Fluorescence confocal scanning laser microscopy (CSLM) has several distinctive features which make it excellently suited to this problem. First, the use of both a point source and a point detector results in a powerful depth discrimination so only a thin slice of the sample around the focal region of the microscope objective is imaged. Second, the optical resolution is comparable to colloidal dimensions, so single-particle positions can be readily identified. Third, contrast relies on a fluorescent dye, so by labeling alternately the large and small particles in a binary suspension, the structure of mixed crystals may be determined and, finally, suspensions may be studied which are thick enough to show the same phase behavior as they would in the bulk.

High-contrast single-particle images were achieved by incorporating the fluorescently tagged monomer 2-(methyl-(8-nitro-benzo [1,2,5] oxadiazol-1-yl)-amino)methyl methacrylate (NBD-MMA) into the core of the colloidal particle [25]. To clearly differentiate between a NaCl-type superlattice and a crystal of large spheres, only the small particles in the mixture were fluorescently labeled. The large particles are nonfluorescent and are consequently not imaged.

Figure 8(b) shows a fluorescent confocal image of the crystalline phase formed in a mixture of small NBD-labeled and large unlabeled PMMA particles, dispersed in an index-matched mixture of decalin and CS_2, with composition $n_S/n_L=1$ ($\phi_S/\phi_L=0.06$) and volume fraction $\phi=0.532$. The image was recorded about 15 μm below the top glass wall and four days after mixing. Although the image is noisy, it is apparent that the small fluorescent particles are highly localized within a three-dimensional periodic structure. A careful analysis of this micrograph demonstrates that the crystal consists of hexagonal layers of small spheres. The center-to-center distance in the hexagonal plane is 1080 $\pm$ 100 nm, which is considerably larger than the diameter ($2R_S=350$ nm) of the small particles but comparable to the size of the large particle ($2R_L=896$ nm). This suggests that in the images of Fig. 8(b), the small spheres are separated by nonfluorescent (and thus not visible) larger particles. Given these observations, the view in Fig. 8(b) can be identified as the (001) plane of the *LS* superlattice, in the reduced hexagonal basis (*a,b,c*) introduced in Sec. V. The crystal is orientated with the close-packed (001) plane parallel to the walls of the cuvette.

A sketch of this close-packed plane is reproduced in Fig. 8(a), from which it is apparent that the center-to-center separation of the small spheres is identical to that of the large particles and equal to the lattice parameter *a*. Further confirmation for this identification comes from scattering measurements. If a *LS* structure is formed, then the intense first Bragg peak at $q_{001}=7.91\times10^{-3}$ nm^{-1} corresponds to a reflection from the (001) planes of the superlattice. The interplane spacing is $c=2\pi/q_{001}=794$ nm. The hexagonal (001) planes are close-packed in the *LS* structure so the center-to-center separation within the plane is $a=c\sqrt{3/2}$ or 973 nm. This value is in good agreement with the directly measured interparticle spacing, obtained from Fig. 8(b), of $a=1080$ $\pm$ 100 nm.

These results demonstrate that a hexagonal layer of large and small spheres, the basic element common to all of the *LS* structures, is formed in a binary hard-sphere mixture of $\alpha=0.39$. In order to distinguish between NaCl, NiAs, or a random-stacked crystal, it is necessary to determine the stacking sequence of the hexagonal layers. To this end, we recorded a series of confocal micrographs of the same lateral position in the crystal at depths 0.6 μm apart. Unfortunately, thermal drift prevented us from accurately superimposing the optical sections at different heights through the crystal, so we could not reliably identify the sequence of small-particle positions in the stacked layers. Consequently, we are unable to distinguish between NaCl, NiAs, or a random-stacked crystal.

VII. COMPARISON WITH THEORY

A. Size ratio $\alpha=0.72$

The phase behavior reported above provides broad confirmation of the theory outlined in Sec. II. First, CsCl is not observed in our experiments, in agreement with the predictions of Eldridge *et al.* [14] and Cottin and Monson [5]. This is the case even though the experimental size ratio is close to the peak in the maximum packing curve at $\alpha=0.732$, where we expect the formation of CsCl, if it is to occur, to be most favorable. Second, with no superlattice we expect the two different-sized spheres to be totally immiscible in the solid state [16] and the fluid-solid phase diagram to contain a eutectic. The equilibrium phase behavior predicted by the immiscible model of Bartlett [34] for a size ratio of $\alpha=0.72$ is plotted in Fig. 10 together with the experimental samples studied in this work. We find very close agreement between the predictions of theory and observations in samples with either an excess of large or small spheres. So for mixture compositions $n_S/n_L=0.5$ and 1.0 ($\phi_S/\phi_L=0.2$ and 0.4) we predict and find crystals of large spheres coexisting with a fluid (the filled circles in Fig. 10) while for mixtures with $n_S/n_L=13.0$ or equivalently $\phi_S/\phi_L=5$ (the open circles in Fig. 10) we observe and predict two-phase coexistence between a crystal of small spheres and a fluid. In particular, in the region of two-phase coexistence, we find essentially quantitative agreement with the theory of Ref. [34]. The inset diagram in Fig. 10 compares the large-sphere crystal density predicted (ϕ_{calc}) with values measured from crystallography (ϕ_{exp}) for samples in the fluid-crystal *L* region. As is clear, the theoretical and experimental values for the crystal density are in excellent agreement (the dashed line depicts the condition $\phi_{exp}=\phi_{calc}$). Although the phase behavior predicted in Ref. [34] for mixtures rich in small or large spheres is confirmed in this work, there is clearly a striking disagreement in samples with a significant concentration of both

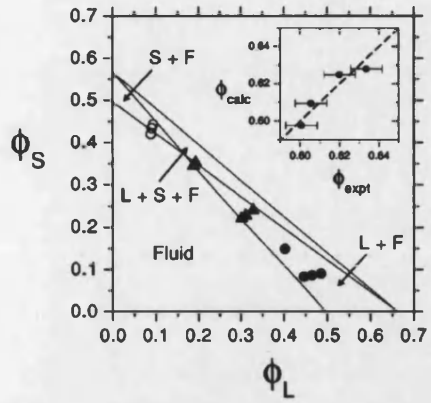

FIG. 10. A comparison between the phases observed and those predicted from the immiscible mixture model [34] for a size ratio of $\alpha=0.72$. See Fig. 2 for symbol definitions. In the inset plot the crystal volume fractions measured (ϕ_{exp}) for mixtures in the two-phase $L+F$ region are compared with predictions from theory (ϕ_{calc}). The line shows the limit $\phi_{calc}=\phi_{expt}$.

large and small spheres (the filled triangles in Fig. 10). Experimentally, we observe amorphous "glassy" phases where theory predicts two-phase coexistence.

B. Size ratio $\alpha=0.52$

The observed behavior at this size ratio is broadly in line with simulation predictions. Cell-model calculations [5,35] show that the LS_{13} lattice is stable for size ratios $0.54\leq\alpha<0.62$ while the LS_2 lattice is stable over the wider range of $0.42<\alpha<0.6$. The mixtures studied at $\alpha=0.52$. are accordingly just below the lower stability boundary of the LS_{13} structure. Figure 11 depicts the equilibrium phase diagrams (calculated from the cell model) for size ratios $\alpha=0.52$ and 0.54, just below and above this boundary. At $\alpha=0.54$, the region where the LS_{13} phase is formed has already shifted to high densities. With a further reduction in α, the LS_{13} phase disappears completely from the equilibrium phase diagram and is replaced by a wide region of fluid-LS_2 coexistence.

Although the overall pattern predicted by theory is confirmed, there is clearly disagreement in matters of detail. A closer comparison between the behavior of samples with α

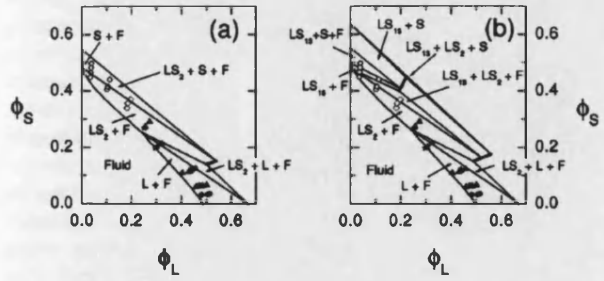

FIG. 11. A comparison of the phases observed in a colloidal mixture of $\alpha=0.52$ with predictions from the cell model for (a) $\alpha=0.52$ and (b) 0.54. The two superlattice phases, LS_2 and LS_{13}, are shown in bold. The symbols denote the experimental data and are defined following Fig. 2.

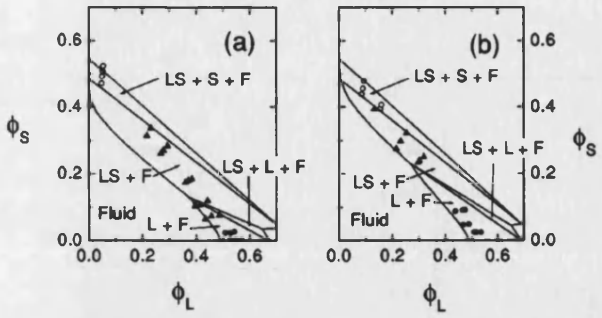

FIG. 12. A comparison between the phases observed and those predicted from the cell model for (a) $\alpha=0.39$ and (b) 0.42. The symbols are defined following Fig. 2.

$=0.52\pm0.01$ (shown by the points in Fig. 11) and the theoretical predictions [35] at $\alpha=0.52$ [Fig. 11(a)] reveals discrepancies. First, and most obvious, LS_{13} is predicted not to be stable. The thermodynamic state predicted for the experimental samples with $n_S/n_L=14$ (the open diamonds in Fig. 11 at $\phi_S/\phi_L=2$) is instead a two-phase (or for the most concentrated sample a three-phase) coexistence between LS_2 and fluid. A thermodynamically stable LS_{13} phase is only achieved if the radius ratio is increased to 0.54 [Fig. 11(b)], above the experimental limit of $\alpha=0.52\pm0.01$. However, comparing the experimental data with the 0.54 predictions, it is clear from Fig. 11(b) that only the most concentrated of the three experimental samples with $n_S/n_L=14$ lies in a region where the LS_{13} crystal is predicted to be thermodynamically stable. We interpret this observation as evidence for kinetics factors favoring the formation of metastable LS_{13} in our experiments. Second, the two most concentrated samples at $n_S/n_L=8$ ($\phi_S/\phi_L=1.1$) which remain amorphous in our experiments (depicted by the central line of solid triangles in Fig. 11) are predicted to lie in a broad zone of two-phase AB_2-fluid coexistence. Third, the samples at $n_S/n_L=2$ and 1 ($\phi_S/\phi_L=0.3$ and 0.15) remain amorphous in our experiments (the filled triangles at the bottom of Fig. 11), whereas we expect formation of a (dense) L crystal and fluid. Although we have concentrated on the discrepancies, on a qualitative level there is a broad degree of agreement between the experimental observations and theory. For instance, the theoretical calculations rationalize why the LS_2 superlattice is not readily formed in samples with composition $n_S/n_L=2(\phi_S/\phi_L=0.3)$, whereas LS_{13} is readily formed in samples of composition $n_S/n_L=13$ ($\phi_S/\phi_L=1.8$). From Fig. 11(a), it is clear that at $n_S/n_L=2$ there is a wide zone of L crystal-fluid coexistence prior to LS_2 formation at higher densities.

C. Size ratios $\alpha=0.42$ and 0.39

There are substantial differences between theory and experiment at $\alpha\sim0.4$ in contrast with the reasonable agreement found at other size ratios. The predictions of the cell theory [35] are reproduced in Fig. 12 for size ratios $\alpha=0.39$ and 0.42, respectively. These diameter ratios are close to the substantial maximum ($\phi_{max}=0.79$ at $\alpha=\sqrt{2}-1$) seen in the close-packing curve for the NaCl structure (see Fig. 1). Consequently, the phase diagrams are dominated by the appear-

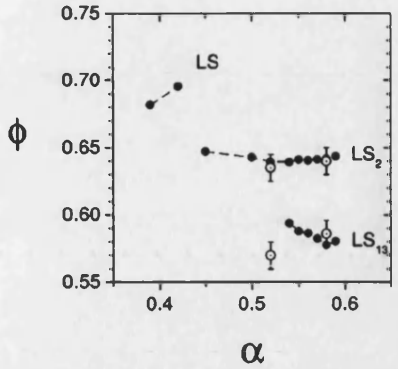

FIG. 13. The lowest densities (ϕ) for each superlattice in coexistence with a fluid, as a function of size ratio α. The filled circles are the simulation predictions of Eldridge *et al.* [14,4] while the experimental values are shown by the open points.

ance of an *LS* superlattice (the LS_2 and LS_{13} phases are no longer stable at these low diameter ratios). A notable feature of the phase diagrams is the very broad region of two-phase coexistence found between *LS* and fluid. The regions of coexistence between fluid and the large or small fractionated crystals, found near each of the axes, are considerably reduced in comparison with the larger diameter ratios (compare, for instance, Figs. 10 and 12). Indeed, comparing the two phase diagrams in Fig. 12, it is clear that the extent of the two-phase *LS*/fluid region expands rapidly with reducing α.

The observed phase behavior is shown by the points in Fig. 12. The disagreements between theory and experiments are most evident in the region where coexistence is predicted between a large-sphere crystal and fluid. The $\alpha=0.39$ mixture studied with confocal microscopy [marked by the half-filled circle in Fig. 12(a)] lies in the middle of this region, yet the data, reported above, clearly identify coexistence between an *LS* superlattice and fluid. A remarkable feature of the remaining data is the strong coincidence between the changes in the observed behavior and the theoretical boundaries, even though the actual phase behavior observed is different from that predicted. So, for instance, all of the mixtures (the filled triangles) which are predicted to lie in the region of two-phase coexistence *LS*/fluid remain amorphous in our experiments, while all those samples (the open circles in Fig. 12) which lie within the three-phase coexistence region between crystals of *LS*, *S*, and fluid separate into a crystal of small spheres and a second fluid phase. At present, the exact reasons for the disparities seen between theory and experiment at small diameter ratios are far from clear. An important factor in the difficulty seen in our experiments in crystallizing the *LS* lattice is probably the high densities predicted for the stable *LS* compound. Figure 13 summarizes the densities, predicted from simulation [4,14], at which each stable superlattice structure is first thermodynamically stable as a function of the relative radius ratio together with the densities found in experiment for the LS_2 and LS_{13} phases (the open circles). Two features are evident from this comparison. First, there is a close correspondence between theory and experiment for the densities found for the LS_2 and LS_{13} phases, and second, the densities predicted decrease quite markedly in the sequence $\phi(LS)>\phi(LS_2)>\phi(LS_{13})$. This order mirrors the observed difficulty with which each superlattice is nucleated. So, for instance, at $\alpha=0.58$, LS_{13} forms within a few weeks while the LS_2 lattice takes several months to grow and the *LS* structure is sufficiently slow as not to be observable at many compositions over the year-long course of our experiments at $\alpha\sim0.4$. It is probable that the difficulty nucleating the *LS* crystal reflects the density dependence of the solid-fluid interfacial tension γ. Little is known about how γ depends on the density mismatch between between fluid and crystal, but it seems clear that the strain at this interface will become larger as the difference in densities between the two phases increases. The large density mismatch predicted for the fluid-*LS* system increases γ for the solid-fluid interface and reduces the rate of nucleation markedly.

VIII. CONCLUSIONS

In this paper we have presented a detailed comparison between the phase behavior and structures found in binary mixtures of colloidal hard spheres and Monte Carlo and cell-model predictions for a mixture of hard spheres. Phase diagrams have been experimentally determined for systems with size ratios of $\alpha=0.72$, 0.52, 0.42, and 0.39 which agree reasonably well with the theoretical predictions. We have observed three distinct types of fluid-solid organization depending on the size ratio α. First, at $\alpha=0.72$ the large and small particles are almost completely immiscible in the solid phase, and the crystalline phase formed at high densities consists of a crystal of predominately either large or small spheres depending on the initial mixture composition; second, reducing the size ratio to $\alpha=0.52$ generates two ordered binary structures which we identify as the LS_2 and LS_{13} superlattice; and finally, at smaller size ratios $\alpha\sim0.4$, we observe an ordered binary *LS* structure which is isostructural with either NaCl or NiAs.

A detailed comparison of our observations with theoretical predictions shows several discrepancies which we attribute to kinetic factors. First, at $\alpha=0.52$ we observe both LS_2 and LS_{13} structures while only LS_2 is expected from cell-model calculations or simulations. The tendency for LS_{13} to be formed at size ratios where it is not stable may reflect the high degree of local icosahedral order present in dense fluids [3]. Second, at $\alpha=0.42$ the observed phase diagram contains a very substantial region of amorphous ordering. The extent of the amorphous region increases as α is reduced to 0.39 and probably reflects the difficulty in nucleating a high-density crystal from a low-density fluid at these size ratios.

ACKNOWLEDGMENTS

This work was supported by the Engineering and Physical Sciences Research Council. We thank Alfons van Blaaderen for his generous assistance with the confocal microscopy experiments. We also acknowledge many valuable discussions with Peter Pusey, Harmut Lowen, and Stuart Henderson.

[1] P. M. Chaikin and T. C. Lubensky, *Principles of Condensed Matter Physics*, 1st ed. (Cambridge University Press, Cambridge, 1995).
[2] P. Bartlett, R. H. Ottewill, and P. N. Pusey, Phys. Rev. Lett. **68**, 3801 (1992).
[3] M. D. Eldridge, P. A. Madden, and D. Frenkel, Nature (London) **365**, 35 (1993).
[4] E. Trizac, M. D. Eldridge, and P. A. Madden, Mol. Phys. **90**, 675 (1997).
[5] X. Cottin and P. A. Monson, J. Chem. Phys. **102**, 3354 (1995).
[6] P. N. Pusey and W. van Megen, Nature (London) **320**, 340 (1986).
[7] S. Hachisu and S. Yoshimura, in *Physics of Complex and Supermolecular Fluids*, edited by S. A. Safran and N. A. Clark (Wiley, New York, 1987), pp. 221-240.
[8] C. J. Kiely, J. Fink, M. Brust, D. Bethell, and D. J. Schiffrin, Nature (London) **396**, 444 (1998).
[9] J. V. Sanders, Philos. Mag. A **42**, 705 (1980).
[10] M. J. Murray and J. V. Sanders, Philos. Mag. A **42**, 721 (1980).
[11] E. Yablonovitch, Phys. Rev. Lett. **58**, 2059 (1987).
[12] S. John, Phys. Rev. Lett. **58**, 2486 (1987).
[13] D. Frenkel, Phys. World **6**, 24 (1993).
[14] M. D. Eldridge, P. A. Madden, P. N. Pusey, and P. Bartlett, Mol. Phys. **84**, 395 (1995).
[15] H. Xu and M. Baus, J. Phys.: Condens. Matter **4**, 663 (1992).
[16] W. G. T. Kranendonk and D. Frenkel, Mol. Phys. **72**, 679 (1991).
[17] S. M. Underwood, W. van Megen, and P. N. Pusey, Physica A **221**, 438 (1995).
[18] A. R. Denton and N. W. Ashcroft, Phys. Rev. A **42**, 7312 (1990).
[19] S. J. Smithline and A. D. J. Haymet, J. Chem. Phys. **86**, 6486 (1987).
[20] P. Bartlett, R. H. Ottewill, and P. N. Pusey, J. Chem. Phys. **93**, 1299 (1990).
[21] M. D. Eldridge, P. A. Madden, and D. Frenkel, Mol. Phys. **80**, 987 (1993).
[22] M. D. Eldridge and P. A. Madden, Mol. Phys. **79**, 105 (1993).
[23] The NiAs structure was not actually included in either calculation. However, the packing efficiencies of NiAs are identical to NaCl and so in the spirit of the maximum packing principle we expect the free energies of these two structures also to be very similar. In that case, the *LS* compound predicted by both of these approaches at $\alpha \sim 0.4$ probably should have either a NaCl, NiAs, or an equivalent random-stacked structure (see Sec. V).
[24] L. Antl, J. W. Goodwin, R. D. Hill, R. H. Ottewill, S. M. Owens, S. Papworth, and J. A. Waters, Colloids Surface **17**, 67 (1986).
[25] R. Jardine and P. Bartlett (unpublished).
[26] P. N. Pusey and W. van Megen, J. Chem. Phys. **80**, 3513 (1984).
[27] W. G. Hoover and F. H. Ree, J. Chem. Phys. **49**, 3609 (1968).
[28] P. N. Pusey, W. van Megen, P. Bartlett, B. J. Ackerson, J. G. Rarity, and S. M. Underwood, Phys. Rev. Lett. **63**, 2753 (1989).
[29] P. Bartlett, P. N. Pusey, and R. H. Ottewill, Langmuir **7**, 213 (1991).
[30] A. Guinier, *X-Ray Diffraction* (Freeman, London, 1963).
[31] The definition of c^* used here is twice the commonly used hcp reciprocal-lattice spacing. As a result, the index l is half the value of the conventional hcp value.
[32] B. E. Warren, *X-Ray Diffraction* (Addison-Wesley, Reading, MA, 1969).
[33] P. Pusey, in *Liquids, Freezing and Glass Transition*, edited by J. P. Hansen, D. Levesque, and J. Zinn-Justin (North-Holland, Amsterdam, 1981), pp. 763–942.
[34] P. Bartlett, J. Phys. C **2**, 4979 (1990).
[35] J. P. Voisey and P. Bartlett (unpublished).